

LUND UNIVERSITY

Λ/K0s Associated with a Jet in Central Pb–Pb Collisions at √sNN = 2.76 TeV Measured with the ALICE Detector

Richert, Tuva

2016

Document Version:
Publisher's PDF, also known as Version of record

Link to publication

Citation for published version (APA):
Richert, T. (2016). *Λ/K0s Associated with a Jet in Central Pb–Pb Collisions at √sNN = 2.76 TeV Measured with the ALICE Detector*. Lund University, Faculty of Science, Department of Physics.

Total number of authors:
1

General rights
Unless other specific re-use rights are stated the following general rights apply:
Copyright and moral rights for the publications made accessible in the public portal are retained by the authors and/or other copyright owners and it is a condition of accessing publications that users recognise and abide by the legal requirements associated with these rights.
• Users may download and print one copy of any publication from the public portal for the purpose of private study or research.
• You may not further distribute the material or use it for any profit-making activity or commercial gain
• You may freely distribute the URL identifying the publication in the public portal

Read more about Creative commons licenses: https://creativecommons.org/licenses/

Take down policy
If you believe that this document breaches copyright please contact us providing details, and we will remove access to the work immediately and investigate your claim.

LUND UNIVERSITY

PO Box 117
221 00 Lund
+46 46-222 00 00



Λ/K^0_S Associated with a Jet in Central Pb–Pb Collisions at $\sqrt{s_{NN}}$ = 2.76 TeV Measured with the ALICE Detector

TUVA RICHERT | FACULTY OF SCIENCE | LUND UNIVERSITY



Front page illustration by Lena Richert

Λ/K^0_S associated with a jet in central Pb–Pb collisions at $\sqrt{s_{NN}}$ = 2.76 TeV measured with the ALICE detector

Tuva Richert

Thesis submitted for the degree of
Doctor of Philosophy

2016



Lund University

ABSTRACT

In high energy heavy ion collisions, the QCD matter undergoes a phase transition to a hot and dense strongly coupled *Quark Gluon Plasma*, where quarks and gluons are deconfined in a volume of nuclear dimensions. At intermediate p_{T}, $2 < p_{\mathrm{T}} < 8$ GeV/c, a decoupling from pure hydrodynamical flow is observed, most noticeable in central collisions, demonstrated by the peak in the ratio of baryons to mesons, e.g. the $\Lambda/\mathrm{K}^0_{\mathrm{s}}$ ratio, compared to measurements in pp collisions. At high p_{T} (>10 GeV/c), the particle production is dominated by jet fragmentation, where it is understood that these jets have suffered large energy losses propagating through the dense QGP.

The goal of this thesis is to experimentally investigate the baryon-to-meson anomaly at intermediate p_{T}, and to determine its origin, i.e. if it is an effect arising from the soft, collective, part (the bulk) of the medium, or from the hard processes (modified jet fragmentation). This will be done by analyzing central Pb–Pb collisions at $\sqrt{s_{\mathrm{NN}}} = 2.76$ TeV from the ALICE experiment recorded in the 2011 heavy ion run period. For this analysis, a novel two-particle correlation technique called the *η-reflection method* is developed, where a separation can be made of the contributions from Λ and $\mathrm{K}^0_{\mathrm{s}}$ particles produced in the soft underlying events from those which are produced in association with a high-p_{T} trigger particle, representing a jet-like environment. The aim of this analysis is to separate the hadron production associated with the jet from that of the bulk, and to measure the $\Lambda/\mathrm{K}^0_{\mathrm{s}}$ ratio at intermediate p_{T} in the bulk and jet-like environment, to see how the baryon-to-meson anomaly differs in the two regions.

The results show that at intermediate p_{T} the hadron formation is dominated by the expanding and cooling Quark Gluon Plasma, giving rise to the anomalous overabundance of Λ over $\mathrm{K}^0_{\mathrm{s}}$ which characterizes the inclusive results. The production of $\mathrm{K}^0_{\mathrm{s}}$ and Λ associated with a high-p_{T} trigger particle (presumably a leading hadron in a jet) is quite similar to that observed in pp collisions, i.e. unaffected by the processes in the dense, colored medium.

POPULÄRVETENSKAPLIG SAMMANFATTNING

Denna studie handlar om att experimentellt karakterisera ett materietillstånd som existerade under de första miljondelarna av en sekund under Big Bang, som vi kallar för *Kvark-Gluon-Plasma*. Med stora partikelacceleratorer som Large Hadron Collider (LHC) vid CERN, kan vi genom kärnkollisioner med mycket hög energi nå så pass extrema temperaturer och densiteter att vi kan återskapa och studera detta tillstånd under kontrollerade former i laboratoriet. Mätinstrumentet som används är ALICE-experimentet.

För att sätta mitt forskningsområde i perspektiv, måste vi först prata om materia i allmänhet. Den stabila materiens minsta byggstenar är kvarkar som binds samman till protoner och neutroner med kraftförmedlare för den starka kraften, gluoner. Egenskapen hos kvarkarna som genererar den starka växelverkan benäms *färgladdning* (i analogi med den elektriska laddningen som genreras av elektroner och förmedlas av fotoner). Standardmodellen är en teori som med fantastisk noggranhet beskriver hur alla fundamentala partiklar växelverkar, trots att man inte kan detektera en *fri* kvark. Kvarkar uppträder nämligen alltid bundna till större partiklar med totalt tre kvarkar ("baryoner"), eller en kvark och en antikvark ("mesoner"), med samlingsnamnet *hadroner*. I denna avhandling studerar jag neutrala Λ-baryoner och neutrala K^0_s-mesoner, och hur deras produktion i kärnkollisionerna påverkas av Kvark-Gluon-Plasmat vi skapar i dessa kollisioner.

Anledningen till att kvarkarna är bundna till andra kvarkar eller antikvarkar är en fundamental egenskap hos den starka kraften. Om man försöker sära på kvarkarna i en proton genom att tillföra energi, kommer den sammanhållande kraften inte avta med avståndet (som t.ex. den elektromagnetiska kraften gör), utan förblir istället konstant med det ökade avståndet. En analogi som vi alla känner igen är kraften i ett gummiband som ökar ju mer det sträcks ut, tills det till slut går sönder. När "gummibandet" mellan kvarkarna sträcks ut med hjälp av den tillförda energin, kommer man så småningom till ett läge där det blir lättare att skapa ett nytt kvark-antikvarkpar från energin (enligt Einsteins berömda ekvation som omvandlar energi till massa, $E = mc^2$) än att fortsätta dra iväg kvarken. De nya materialiserade kvarkarna bildar således nya hadroner.

I denna avhandling går vi åt andra hållet. Om vi fortsätter analogin

med gummibandet mellan kvarkarna, skulle detta, om man pressar ihop kvarkarna, hänga slakt, och kraften mellan kvarkarna skulle minska. De skulle *känna* sig fria, men förstås fortfarande inte kunna sticka iväg. För att pressa samman kvarkarna, och dessutom bilda tusentals nya kvark-antikvarkpar, låter vi blykärnor kollidera vid mycket hög energi i acceleratorn på CERN. Det sker tusentals proton-proton kollisioner i en och samma smäll, och vi får då ett sammanpressat system där kvarkarna och gluonerna inte vet till vilken proton eller neutron de tillhörde från början. Det är detta tillstånd som är Kvark-Gluon-Plasma. När vi krockar blykärnor med varandra skapar vi alltså först ett Kvark-Gluon-Plasma som är extremt hett; med en temperatur på 1000000000000 grader — hundratusen gånger temperaturen i solens centrum — slår vi faktiskt världsrekord i temperatur som uppnåtts i laboratorie-experiment. Den heta materian expanderar snabbt och kyls ned, följt av hadron-bildning, likt den som skedde när universum expanderades och kyldes ner efter Kvark-Gluon-Fasen i Big Bang. Restprodukten av den här hadroniserings-processen är de partiklar som kan detekteras — antingen direkt, om de är långlivade nog att nå vårt detektorsystem ALICE, eller via deras dotterpartiklar, om de hinner sönderfalla på vägen. De hadroner som studeras i avhandlingen (K^0_s och Λ) är sådana som måste fångas via deras sönderfall till dotterpartiklar.

När man studerar blykollisionerna vill man ha något att jämföra med som vi känner till väl. Om kärn-kärn kollisionen bara vore en överlagring av ett tusental oberoende proton-proton kollisioner, vore det en ointressant komplikation av mätningen med tusen gånger fler partiklar på samma gång. Så är det förstås inte. En mängd nya fenomen uppträder när man jämför proton-proton data med kärn-kärn data. Skillnaden är att Kvark-Gluon-Plasmat bildas, och detta sker vid en viss temperatur och energitäthet. När det bildats flera tiotusentals beståndsdelar i en volym som motsvarar en atomkärnas storlek, blir det möjligt att studera detta komplicerade mångpartikelsystem med något som kan beskrivas som den starka växelverkans termodynamik, eller snarare hydrodynamik, d.v.s. statistiska system som kan karakteriseras med relativt enkla sammanfattande storheter som temperatur, tryck, täthet och entropi.

Även om det makroskopiska systemet som helhet kan beskrivas i enkla termer, vill vi ju också studera plasmats egenskaper på mikroskopisk nivå eftersom vi där kan analysera kvarkar som är så "fria" som vi för-

modligen någonsinn kan hoppas på (enligt standardmodellen). En speciell typ av reaktion på kvarknivå kallas för *hård spridning*. Det innebär att en stor del av den inkommande rörelsemängden i strålriktningen hos två kolliderande kvarkar omvandlas till rörelsemängd vinkelkrätt mot strålriktningen. När detta sker i proton-proton kollisioner är resultatet slående: två skurar av hadroner, så kallade *jets*, kommer ut i diametralt motsatta riktningar. När motsvarande fenomen uppträder i kärn-kärn kollisioner med Kvark-Gluon-Plasma ser man ofta bara *en* jet istället för två. Eftersom rörelsemängden måste bevaras, måste den ena kvarken växelverkat med Kvark-Gluon-Plasmat, och därmed förlorat energi och rödelsemängd. Att förstå de mekanismer med vilka detta sker är nyckelfrågor när vi ska studera Kvark-Gluon-Plasmats egenskaper.

I denna avhandling utvecklar och testar vi först en metod att isolera jets som har förlorat energi till plasmat och därför bromsats ner så att dess hadroner har energier som är ganska lika de hadroner som härrör från det expanderade plasmats avkylning och kondensation till hadroner. Metoden visar sig fungera utmärkt. Genom att specialstudera förekomsten av K^0_s-mesoner och Λ-baryoner finner vi att det kondenserande plasmat ger ca 1.6 gånger fler Λ-baryoner än K^0_s-mesoner, medan hadroner som har jet-ursprung innegåller ungefär 3 gånger fler K^0_s än Λ. Det senare förhållandet är i huvudsak detsamma som man ser i jets från proton-proton kollisioner där inget Kvark-Gluon-Plasma bildas — med andra ord: passagen genom plasmat verkar inte ha förändrat jetens hadronsammansättning, trots att den kinematiskt ändrats mycket genom energiförlust i sin väg genom plasmat. Att förstå det abnorma förhållandet mellan baryonen Λ och mesonen K^0_s när Kvark-Gluon-Plasmat hadroniserar är förstås ett viktigt led i forskningen. Att kunna separera bidragen från hård spridning med nedbromsade jets från bidraget från det avsvalnande plasmat, som introduceras i detta arbete, är därför av utomordenlig vikt för de fortsatta studierna.

PERSONAL ACKNOWLEDGMENTS

During the course of this work, I have had the opportunity to get to know, and work with, so many fantastic people. The CERN atmosphere, and the work environment in Lund, have inspired me in many ways. It has not always been easy, but my colleagues, friends and family have always been there for me. Always. Each and every one of you have contributed in one way or another, and I want to thank all of you.

Special thanks goes to my supervisors, who have known me for a long time now, and who truly are the best three persons I could have had at my side during this time. Peter, thank you for making this possible, for always starting a conversation with positive feedback, for believing in this analysis, for your invaluable help and ideas, and for your endless patience with me. Anders, thank you for your unlimited support, for never saying no to anything I want to do, for always having time for me, explaining how everything works (sometimes it feels like your brain is an extension of my own) — you are my scientist role model. Evert, thank you for always being on my side and for making Lund a better place!

I want to thank Martin and Vytautas for sharing many days and office hours together, for hugging me when I have a bad day, and for always making conferences fun. Thanks to Bozena for all help and for giving me so many vegetables from your garden, David and Else for support and reading, Torsten for always ending up saving my life, and many thanks to all others at the particle physics division in Lund. And, of course, I want to thank the ALICE collaboration which has provided enormous resources for me to use, my Physics Working Groups, both the Light Flavor and Correlations, especially the conveners of these groups. David for believing in my analysis and inviting me to Brazil to work with you, Xitzel and Antonin for the nice cooperation. Thanks to Christian for trusting me with the TPC, and for giving me so many responsibilities. I have really grown with it. Believe it or not, I have loved to work in the cave, and I'm proud of every single scar on my body (I have at least two that will last for life — I will show them to my grandchildren).

Lene. Yes, I admit it's a crazy adventure. Do you remember when we built those horrible cooling fans? I hope I will have the possibility to show you the real TPC one day... It's a master piece. Thanks for everything. From the beautiful christmas, whiskey evenings, vacations, and kitchen

hang-outs, to the early morning walks to Fysicum, problem solving, and the thorough reading of my thesis draft.

Mom, I want to thank you for always encouraging me to grow in all directions, and helping me to reach my goals. For listening and comforting. For being my feminist role model. Dad, I want to thank you for showing me the other side of the world when work&winter is just too much. Even though I met you for the first time 8 years ago, I have felt your love my whole life. Thank you for being in my life. Many thanks to Simon, Arbulena, and Jet for thinking I'm doing something big. Sabina for comfort, joy and walks on Alvaret. Thanks to Camilla&Len for always making me feel so welcome in your home. Jag vill också tacka Caspian&Miranda för alla mysiga bus-kvällar med bakning, mahjong, fotboll och sagostunder — jag älskar er så mycket att jag nästan spricker!

Gog, thank you for breaking all the norms with me, for the trusting atmosphere, the stability, emotions and adventures. For the endless number of butterbrot breakfasts. Ulrika for the Wine&Kotch; tent nights, dance nights, summer nights. For always being only one stair away, and for so often giving me your shoulder to cry on. Thanks to Annelie for making me happy, Matilda for cosy hang-outs, Ida for waking me up with your trumpet and for cooking amazing Asian dinners, Maria for intense discussions about art&science&human behavior, Marta for sharing your dreams, Sofie for Skog&Mark, Lena for the love we shared, Stefanie for all lunches, Hanno for your wonderful friendship, and Leonora for being exactly what I need at CERN.

...and a last thank to Pink Floyd and Virginia Woolf who made me survive all this.

Table of Contents

1 Preamble **13**

1.1 The Quark Gluon Plasma 13
1.2 Measuring Quark Gluon Plasma 15
1.2.1 Heavy Ion Collisions 15
1.2.2 A Large Ion Collider Experiment 17
1.3 Research Focus 18
1.4 The Author's Contributions 19
1.5 The Outline of This Thesis 22

2 Fundamental Description of The QGP **23**

2.1 The "Quark" in Quark Gluon Plasma 23
2.1.1 Spin 24
2.1.2 Electric Charge 25
2.1.3 Color Charge 25
2.1.4 Weak Isospin 26
2.1.5 A Word About Forces 27
2.2 The "Gluon" in Quark Gluon Plasma 28
2.2.1 Screening in QED 29
2.2.2 Screening and Anti-Screening in QCD 29
2.2.3 The Strong Coupling Constant 31
2.2.4 Color Confinement 33
2.3 The "Plasma" in Quark Gluon Plasma 33
2.3.1 Deconfinement 33
2.3.2 The QCD Phase Diagram 34

3 QGP in Heavy Ion Collisions **37**
3.1 Collision Geometry . . . 38
3.2 Quark Gluon Plasma Formation . . . 40
3.3 Expansion, Hadronization and Freeze-out . . . 41
3.3.1 Particle Yields . . . 43
3.3.2 Collectivity . . . 46
3.4 Jet Quenching . . . 53
3.4.1 Parton Fragmentation . . . 53
3.4.2 Reference Data . . . 55
3.4.3 The Nuclear Modification Factor . . . 56
3.4.4 Particle Production Ratios . . . 58
3.5 Quark Coalescence . . . 61
3.5.1 The EPOS Model . . . 63
3.6 Thesis Research Focus . . . 64

4 ALICE **67**
4.1 Subsystem Detectors . . . 70
4.1.1 Central Detectors . . . 70
4.1.2 Forward Detectors . . . 72
4.2 The Inner Tracking System . . . 72
4.2.1 The Silicon Pixel Detector . . . 73
4.2.2 The Silicon Drift and Strip Detectors . . . 74
4.3 The Time Projection Chamber . . . 74
4.3.1 The Detector Design . . . 75
4.3.2 Operation . . . 76
4.3.3 Replacing FECs . . . 79
4.3.4 Read Out Control Unit Upgrade . . . 80
4.4 The VZERO Detector . . . 81
4.5 Data Acquisition and The Trigger System . . . 83
4.6 Track Reconstruction . . . 84
4.6.1 Cluster Finding and Preliminary Primary Vertex . . . 84
4.6.2 TPC-ITS inward tracking . . . 84
4.6.3 Outward Tracking . . . 86
4.6.4 Last Tracking Stage and Final Vertex Position . . . 86
4.7 Particle Identification (PID) . . . 87
4.7.1 Charged Hadrons . . . 87
4.7.2 **V0** Particle Identification . . . 90

5 Analysis: Λ/K_s^0 associated with a jet **93**
5.1 The η-reflection Method . . . 93
5.2 Selections . . . 98
5.2.1 Data and Event Selection . . . 98
5.2.2 $\mathbf{K_s^0}$ and $\mathbf{\Lambda}$ Particle Selection . . . 100
5.3 Inclusive Particle Yields . . . 112
5.3.1 The Transverse Momentum Spectra . . . 112
5.3.2 Signal Extraction and Uncorrected Yields . . . 113
5.3.3 Corrections . . . 116
5.3.4 MC Closure . . . 121
5.3.5 Corrected Inclusive Yields . . . 122
5.3.6 Investigating Experimental Period Dependences . . . 125
5.4 A Word Before Starting . . . 129
5.5 Trigger Particle and Region Selection . . . 129
5.5.1 Track Quality . . . 129
5.5.2 Peak and Bulk Region . . . 132
5.6 Signal Extraction . . . 132
5.6.1 Raw p_T spectra . . . 134
5.7 Corrections . . . 137
5.7.1 Acceptance Effects . . . 137
5.7.2 Underlying Event Structures . . . 140
5.7.3 Efficiency . . . 140
5.7.4 Feed-down . . . 145
5.7.5 Corrected Spectra And Ratios . . . 149
5.8 Varying $\Delta\eta$ And $\Delta\varphi$ . . . 150
5.9 Systematic Uncertainties . . . 154
5.9.1 Uncertainties Associated to Corrections . . . 154
5.9.2 Selection Criteria Variations . . . 156
5.9.3 Total Systematic Uncertainties . . . 160

6 Results **165**
6.1 The K_s^0 and Λ Bulk, Peak and Jet Yield . . . 166
6.2 The Λ/K_s^0 Ratio . . . 168

7 Discussion and Conclusion **173**
7.1 Surface bias . . . 173
7.1.1 Theoretical Considerations . . . 174

7.1.2 Experimental Considerations 174
7.2 The Λ/K_s^0 Ratio Compared To Other Results 178
7.3 Summary of Observations and Conclusions 181
7.3.1 Physics Conclusions 181
7.3.2 Method Conclusions 182
7.4 Outlook 183

A The Inclusive Analysis **185**
A.1 Anti-Lambda 185
A.2 2010 vs. 2011 MC difference 186

B The η-reflection Correlation Analysis **187**
B.1 Invariant Mass Distributions and Fits 187
B.2 Injected MC Efficiency 187
B.3 Systematic Uncertainties for Spectra 187

C Units and variables **197**
C.1 Rapidity and Pseudo-Rapidity 197

Chapter 1

Preamble

From what we know about the stars and galaxies, the universe evolved from the Big Bang 14 billion (10^9) years ago. After $\sim$10 μs the quarks formed protons and neutrons, which built up light nuclei in the coming seconds up to a few minutes, and 400 thousand years before atoms formed and the universe became transparent. It took 300 million years for stars to form, where heavier nuclei were created by fusion in supernovae. Debris from these exploding supernovae could then form planetary systems, like the solar system. This evolution is illustrated in Fig. 1.1. Before the existence of protons and neutrons, the quarks and gluons (*partons* with a common name) were in a deconfined phase called Quark Gluon Plasma (QGP).

The structure, behavior, and interaction patterns of atoms, nuclei, protons and neutrons, can be studied in laboratories, and are relatively well known today. The properties of the state of matter before these well known objects were created, are still a bit of a mystery due to the obstacles we are facing when studying it — even though we have been able to create QGP in the laboratory for $\sim$30 years. One of these obstacles is the need for internal "probes" instead of being able to observe the properties directly.

1.1 The Quark Gluon Plasma

Quarks are bound together within hadrons via the strong interaction — one of the fundamental forces of the universe. The theory of the strong interaction is *Quantum Chromodynamics* (QCD). The force is mediated by

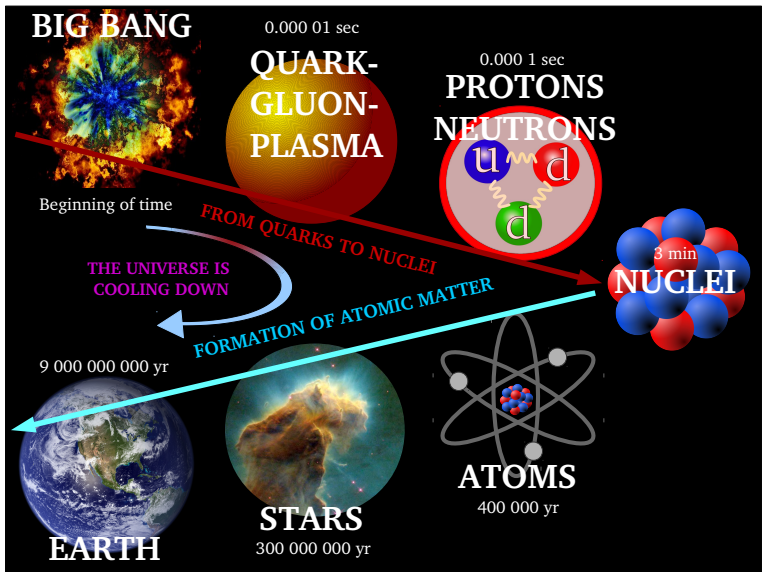


Figure 1.1: An illustration of the evolution of the universe from Big Bang to today. The QGP deconfined state existed before the formation of protons and neutrons.

exchange particles called *gluons*, which carry the property of *color charge*, just like the quarks themselves. This causes the gluons to not only interact with the quarks, but also with other gluons (unlike the photons in the electromagnetic interaction), making QCD an extremely complex theory.

In the complex nature of this theory, the concept of *confinement* arises. Simplified, this means that the strong coupling between quarks and gluons is large at large distances; if one attempts to separate two quarks, a strong color field will be built up to keep the quarks confined. If the energy of these strings is larger than the energy it takes to form a quark+antiquark pair, the string will split to form new hadrons.

The other phenomenon special for the strong interaction is *deconfinement*, which acts in the opposite way: at very small distances, the strong coupling decreases. In extreme temperature and/or density conditions, such as the environment during Big Bang, normal nuclear matter will (according to the theory of QCD) undergo a phase transition to a plasma where the partons are *deconfined* due to the dominance of short distanced interactions.

1.2 Measuring Quark Gluon Plasma

To mimic the universe's Big Bang, we can perform our own human-made Little Bangs. This is done by accelerating heavy ions, e.g. Lead (Pb) or Gold (Au) ions, to ultra-relativistic speeds, and then make them collide. In such collisions, we create the extremely hot and dense environment it takes for normal nuclear matter to undergo the phase transition to a strongly interacting colored plasma.

The goal of creating the QGP in the laboratory is to explore the nuclear matter phase diagram, and the phase transition at extreme temperatures predicted by QCD, study the properties of the QGP, and investigate the hadronization mechanisms, i.e. how particles are created from the QGP. By doing this, we advance our understanding of QCD, including open questions about color confinement.

In addition, results from these collisions are used when constructing models of supernova explosions and neutron stars (which are believed to form QGP in their high density cores) at both sides of the phase transition [1]. Furthermore, it will help us to add more of the missing pieces in the Big Bang puzzle.

1.2.1 Heavy Ion Collisions

In heavy ion collisions, the QGP state lasts for a very short time ($\sim 10^{-22}$ s), before it expands under its own thermal pressure and cools down, so that the strong potential increases. In the *hadronization* phase, partons will again form — and be bound within — colorless hadrons, just as they did in the evolution of primordial universe.

Since the time window where the QGP exists after the collision is extremely short, the QGP will not have time to reach our detectors that we place around the collision point. It is thus impossible to observe the QGP directly, and we will instead measure its final state products, i.e. hadrons from the hadronization process, and use them to derive information about the QGP.

Parallel Lives

The year I was born, 1986, was also the start up of experiments with ultra-relativistic ion collisions at the AGS at BNL, and the SPS at CERN. The year I started school — the same year I had to demolish my own view of the people of Earth living *inside* the planet, with the stars as the roof of the planet, and the land as the floor — AGS started having beams with the very heavy Gold nucleus. When I was 9 years old and Spice Girls was the coolest thing I knew, the SPS fixed target experiments at CERN were using Lead nuclei for the first time in — even heavier than Gold — and came with the first results showing signatures, however not fully conclusive, of the creation of QGP [2]. These initial years of heavy ion physics were very important in the development of the nuclear physics toolkit by which these complicated colliding systems are studied systematically. More or less all what we today call *global observables*, were developed during these years.

During my first teenage year, I had Metallica's symphony album on repeat, completely unaware of RHIC's (at BNL) first results from their 200 GeV/nucleon center of mass energy Gold collisions, showing that the hadron production at high particle transverse momentum (p_{T}) was suppressed compared to collisions of smaller systems, such as Deuteron-Gold (or proton-proton)[1], where no QGP was expected to form, thus indicating the formation of a medium with properties that could quench jets. This medium was also shown to have strong collective behavior, in agreement with expectations based on ideal hydrodynamic flow [3], but quite contrary to asymptotically free constituents of an ideal gas, which had been the prevailing prediction about the QGP up to this result.

A decade later, in 2010, I was a summer student at CERN, just in time for the new accelerator with the highest energy in the world, the Large Hadron Collider's (LHC) first Lead collisions, making a remarkable energy record while producing the hottest state of matter ever created in laboratory, with a temperature of 100 000 times that of the core of the sun. This was the beginning of a new chapter — not only for the field, but also for me.

[1] Today we know that these collisions *might* get close to the phase transition boundary as well. However, the effects are not as pronounced as the matter formed in heavy ion collisions.

1.2.2 A Large Ion Collider Experiment

I will leave the description of the ALICE experiment to Chapter 4, and only explain the concept here. The complex ALICE system must manage to separate and identify up to several thousand particles with a wide range of transverse momenta (typically from 0.1 to 100 GeV/c) in each collision. For this we use different subdetectors that serve different measuring purposes to be able to fully reconstruct the event. The innermost detectors give a picture of the charged particles' tracks, i.e. their path in terms of position in space, direction, and curvature in the magnetic field. From this information, the particle momentum and charge can be revealed. The outer detectors are used to measure the energy deposited by the particles.

In Fig. 1.2, an event display from a Lead-Lead (Pb–Pb) collision, recorded by the ALICE detector system, is shown, making the high multiplicity of tracks in such an event clear; the colored lines represent all reconstructed electrons, muons and charged hadrons. Neutral hadrons are reconstructed by their decay topology (if long-lived enough) combined with the identification of their decay products, which will be described in detail in Sec. 5.2.2.

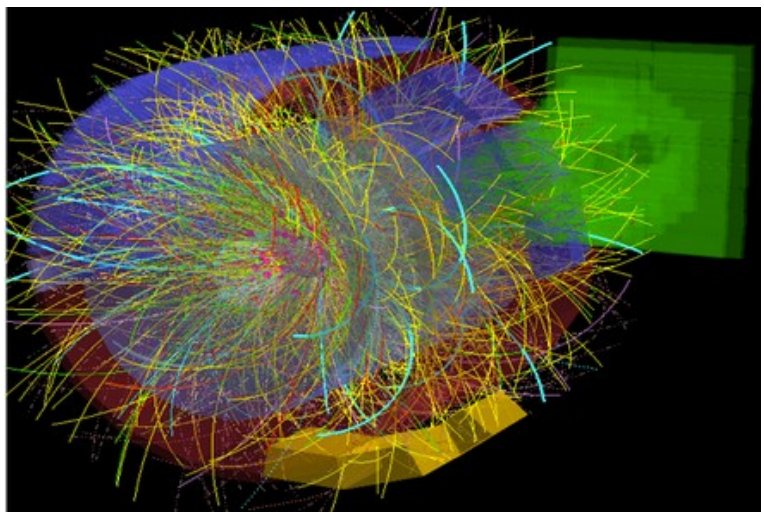


Figure 1.2: Event display from a Pb–Pb collision at a center of mass energy of 2.76 TeV per nucleon pair, recorded by ALICE (6.11.2011). The color lines represent all reconstructed particles.

1.3 Research Focus

The research performed in this thesis, focuses on how particles are produced from the QGP medium, and how the production differs for different kinds of particles. From previous studies, we know that particles with high transverse momentum must have been created in a *hard* physics process, such as jet production (and fragmentation). The particles with low transverse momentum (created in the central rapidity region), on the other hand, are most likely created by thermal *soft* physics processes when the strongly coupled, fluid-like, quark gluon plasma hadronizes.

What happens when we go from the soft to the hard particle production mechanisms? By investigating the particles at the intermediate transverse momentum region, and especially when comparing particles made up by two quarks (mesons), to those which are made up by three quarks (baryons) (examples of such particles are the K^0_s meson and Λ baryon), it is seen that baryons are more frequently produced compared to mesons. This suggests an interplay between the soft and hard production mechanisms. Is there a third production mechanism present in addition to the two mechanisms mentioned above?

There are theoretical models attempting to describe this *baryon-to-meson* anomaly, one of them being the *quark recombination* model, which allows for two or three soft quarks from the bulk of the quark gluon plasma to recombine into a meson or a baryon. These models, however, cannot fully describe the phenomenon, and a more detailed investigation is necessary.

The goal of this thesis is to investigate the baryon-to-meson anomaly at intermediate transverse momentum, and to determine its origin, i.e. if it is an effect arising from the soft, collective, part of the medium, or from the hard processes. This will be done by analyzing heavy-ion collisions from the ALICE experiment by a novel two-particle correlation technique called the *η-reflection method*. This method is able to separate the contributions from K^0_s and Λ particles produced in association with a high-p_T *trigger* particle, representing a jet-like environment, from those produced in the soft bulk of the medium. The aim of this analysis is to study the relative production of K^0_s and Λ particles in the bulk and jet-like environment, to see how the baryon-to-meson anomaly differs in the two regions.

1.4 The Author's Contributions

In a large collaboration like ALICE, with ∼1500 people, nothing is produced entirely by one person. Everyone profits from the work of many others, like those designing and building the experimental setup, people who have built the analysis software packages, and others who maintain, operate, and calibrate detectors so that each detector gives proper information about each particle hit. Every institute being part of the collaboration is expected to contribute to the collective effort by participating in such work. Experimental hardware laboratory work has been an important part for me during the course of this thesis. I have been heavily involved in detector hardware installation of improved front end electronics and read out for the Time Projection Chamber. I was one of two coordinators during the successful installation of the TPC Read Out Electronics upgrade to RCU2, which will be described in the detector overview part, Chapter 4, of this thesis.

Due to the collective effort of all people involved in the experiment, the articles produced by ALICE always have the names of everyone in the collaboration as authors, even though only a small group of people have been performing the analysis itself. The analysis, however, must be continuously followed up by the Physics Analysis Group (PAG), which, in practice implies that one has to make regular reports and updates to the specific PAG so the other members can give feedback and suggestions. This effectively means that everyone in a PAG contributes to its associated analyses.

Since everybody in the collaboration is an author to all ALICE papers, the analysis and its results need to be approved by the whole collaboration to be published. This is done in different steps: first on PAG-level, then in the Physics Working Group, and then the final Physics Forum approval. Through each of these steps, a dedicated Analysis Review Committee is appointed, whose task is to carefully review the documentation about the analysis, and suggest improvements and give feedback.

Since ALICE is the only experiment focusing on heavy ion collisions at LHC energies, the results produced here cannot be reproduced by an independent experiment, which otherwise is an important part of science in general. Therefore, it is crucial to repeat the *analysis* itself, to cross check the validity of that specific measurement. Along the way of my analysis,

carried out in this thesis, I reproduced already published results as a cross check that my analysis framework is accurate, and as a validation of the existing results.

The η-reflection analysis presented in this thesis, with results being the $\Lambda/\mathrm{K}^0_\mathrm{s}$ ratio in jet and bulk, are produced by myself as the main analyzer, and approved by the ALICE collaboration Physics Forum for publication, where I am the chair of the paper committee. The study aims to provide further insight into the strongly enhanced baryon-to-meson ratio observed at intermediate p_T in central Pb–Pb collisions. This novel method used for the analysis has been developed by myself and my supervisor Peter Christiansen, where the jet component of the near-side peak correlation function is isolated by subtracting the bulk component measured at a large pseudo-rapidity difference, but at a similar azimuthal angle, to properly subtract the flow modulation.

Additional specific contributions are listed on the next page.

Specific publication contributions:

1. "ALICE summary of light flavour results at intermediate and high p_T", T. Richert for the ALICE Collaboration, *J.Phys.Conf.Ser.* **636** 012009 (2015)

   → [I was active in the Physics Working Group when the results were produced, and selected by the conveners to present a summary of the results at the Winter Workshop Of Nuclear Dynamics, Colorado, 2015. This proceeding is written by myself, and it serves as a basis for the overview of heavy-ion physics in Chapter 3, as well as a motivation for the analysis performed in the thesis.]

2. "Multiplicity dependence of charged pion, kaon, and (anti)proton production at large transverse momentum in p-Pb collisions at $\sqrt{s_{NN}}$ = 5.02 TeV", ALICE Collaboration, arXiv:1601.03658 [nucl-ex] (2016)

   → [My active part was as a member in the Analysis Review Committee, assigned by the Physics Working Group conveners to review and scrutinize the analysis note prepared by the analyzers. Some of the results from this paper are used in the thesis to highlight the difficulty in determining the origin of the baryon-to-meson anomaly, which is the focus of the analysis.]

3. "Trigger-Induced Mechanical Resonances of Gating Grid Wires in the Multi-Wire Proportional Chambers of the ALICE TPC", ALICE Collaboration, *Physics Procedia* **37**, 472-477 (2012)

   → [I am one of the main authors and contributers to the results presented here. It is reflected in the ALICE overview part of the thesis.]

1.5 The Outline of This Thesis

The basic theoretical background to QCD is given in Chapter 2, starting out with introducing quantum numbers, quickly moving on to the properties of the strong force, and ending in the QCD phase diagram. Chapter 3 is a description of how QGP is created with Heavy Ion Collisions, and the different phases the QGP undergoes before the final state particles reach the detectors. The chapter then continues with an overview of QGP signature observables and results related to the research focus of this thesis, placing the analysis topic in a big picture. Before coming to the analysis part, however, the ALICE experiment and sub-detectors are introduced, also here describing the technical hardware part I contributed with, concerning the main tracking detector in ALICE, the Time Projection Chamber.

The next part of the thesis, starting with Chapter 5, is where my own work is described in detail: I give an outline of the new analysis method, continued by the V0 identification (including reproducing the published inclusive K^0_s and Λ particle yields) and region selection procedure, signal extraction, and Monte Carlo corrections. The last part of this chapter is an evaluation of the systematic uncertainties. The results are presented in Chapter 6, followed by a discussion given in Chapter 7, where the results obtained in this thesis are compared to other results. The chapter ends with a summary of the obtained results and the conclusions on both the physics and the method itself, and a short outlook.

> *"Prokrastinerar så det står härliga till. Gör pannkakor med små små urskurna figurer i mango till, upptäcker att jag har mjölbaggar (efter att jag ätit upp pannkakorna) och städar ur alla skåp, läser klart romanen, syr igen ett hål i tröjan, sorterar snäckorna i uppskattad färgyta/totalyta -kvot, tycker plötsligt att det är världens viktigaste att teerna står i godhetsordning, pumpar cykeldäcken trots att jag gjorde det igår, stirrar in i ljuslågan så att ljuspricken inte försvunnit än, skriver facebook-status. Skriver inte avhandling."* (5 Feb 2016)

Chapter 2

Fundamental Description of The Quark Gluon Plasma

2.1 The "Quark" in Quark Gluon Plasma

The quark is a particle with no (known) internal structure, and therefore considered as an *elementary* particle. Together with other elementary particles, for example the electron (belonging to the *lepton* class), they make up matter. The simplest atom is the hydrogen atom, consisting of one proton constituting the nucleus, surrounded by one electron bound to the nucleus by the electromagnetic force (mediated by the photon, γ), one of the four fundamental forces in nature, described by Quantum Electrodynamics (QED). The protons and neutrons are composed of two types of quarks, namely the up and the down quark. The quark model was confirmed in 1969 by deep inelastic scattering experiments at the Stanford Linear Accelerator Center (SLAC) [4] — where it was proven that the proton has an internal structure of point-like objects — but independently predicted 5 years earlier by M. Gell-Mann [5] and G. Zweig [6].

Particles built up by quarks are called *hadrons*. There are two types of hadrons: the *baryon* is made up by three quarks (for example the proton with two up and one down quark), and the *meson* by two quarks (a quark and an anti-quark, e.g. the π^+ meson with one up and one anti-down quark). All hadrons has a quantum number called the *baryon number* defined as $B = (n_q - n_{\bar{q}})/3$, where n_q ($n_{\bar{q}}$) is the number of quarks (anti-quarks) in the particle. Thus, baryons have a baryon number of +1,

mesons have a baryon number of 0, and anti-baryons have a baryon number of -1.

In the years from the first validation of the quark model, up to 1973, there were theoretical predictions (based on e.g. hadron masses and decay pattern observations) about further types of quarks, in addition to the up and down quark. By 1977, five of the total six postulated quarks were discovered at SLAC, Brookhaven National Laboratory (BNL) and Fermilab, and in 1995 the sixth quark (the *top* quark) could be observed at Fermilab.

The up and down quarks were discovered first since they have the lowest masses, consequently, particles made of up and down quarks, such as pions, were easier to produce in collision experiments than particles made of heavier quarks. This also explains why the very heavy top quark was discovered so much later than the others.

The Standard Model is the theoretical framework describing the elementary particles, and with the current knowledge, six types ("flavors") of quarks exist, called *up* (u), *down* (d), *charm* (c), *strange* (s), *top* (t), and *bottom* (b), with their corresponding anti-quark. The different quarks have various intrinsic properties, see Fig. 2.2, such as spin, mass and electric charge. In addition to these, a new *color charge* had to be introduced for the quarks.

2.1.1 Spin

Spin is a particle's intrinsic angular momentum. Its magnitude and direction is assigned as a quantum number to the particles. A particle with integer spin is called a *boson*, and a particle with half-integer spin is a *fermion*. Fermions obey the Pauli exclusion principle [1], stating that two identical fermions cannot occupy the same quantum state at the same time, i.e. at least one property of two fermions has to be different, which can be expressed with an anti-symmetric total wave function.

The six quarks, that can be divided in three families, or *generations*, according to their charge and mass,

$$\begin{pmatrix} \mathrm{u} \\ \mathrm{d} \end{pmatrix} \begin{pmatrix} \mathrm{c} \\ \mathrm{s} \end{pmatrix} \begin{pmatrix} \mathrm{t} \\ \mathrm{b} \end{pmatrix}$$

and the three lepton families — the electron, muon, and tau (e, μ, τ), to-

gether with their corresponding neutrinos (ν_e, ν_μ, ν_τ)

$$\begin{pmatrix}\nu_e\\ e\end{pmatrix}\begin{pmatrix}\nu_\mu\\ \mu\end{pmatrix}\begin{pmatrix}\nu_\tau\\ \tau\end{pmatrix}$$

— are classified as fermions due to their half-integer spin.

2.1.2 Electric Charge

Since all hadrons have integer (0 included) electric charge in units of the elementary charge of the electron (e), e.g. the proton, p (uud), with charge +1, negative kaon, K^- (u$\bar{\text{s}}$), with charge -1, and the neutral lambda, Λ^0 (uds), they must be built up by quarks with charges summing up to an integer. This implies that the values can be either $\pm 1/3$ or $\pm 2/3$, and it turns out that the "up"-type quarks (u, c, and t) have +2/3, the "down"-type quarks (d, s, and b) have -1/3, while the corresponding anti-quarks have the opposite charge. Quarks are subject to electromagnetic interactions since they have electric charge.

We saw examples of particles with -1, 0, and +1 elementary charge, but are there hadrons with other integer charge, like +2? A particle with charge +2 could then contain three up-type quarks, e.g. uuu, since they carry +2/3 elementary charge, but according to Pauli's exclusion principle three identical spin-1/2 quarks cannot be combined. Despite of this, hadrons do exist with +2 elementary electric charge and a total angular momentum of 3/2: "$|\uparrow\uparrow\uparrow\rangle$" — an example is the Δ^{++} resonance. We must therefore introduce an additional quantum number to not violate the exclusion principle, and we call this quantum property *color charge*.

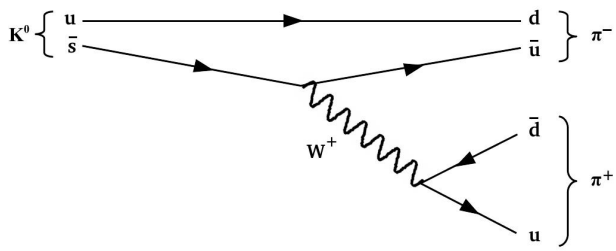
2.1.3 Color Charge

Discovering the spin symmetrical Δ^{++}-state gave birth to the quantum number color charge, and the theory describing interactions between color charged particles, Quantum Chromodynamics (QCD). A quark can have three different color quantum states: red (r), blue (b), or green (g), and the anti-quarks can carry either anti-red ($\bar{\text{r}}$), anti-blue ($\bar{\text{b}}$), or anti-green ($\bar{\text{g}}$). The three different color or color+anticolor states, add up to a colorless state. In this way the baryons, q(r)q(g)q(b), and mesons, e.g. $\text{q(r)}\bar{\text{q}}(\bar{\text{r}})$, are always color neutral particles. It is also due to the fact that quarks

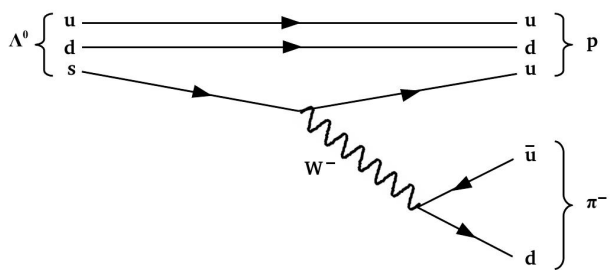
possess color that they cannot exist individually, but only as hadronic confined states. This confinement is a consequence of the strong force where another color carrying particle is the force mediator, namely the *gluon*, described in Sec. 2.2.

2.1.4 Weak Isospin

Quarks can transform into other quarks, thus changing flavor. The flavor changing transformation occurs via the weak interaction[1]. These decays are described by the *weak isospin* (T_3) quantum number — a component of the weak hypercharge unifying the weak and electromagnetic interactions. The up-type quarks have $T_3 = +1/2$, and the down-type quarks have $T_3 = -1/2$. Quarks with the same-sign T_3 never transform weakly into each other, but up-type quarks can transform into down-type quarks, and vice versa.



(a) K^0_S meson decaying to a positive and negative pion



(b) Λ baryon decaying to a proton and a pion

Figure 2.1: Weak decay of K^0_S and Λ represented in Feynman diagrams.

[1]The weak interaction is together with the electromagnetic, strong and gravitational force belonging to the four fundamental forces of the universe.

In these transformations the quark emits or absorbs a weak force mediator particle called $W^{\pm}$ boson (due to their integer spin), and thereby changes flavor. In Fig. 2.1 the Feynman diagrams are drawn for two different hadron decays, where Fig. 2.1(b) illustrates the decay of a Λ-particle into a proton and π^- by emitting a virtual W^--boson from the s-quark, changing the quark flavor from s to u, transforming the Λ to a proton, and in addition forming a π^- by the decay of the W^--boson into the $\bar{u}d$-state. In a similar way the K^0_s-particle can decay into a $\pi^+\pi^-$-pair, but now with the W^+-boson as the force mediator since charge has to be conserved at each vertex.

The example of K^0_s and Λ decay is used here for a reason: it is these two particles that will be used in the analysis of this thesis. To be able to study them, they need to be identified among all the other particles created in a collision experiment, which can be done due to their specific decay topology shown in the diagrams. Since they are both electrically neutral, they will not leave a visible track in the detector, and they have to be identified via their oppositely charged decay products (which do leave tracks in the detector). This, together with the knowledge about their relatively long life time, thus having their point of decay well separated from the point of the collision with a distance long enough for the detector to resolve it.

2.1.5 A Word About Forces

I have so far mentioned the electromagnetic force that couples to electrical charge mediated by photons, the strong force coupling to color charge mediated by gluons (see Sec. 2.2), and the weak force coupling to weak isospin/flavor with $W^{\pm}$ and Z^0 as force carriers. Since quarks have electric charge, color charge and weak isospin, they are affected by all these corresponding forces. Quarks (together with leptons) also have mass, and are then influenced by the fourth fundamental force, gravity. The force mediating particles are all bosons, since they have integer spin. In Fig. 2.2 a summary of all elementary particles and force carriers is given, indicating their mass, electric charge, and spin.

The range of the fundamental forces is determined by the mass of their force mediating particles. The mediator of the gravitational force is still

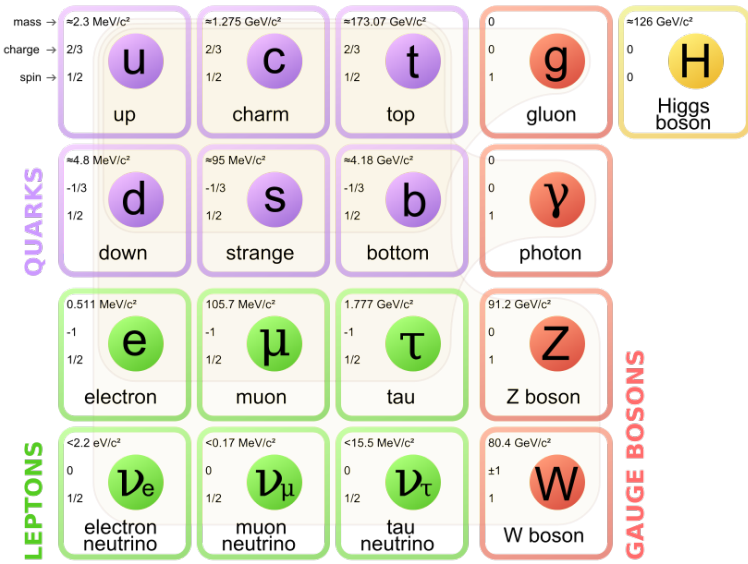


Figure 2.2: The elementary particles of the Standard Model. The mass values are from the Particle Data Group, 2008. Figure taken from [7].

not observed[2], but the prediction is a massless *graviton*, thus explaining why gravity interacts over infinite distances, just like the massless photon gives the electromagnetical force an infinite interaction range. The strong force is different from the other forces: despite the fact that the mediating gluon is massless, the range of the force is short, and in contrary to the other forces, remains nearly constant for distances above $\sim$1 fm.

2.2 The "Gluon" in Quark Gluon Plasma

As briefly mentioned in Sec. 2.1.3, the massless gluon is the force carrier of the short ranged strong force. To have a massless mediator and a short ranged force seems like a contradiction, but the gluon has a property that for example the photons do not have, namely the ability to couple to their own species, i.e. a gluon can couple to other gluons, as well as to quarks. This is because gluons also carry color charge. There are 8 gluon color-anticolor states.

[2]However, recent discoveries confirm the existence of gravitational *waves* [8]

2.2.1 Screening in QED

In QED, a concept called *screening* is introduced to explain the effect of loop diagrams. The Feynman diagram seen in Fig. 2.3(a) shows the loop diagram where a propagating electron emits a virtual photon that fluctuates into an e^+e^- pair for a short time window, and is then absorbed again by the original electron. In the figure, the direction of the electric field is marked with red arrows, indicating that the e^+e^- loop gives rise to vacuum polarization effects, and will generate a field in the opposite direction of the original electron's field, thus creating a smaller total net field.

Scattering diagrams, such as the one seen in Fig. 2.3(b), also contribute to the screening effect, so that the measured response of the coupling constant strength, α_{EM}, depends on the wavelength we probe with; $\alpha_{EM} \sim 1/137$ far away from the electron where the screening effect is large, but with a wavelength 100 times smaller than the proton radius, the screening effect will be reduced since we are getting closer to the electron. The apparent charge of the electron will be $\sim$10% stronger.

The probing wavelength, i.e. the scale of the interaction, is related to the four momentum transfer, Q, of the interaction. Therefore, the coupling strength is often associated with the square of the four momentum transferred in an interaction.

2.2.2 Screening and Anti-Screening in QCD

QCD has a similar vacuum polarization effect illustrated in Fig. 2.3(c) where a virtual $\mathrm{b\bar{r}}$ (blue-anti-red) gluon emitted from the propagating $\mathrm{q(b)}$ (blue quark) splitting into a $\mathrm{q(b)\bar{q}(\bar{r})}$-pair, leaving the original quark with a red color which again absorbs the re-formed gluon. The color field will point away from the initial quarks, as seen by a red arrow, and since the fluctuating $\mathrm{\bar{q}(\bar{r})}$ will be attracted by the original, now *red*, quark, this additional color field will be anti-parallel, resulting in a screening effect. A higher order scattering diagram can be seen in Fig. 2.3(e).

If one-gluon exchanges were the only contribution, the interaction would increase at short distances, just as in QED. This, however, is only a secondary contribution compared to the more dominating effect of *anti-screening*, arising from the gluon self interaction property, giving rise to fluctuations with gluon loops, seen in Fig. 2.3(d) and (f). In this case,

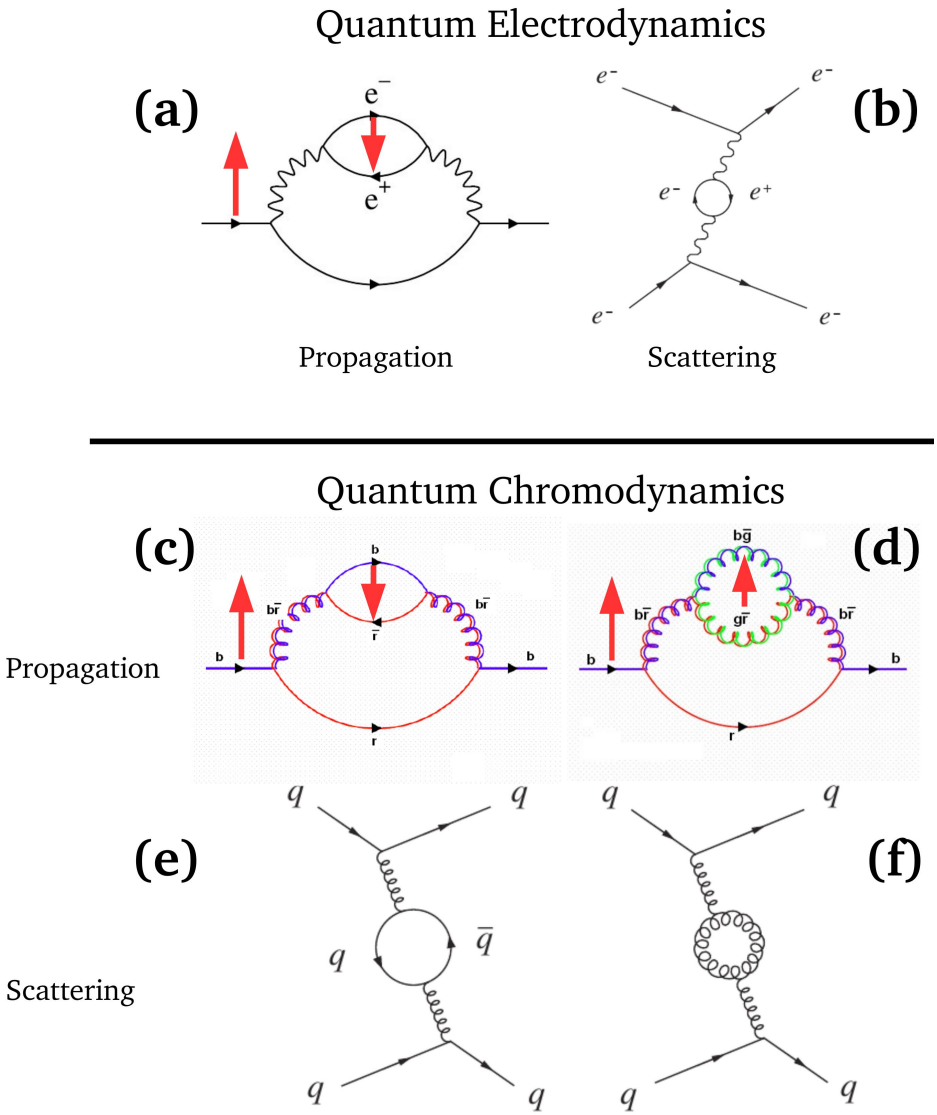


Figure 2.3: QED screening (the electric field arrows in (a) are reversed — pointing *from* the negative charge, for a clearer comparison of QED and QCD screening), and QCD anti-screening concepts.

the green charge (in (d)) will create a field pointing towards the anti-green charge, resulting in a parallel, anti-screening, sub-field compared to the main field, hence enhancing it. The proposal of this phenomenon by Wilczek, Gross, and Politzer 1973 [9] lead to a Nobel Prize in 2004.

2.2.3 The Strong Coupling Constant

The strong coupling strength, g_S, is a QCD parameter depending on the mass scale, μ. The effective coupling constant, α_S, is expressed in terms of the coupling

$$\alpha_S = \frac{g_S^2}{4\pi} \tag{2.1}$$

Due to screening and anti-screening, α_S will have a strength varying with the momentum transfer, Q, where higher order loop diagrams are considered by introducing inverse Q^2-order corrections to the perturbative QCD calculations. At large momentum transfers, α_S is

$$\alpha_S(Q^2) = \frac{\alpha_S(\mu^2)}{1 - b_0\alpha_S(\mu^2)ln(Q^2/\mu^2)} \tag{2.2}$$

where $b_0 = \frac{1}{12\pi}(11N_C - 2N_f)$; N_C originates from anti-screening loops, and is the number of colors, while N_f emerges from screening loops, and is the number of quark flavors [1]. Since there are 3 colors, and 6 flavors, b_0 is positive, explaining why anti-screening dominates.

Where α_S is responsible for confinement, the coupling is equal to the so called "QCD scale": $\mu = \Lambda_{QCD} \approx 200$ MeV. Leading order (LO) perturbative QCD (pQCD) then gives

$$\alpha_S(Q^2) \cong \frac{12\pi}{(11N_C - 2N_f)ln(Q^2/\Lambda_{QCD}^2)} \tag{2.3}$$

This means that for large momentum transfers, the coupling becomes smaller, causing the interaction to be weaker at short distances, a phenomenon called *asymptotic freedom*; at a scale 100 times smaller than the proton radius, $\alpha_S \sim 0.1$. On large distances the interaction strength grows, called *confinement*, discussed in the next section.

In Fig. 2.4 the experimental measurements of the strong coupling constant, α_S, at different energy scales from various scattering processes, together with QCD theoretical calculations taking into account higher order contributions, are shown [10].

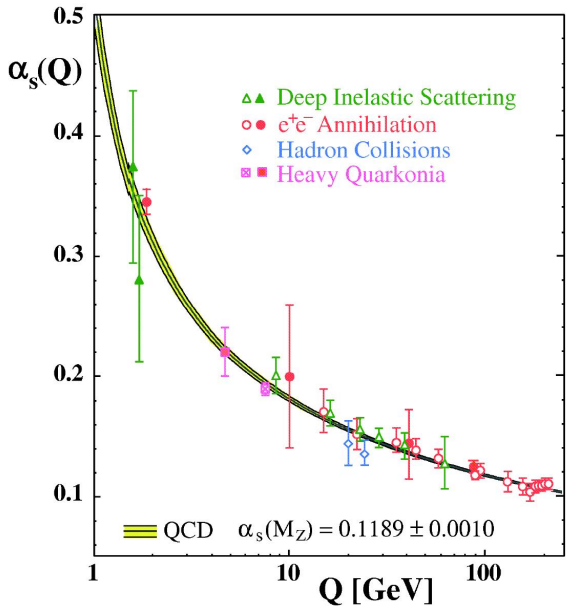


Figure 2.4: Summary of measurements of α_S as a function of the respective energy scale Q. Open symbols indicate NLO, and filled symbols NNLO QCD calculations. The curves are the QCD predictions for the combined world average value of $\alpha_S(M_Z)$, where the scale is M_Z, the mass of the Z boson. Figure taken from [10].

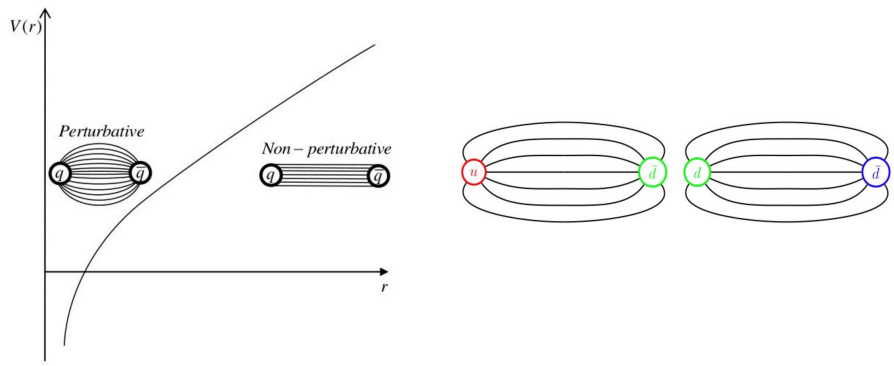


Figure 2.5: The strong interaction potential (left) and an illustration of the splitting of a color string between two separated quarks (right). Image taken from [11].

2.2.4 Color Confinement

The gluon self coupling property leading to the dominant anti-screening of the color charge causes the strong coupling constant to grow as the distance between two color charged objects increases. This is referred to as color confinement. It explains why quarks are bound within hadrons, and cannot be observed individually.

If an attempt to separate two quarks is made, the interaction gets stronger, and higher order diagrams become more important. According to the Lund String Model [12, 13], the gluon field between them will, on large distances, become an almost one-dimensional string with an essentially constant force of $\sim$1 GeV/fm. This string will gain more and more potential energy and eventually favor splitting up by forming a new quark-antiquark pair, making two mesons, as illustrated in Fig. 2.5.

Even though we know the potential of the strong force, the strong interaction regime is very complicated and it has not been possible to calculate exactly how confinement works since the theory cannot be evaluated precisely (approximate results can be obtained from lattice QCD calculations, introduced in the next section). Therefore, to solve this is a long-term goal of heavy ion physics and collider experiments.

2.3 The "Plasma" in Quark Gluon Plasma

2.3.1 Deconfinement

In, for example, a heavy ion collision, the density of mobile charges will be high, in analogy with an electromagnetic plasma (hence the name Quark Gluon *Plasma*) — in this case "charge" refers to color, and "mobile" refers to asymptotically free. The force between two of these charges will be screened by the polarized charges between them (i.e. a different screening than that of vacuum fluctuations), called *Debye screening*. The effect on the strong potential, V_S, in the region where the Coulomb-like potential dominates (i.e. at distances comparable to the nucleon radius) over the almost linearly increasing potential (larger distances) is

$$V_S \propto -\frac{\alpha_S}{r} e^{-r/r_D} \tag{2.4}$$

where r is the distance between the quarks, and r_D is the Debye screening length.

A heavy ion collision creates a dense environment for the participating nucleons. There, the Debye screening length will decrease and at some point pass the radius of a given hadron (all the time with a decreasing potential energy as a result), which will thus *melt* into the rest of the medium, making the partons of that hadron un-bound to that specific hadron, and free to strongly[3] interact with other partons, also initially belonging to other hadrons or $q\bar{q}$-pairs formed in the process. This phenomenon is thus different from asymptotic freedom, but still regarded as a *deconfined* state, in the sense that the partons continue to interact, but now with partons from the whole system volume. This is what we call Quark Gluon Plasma.

2.3.2 The QCD Phase Diagram

The different phases in QCD matter can be mapped in a diagram (similar to that of the phase diagram of e.g. water) showing at what values of temperature, T, and the net baryon number density, a transition from normal hadron matter to a deconfined QGP phase takes place. As seen in Fig. 2.6, at low temperature and baryon number density, the partons are confined to form ordinary colorless hadron matter, but at high temperature and/or baryon number density, the quarks and gluons pass the phase transition and form the deconfined strongly coupled plasma.

Just after Big Bang, the universe started out as a QGP state with a very high temperature but zero net baryon number density (indicated by an arrow in the phase diagram), and during the expansion of the early universe the temperature quickly dropped and the universe entered the hadron gas phase. Another astrophysical example of predicted QGP formation with the completely opposite environment to the early universe, at low temperature and high baryon number density, is the core of a very heavy neutron star.

Also marked in Fig. 2.6 is a *critical point*, T_c, that separates two regions of phase transitions; the transition to QGP is different to the "left" (at lower density and higher temperatures) and to the "right" (at higher density and lower temperatures) with respect to this point. At high densities

[3] The whole system is still color-neutral.

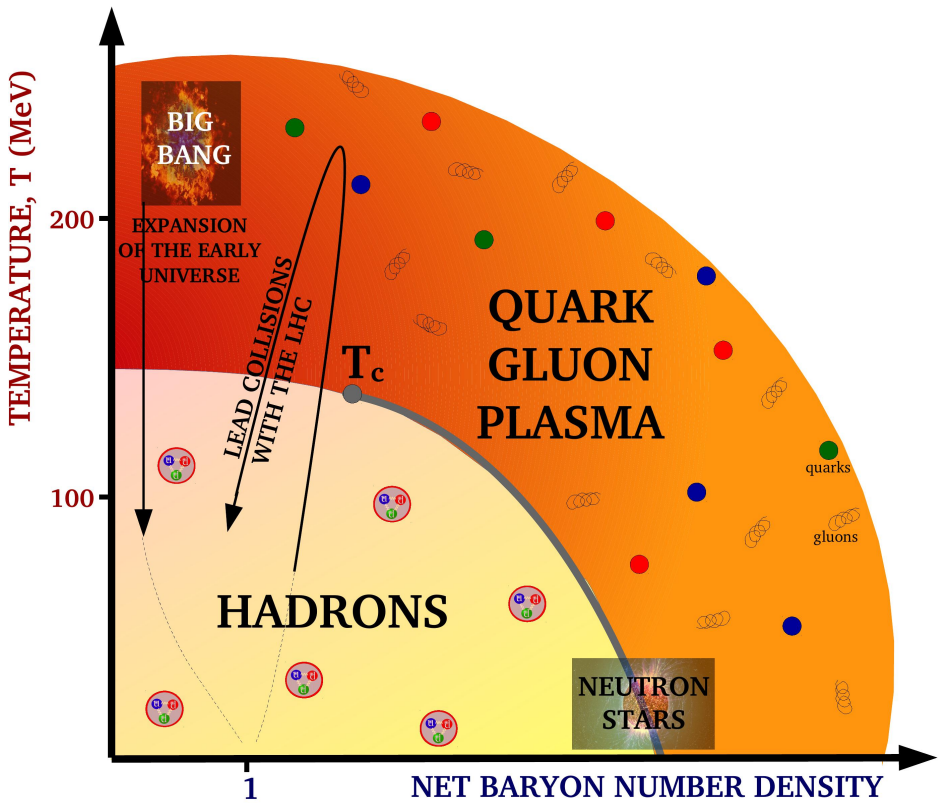


Figure 2.6: Phase diagram of QCD matter in the temperature-net baryon number density plane. At low temperatures and low baryon number densities the phase is ordinary hadron-matter, and at high temperatures and/or high baryon number density the matter enters the QGP phase. The diagram also indicates how the early universe evolved through the phases, where the neutron stars are located, and the time evolution of a heavy ion collision.

and low temperatures, the phase transition is expected to be of first order with a distinct boundary, while for low densities and high temperatures it is a second order phase transition, i.e. it is a smooth change between the two phases, in which a mixture of both hadrons and parton plasma exists [14]. To understand the nature of the phase transition is one of the goals of heavy ion physics.

In highly relativistic collisions of heavy ions, a fireball is created which expands under its own thermal pressure and thereby cools down. Collisions of this type are characterized by high initial temperature and pressure, and the time evolution during these heavy ion collisions is described by a loop (indicated by the arrow in Fig. 2.6) in the phase transition diagram.

Lattice QCD

As mentioned in Sec. 2.2.3, perturbative methods can be used in some limited cases, for example at large momentum scales when the strong coupling is small, or when studying the interactions of high-p_{T} partons traversing the QGP, resulting in a suppression of high-p_{T} hadrons, a phenomenon called *jet quenching*, discussed in Sec. 3.4.1. But pQCD is far from a satisfying theory framework to describe the bulk partonic phase in a QGP.

The QCD calculations are instead done numerically on a *lattice* ("lattice QCD"), meaning that space-time is descretized, and finite temperature equilibrium systems can be studied [15] and used as input for (e.g. hydrodynamical) models of the QGP. This lattice gauge theory is the best existing theoretical tool describing QGP properties and predicts experimental observables, but it can only calculate static quantities.

By these simulations, a phase transition and the critical temperature, T_c, of the medium when the transition takes place can be predicted. Current calculations predict $T_c \approx 160$ MeV [16], corresponding to an energy density of $\epsilon_c \sim 1\ \mathrm{GeV/fm^3}$.

> *"Is it time for a few days vacation when I start to seriously consider if it's not faster to figure out a way to get my thesis from the parallel universe where it's already written, than to actually write it...?"* (31 Dec 2015)

Chapter 3

Quark Gluon Plasma Created in Heavy Ion Collisions

The main purpose of heavy-ion physics is to explore the QCD phase transition. Relativistic heavy ion collision experiments make it possible to reach sufficiently high energy densities to study the different stages of the QGP formation and hadronization. Figure 3.1 illustrates how the QGP passes through two stages, the hadronization and the freeze-out, before the final particle composition that we observe is fixed.

Studying the QCD phase transition can only be done by comparing real data to theoretical models, and since many of the models are based on observed experimental results, it is difficult to discuss the theory and data results separately. In this thesis I have chosen to present the definitions of the collision geometry and the stages of the time evolution before introducing and discussing the QGP observables and results of heavy ion collisions, also then reflecting on the particle production mechanisms, and the interpretation of how the probes (the produced particles) are affected by the medium.

This chapter serves as an overview of heavy ion physics in the eyes of ALICE, with the purpose to lead up to the research topic presented in the analysis chapter, where all results are produced by myself.

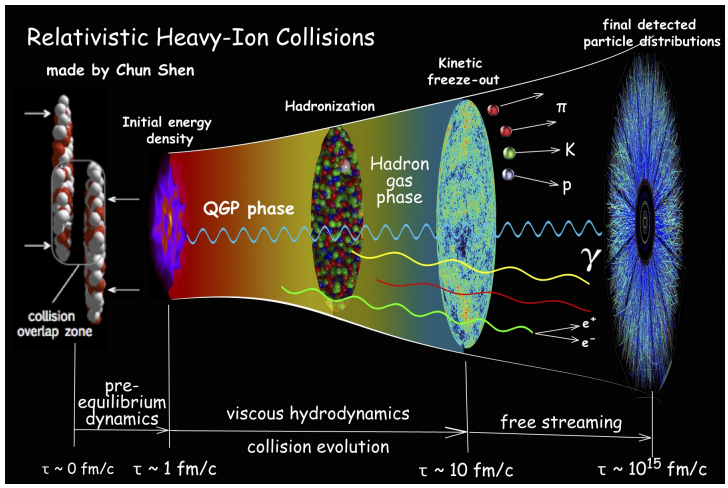


Figure 3.1: An illustration of a heavy ion collision, made by Chun Shen, where the ions are Lorentz contracted under the collision. The final particle composition and distribution is impacted by physics processes from the hadronization to the freeze-out stage. Figure taken from [17].

3.1 Collision Geometry

Due to the relativistic nature of the collision, the ions are Lorentz contracted when they collide. In the collision, the number of nucleons in the two ions which undergo at least one inelastic collision are called *participants*, while the non-interacting nucleons are called *spectators*, see Fig. 3.2. The collision overlap volume (also seen in Fig. 3.1) can be related to the transverse distance, b, between the centers of the two disk-shaped nuclei, called the *impact parameter*[1], also indicated in Fig. 3.2. The collision events with largest collision volume, hence having the smallest impact parameter, have the highest density. This is where the QGP effects are expected to be most pronounced since the zone of deconfined matter is largest, and thereby also the events with the highest amount of particles created in the collision and hadronization process.

Since the impact parameter cannot be measured, the events are instead

[1]The terminology is specific for nuclear physics, and means something else in e.g. particle physics terminology.

classified according to their particle multiplicity in a rapidity range separated from the central tracking region, an observable which is on average increasing monotonically with the number of participants. The multiplicity is measured by the amplitude in the VZERO detector (described in Sec. 4.4). A comparison between the particle multiplicity in data and *Glauber Monte Carlo* [18, 19] simulations is done to extract the centrality of an event, as shown in Fig. 3.3. The Glauber Model describes the collision geometry by a nuclear density profile, or *nuclear thickness function*, T_{AA} [19] (measured in units of $1/\text{mbarn}$), by scaling the number of binary nucleon-nucleon collisions, N_{coll}, to the inelastic nucleon-nucleon cross section, σ^{inel}_{NN}.

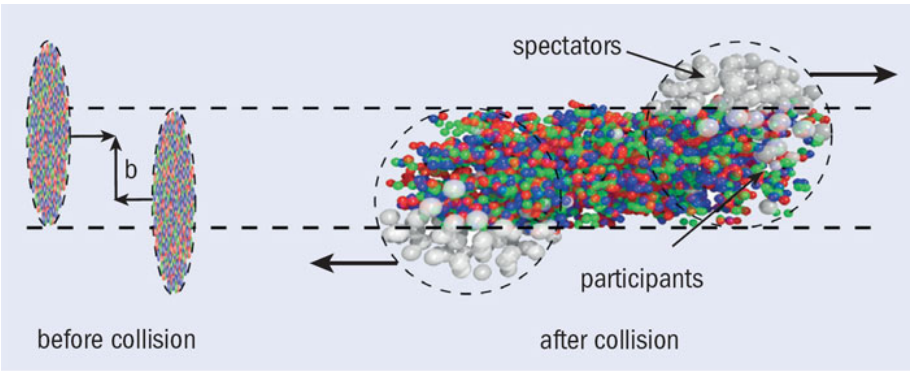


Figure 3.2: The concept of centrality and impact parameter: the interacting nucleons are called *participants*, while the non-interacting nucleons are called *spectators*. The collision overlap volume is related to the impact parameter, b. Figure from [20].

The model sets the absolute scale (the red line in Fig. 3.3), and the centrality bins are defined by integrating from high to low VZERO amplitudes (multiplicities), expressed as the percentile of the overall hadronic cross section. For example, the 0-5% centrality bin contains the 5% of all events with the largest multiplicity (smallest impact parameters), and, correspondingly, the 90-100% centrality bin consists of the 10% of all events with the smallest multiplicity (largest impact parameters). The analysis presented in this thesis is done for 0-10% central Pb–Pb collisions.

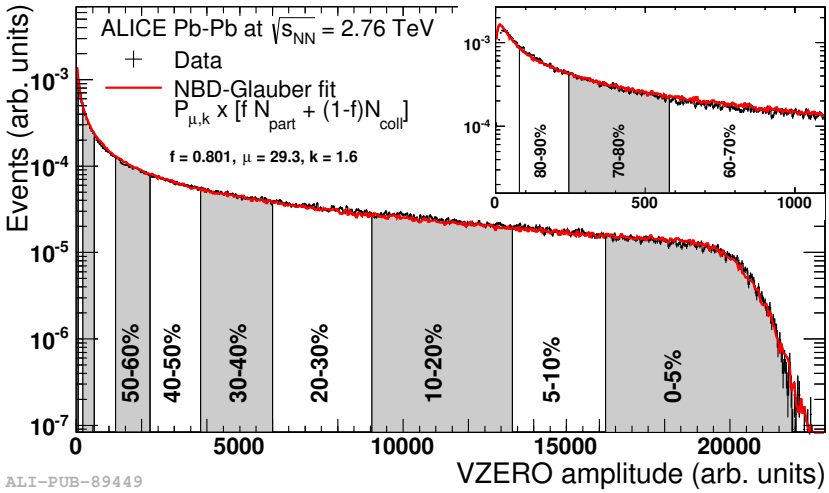


Figure 3.3: Distribution of the sum of amplitudes in the VZERO scintillators fitted with the negative binomial distribution (NBD [19]) Glauber fit shown as a line. The centrality classes are shown as vertical lines. The inset shows a zoom of the most peripheral region. Figure from [19].

3.2 Quark Gluon Plasma Formation

It is an open question how the Quark Gluon Plasma is produced in the heavy-ion collisions. In an initial-state model called the Color Glass Condensate [21], the ions are described as dense objects of low energy gluons, and it is these gluon objects that collide. In this thesis I will give a simpler picture based on ideas from the Lund String model, suggesting QCD string breaking as production mechanism.

The hadron structure is studied via the parton distribution as a function of different energy scales, the so-called Parton Distribution Function [22, 23, 24][2]. It reveals that, at high energies, hadrons consist of abundant *sea* partons with low fractional momenta, x, i.e. the fraction of longitudinal momentum carried by a parton in a hadron (called "Bjorken x"), and only a few high-x *valence* partons.

It is very likely, when two hadrons interact, that some of the low-x

[2]The parton distribution function is measured by deep-inelastic scattering experiments [23, 24].

partons exchange color. When the low-x partons move away from each other, part of their kinetic energy is transformed into a color field stretching between the two nuclei. This color field then decays into a dense state of quarks and gluons. It has been argued that it takes very short time ($<$1 fm/c) for this state to thermalize [25]. This thermalized dense state of quarks and gluons is the Quark Gluon Plasma.

The measured multiplicity in units of pseudo-rapidity, $\mathrm{d}N_{ch}/\mathrm{d}\eta$, together with a formula proposed by Bjorken, using the transverse energy, E_T, can be used to estimate the energy density, ϵ [26]:

$$\epsilon \geq \frac{\mathrm{d}E_T/\mathrm{d}\eta}{\tau_0 \pi R^2} = \frac{3}{2} < E_T/N > \frac{\mathrm{d}N_{ch}/\mathrm{d}\eta}{\tau_0 \pi R^2} \tag{3.1}$$

where τ_0 is the thermalization time, R is the nuclear radius, and $E_T/N \approx$ 1 GeV is the transverse energy per emitted particle. The initial energy density for Pb–Pb at $\sqrt{s_{\mathrm{NN}}} = 2.76$ TeV at $\tau_0 = 1$ fm/c is measured at LHC to be $\sim$15 GeV/fm^3 [25, 26, 27]. This is approximately a factor three higher than for Au+Au collisions at RHIC where the center of mass energy is 200 GeV [28, 29]. The higher energy densities at LHC indicate that a larger system with a longer lifetime is created at LHC compared to RHIC.

3.3 Expansion, Hadronization and Freeze-out

The QGP will, after production, expand in an almost explosive manner. Surprisingly, this expansion is extremely well described by nearly ideal (reversible) hydrodynamics, where the expansion is driven by local pressure gradients. This expansion generates a phenomenon known as collective flow, one of the most important characteristics of the QGP. Because of the expansion, the temperature will drop and eventually it will go below the critical temperature, making the quarks and gluons hadronize.

Hadronization is a process which, again, is not fully understood. It has turned out that, for soft medium particle production, the overall abundances of different particle species are well described by statistical thermal models [30, 31]. Due to the ongoing expansion of the medium, the density of the hadron gas will decrease, and the hadrons will eventually cease interacting. This is referred to as the freeze-out stage — the last state before the hadrons enter the detectors. The freeze-out passes two steps:

the chemical and the kinetic/thermal steps. The inelastic interaction rate of the hadrons decreases faster than the elastic interaction rate when the gas density and temperature drops. The hadro-chemical composition of particles will be fixed at the point when the inelastic collisions stop, and this is what we refer to as the chemical freeze-out.

The elastic scattering will however continue beyond this point, thus still changing the momenta of the particles, until the hadron gas becomes so dilute so that the mean free path of the particles is of the same size as the system itself, and the time scale connected with the collisions becomes larger than the expansion time scale [1], making rescattering negligible. This is the kinetic freeze-out, transforming the system from a strongly to a weakly coupled system. After this point, the momentum distributions are fixed, and the particles propagate to the detectors without further interactions.

The thermalized hadrons measured by the detectors are *final state* particles, and reveal information about the state of matter at freeze-out. However, we want to extract information about the state before hadronization, so it is important to have a picture of how the final state hadronic properties reflect each stage of the collision.

To display the experimental QGP observables in a way that facilitates the interpretation of the QGP phenomenon, it has turned out that some useful observables are:

1. The relative particle abundances, and e.g. strangeness enhancement, can be explored by analyzing the ratio of particle yields, which is related to the chemical freeze-out

2. Collective phenomena, and early QGP evolution, can be investigated by correlations and flow components by azimuthal angular correlations

3. Jet quenching, angular correlations, and parton energy loss in the medium compared to reference data can be examined by the nuclear modification factor, R_{AA}

The above mentioned observables will be the focus of the following sections since they are leading up to the analysis of this thesis, but I have left out many important QGP signatures that are not directly related to the topic of this thesis, e.g. thermal photons and Quarkonia suppression.

3.3.1 Particle Yields

A crucial measurement for characterizing the properties of the QGP created in heavy ion collisions is to group all produced hadrons into their different hadron species (e.g. pions (π), kaons (K), protons (p), lambdas (Λ)), count the number of hadrons in each group, and sort them according to their transverse momentum. The normalized p_{T} distributions of the different particle species, called *particle yields*, are the most basic quantities, and reflect the conditions during the kinetic freeze-out, where the momentum of the particle is settled. It will become clear that by using these yields, one can extract many interesting results.

The ultimate goal is to have a theory by which the shape and magnitude of such spectra are explained. As input for such theory building, the experimentalist extracts different notable features by constructing different ratios and comparing to phenomenological models (like thermal models) to put numerical values on different aspects of the otherwise rather featureless spectra. This is a way to synthesize the observations, so that one from these yields can extract and point at interesting features as guidance to theory about observations which should be explained.

While leaving the discussion about the high transverse momentum part of the particle spectra to the section about parton fragmentation and jet quenching (Sec. 3.4.1), the low-p_{T} part will be discussed in the next-coming sections.

95% of all particles produced in heavy ion collisions populate the low-p_{T} part of the spectrum (<1.5 GeV/c [26]). In this momentum range the single particle spectra are consistent with statistical/thermal and hydrodynamical models [30, 31, 35], as can be seen in Fig. 3.4 where the p_{T} distributions of π, K, and p for LHC and RHIC energies can be seen compared to hydrodynamical models (VISH2+1 [36, 37], HKM [38], Krakow [39, 40]). In the context of the hydrodynamical models, some basic QGP characteristics can be determined, e.g. the temperature of the chemical freeze-out stage.

In order to extrapolate the individual spectra down to zero p_{T} to extract the integrated yields, the spectra are fitted with blast-wave functions [32, 33], which is a function depending on a few collective variables such as temperature, longitudinal and transverse flow.

The overall abundances of hadron species are fixed at chemical freeze

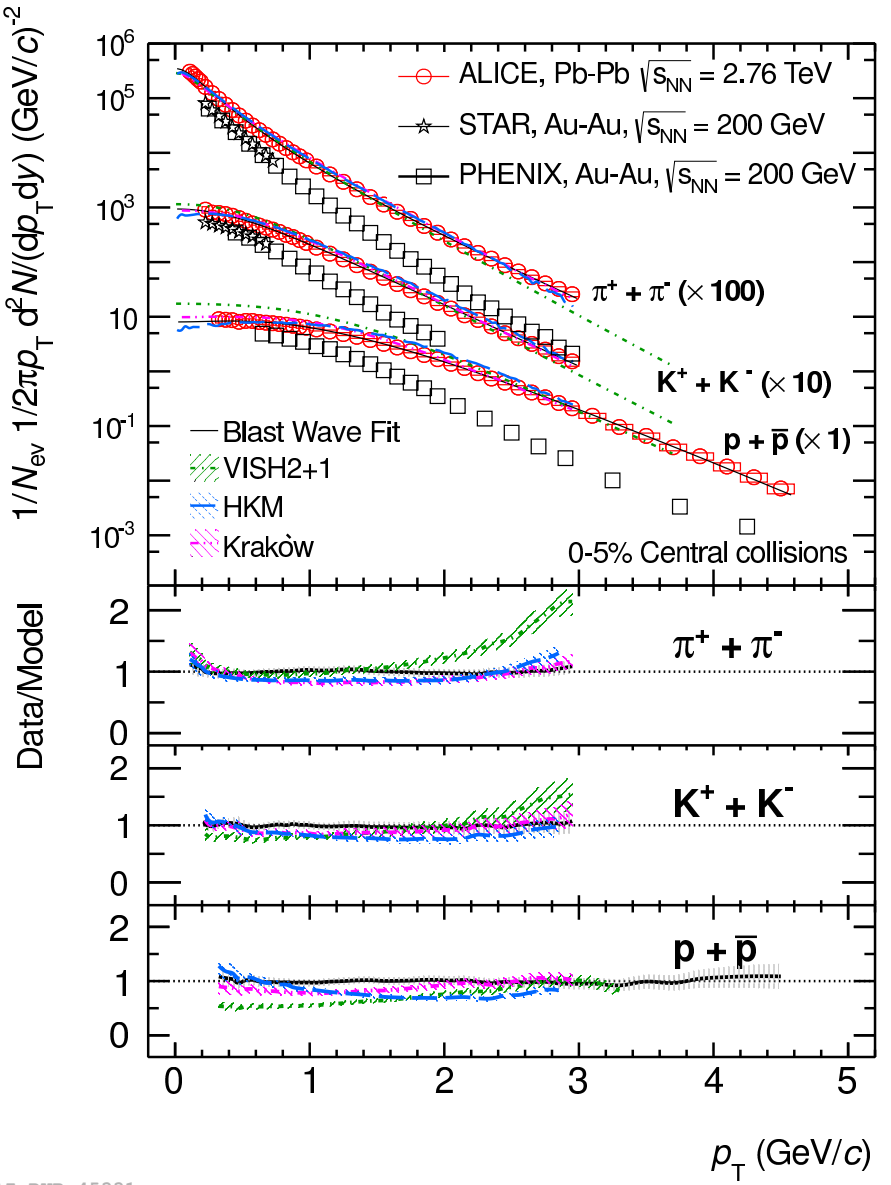


Figure 3.4: Transverse momentum distributions of the sum of positive and negative particles (box: systematic errors; statistical errors smaller than the symbol for most data points), fitted individually with a blast wave function [32, 33], compared to RHIC data and hydrodynamic models. Figure taken from [34].

out, and the relative yield for different particle species turns out to be well described by thermal models. The model can statistically, via a hadron gas in thermal and chemical equilibrium (a so called *Grand Canonical Ensemble* [41]), describe the particle yields of a specific species — or, rather, a specific *mass* — by three parameters: (*i*) temperature, (*ii*) baryochemical potential, and (*iii*) the volume of the system.

In Fig. 3.5 it is seen that particle yields of light flavor hadrons are described over 7 orders of magnitude within 20% (except K^*) with a common chemical freeze-out temperature of $T_{ch} = 156$ MeV, determined independently by three different versions of the statistical thermal model (THERMUS 2.3 [42], GSI-Heidelberg [43] and SHARE [44]). From these studies, the baryochemical potential is measured to be 0, and the volume is 5330 fm^3 [15].

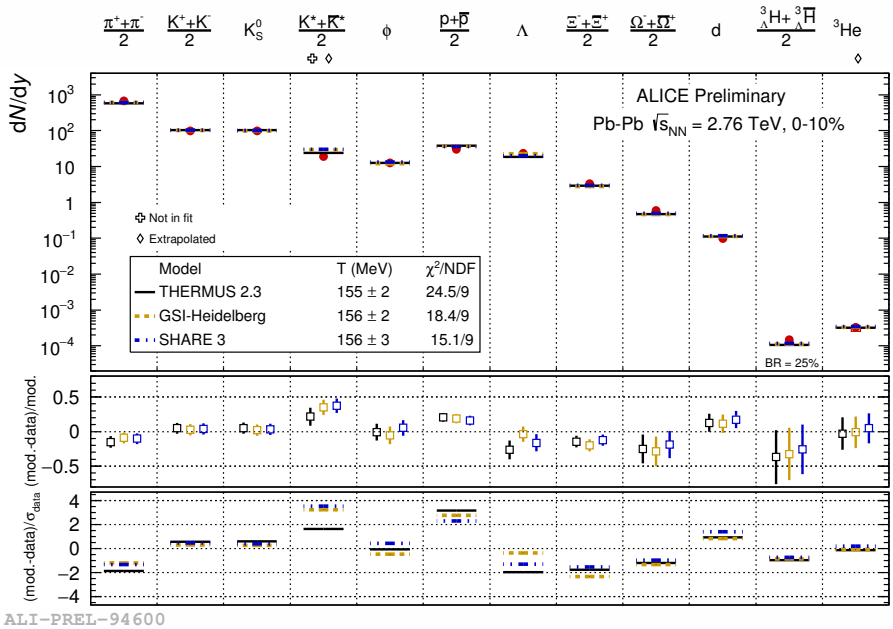


Figure 3.5: Grand canonical thermal fit of 0-10% central Pb–Pb at $\sqrt{s_{\rm NN}} = 2.76$ TeV collisions, with 3 models (THERMUS, GSI, SHARE). Figure taken from [41].

3.3.2 Collectivity

The low p_T particle production is governed by soft processes taking place in the bulk of the medium. Looking at the low momentum part ($p_T < 3$ GeV/c) of the light flavor particle spectra in central Pb–Pb collisions, Fig. 3.6, the spectral shapes differ significantly from pp collisions, with a larger difference for heavier particles. For Pb–Pb collisions, the slope of the p_T distributions increases with increasing hadron mass; at a given p_T, there are more lighter hadrons (pions) than heavier (protons), thus this mass ordering phenomenon leads to a strong relative depletion of protons at low p_T, and to an overall over-abundance at intermediate and high p_T [45].

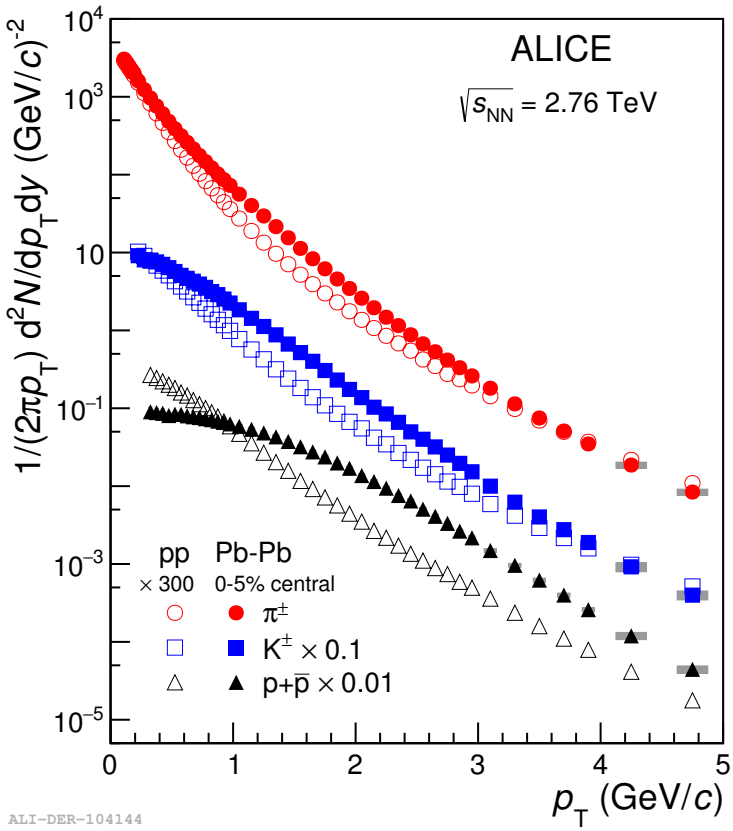
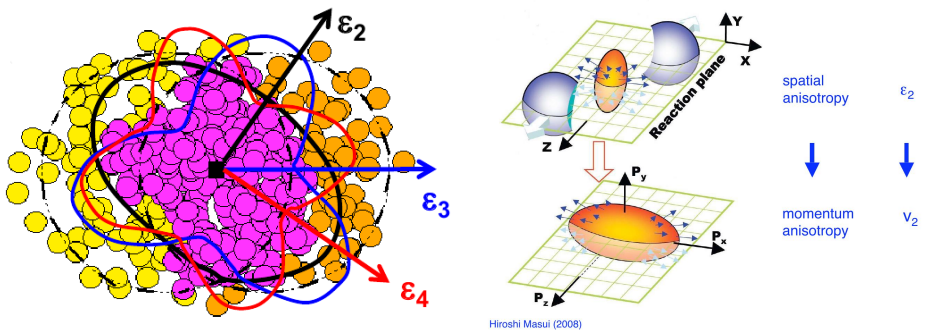


Figure 3.6: Pion, kaon and proton spectra in pp and Pb–Pb collisions at $\sqrt{s_{NN}}$=2.76 TeV [45]. The pp spectra are scaled for a better comparison of the shapes.

The Concept Of Flow

This mass hierarchy is induced by collective, soft process, in the radially expanding thermalised medium called *radial flow*, where hadrons are boosted with a common average velocity (**v**). A heavier hadron at rest in the local fluid frame will then gain a larger momentum (**p**) than the lighter, according to $\mathbf{p} = \gamma m \mathbf{v}$, thus depleting the low p_{T} part of the spectra and filling up at intermediate p_{T}.

The QGP also shows other strong collective effects in terms of higher orders of flow, illustrated in Fig. 3.7(a), where the second order, *elliptic* flow, is the most prominent in less central Pb–Pb collisions. The elliptic flow arises from the initial almond shaped geometry of the collision volume, see Fig. 3.7(b), leading to a pressure gradient in the reaction plane in spatial coordinates so that particles are pushed outwards in an anisotropic momentum distribution. In other words: an anisotropic initial energy-density distribution in coordinate space translates to an anisotropic momentum distribution of the observed particles. This can be measured by two-particle correlations.



(a) (b)

Figure 3.7: (a) An illustration of higher order flow harmonics due to geometrical fluctuations, ϵ_n [46]. (b) The concept of elliptic flow, v_2, arising from the almond shape geometry, ϵ_2, of a peripheral collision.

In Fig. 3.8 the results from such measurement are presented. The angular pair-correlation distribution, C($\Delta\varphi$,$\Delta\eta$), in central Pb–Pb collisions between charged hadron trigger (t) particles and associated (a) particles are seen in the $\Delta\eta\Delta\varphi$-plane ($\Delta\varphi = \varphi_{\mathrm{trig}} - \varphi_{\mathrm{V0}}$ and $\Delta\eta = \eta_{\mathrm{trig}} - \eta_{\mathrm{V0}}$). The

peak structure at $\Delta\eta\Delta\varphi$ = (0,0) is representing the near-side jet. An additional "ridge" (first measured at RHIC [47, 48]) is observed at $\Delta\varphi = 0$, and extended in the full $\Delta\eta$ range, representing the flow of the medium bulk. This is of great importance for the analysis in this thesis since the bulk and peak region will be sampled in the same $\Delta\varphi$ window ($|\Delta\varphi|$<0.92) to be able to assume that the flow contribution and enhanced background present in the peak region can be corrected for by subtracting the bulk from the peak to obtain the near-side jet. This is discussed further in Sec. 5.1.

The away-side jet correlation is weaker, but shows a clear $\Delta\eta$-extended ridge structure. The correlation distributions projected in $\Delta\varphi$ (excluding the jet contributions by an η-gap of $|\Delta\eta| > 0.8$) can be decomposed in Fourier components to measure the different flow contributions, discussed in the next section.

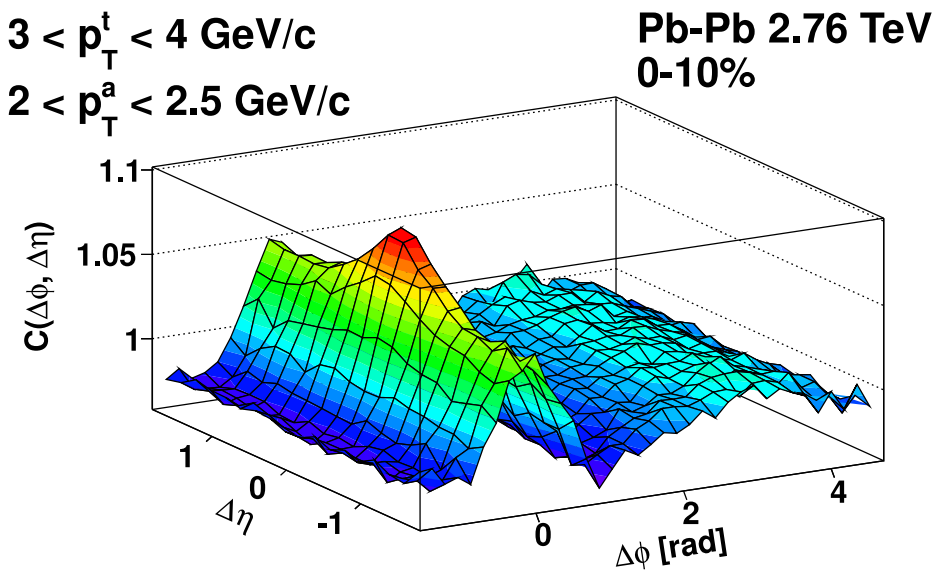


Figure 3.8: Examples of two-particle correlation functions for central Pb–Pb collisions at low to intermediate transverse momentum. Figure taken from [49].

Measuring Flow

If no medium is formed during the collision, the azimuthal angle (φ) distribution is expected to be homogeneous (meaning that the particles are emitted in random directions in individual nucleon-nucleon collisions). As introduced in the previous section, in the presence of an expanding medium, the final state particles will instead have non-isotropic spatial distribution due to the fact that the expansion follows the energy density gradients.

The different initial state geometries resulting in flow, is characterized by the flow parameters v_n. These parameters are determined according to the measured particle's spatial distribution, i.e. their azimuthal angle (φ) dependence with respect to the reaction plane, Ψ_R, which is the plane determined by the beam direction and the impact parameter vector, illustrated in Fig. 3.7(b). The φ-averaged component is the radial flow.

The φ-anisotropy can be expressed with a Fourier expansion, where the coefficients describe the different flow effects on the φ-distribution [49]

$$f(\varphi) \propto 1 + 2v_1\cos[1(\varphi - \Psi_1)] + 2v_2\cos[2(\varphi - \Psi_2)] + ... \qquad (3.2)$$

If Ψ_R were known, then v_n could be determined. However, a direct measurement of the reaction plane Ψ_R is not possible due to the statistical anisotropy of the event. Instead, v_n can be determined in each event by the *event plane method* [50], estimating the *event plane angle*, Ψ_n, i.e. the actual plane of symmetry of harmonic n. Another method that does not depend on the reaction plane resolution is the *cumulant method* [51, 52], where the v_2 coefficients are extracted by studying multi-particle azimuthal correlations.

Coming back to the two-particle correlation study described in the previous section, which measure the distributions of φ and/or η between a trigger particle and an associated particle, the higher-order harmonics can be expressed via [49]

$$f(\Delta\varphi) \propto 1 + \sum_{n=1}^{\infty} 2v_n(p_T^t)v_n(p_T^a)\cos(n\Delta\varphi) \qquad (3.3)$$

Flow Results

Fig. 3.9 shows the p_{T}-dependent v_2 results for different particle species in Pb–Pb at $\sqrt{s_{\mathrm{NN}}} = 2.76$ TeV, 10-20% and 40-50% centrality obtained by the Event Plane based Scalar Product (SP) method [53], which is a two-particle correlation method using a pseudo-rapidity gap between the hadron and the reference particles. The η-gap reduces correlations not related to the symmetry plane. It is seen that the elliptic flow grows from the low centrality bin to the higher, explained by the non spherical geometry of the collision as the centrality decreases. It is worth mentioning that the largest elliptic flow, however, is observed at mid-central collisions, and not at the most peripheral, since there must still be enough particles to actually build up the pressure gradients, and a QGP must be present.

The increase of v_2 with p_{T} is also interpreted intuitively by the previous discussion about how the elliptic flow will provide a boost in p_{T}. The boost is larger for heavier particles. This mass ordering is clearly visible in the measured p_{T}-range ($p_{\mathrm{T}} < 2.5$ GeV/c), i.e. the v_2 is smaller for heavier particles, predicted (and qualitatively well described) by hydrodynamical calculations [54] — indicated in the figure as solid or dashed lines.

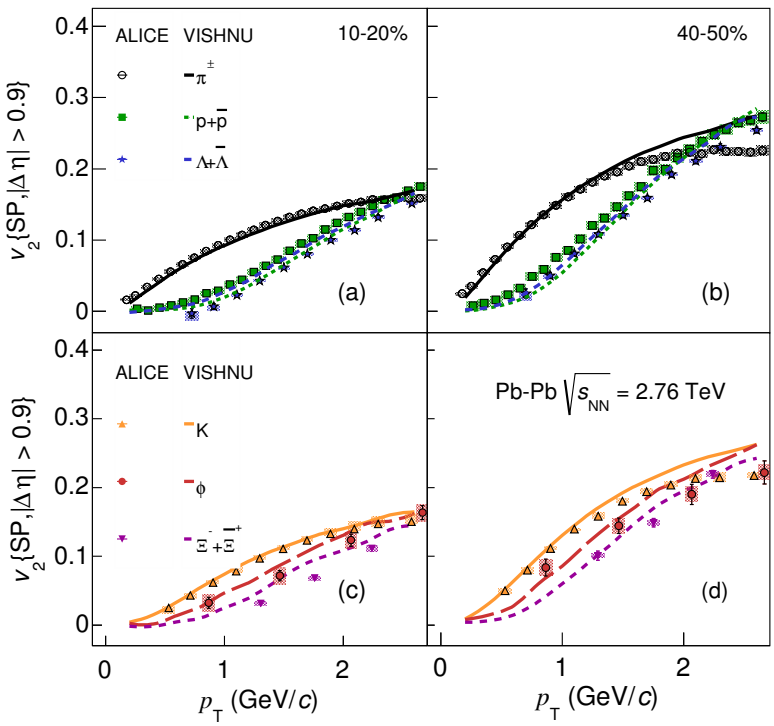
Studying QGP flow observables will give us information about the transport properties of the medium, such as the shear viscosity[3]. Before one measured the collective properties of the QGP at LHC, they were measured at RHIC. There, the size of v_2 clearly indicated a collective behavior of the system, and it turned out that comparison to hydrodynamical models revealed that the kinematic shear viscosity is very close to that of a perfect fluid, i.e. it flows like a fluid with very little friction. More precisely, one can look at how the shear viscosity compares to the entropy density, η/s, i.e. the "medium's ability to resist flow, or, in other words, its in-ability to transport momentum" [55]. When comparing v_2 (and actually also v_3) with the theoretical models, the η/s is calculated to be very close to the theoretical limit of $\hbar/4\pi k_B$ [56], where $\hbar$ is Planck's constant, and k_B is the Boltzmann constant. These results were revolutionary when they came, since it changed the view of the QGP as a weakly coupled gas, to the strongly coupled liquid we think of today.

At RHIC it was observed that v_2 scaled by the number of constituent quarks, n_q [57]. As soon as this could be tested at LHC energies out to

[3]The viscosity probes how strongly the material constituents are coupled.

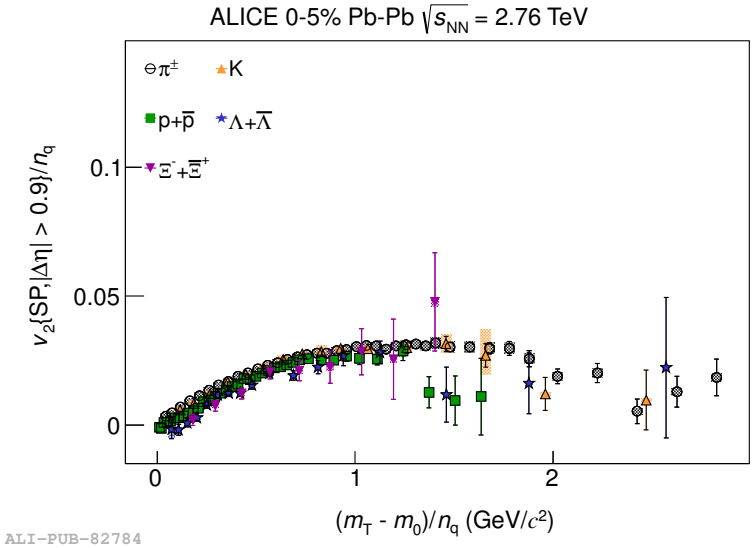
larger transverse momenta, it was seen that this picture is perhaps too simplistic. In Fig. 3.10, v_2 is presented as a function of quark-scaled (n_q) transverse kinetic mass, $m_T - m_0$, where $m_T = \sqrt{p_T^2 - m_0^2}$ is the transverse mass.

With increasing flow, in more peripheral collisions, such as the one shown in Fig. 3.10(b) for 20-30%, the particles tend to group together depending on if it is a baryon or a meson. The different behavior of mesons and baryons could be interpreted as a sign of quark coalescence. This will be discussed in much more details in the following sections since it is a possible interpretation of the physics results presented in this thesis.

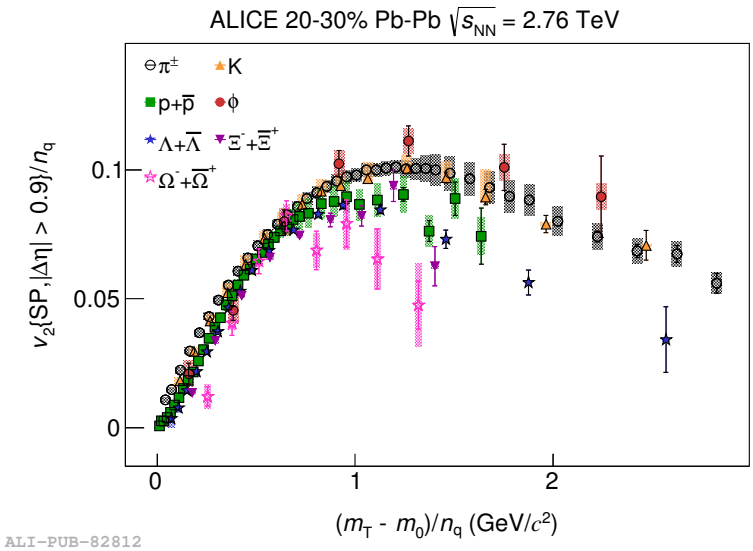


ALI-DER-85768

Figure 3.9: The p_T-differentiated v_2 for different particle species in Pb–Pb collisions at $\sqrt{s_{NN}} = 2.76$ TeV, compared with the theoretical hydrodynamical calculations of VISHNU [54]. Figure taken from [53].



(a)



(b)

Figure 3.10: The $(m_T - m_0)/n_q$ dependence of v_2/n_q for different particles in Pb–Pb collisions at $\sqrt{s_{NN}} = 2.76$ TeV, (a) 0-5% centrality, (b) 20-30% centrality. Figure taken from [53].

3.4 Jet Quenching

Having given a picture of the medium and bulk particle production and a highlight of the most important experimental results, the following will be about jets as probes of this medium, which is the topic of this thesis.

3.4.1 Parton Fragmentation

When an initial quark or gluon in one of the nucleons scatters off another quark or gluon in a nucleon in the other nucleus with a large transverse momentum transfer, and is pushed out back-to-back (due to momentum conservation) with a large energy, color strings are built up according to e.g. the Lund String Model (as the partons cannot exist in isolation). The parton will hence radiate gluons that fragments along the way and thereby form a collimated shower of high-p_{T} hadrons, also referred to as a jet, moving in the direction of the original parton. It is a pure QCD process, and in pp collisions, where there is no strongly coupled medium created, the jet production and propagation can be measured precisely, and the underlying scattering itself can be calculated via pQCD.

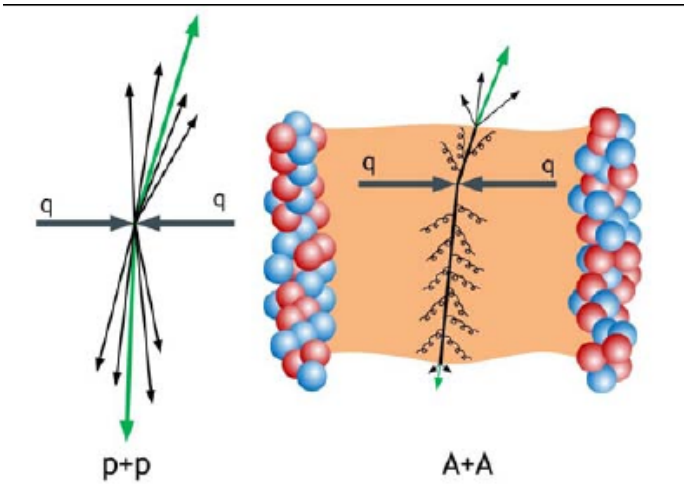


Figure 3.11: Illustration of the jet quenching phenomenon: two quarks suffer a hard scattering, one fragments directly after production into the vacuum, while the other goes through the QGP and loses energy.

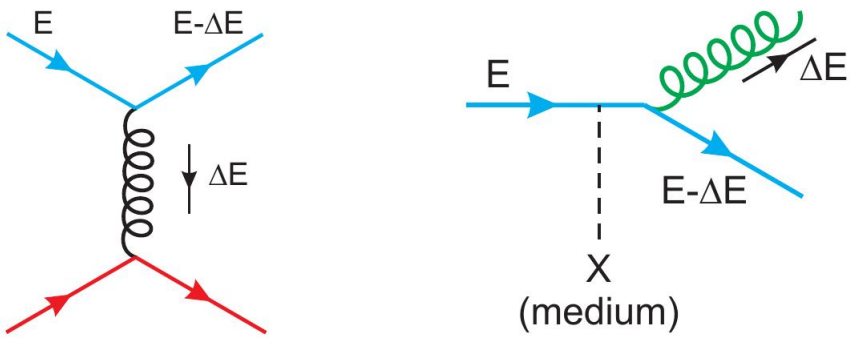


Figure 3.12: Diagrams for elastic collisional (left) and radiative (right) energy losses of a quark traversing a strongly coupled medium. Figure from [58].

In heavy-ion collisions, the scattered partons must to some extent traverse the colored medium, illustrated in Fig. 3.11, acting as a probe-particle of the medium. Doing so, the parton interacts with the medium via either elastic collisions, passing energy to the thermal partons of the medium ("collisional energy loss"), or inelastic collisions followed by a large-angle gluon bremsstrahlung ("radiative energy loss", in which the amount of radiated energy depends on the density of the medium and distance travelled by the parton in the medium) which will broaden the jet [58, 59]. Both mechanisms are shown in Fig. 3.12.

These processes lead to parton energy loss, where the total energy loss of a particle traversing a medium is the sum of the collisional and radiative mechanisms, resulting in a modification of the energetic jet (jet quenching), and can be confirmed by measuring the energy imbalance of the two back-to-back jets, thus using the propagation of these high-p_{T} probes to investigate the parton energy loss and deconfinement in the QGP.

Hard scattering processes have low probability compared to soft processes. A given nucleon is expected to suffer at most one hard collision in a nuclear collision. Thus hard scattering, or rare processes on the nucleon-nucleon level in general, are expected to scale with the number of binary nucleon-nucleon collisions.

A way of quantifying jet quenching is by measuring the suppression of single hadron yields at high p_{T} relative to those measured in proton-proton (pp) collisions, discussed next.

3.4.2 Reference Data

Before conclusions from the results of the analysis of heavy ion collisions can be drawn, a comparison must be done to reference data from collisions where the physics processes are well understood, and where we believe that no QGP is formed.

With the accelerator LHC, pp collisions are also produced[4], and ALICE records them in the same way as for the Pb–Pb collisions. The part of the QCD theory describing hadron production and fragmentation at high momentum transfer ("hard") parton-parton scattering is called *perturbative* QCD (pQCD), which can very well describe pp collisions — and it is of special interest in this analysis since it can describe the jets arising from the fragmentation of these high-p_{T} partons.

When the corresponding analysis is done for pp as for Pb–Pb collisions, the results are compared with the purpose of more closely investigate any difference in the results between the two collision systems; all deviation of the Pb–Pb results from the pp reference data are worth studying, considering that this can be not only a sign of QGP formation, but also an indication of how the QGP behaves.

ALICE also records p–Pb collisions which were initially thought of as reference data used in order to identify initial and final-state effects. It is now clear that neither pp nor p–Pb collisions can be used as *pure* reference data due to recent results indicating that these systems also show collective behavior, which may be viewed as signs of QGP formation [60, 61, 62]. However, these systems still serve many of the purposes for being a reference to Pb–Pb.

Reference values can also be obtained by computing extrapolations of pp collision models (e.g. pQCD) via a random sampling, so called *Monte Carlo* (MC) simulations, to predict what arises in collisions with many nucleons involved.

[4]It is in fact dominating the physics program of LHC, while the Pb–Pb collision period lasts for 1 month per year.

3.4.3 The Nuclear Modification Factor

This section, and the next, is partially based on the conference proceeding [63] written for the talk I gave at the Winter Workshop in Nuclear Dynamics 2015, Colorado.

To isolate jets and sum up the jet energy in a heavy ion collision is a difficult task. Instead of measuring the energy of the jets when studying the jet quenching phenomenon, a comparison of the high p_{T} hadron yield distributions between Pb–Pb and pp collisions by forming the quantity called *nuclear modification factor*, R_{AA} [62], is made.

R_{AA} is defined as the ratio of the particle yield in Pb–Pb to that in pp collisions scaled by the number of binary nucleon-nucleon collisions

$$R_{\mathrm{AA}}(p_{\mathrm{T}}) = \frac{\mathrm{d}^2N_{\mathrm{AA}}/\mathrm{d}\eta\mathrm{d}p_{\mathrm{T}}}{\langle T_{\mathrm{AA}}\rangle \mathrm{d}^2\sigma_{\mathrm{pp}}/\mathrm{d}\eta\mathrm{d}p_{\mathrm{T}}} \tag{3.4}$$

where $\mathrm{d}^2N_{\mathrm{AA}}/\mathrm{d}\eta\mathrm{d}p_{\mathrm{T}}$ is the differential particle yield in A–A collisions, $\mathrm{d}^2\sigma_{\mathrm{pp}}/\mathrm{d}\eta\mathrm{d}p_{\mathrm{T}}$ is the invariant cross section for particle production in inelastic pp collisions, and $\langle T_{\mathrm{AA}}\rangle$ is the average nuclear thickness function [62], introduced in Sec. 3.1. In the absence of nuclear modifications, R_{AA} is unity for hard processes which are expected to exhibit binary collision scaling. If R_{AA} is below unity it implies that the hadron production is suppressed in Pb–Pb collisions compared to pp. In this way we can analyze medium properties, parton energy loss mechanisms, and particle production. In this context it is worth mentioning that the relevant part of the R_{AA} is at intermediate and high p_{T}, since the bulk particle production from soft processes should rather scale with the number of participants — and not the number of binary nucleon-nucleon collisions[5].

The nuclear modification factor for charged hadrons presented in Fig. 3.13 [64] (the black points labelled $h^+ + h^-$), shows that the shape of the invariant yield for peripheral Pb–Pb collisions at $\sqrt{s_{\mathrm{NN}}} = 2.76$ TeV is similar to those observed in pp collisions due to the flatness of the R_{PbPb}. In central collisions, however, a strong suppression of charged hadron production is observed (this is the sign for jet quenching). At $\sim$6 GeV/c, the suppression factor is at its maximum of $\sim$5 where R_{AA} is at its minimum, with a slight rise in R_{AA} after this value.

[5] With this said, the "peak" at low p_{T} in the R_{AA} shown in Fig. 3.13, is likely attributed to the collective flow.

To establish whether the initial state of the colliding nuclei plays a role in the observed suppression, the nuclear modification factor in p–Pb for charged particles has been measured and established that R_{pPb} is consistent with unity for $p_{\mathrm{T}} > 2$ GeV/c [62], and hence the suppression in Pb–Pb collisions is not due to initial state effects, but to final bulk matter effects, such as jet quenching in the hot QCD medium.

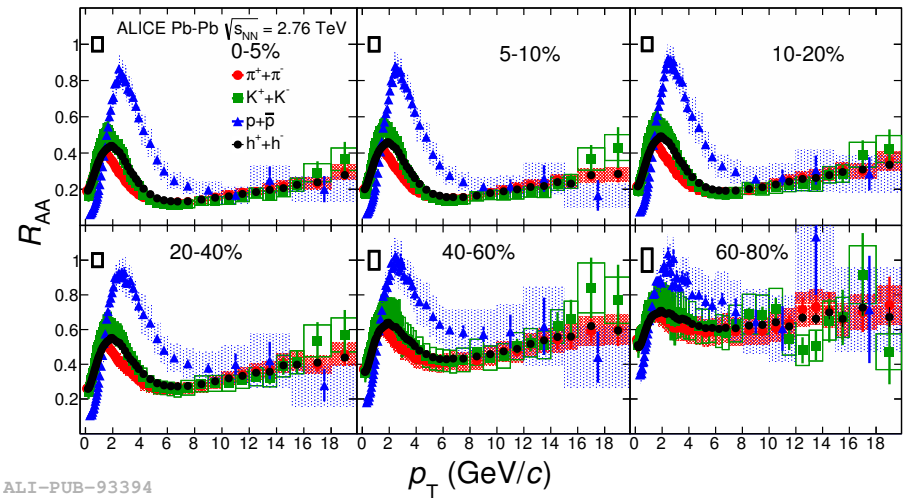


Figure 3.13: The nuclear modification factor, R_{AA}, as a function of p_{T} for different particle species, and different collision centralities. Figure taken from [64].

When constructing R_{AA} for identified light flavor hadrons [64], we see in the colored points in Fig. 3.13 that, within systematic and statistical uncertainties, the same suppression is seen for all light quark systems created in Pb–Pb collisions at $p_{\mathrm{T}} > 10$ GeV/c, which suggests that the chemical composition of leading particles from jets in the medium is similar to jets produced in vacuum, and there is no strong flavor or meson/baryon dependence. The large suppression is a sign of considerable energy loss.

For the intermediate p_{T}-range, the protons are less suppressed than the kaons and pions. In Sec. 3.3.2, the mass ordering is argued to arise from collective flow and is described by hydrodynamical models up to ~2.5 GeV/c. When approaching the intermediate p_{T}-range, however, the mass ordering seen in v_2 is broken, and the difference in suppression seen in the R_{AA} is attributed to a *baryon-to-meson anomaly*. In the thesis of Si-

mone Schuchmann [65], R_{AA} is also constructed for K^0_s and Λ, and they follow the pattern seen for other identified particles. At high p_T, they are both equally suppressed, while the Λ is less suppressed than K^0_s for intermediate p_T, in line with a baryon enhancement over mesons. As mentioned before, the goal of this thesis is to investigate the origin of the baryon-to-meson anomaly by looking at the Λ/K^0_s ratio in different regions of the QGP. First, the Λ/K^0_s ratio, together with other particle ratios, will be discussed in the inclusive case in the following section.

3.4.4 Particle Production Ratios

In Pb–Pb collisions, both Λ/K^0_s and p/π [45, 64, 66] (Fig. 3.14) in central and peripheral collisions are consistent with pp for $p_T > 8$ GeV/c, indicating that the processes are dominated by vacuum-like fragmentation.

Looking in the intermediate p_T range for Λ/K^0_s, an enhancement is visible towards more central collisions, see Fig. 3.14, and a shift of the maximum position towards higher p_T is observed: in the most peripheral collisions (60-80% centrality) there is a maximum of about 0.75 at $p_T \sim$2.5 GeV/c, while the maximum value of the ratio for the most central collisions (0-5% centrality) is about 1.6 at $p_T \sim$3.5 GeV/c. This shift is consistent with an increasing radial flow towards more central collisions.

The magnitude of the maxima increases by almost a factor of three between most peripheral and most central Pb–Pb collision. Hydrodynamical models such as VISH2+1 [36, 37, 39] are able to describe the rise at low p_T. VISH2+1 is a model incorporating a low-viscous fluid, which in the evolution in the radial dimension is based on Bjorken Scaling[6] [1].

At higher p_T, models with modified fragmentation ("EPOS") and coalescence of quarks ("Recombination") describe the shape qualitatively well, but overestimate the enhancement [66].

Fig. 3.14 also shows the p/π and K/π ratio up to p_T =20 GeV/c for central events, both presenting an enhancement at intermediate p_T, with the peak at p_T = 3 GeV/c. As K and π are both mesons, the K/π result was a surprise. However, the baryon-to-meson ratio p/π presents a much more pronounced increase, reaching a value of about 0.9, compared to the two-meson ratio K/π. As for the Λ/K^0_s case, the ratios are in good

[6] Bjorken Scaling suggests that hadrons behave as collections of point-like constituents when probed at high energies, due to the independence of the absolute resolution scale.

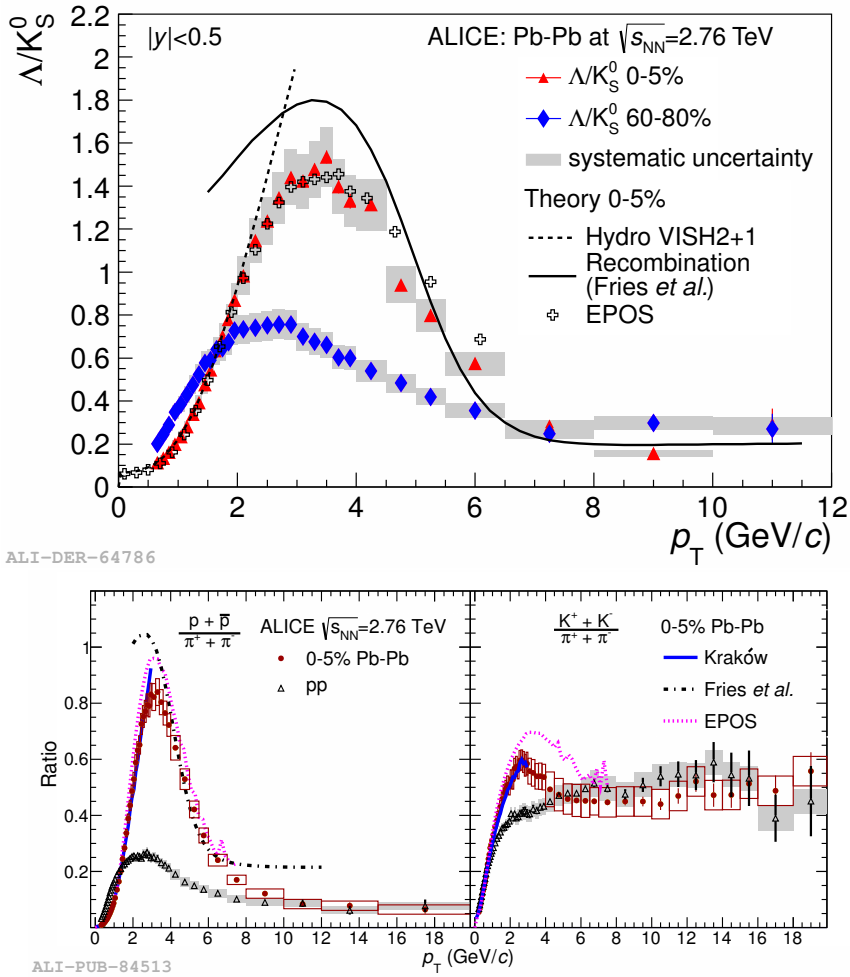


Figure 3.14: Top: $\Lambda/\mathrm{K}^0_\mathrm{s}$ particle ratio as a function of p_T in central (0-5%) and peripheral (60-80%) Pb–Pb collisions at $\sqrt{s_\mathrm{NN}} = 2.76\,\mathrm{TeV}$ compared to models in central (0-5%) events [66]. Bottom: p/π and K/π ratio as a function of p_T in central (0-5%) Pb–Pb collisions at $\sqrt{s_\mathrm{NN}} = 2.76\,\mathrm{TeV}$ compared to pp collisions at $\sqrt{s} = 7\,\mathrm{TeV}$ and models [45].

agreement with hydrodynamical calculations ("Krakow" [39, 40]) for p_T <2 GeV/c, indicating that the rise of the peak can be described by the mass ordering induced by radial flow. At intermediate p_T, around the maxima and up to $p_T \sim 8$ GeV/c, the data are qualitatively described by the recombination model, and the EPOS model [67, 68], but these models also overestimate the maximum values.
To summarize the particle ratios observations so far:

- **High p_T:** Particle ratios (and R_{AA}) are similar to the pp ratios
  $\Longrightarrow$ The dominating particle production process is fragmentation

- **Low p_T:** Particle ratios and the shift of the maxima towards higher p_T-values for higher centralities are consistent with hydrodynamical models
  $\Longrightarrow$ The dominating particle production process is thermal

- **Intermediate p_T:** A baryon-to-meson anomaly is seen, more prominent for higher centralities
  $\Longrightarrow$ Is there a mix between soft and hard processes, i.e. where does the anomaly come from? This is the subject of the thesis.
  $\Longrightarrow$ Does this suggest another particle production mechanism, such as recombination of quarks? This will be discussed in the next section, and will be referred to when discussing the results of the analysis in this thesis.

To further investigate the main driving parameter in the spectral shape at intermediate p_T, we study a baryon-to-meson ratio in which the baryon and meson are of similar mass, namely the p/ϕ ratio. In Fig. 3.15 [69] the p/ϕ ratio is shown as a function of p_T, and it is observed that in *central* Pb–Pb collisions there is a very small difference in their p_T distributions.

Interestingly, the Λ/K^0_s and p/π in p–Pb collisions show the same qualitative behavior as in Pb–Pb collisions: a multiplicity dependent baryon-to-meson enhancement at intermediate $p_T \sim 3$ GeV/c is seen in Fig. 3.16 [62] for two different multiplicity event classes. The results show that p–Pb presents features that are similar to Pb–Pb, even though the magnitude of the enhancement in p–Pb is significantly lower compared to the one observed in Pb–Pb. The maximum of the p/π ratio reaches 0.8 in central Pb–Pb collisions, but only 0.4 in the highest multiplicity p–Pb events,

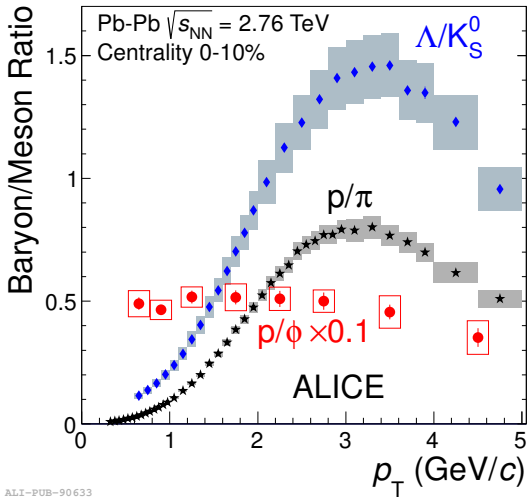


Figure 3.15: Ratio p/ϕ (scaled with 0.1 for visibility) as a function of p_T up to 5 GeV/c for 0-10% central Pb–Pb collisions at $\sqrt{s_{NN}} = 2.76$ TeV, compared to Λ/K^0_s and p/π in the same centrality bin. Figure taken from [69].

and the Λ/K^0_s maximum in central Pb–Pb is 1.5, while it is 0.8 in corresponding p–Pb collisions. The highest multiplicity bin in p–Pb collisions exhibits ratios of p/π and Λ/K^0_s which have maxima close to the corresponding ratios in the 60-70% centrality bin in Pb–Pb collisions, but differ somewhat in shape at lower p_T [62].

3.5 Quark Coalescence

Due to the anomaly seen in baryon-to-meson ratios which cannot be described by neither flow (the rise of the enhancement is, however, described by hydrodynamical models — but starts to deviate from the models at ∼2 GeV/c), nor fragmentation (the intermediate region of the ratio in Pb–Pb deviates from the ratio in pp), an additional mechanism for hadronization has been suggested. This model [70], called quark *recombination* or *coalescence*, allows for two or three soft quarks from the dense partonic bulk to recombine into a meson or a baryon. If the recombining quarks have similar momenta, the baryons will have a higher p_T than the mesons, since they are the sum of three quarks, compared to two. This is the basic idea.

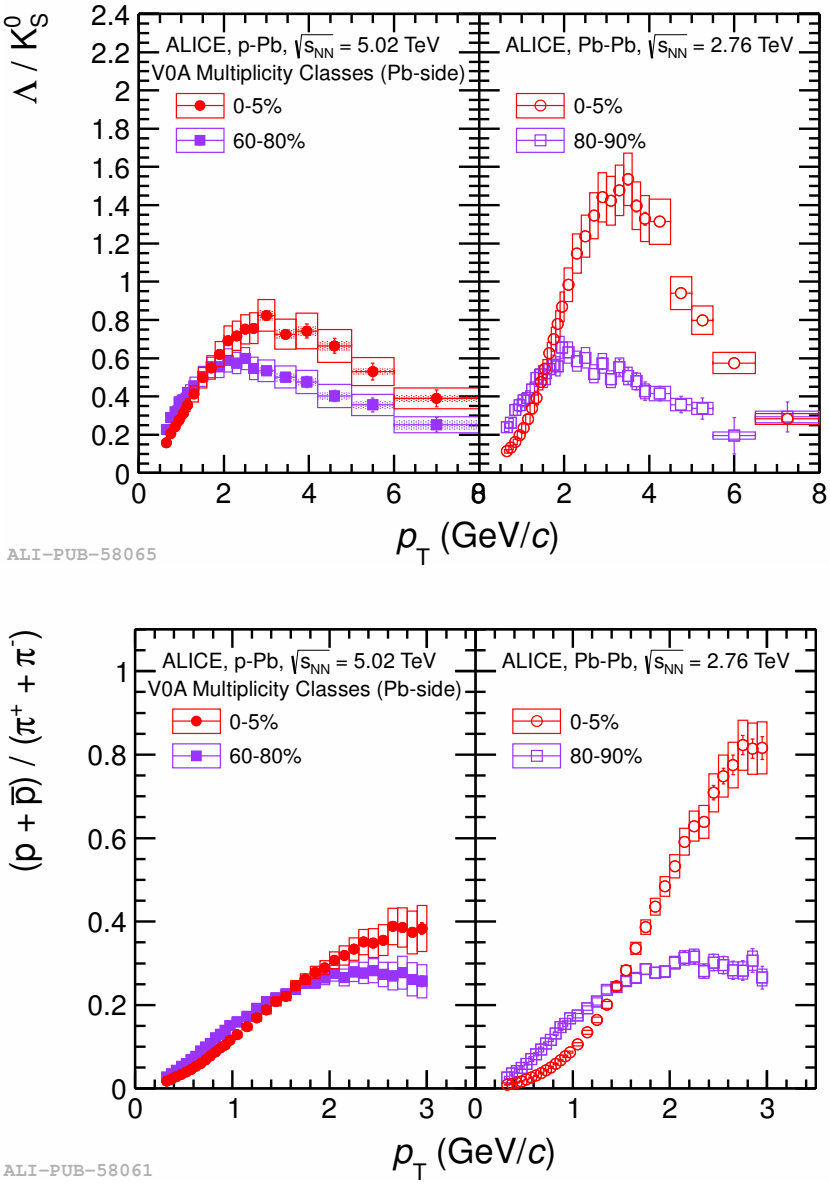


Figure 3.16: $\Lambda/\mathrm{K}^0_\mathrm{s}$ (top) and p/π (bottom) in $\sqrt{s_{\mathrm{NN}}} = 5.02\,\mathrm{TeV}$ p–Pb collisions (left panel) as a function of p_T in one central (0-5%) and one peripheral (60-80%) multiplicity bin. The ratios are compared to results in Pb–Pb collisions (right panels) where central multiplicity bin is 0-5%, and the peripheral multiplicity bin is 80-90%. Figures from [62].

In the exponentially falling thermal region (low p_T) of the parton spectrum in heavy ion collisions, the recombination process may dominate over fragmentation due to the high population of partons [70, 71], resulting in hadrons with intermediate p_T values. In the high-p_T region, where the spectrum behaves like a power-law function, the fragmentation will be the dominating hadronization mechanism since the parton density is lower there. The threshold between the two p_T-domains depends on the size of the system and the hadron species.

3.5.1 The EPOS Model

As seen in Fig. 3.14, pure recombination overestimates both the Λ/K_s^0 and p/π ratio, even though it reproduces the shape of the enhancement seen in data quantitatively well — indicating that recombination can not be the single answer to the enhancement, and models that include an interplay between different mechanisms have to be developed.

One such model is the EPOS event generator [67, 68], which is an attempt to describe the interplay between soft and hard processes. EPOS generates initial scatterings creating "flux tubes" strings that break into segments. A region with a high density string segment core is then defined in this system, with a low-density string-segment corona. The core-region string segments suffer a simulated hydrodynamic behaviour, which eventually hadronizes as soft hadrons. Real experimental results are used as input for the free parameters of the core, such as the energy density and temperature at freeze-out, and of course there are requirements of total energy conservation.

The high-p_T strings that escape the core, and enter the corona, are observed as jets. Strings that are generated at the surface of the core, will continue to fragment unmodified. In the core, however, not only soft recombination is allowed, but also string segments in neighboring jets can recombine. In this sense, the interaction between jets and the expanding bulk is taken into account, making EPOS able to provide predictions in a wide p_T-region.

Looking at the EPOS generated results for Λ/K_s^0 and p/π in Fig. 3.14, it is seen that it describes the enhancement qualitatively well on both sides of the peak, but the peak itself is overestimated, as pointed out in Sec. 3.4.4. It is still, however, better than pure recombination in reproducing the data.

3.6 Thesis Research Focus

As a brief summary of the previous sections, we know that the relative contribution of different hadronization mechanisms changes with hadron momentum: the hydrodynamical model describes the data well up to intermediate p_{T}, which starts at around 2 GeV/c, and fragmentation explains the behavior at high p_{T}, starting from $\sim$8 GeV/c. The intermediate region is much more difficult to explain because a mixture of soft and hard processes contributes to the particle production. This complex interplay manifests itself already in the R_{AA}, where it is noted that the protons are less suppressed than the kaons and pions.

To better illustrate the intermediate p_{T} nature of these types of particles, we compute the baryon-to-meson ratio for p/π and $\Lambda/\mathrm{K}^0_{\mathrm{s}}$. The intermediate p_{T} region shows a decoupling of hadrons from pure hydrodynamical flow, demonstrated by the enhancement of the ratio of baryons to mesons compared to pp measurements, most noticeable towards more central collisions. Around the enhancement maxima and up to $p_{\mathrm{T}} \sim$8 GeV/c, the data are qualitatively described by the recombination model by Fries *et al.*, and the EPOS model, but these models overestimate the maximum values. This indicates that the many available theoretical descriptions are not yet satisfactory in describing the interesting enhancement phenomena, and a more detailed experimental study needs to be carried out in order to determine the origin of the enhancement.

The goal of the analysis in this thesis is to experimentally investigate the baryon-to-meson anomaly at intermediate p_{T} further, and to determine its origin, i.e. if it is an effect arising from the soft, collective, part (the bulk) of the medium, or the hard processes (jet fragmentation).

This will be done by an analysis of central Pb–Pb collisions at $\sqrt{s_{\mathrm{NN}}} =$ 2.76 TeV from the ALICE experiment recorded in the 2011 heavy ion run period. For this analysis, a novel two-particle correlation technique called the *η-reflection method* is developed, where a separation can be made of the contributions from Λ and $\mathrm{K}^0_{\mathrm{s}}$ particles produced in the soft underlying events, i.e. the *bulk*, from those which are produced in association with a high-p_{T} *trigger* particle, representing a jet-like environment, or the *peak* region. The aim with this analysis is to measure the $\Lambda/\mathrm{K}^0_{\mathrm{s}}$ ratio at intermediate p_{T} in the bulk and jet-like environment, to see how the baryon-to-meson anomaly differs in the two regions, and is they are compatible with inclusive Pb–Pb measurements or pp collisions.

"Idag har jag glömt: plånboken, nyckeln till kontoret, penna (det är faktiskt ett problem!) och datorladdare. Och det är faktiskt inte den enklaste sak att gå tillbaka till hotellet i 40 min när det ösregnar och en har glömt paraplyt på kontoret en inte kommer in i. Särskilt inte när en råkade ha sönder cykeln som Lunds universitet har här på cern och fick lifta hit på morgonen för att bussarna från Frankrike (där mitt hotell ligger) till Schweitz (där mitt kontor ligger – och som jag FORTFARANDE inte kan stava till) går så pissigt sällan, och som jag dessutom inte hade haft pengar till. Och nu kan jag snart inte kolla upp busstiderna eftersom jag slösar datorbatteri på facebok." (21 Aug 2014)

Chapter 4

ALICE — A Large Ion Collider Experiment

The Large Hadron Collider (LHC) is a 27 km long synchrotron and collider storage ring placed 50-100 m under ground on the French-Swiss border outside the city of Geneva. It is located at the international nuclear and particle physics laboratory CERN. Beams of proton or lead-ion[1] *bunches* are accelerated. From the LHC circumference and maximum B-field, the maximum center of mass energy for proton collisions is $\sqrt{s} = 14\,\text{TeV}$, and $\sqrt{s_{\text{NN}}} = 5.5\,\text{TeV}$ for lead collisions. For nuclear beams we use the notation $\sqrt{s_{NN}}$, which refers to the available energy per colliding nucleon pair. Last year, LHC reached proton collision energies of $\sqrt{s} = 13\,\text{TeV}$, and lead collisions of $\sqrt{s_{\text{NN}}} = 5.02\,\text{TeV}$ in the center of mass frame. The analysis performed here, however, uses data from 2011, where the lead collisions had a center of mass energy of $\sqrt{s_{\text{NN}}} = 2.76\,\text{TeV}$. If nothing else is mentioned, the default description of the detectors will be given based on the state they were in at the time the data was recorded for this analysis.

There are eight beam crossing points along the LHC, and the ALICE experiment — one of the 4 main LHC experiments — is located at point 2. The electromagnets focus the beams spatially at the crossing points to reach a high number of crossing particles per area, called *luminosity*. The luminosity also depends on the the number of particles per bunch, how

[1] Typically 4 weeks of heavy ion physics per year.

often the bunches collide, and the cross section area. In the 2011 heavy ion run period, LHC was running with 336 bunches per lead beam, for a delivered integrated luminosity of 146 μb^{-1} [72].

ALICE is the only LHC experiment specifically designed for Pb–Pb collisions[2], with the goal to study the QGP, and it is therefore required to handle the extremely large particle multiplicities arising from these collisions. The charged track density in central (0-5%) Pb–Pb collisions is about $dN_{ch}/d\eta \sim 1600$ [73], which is ∼400 times larger than in pp collisions at the same energy per nucleon pair. The track density is highest at mid-rapidity, where ALICE has its physics focus. ALICE central barrel covers a pseudo-rapidity region of -0.9 $< \eta <$ 0.9, and close to full azimuthal coverage.

Since Particle Identification (PID) is an important tool for QGP observables, ALICE needs to have excellent particle identification capabilities over a wide momentum range: low-p_{T} to cover thermal particle production, collective and soft physics, and high-p_{T} for hard phenomena, such as jets. ALICE is capable of PID of charged hadrons in the region $0.15 < \mathrm{p} < 20$ GeV/c — with the ability to reconstruct charged particles up to 50 GeV/c without identification. These goals are achieved by incorporating different tracking detectors with high granularity that, combined, can reach an excellent tracking performance.

The central detectors are surrounded by a solenoid magnet with a magnetic field of 0.5 T, parallel to the beam axis. The magnetic field is also a key ingredient in track reconstruction at low p_{T}, since a charged particle with a certain p_{T} will bend off in the magnetic field, with a momentum dependent curvature. A schematic view of the ALICE experiment is shown in Fig. 4.1.

The coordinate system in ALICE is a right-handed orthogonal Cartesian system with $(x, y, z) = (0, 0, 0)$ at the detector center (the nominal collision point), the horizontal x-axis is pointing towards the center of LHC, the y-axis vertically upwards, and the z-direction is along the beam-line, away from the muon arm (pointing *left* in Fig. 4.1). The azimuthal angle, φ, is 0 along the positive x-axis, and increases counter-clockwise, reaching $\pi/2$ when aligned with the positive y-axis. The polar angle, θ, is the angle from the z-axis, relating to the pseudo-rapidity (a crucial concept

[2]It must also be able to record pp (and p–Pb) collisions.

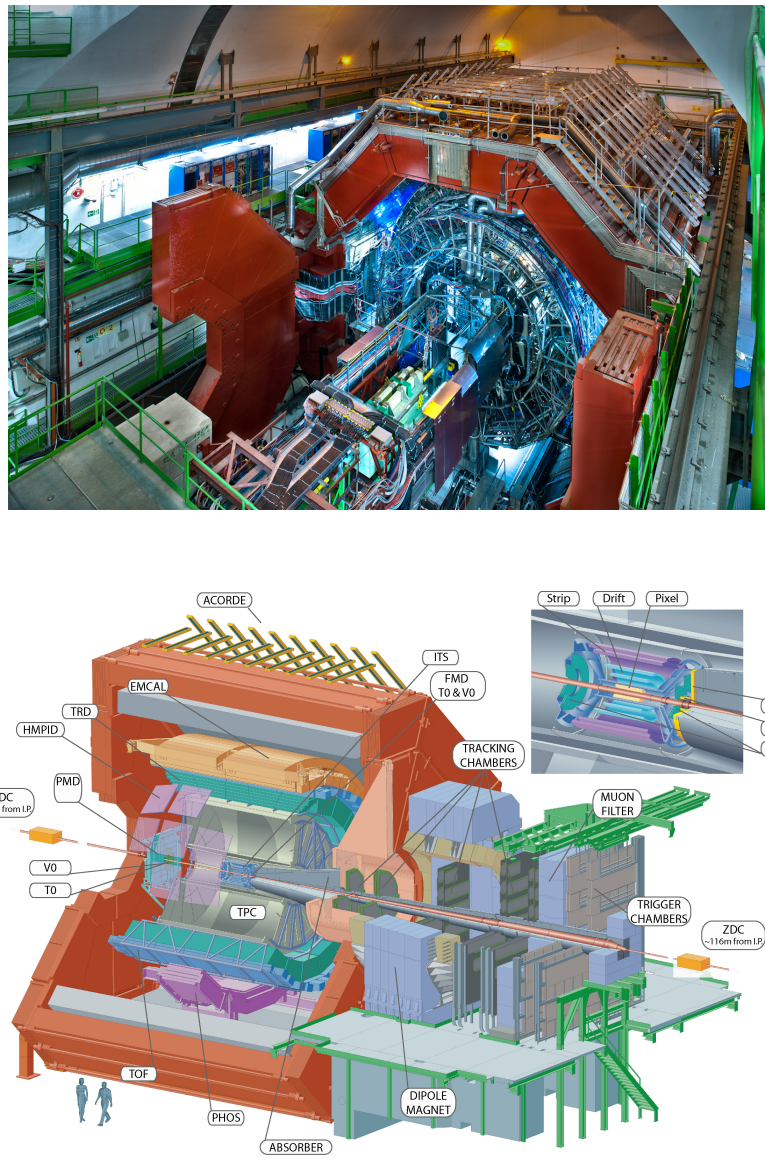


Figure 4.1: The ALICE experiment. The central-barrel detectors (ITS, TPC, TRD, TOF, PHOS, EMCal, and HMPID) are inside in a solenoid with magnetic field B = 0.5 T and address particle production at mid-rapidity. Forward detectors (PMD, FMD, V0 (called VZERO in the text), T0, ZDC, and the MUON-arm) are used for triggering, event characterization, and multiplicity studies. Photo from CERN Document Server: ALICE-PHO-GEN-2012-001-12. Schematic Illustration Credits: Jochen Thaeder (ALICE).

when describing the analysis), η, by

$$\eta \equiv -\ln\left[\tan\left(\frac{\theta}{2}\right)\right] \tag{4.1}$$

4.1 Subsystem Detectors

First, a short summary of the most important subsystem detectors (seen in Fig. 4.1) will be given, and in the following sections, the analysis specific detectors, the ITS, TPC, and VZERO, will be described in more details.

4.1.1 Central Detectors

The subdetectors inside the solenoid magnet closest to the beam-line, the inner tracking system (ITS), and the time projection chamber (TPC), measure the curvature (momentum) of charged particles, thus functioning as the tracking and vertex finding detectors. These will be covered in Sec. 4.2 and 4.3.

The **Transition Radiation Detector (TRD)** is placed outside the TPC, segmented into 18 azimuthal sectors, each 7 m long. Only 10 sectors were installed for the 2011 physics runs, see the detector configuration during 2011 in Fig. 4.2. Each module is composed of 6 layers of multi-wire proportional chambers (MWPC) filled with a $XeCO_2$-gas mixture. In front of each MWPC, a fiber radiator is placed, which is used for electron identification via transition radiation and energy deposition, and thus, the TRD can separate electrons from pions very well. The TRD is also used for tracking and triggering on electrons and jets.

The **Time-Of-Flight (TOF)** detector is covering the full azimuthal angle, thus being a crucial component in the angular distribution and correlation measurements with identified particles. TOF measures the time it takes for a particle to travel from the interaction point to the detector using gas-filled multi-gap resistive plate chambers (MRPC). The glass plate stack has voltage applied to the surface, making the ionization from a traversing particle create an electron avalanche which is picked up by electrodes. The avalanche is stopped by the resistive plates in each gap, but the charge induced on the electrodes gives a fast signal with a time resolution of 50 ps. The velocity of the particles can be extracted via the

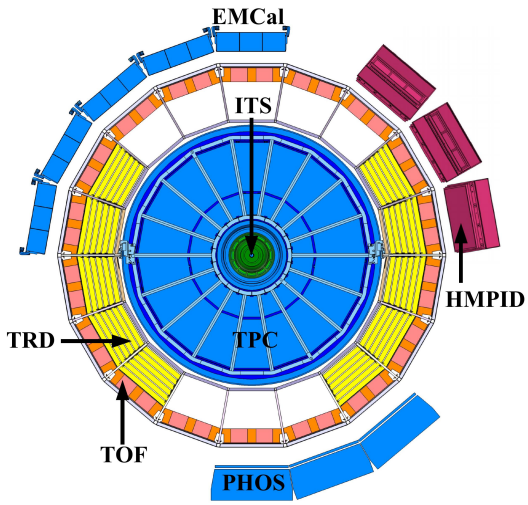


Figure 4.2: Cross section of the ALICE central barrel detectors. Schematic Illustration Credits: Jochen Thaeder (ALICE).

time information and the estimated flight length. If the momentum of the particle is known, the mass — and hence the identity — can be derived. The TOF separates well the $\pi^{\pm}$, $K^{\pm}$, and p($\bar{p}$) in the momentum range 1-3 GeV/c.

Further out, located radially from the detector center, is the 20 radiation lengths thick (corresponding to 1 nuclear interaction length) **Electromagnetic Calorimeter (EMCal)**, and the high-resolution crystal **Photon Spectrometer (PHOS)**. These two detectors accurately measure the energy deposited by mainly electrons and photons, but also charged hadrons. For electrons and photons the deposited energy equals the particle energy, while for hadrons it is only a fraction of the hadron energy.

The ring-imaging Cherenkov detector (**HMPID**) is placed at the same radial distance as PHOS. This is an intermediate momentum (3-5 GeV/c) char-ged hadron identification system, making use of Cherenkov light, produced by particles moving faster then the speed of light in the specific detector material (radiator). The Cherenkov angle depends only on the particle velocity.

4.1.2 Forward Detectors

While many central barrel detectors are symmetric around $\eta = 0$, the forward detectors are not symmetric in η because of the asymmetric design in ALICE with one muon arm. Forward detectors are placed at small angles (large η) with respect to the beam.

The **Muon Spectrometer** is placed outside the central barrel magnet, covering -4.0$<\eta<$-2.5, and has an additional dipole magnet installed. It consists of a thick absorber that stops all particles but muons, since they penetrate matter due to their lack of strong interaction, if the energy is high enough. With the identified muons, heavy quarkonia decaying into muons can be studied, e.g. $J/\psi \rightarrow \mu^+ + \mu^-$.

The other forward detectors are mainly installed for triggering purposes and multiplicity measurements. The **Time Zero (T0)** measures the start time needed by the TOF measurements for accurately calculating the time of flight. Other multiplicity and triggering detectors are the plastic scintillator **VZERO** (discussed in Sec. 4.4), the silicon **Forward Multiplicity Detector (FMD)** (placed at -3.4$<\eta<$-1.7 and 1.7$<\eta<$5), the gas-counter **Photon Multiplicity Detector (PMD)** (2.3$<\eta<$3.7) which measures the number of photons, and the **Zero Degree Calorimeter (ZDC)** ($z = \pm 116$ m) which triggers on the impact parameter, by measuring the energy of the spectator remnant nucleons, thus providing information about the centrality. The last trigger detector is **ACORDE**, an array of scintillators placed on top of the magnet, used as a cosmic ray trigger for calibration purposes when there is no beam.

4.2 The Inner Tracking System

The ITS is one of the main tracking detectors of ALICE, together with the TPC. It is the detector closest to the beam pipe, covering the full azimuthal angle, consisting of 6 different silicon semiconductor layers, seen in Fig. 4.6 (the figure shows both the ITS and VZERO detectors), with three different detector techniques. The inner-most two layers (a radius of 3.9 cm) are Silicon Pixel Detectors (SPD) (also used for triggering) with an acceptance of $|\eta| < 2.0$. The middle two layers are Silicon Drift Detectors (SDD), and the outer-most two layers (at a radius of 43 cm, and acceptance $|\eta| < 1.0$) are Silicon Strip Detectors (SSD).

The general function of a silicon semiconductor detector is to have a p-n junction, on which a reverse bias potential is applied to form a depletion zone without movable charges. When a charged particle is passing through the depletion region, it will create electron-hole pairs which are transported by the reverse biased field and read out as a signal proportional to the energy loss of the ionizing particle.

The ITS serves the following purposes:

- Mid-rapidity ($|\eta| < 0.9$) tracking
- Vertex finding, with a resolution of <10 μm in the z-direction, and $\sim$35 μm in the $r - \varphi$-plane for Pb–Pb multiplicities (of special importance for the V0 analysis)
- Low-p_{T} (< 1 GeV/c) PID by energy loss measurements (SDD and SSD)
- Improving the angle and momentum resolution from the TPC
- Complementary multiplicity estimation in terms of event-by-event impact parameter deduction from multiplicity ($|\eta| < 2$)
- Triggering (SPD)

It is important to note here, that with the high spatial resolution, the ITS is not only capable of finding the primary vertex, but also the secondary vertices close to (but separated from) the collision vertex. In particular, it can look for heavy quark decays.

4.2.1 The Silicon Pixel Detector

The SPD is designed for high spatial granularity due to the large track density so close to the collision point. The high granularity and close distance makes it ideal for both primary and secondary vertex reconstruction, as well as track separation. The detector is built up by two-dimensional sensor modules (with an active area of 12.8 mm in $r - \varphi$, and 70.7 mm in z) consisting of 256$\times$160 cells (pixels of 50 μm $\times$ 425 μm, 200 μm thick) in *ladder* structures. The matrix is read out by the fast front end electronics in chunks of cells when they register a "hit" above the preset threshold. The signals are then combined in a logic unit, which deliver a trigger decision.

During the 2011 physics run, the fraction of active outer SPD channels was ∼80%, leading to an inhomogeneous φ-distribution of the reconstructed tracks, as will be discussed and corrected for in the analysis part.

4.2.2 The Silicon Drift and Strip Detectors

The SDD has an inner radius of 15 cm, where the track density is not as high as for the first few centimeters from the collision point, hence making it possible to move from the expensive pixel concept, and instead introduce larger drift structures constructed to give a good tracking and PID performance at low-p_{T} by measuring the transport time of the electrons and holes created in the ionization by the particle passing through the 300 μm thick p-n junction. By using the time dimension, a highly granular readout with much fewer (compared to pixels) electronics channels is achieved.

The two SSD layers start at a radius of 39 cm and consist of 300 μm thick, 40 mm long, double-sided — p^- on one side, and n^- on the other — silicon strip sensors separated by 95 μm. Each strip is tilted by 17.5 mrad, giving an $r-\varphi$-resolution[3] of 20 μm, convenient for two dimensional precision matching of tracks between the ITS and TPC.

Due to the analog readout of the SDD and SSD layers, the energy loss ($\mathrm{d}E/\mathrm{d}x$) information can be extracted and PID can be performed up to ∼1 GeV/c.

4.3 The Time Projection Chamber

The TPC is the heart of ALICE. It is built on a 3-dimensional pattern recognition idea to be able to reconstruct and identify particles in a very high multiplicity environment. This is done by measuring the particle ionization trajectory (for tracking and PID), and the ionization energy loss (for PID), $\mathrm{d}E/\mathrm{d}x$, i.e. the mean deposited energy per unit path length, for a charged particle traversing the gas volume of the TPC cylinder.

The goal is to be able to detect electrons, charged pions, protons and

[3]The z-resolution is ∼800 μm.

charged kaons and light nuclear species[4]. From the reconstruction of these particles, many other particles can be identified through their decay channels into these species.

4.3.1 The Detector Design

The TPC is a hollow 5×5 m cylindrically shaped chamber surrounding the ITS, with an active volume between $85 < r < 247$ cm, where r is the radius. It is the biggest TPC in the world with its gas volume of $\sim$90 m^3, covering $|\eta| < 0.9$ in pseudo-rapidity, and the full azimuthal angle.

The field cage is divided in two parts by a central electrode with a high-voltage of -100 kV applied, see Fig. 4.3. The field cage in combination with this electrode provides a uniform electrostatic field in the z-direction.

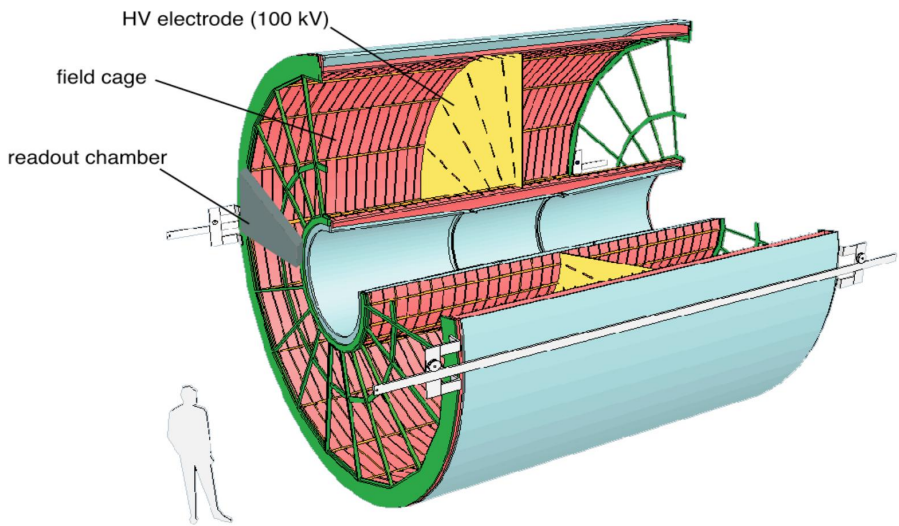


Figure 4.3: The TPC detector design. Figure taken from [74].

During the data taking period of 2011, the volume was filled with a gas consisting of 90% Ne and 10% CO_2. Since the active detector material of the TPC is a gas, it will have a low material budget (less than 3% of the

[4]For example Deuterons, 3He, and 4He.

radiation length), which minimizes multiple scattering of particles in the material and the production of secondary particles.

The beam-perpendicular end-caps readout chambers are divided in 18 sectors with MWPCs, each sector with an inner (IROC) and outer (OROC) readout chamber with different granularity to optimize the read out for high multiplicity Pb–Pb collisions. The IROC is segmented into 63 cathode pad-rows, parallel to the wires, with a pad size of 4×7.5 mm^2, giving a total number of 5732 pads per sector. The OROC has 10110 pads split on 64+32 pad rows (pad size 6×10 mm^2 and 6×15 mm^2, respectively). The total number of rows in IROC+OROC is 159.

As seen in Fig. 4.4, there are three wire planes before the cathode read out pads. Closest to the pads is an anode wire plane, followed by a plane of cathode wires, and last, nearest to the drift volume, the *gating* grid.

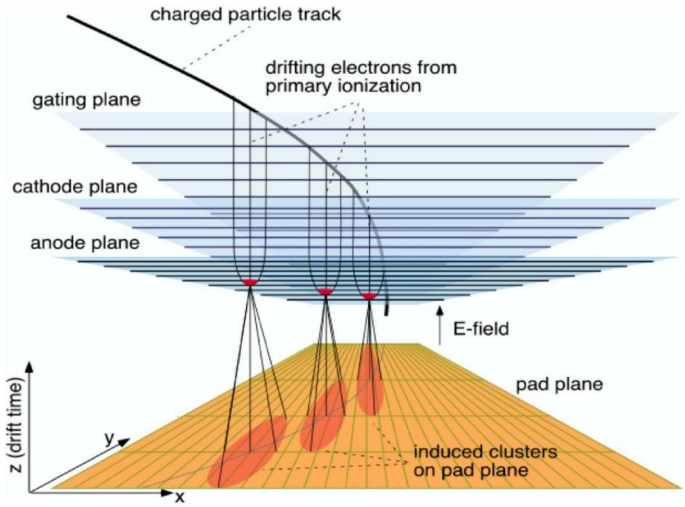
4.3.2 Operation

Ionization

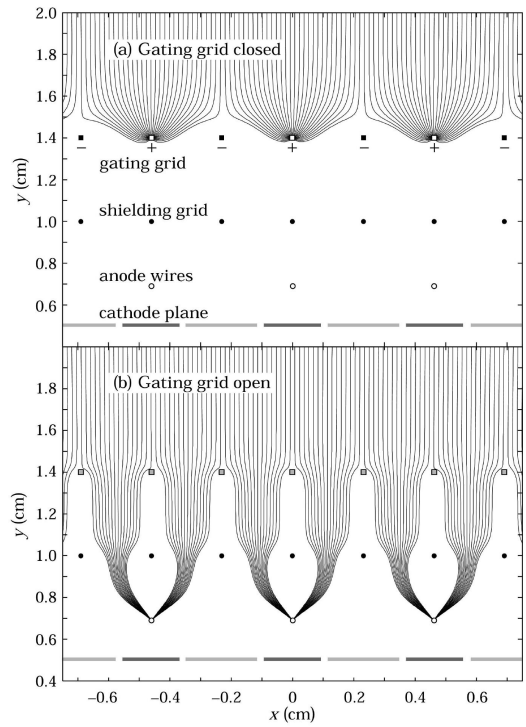
When a charged particle from the collision traverses the gas filled chamber volume, it will ionize the gas along its trajectory (the trajectory will have a momentum-dependent curvature in the transverse plane due to the magnetic field along the z-direction), with a specific energy loss depending on the particle velocity. The electrons released in the ionization process will drift towards the end-caps due to the homogeneous electric field of 400 V/cm generated by the central cathode, with a drift velocity of $\sim$2.7 cm/μs. The electric and magnetic field point in the z-direction, which will lead to a reduction of the diffusion (transverse spread) of the electrons.

Signal Amplification From Avalanches

When the electrons reach the gating grid, the trigger decision of the collision determines if the gating grid should open (accept) or remain closed (see the difference in Fig. 4.4(b)), to prevent the electrons from entering the amplification region. If the gating grid opens, it will remain open during $\sim$90 μs to allow the electrons to drift to the end-caps.



(a) The structure of the read out chambers.



(b) The concept of open and closed gating grid.

Figure 4.4: An illustration of the wire chamber principles. Figure taken from [75].

With an open gating grid, the electrons will continue to the anode wire plane, where the field strength increases as $1/r$, making the electrons accelerate and ionize the surrounding gas further, thus multiplying the number of electrons to enhance the signal. The electron avalanche will of course release ions in the process, which will induce charge on the cathode pad plane by their motion. When the gating grid closes after having let through all electrons from the ionizing event, it is not only preventing electrons from other events to enter the amplification region, but it is also preventing ions created in the avalanche to drift back to the main volume. The latter would cause a distortion of the drift field leading to deteriorated tracking performance. The gate has to be closed for $\sim$188 μs to stop all the ions created in the avalanche belonging to the actual event. This will effectively lead to a dead time of the TPC of $\sim$280 μs (90+188 μs), which in turn limits the rate at which events can be measured to $1/0.000280\,s = 3600$ collisions per second.

Reading Out The Signal

The position of the induced signal on the pad plane gives two-dimensional information about the particle trajectory. Due to the 159 pad rows, the TPC allows up to 159 *clusters* (position signals) for each track. The coordinate in the third dimension (z) is obtained by knowing the drift velocity of the electrons in the gas, and the information about the time it took for the electrons to drift from the point of ionization to the anode plane. The three dimensional diffusion of the electrons in the gas sets the spatial segmentation, to which the TPC pad size[5] and digitization sampling frequency was designed. The TPC Analog-to-Digital Converter (ADC) sampled with a rate of 10 MHz during the 2011 Pb–Pb run.

The signals are transferred via Kapton cables from the readout pads to a total of 4356 TPC Front End Cards (FEC), in which a custom-made charge sensitive shaping pre-amplifier (PASA) converts the induced charge to a voltage, and amplifies the signal in each pad. The signal has a specific time distribution with a relatively fast rise time, but a long tail due to the slow back-flow motion of the drifting ions. To extract the necessary in-

[5]The resolution will however be better than the actual pad size due to charge smearing over several pads, so that the weighted centroid can be determined with a better accuracy than the pad sizes.

formation about the signal (amplitude and time of occurrence), the signal is shaped into a differential Semi-Gaussian signal with a shaping time of 190 ns. The signal is then fed to the input of the ALTRO chip [76]. The custom made ALTRO chip is an integrated circuit containing 16 channels that digitize, process (baseline correction, tail cancellation, zero suppression), and buffer[6] the digitized data. The ADC embedded in the chip has a 10 bit dynamic range.

The FECs are read out via a 40 bit wide data bus controlled by a Readout Control Unit (RCU) that transfers the digital data for each time sample and each pad to the DAQ and the High Level Trigger.

4.3.3 Replacing Damaged FECs and Reducing the Gain in 2011

Any gas filled avalanche detector (like the MWPC) has a certain risk that an unusually large avalanche develops into a spark when the gain is set at a high value, such that minimum ionizing particles shall be detected. Sometimes, highly ionizing particles may give too large avalanches which may develop into a spark, causing the High Voltage (HV) to trip because of the current limitation, i.e. a HV trip happens when the current from the high voltage supply to the ROCs is above a certain threshold ($\sim$200 μA). These HV trips are normally occurring in MWPCs at some rate, which is dependent on the rate of particles traversing the detector.

When LHC started to run at higher intensities and luminosities in 2010, the TPC was triggered (gate open) at a higher rate (400-1000 Hz). At this rate, HV trips started to occur frequently (several times per week, sometimes several per day). The problematic consequence here is that, with too large a probability, a spark followed by HV trip lead to a damaged FEC, which in turn means 128 dead channels.

Since sparks are expected to happen, the readout electronics is equipped with input protection which shall protect the circuit. It is thus believed that the damage to the FECs is caused by the HV trip itself — and not from the spark as such. If the threshold limit is exceeded, the power supply ramps down ($\sim$1 kV/s) to ensure safe operation. The ramping down of the HV induces a large negative current at the charge amplifiers which leads to a large negative voltage at the input transistor and a large voltage

[6]The data stream is stored from the L1 trigger to the decision of the L2 trigger, when it is either discarded or read out.

($\sim$ kV) across the feedback transistor. The circuit at the PASA input can therefore be damaged[7].

To avoid this problem in the 2011 Pb–Pb run, it was decided to lower the TPC gain. However, in the cases when a HV trip caused a damaged FEC, it was necessary to replace these cards. I had the opportunity to perform this task. The 2×18 TPC sectors are divided in an outer (OROC) and inner (IROC) read out chamber, as mentioned in Sec. 4.3.1. The IROC and OROC each consists of three FEC rows, called *partitions*, read out by the RCU, with 18, 20, or 25 FECs in each partition (depending on the radial position). The partitions are divided into two branches.

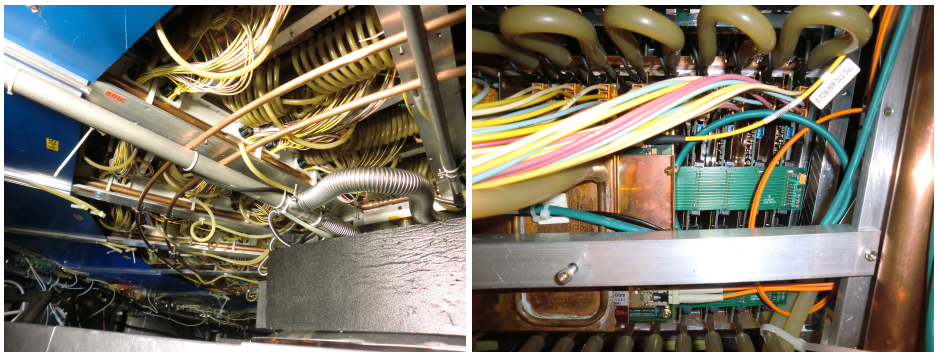
Before a FEC can be replaced, the Front End Electronics (FEE), such as the low voltage cables to the FECs, the RCU with the fiber optics, the control and data busses, and the cooling of the FEE, must be removed, see Fig. 4.5. Due to lack of space, all FECs on one side of the broken FEC on the specific branch must also be removed. One FEC has 6 Kapton cables which connect to the FEC with a so called ZIF connector (Zero Input Force), and closed with a *lock* — approximately 1-2 mm wide, and another connector on the pad plane. To remove a card from the row of FECs, the lock on the pad plane connector must be opened by a custom made hook tool.

When the broken FEC in a row is replaced, the FEC needs to be put back in place again; the Kapton cable is placed in the lock and the lock is closed. To check that Kapton cables are connected correctly, a test is performed by reading out an individual FEC with a portable DAQ system, replacing the RCU and the main ALICE DAQ. Test pulses sent to the wires in the chambers are read out, thus verifying the integrity of the connection.

4.3.4 Read Out Control Unit Upgrade

Continuing my contribution to the TPC hardware, I was also involved as one of two coordinators in the installation of the upgraded read out control units. For the TPC to be able to make full use of the larger amount

[7] The input protection circuit of the amplifier should protect for this, but if the current through the protection diodes becomes too large, they themselves can become damaged and permanently short circuits to ground (or supply voltage) instead of the temporary short circuits which are supposed to occur when acting as protection.



(a) (b)

Figure 4.5: Photos taken at P2 on the A-side of the ALICE-TPC during the FEC replacements. (a) The IROC sectors with the cooling tubes, and low voltage supply. (b) The FECs in one branch with the RCU connected to the buses.

of data in Run2 due to the higher particle interaction rates (8-30 kHz) [77] and higher collision energies of Pb–Pb collisions, and thus the increased amount of data, new RCUs (RCU2) are installed to increase the speed. The RCU2s can record data with double rate compared to the data taking in Run1. With the RCUs in Run1, the TPC could handle an event readout rate of 250 Hz for central Pb–Pb collisions, while with the RCU2 the TPC is foreseen to handle an event read-out rate of at least 400 Hz [77] while still keeping the busy time low. The higher read out speed is achieved by modernization of the RCU circuit, and to split the two existing readout buses into four, and change the readout Detector Data Link (DDL) of the RCU to a higher bandwidth version [77].

4.4 The VZERO Detector

The VZERO detector is a pair of ring-segmented scintillator detectors placed around, and perpendicular to, the beam, asymmetrically (with respect to the collision point) in the forward direction — one at positive η (VZERO-A: $2.8 < \eta < 5.1$) and one at negative η (VZERO-C: $-3.7 < \eta < -1.7$), as shown in Fig. 4.6 together with the ITS detector.

When a charged particle enters the sensitive scintillator material, it

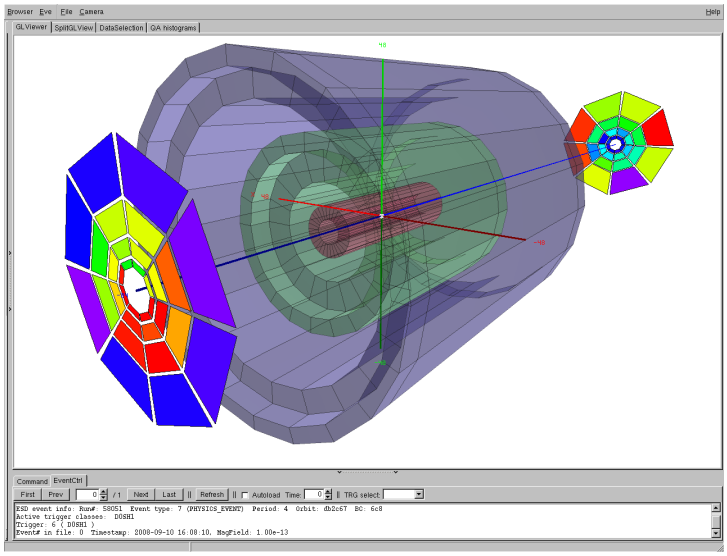


Figure 4.6: A display with the ITS and VZERO detector, illustrating the detector layout.

will excite and ionize the atoms, which releases their surplus energy by emitting scintillation photons. The number of photons is proportional to the energy deposit of the incoming particle. The photons are then guided through fiber-optic cables to the photo multiplier tubes (PMTs) which amplifies the signal by multiplying the electrons released from the photo cathode by the initial photon. The signal is read out by the VZERO front-end electronics, measuring the pulse time relative to the 40 MHz LHC bunch clock.

The timing resolution, the large pseudo-rapidity coverage, and the fact that any charged particle will give the same average response (since all have $\beta = v/c$ very close to 1), gives a total signal correlated with the number of particles in the detector (multiplicity). This makes the VZERO ideal for providing centrality based triggers. As described in Sec. 3.1, the VZERO response amplitude is fitted with a Monte-Carlo simulation of the Glauber Model, used to assign a centrality to every Pb–Pb event. The VZERO can separate the beam-beam interaction events from different sources of accelerator induced background effects, e.g. beam-gas interactions, as well as estimate the beam luminosity in pp collisions.

4.5 Data Acquisition and The Trigger System

The trigger and data acquisition (DAQ) system of ALICE is designed to handle both pp collisions with frequent but small events (an instant luminosity of $10^{30} - 10^{31}\text{cm}^{-2}\text{s}^{-1}$ with 25 ns bunch crossings), and Pb–Pb collisions with the relatively infrequent but very large events (instant luminosity of $10^{26} - 10^{27}$ $\text{cm}^{-2}\text{s}^{-1}$ with 100 ns bunch crossing interval).

In the 2010 run the interaction rate was low, and the focus was to trigger on minimum bias collisions, while the 2011 focus was on central collisions. Since the measurement performed in this thesis is done with the 2011 data due to the large statistics available, it will be done for the 0-10% central collisions. In addition to this reason, the central collisions will most probably reveal the largest effect between bulk and jet. For the data used in this analysis, the central ("CENT": 0-10%), semi-central ("SEMI": 0-50%), or minimum bias ("MB") events are used.

For completeness, the low- and high-level triggers, are very briefly described here since it is an important part of ALICE as a whole, even though it is not used in this thesis.

The low-level (level zero, L0) trigger, the Central Trigger Processor (CTP), is for each bunch crossing combining information from the VZERO (centrality), TOF (multiplicity and back-to-back topology), T0 (event vertex), SPD (multiplicity and topology, based on hits), EMCal, PHOS (photons), MTR (muons), and ACORDE (cosmic rays) subsystems into one single signal, and deliver a decision after 1.2 μs.

The L1 trigger takes a decision after additional 6.5 μs based on the ZDC (minimum bias interaction), EMCal (photons and neutral jets) and TRD (electrons, high-p_{T} particles, charged jets) information. L0 and L1 trigger the buffering of the event data in the front-end electronics.

The L2 decision is taken after 100 μs, i.e. the time it takes for the TPC to read out an event, and if this is a positive decision, the DAQ system will gather information about the event from the individual subdetectors by the Detector Data Links (DDL) to process and build the full global event to be analyzed by the high-level trigger.

While the low-level trigger is hardware based, the High-Level Trigger (HLT) is a software based trigger. It processes the data read out from the detectors, analyzes the detector trigger signals, and make a full online reconstruction of the event (including producing many physics observ-

ables), to be able to make a decision whether to accept (read out and write to disk) or reject the event. If the final trigger decision is positive, it will be stored and available for offline analysis. It could for example be decisions about keeping events with high energy jets. In 2011 the HLT was used to reconstruct the TPC clusters so the output could be compressed with a total a factor of ∼4-5 compared to the raw data [78].

4.6 Track Reconstruction

To reconstruct a track belonging to a charged particle coming from the collision, information from many different subdetectors are needed.

4.6.1 Cluster Finding and Preliminary Primary Vertex

To reconstruct the position, amplitude, and timing of the signal "hits" (charged particles that interact with the detector), a *cluster finding* is performed for each relative detector (ITS, TPC, TRD, TOF, HMPID, EMCal and PHOS – of which the ITS and TPC is the focus in this thesis) separately. Using the cluster distribution in the SPD, coordinates to a preliminary interaction vertex position can be assigned.

4.6.2 TPC-ITS inward tracking

When a preliminary vertex is found, the tracking can start. It is an iterative inward–outward-inward procedure, illustrated in Fig. 4.7, starting from track candidates, or *seeds*, in the two outer TPC pad-rows, where the track density is low. The seeds are initially assumed to belong to tracks from the primary vertex, and are now fitted towards the inner part of the TPC (the TPC has 159 pad-rows, and can thus reconstruct tracks with a maximum of 159 clusters) with the simultaneous track fitting method called *Kalman-filtering*[8] [80].

The Kalman-filter method is based on calculations of the track parameters state vector, using their covariance matrix to propagate to the next pad row. If the Kalman-filter finds a space point compatible with the track

[8]The Kalman-filter is superior to other methods due to its ability to reject "fake" clusters arising from e.g. detector noise or multiple scatterings in the detector material, thus improving the track-finding efficiency down to p_{T} =100 MeV/c.

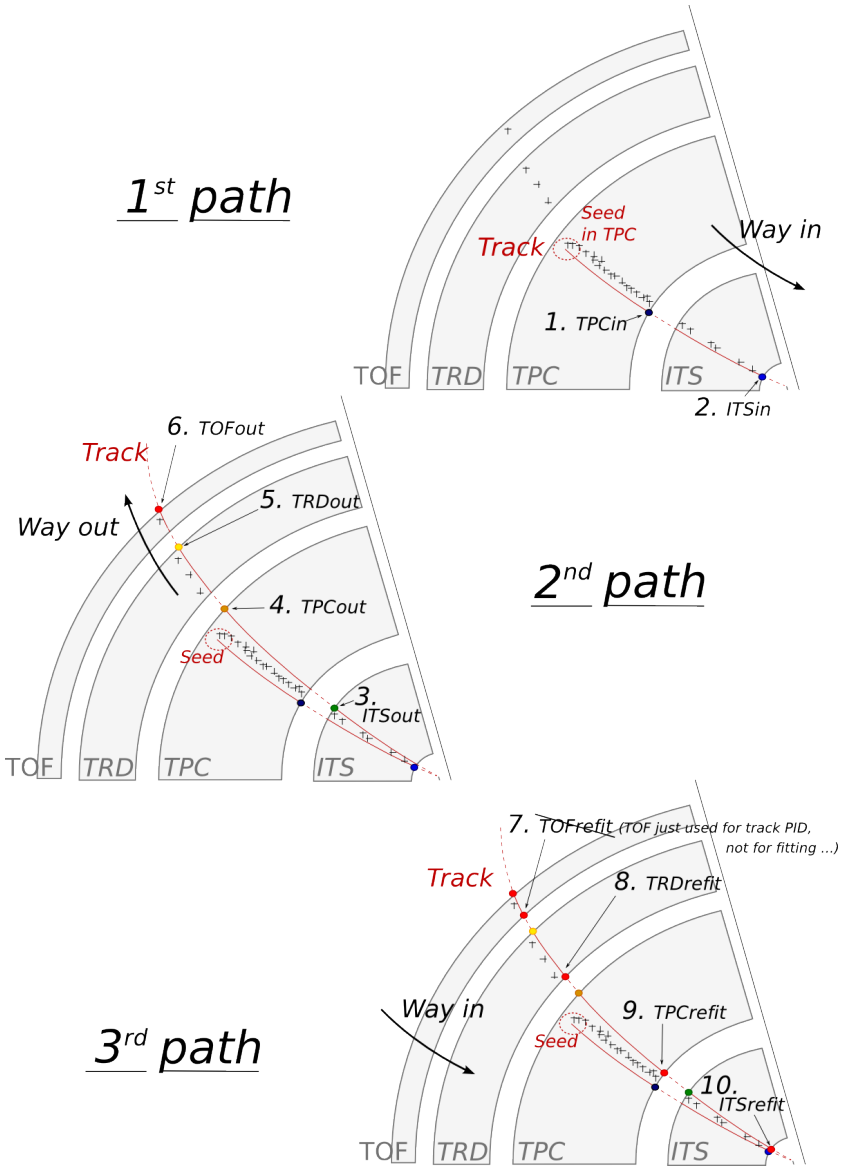


Figure 4.7: Principles of central-barrel tracking for an ALICE event, showing the three successive paths allowing to build a track and refine its parameters. At each point the tracking parameters are stored. The procedure is as follows: (1) track seeding, track matching with TPC-ITS, and first fit to vertex; (2) outward track fit through ITS and TPC, and propagation to TRD and TOF; (3) inward track refitting and attempt to constrain the track to the primary vertex. Figure taken from [79].

prolongation in the new pad row, this measurement is added to the track parameters by updating its covariance matrix.

The essence of this first tracking iteration is to assign clusters to tracks, with an increasing knowledge of the track parameters as the number of associated track clusters grow. At the point where all TPC seeds have been inwards followed, the ITS tracking starts with the goal to extend the tracks with additional ITS clusters — further improving the track parameters — all the way to the preliminary primary vertex.

4.6.3 Outward Tracking

When all TPC seeds have been prolonged through the ITS, the remaining ITS clusters that did not end up in a track from the TPC are used in an ITS tracking. Now the tracks found in the inward tracking are used as seeds for the outward tracking, starting from the primary vertex position propagating back outwards through both ITS and TPC. When the outer pad-row of the TPC is reached, the track parameter precision is sufficient to finally propagate the tracks to the TRD, TOF, HMPID, EMCal, and PHOS cluster signals, producing *global tracks*.

4.6.4 Last Tracking Stage and Final Vertex Position

The last step in the tracking procedure is to make the last Kalman track refit on the global tracks, starting from the TRD ("TRDrefit"), proceeding to the outer part of the TPC ("TPCrefit"), and then inwards towards the vertex ("ITSrefit"). If the refit was successful in the TRD, TPC, and ITS, all final track parameters, such as the position, direction, and curvature are stored. In addition, a new final position of the primary vertex with higher precision is calculated by extrapolating the global tracks to the point of closest approach to the nominal beam line, and using a track weighting to minimize the contribution from outliers [81]. The essence of the Kalman-filter method is that it gives all the track parameters at the *point of the vertex*, i.e. the calculated momentum of a particle is given at the vertex point, and not at any other point along its path.

The tracks that cannot be extrapolated to the primary vertex in this refit stage, are used for the V0 reconstruction (important for the analysis in this thesis). In central heavy-ion collisions, due to high track density,

it can happen that secondary tracks are assigned spurious hits in the ITS and so are considered primary tracks. The MC is not precise enough to correct for the efficiency loss due to this effect and so V0s are only considered in this analysis for decays more than 5 cm away from the beam, see Sec. 5.2.2.

4.7 Particle Identification (PID)

The ITS, TPC, TOF, and HMPID subsystem detectors can perform charged hadron identification at different p_{T}-regions when combined with the measured momentum which normally is measured by the TPC. To improve the separation of the particle species, PID information from different detectors can be combined. This section address the main PID methods used in ALICE.

4.7.1 Charged Hadrons

The tracks found in the event reconstruction are assumed to belong to a particle which we want to identify. The curvature of the track (originating from the magnetic field) gives the momentum of the particle, and the specific energy loss per unit length, $\mathrm{d}E/\mathrm{d}x$, deposited by the particle can be measured. The energy loss is a part of identifying a charged particle, since the energy loss in a specific material depends on particle-specific properties according to the Bethe-Bloch formula [82], expressing the average rate of energy loss per travelled distance as

$$\left\langle \frac{dE}{dx} \right\rangle = \frac{4\pi N e^4}{m_e c^2} \cdot \frac{z^2}{\beta^2} \cdot \left(\ln \frac{2mc^2\beta^2\gamma^2}{I^2} - \beta^2 - \frac{\delta(\beta)}{2} \right) \tag{4.2}$$

where N is the electron density of the material (defined by its atomic number, the mass number, the density, and ionization potential), e is the elementary charge, $m_e c^2$ is the electron rest energy, z is the charge of traversing particle, m is the particle mass, and I is the mean gas atom excitation potential. $\beta = v/c$ is the relative velocity, the Lorentz factor is $\gamma = 1/\sqrt{1-\beta^2}$, and $\beta\gamma = p/(mc)$. The latter relation allows to introduce momentum, p, and particle mass, m, instead of β in the energy loss formula, hence, with this representation, the energy loss can be displayed as a function of momentum, p. The different particle species will cluster in

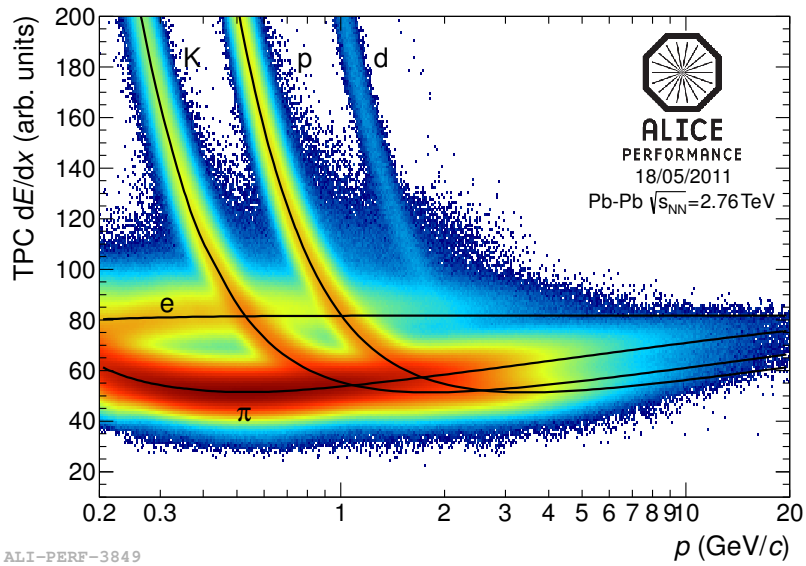
different bands depending on the mass and charge, as seen in Fig. 4.8(a) for the TPC and ITS. The black curves in the figure is calculated by the Bethe-Bloch relation.

When the momentum of the particle is comparable to the mass, the different particle species are well separated. It should be remembered that it is the particle velocity which determines the $\mathrm{d}E/\mathrm{d}x$. Thus, for momenta where relativistic effects (β approaching 1), the velocity is rather independent of momentum, and the $\mathrm{d}E/\mathrm{d}x$ will not contain enough PID information for complete separation between species, and a statistical approach is used in this region. The over-all TPC $\mathrm{d}E/\mathrm{d}x$ resolution is 6.5%.

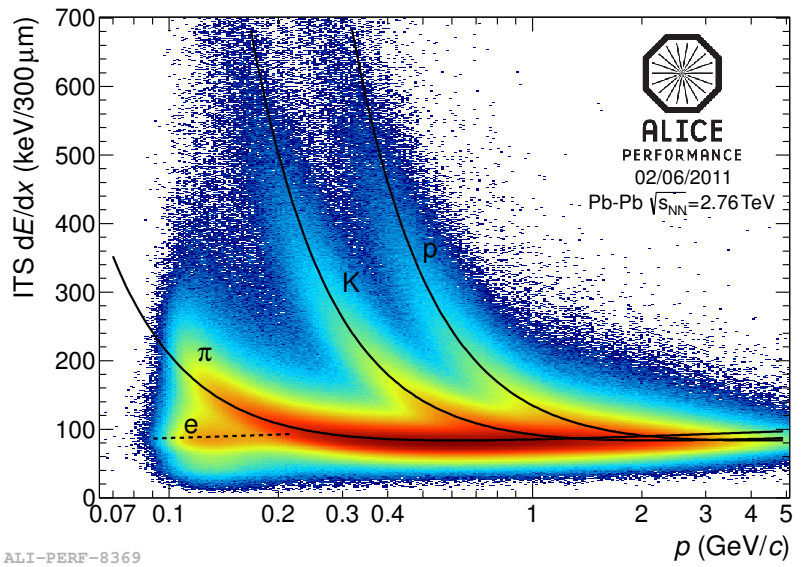
The PID in a TPC is excellent for many reasons. Both p and $\mathrm{d}E/\mathrm{d}x$ comes from the continuously recorded track in the same detector. Thus there is no risk of combinatorial mistakes when combining the two. This is seen in Fig. 4.8(a) where almost all data points are located on the actual bands defined by Eq. 4.2, compared to Fig. 4.8(b), where combinatorial mistakes between $\mathrm{d}E/\mathrm{d}x$ from the ITS and p from the TPC results in data points between the bands.

The other reason is that the $\mathrm{d}E/\mathrm{d}x$ measurement has high resolution in spite of the gaseous thin detector medium with few electrons released for a given deposited energy. The reason is that $\mathrm{d}E/\mathrm{d}x$ is measured in 159 samples and exceptionally high $\mathrm{d}E/\mathrm{d}x$ values corresponding to the Landau tail (see Fig. 32.8 in the 2014 version of the Particle Data Group) in the statistical $\mathrm{d}E/\mathrm{d}x$ distribution can be recognized and omitted.

Another detector contributing to the PID is the TOF, which measures the time of the particles to reach the detector from the collision point. The PID is based on the relation $\beta\gamma = p/(mc)$, and by measuring β and p, the mass, m, can be determined. The charge of the species does not enter, but has to be determined by a $\mathrm{d}E/\mathrm{d}x$ measurement. By using the momentum information from the tracking procedure to present the velocity distribution as a function of particle momentum, the TOF provides good separation of pions and kaons up to $\sim$2.5 GeV/c, and protons up to $\sim$4 GeV/c, while PID particle-by-particle is limited to about 1 GeV/c for $\mathrm{d}E/\mathrm{d}x$.



(a) TPC



(b) ITS

Figure 4.8: Specific energy loss, $\mathrm{d}E/\mathrm{d}x$, in the (a) TPC and (b) ITS, as a function of momentum in Pb–Pb collisions at $\sqrt{s_{\mathrm{NN}}}$ =2.76 TeV. The Bethe-Bloch lines for various particle species are superimposed.

4.7.2 V0 Particle Identification

With particle decays one can do PID to higher p_{T}. If the decay products are occurring with low probability, like leptons and photons[9], one can reconstruct the decaying mother particle, in particular if it is a two particle decay. In case of a weak decay, the reconstruction is helped by the observation of a secondary decay vertex. Secondary vertices can give an identification, particle by particle, but normally one arrives at an integrated number of mother particles in a certain p_{T} bin. For very abundant secondaries, like protons and pions in heavy ion collisions, reconstruction without secondary vertex would, even if the pions and protons were identified, give a huge combinatorial background. Having detected a secondary vertex, on the other hand, gives the possibility to reconstruct the mother particle mass even without PID on the daughters.

The important PID for the analysis carried out in this thesis is the one where the weak decay topology of V0 particles such as $\mathrm{K}^0_{\mathrm{s}}$ and Λ[10] (used in the analysis) is used by kinematical reconstruction of the decay products. The V0 finder method is based on the selection of two oppositely charged secondary tracks, depending on their distance to the primary vertex, in combination with other topological cuts. The technique is presented in Sec. 5.2.2.

[9] Leptons and photons are identified by other means than the ones mentioned in Sec. 4.7.1.

[10] The technique is also applied for multi-strange baryons.



"Now I understand why I do this at all. It's not really for the 1.4 smaller stat error bars (but dear ALICE colleagues, please thank us for this when you sit there with your nice plots), it's more for the tiny portions of pleasure (and big portions of a bit too extreme adventure) — like when you understand that a secret person ten years ago wanted to send a message to the future person (me) that's releasing this screw from its blue cover (ah, and btw, isn't it very cute that the official name is "blue cover" when nothing else is called cover and could equally well just leave the blue out, but no: somehow color stuck here, and it warms my heart every time) saying something like Don't worry, I know you have bruises all over your body, that your back and knees hurt, and that your head got too many bumps in it because you secretly removed your helmet in order to squeeze in to reach partition 0 — but (and here it comes:) it will get better!" (20 Jan 2016)

Chapter 5

Analysis: $\Lambda/\mathrm{K}^0_\mathrm{S}$ associated with a jet and in the underlying event

In this chapter, the analysis of the $\Lambda/\mathrm{K}^0_\mathrm{s}$ associated with a jet and in the underlying event (bulk) will be described in detail: the method, event and V0 selection, yield extraction procedure, corrections to the raw spectra, and uncertainty calculations. In addition to this, the numerous cross checks done to verify the method will also be described, including e.g. construction of the inclusive V0 spectra to show that the published results of Ref. [66] can be reproduced.

5.1 Introduction to the η-reflection Method

The method developed for this analysis is based on correlations between a *trigger particle*, i.e. a high-p_T charged hadron coming from the primary collision vertex, and the associated production of V0 particles. The *peak* is defined as the region in η-φ space around the trigger hadron, while the *bulk* is the region that samples the underlying event activity. In this thesis, the *jet* is defined as the peak signal after the bulk has been subtracted. I want to emphasize that it is not a full event-by-event reconstruction of jets done with a jet finder algorithm, but the selection is representing a *jet-like*

environment defined by a high-p_T particle[1]. The advantage of identifying jets by its leading high-p_T particle is that one can subtract the event averaged background to separate jet and bulk even at low p_T. In heavy ion physics there is considerable interest also in the low-p_T part of jet physics.

A precise definition is illustrated in Fig. 5.1. The two regions are defined symmetrically around pseudo-rapidity $\eta = 0$ (hence the name η-*reflection*) in the following windows:

$$\text{Peak: } |\eta_{\text{trig}} - \eta_{V0}| < 0.2 \text{ , and } |\varphi_{\text{trig}} - \varphi_{V0}| < 0.92$$

$$\text{Bulk: } |\eta_{\text{trig}} + \eta_{V0}| < 0.2 \text{ , and } |\varphi_{\text{trig}} - \varphi_{V0}| < 0.92$$

where φ is the azimuthal angle. If a trigger particle is at η = 0.5, then the peak window will be $0.3 < \eta < 0.7$, and the bulk window will be $-0.3 < \eta < -0.7$, with the same $\Delta\varphi$ interval. If instead η = -0.5, the two regions are interchanged. Furthermore, since the peak and bulk regions are defined in an η window of ± 0.2, an overlap between the different regions is avoided by rejecting trigger particles with $|\eta| < 0.2$, since the η-window is $|\Delta\eta| < 0.2$.

In this way, the η-distance ($2\eta_{\text{trig}}$) between the center of the two regions varies, but the geometrical acceptance and detector performance in each event is the same in the two regions. This will make the efficiencies similar in both regions, hence simplifying the raw spectra correction procedure. The assumption relies on the observations that yields are boost invariant in rapidity, and that long range correlations are largely $\Delta\eta$-independent in the ALICE acceptance, as seen in Fig. 3.8 in Sec. 3.3.2. The same figure also shows that since the bulk and peak region will be sampled in the same $\Delta\varphi$ window ($\Delta\varphi$ <0.92), it is safe to assume that the flow contribution present in the peak region can be corrected for by subtracting the bulk from the peak to obtain the near-side jet.

To define varying symmetric η windows for the peak and bulk regions is the main analysis difference compared to the standard approach of reference [83] and [84]. In a standard di-hadron analysis, the trigger particles are rather homogeneously distributed in η, such that, requiring an "η-gap", $|\eta_{\text{V0}} - \eta_{\text{trig}}|$, the bulk signal will be biased towards large values

[1] In this way a "jet" answers to common Heavy Ion Physics language where e.g. "jet quenching" is referred to a suppression of particle production at high p_T with no other jet criteria.

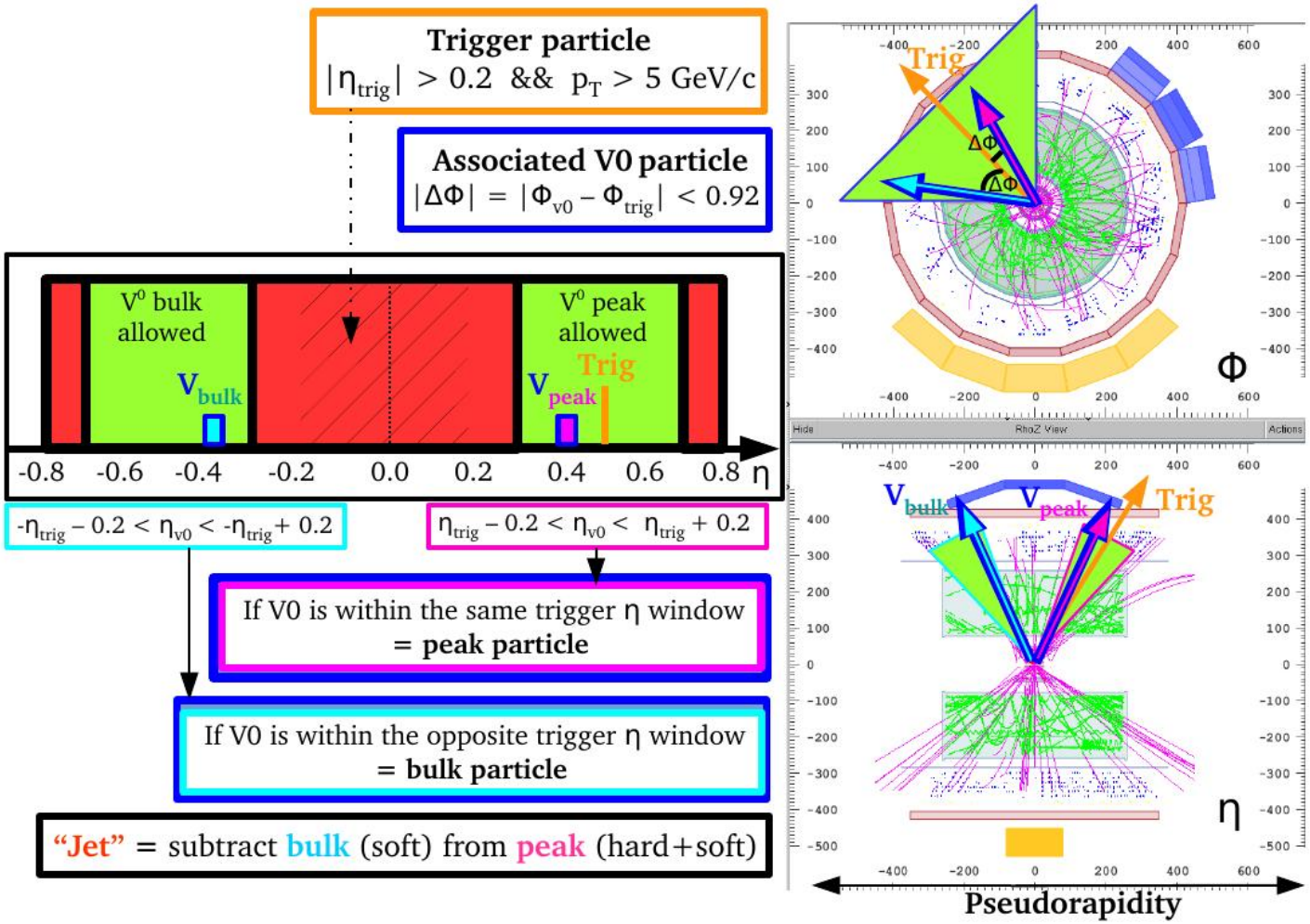


Figure 5.1: A cartoon illustrating the definitions of peak and bulk region.

of $|\eta|$ – leading to different sampling regions for jet and bulk. In the analysis of Ref. [84], one looks at the topology of the angular correlations in a fixed $\Delta\eta\Delta\varphi$ region, where the near-side jet region is defined in $|\Delta\eta| < 0.4$ and $|\Delta\varphi| < 0.94$, and the bulk in $0.7 < |\Delta\eta| < 1.0$ and $|\Delta\varphi| < 0.94$ (the reader can look back at Fig. 3.8 to get a clearer picture of the region selection). The raw angular correlation distributions, C($\Delta\varphi$,$\Delta\eta$), between a high-p_T trigger particle and the V0 candidates are obtained differentially in centrality, primary vertex interval, and transverse momentum of the associated V0. The raw angular correlations are corrected for efficiency and acceptance effects, where mixed event correlations are used. The jet yield is obtained by projecting the two-hadron angular distribution in $\Delta\varphi$ where the flow components have to be subtracted from these projections.

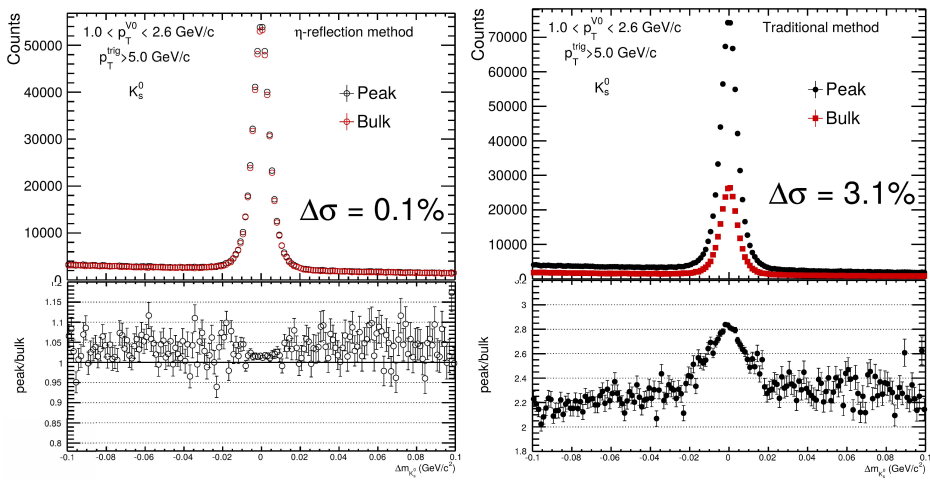
Since the goal of the analysis in this thesis is to subtract the bulk contribution from the peak yield, and since it is of special interest to do this at intermediate p_T in central heavy-ion collisions where the peak and bulk are of a similar magnitude, a comparison of the peak and bulk yields with very good relative precision is necessary. If the true difference is for example 5 %, so that bulk/peak = 1.05, then having 2% imprecision on the relative yields (e.g. if the MC correction in one region is wrongly calculated to be 0.306 instead of 0.300) will result in a $\sim$40 %[2] imprecision of the jet value that we want to study. This motivates the construction of a method where:

- The efficiency of peak and bulk are per construction similar (and testable)
- The extraction of K^0_s and Λ yields is similar, i.e. the signal and background have comparable shapes for peak and bulk

The first bullet will be confirmed in Sec. 5.7.3. The second bullet is confirmed in Fig. 5.2, where the unnormalized peak and bulk invariant mass spectra are plotted for the η-reflection method (varying $\Delta\eta$ regions) and for the standard method (I have run my analysis codes, but with fixed $\Delta\eta$ regions) separately. The mass distributions are fitted with a Gaussian, and the peak and bulk width difference, $\Delta\sigma = (\sigma_{peak} - \sigma_{bulk})/\sigma_{peak}$, is extracted. In the standard method $\Delta\sigma \approx 3\%$, which is a large value considering that we want to measure a difference in the peak and bulk

[2] $(1.05/0.306 - 1.0/0.300)/(1.05/0.300 - 1.0/0.300) = 0.59$

down to this size. The η-reflection method shows a considerably better $\Delta\sigma$ of 0.1%. In addition, the background shape is the same in the two regions with the η-reflection method, seen in the ratio of the invariant mass distribution between the peak and bulk. This demonstrates that the signal characteristics are very similar in the bulk and peak samples for the η-reflection method presented in this thesis.



(a) η-reflection method (b) Standard method

Figure 5.2: $\Delta m_{K^0_s}$ for the peak and bulk regions in $1.0 < p_{\mathrm{T}} < 2.6$ GeV/c comparing the different analysis methods. The ratio plot shows the peak/bulk.

One immediate consequence of the η-reflection method is that event mixing, used to correct for gaps or inefficiencies in the detector acceptance in the standard correlation method, is not needed; the insensitive radial gaps in the TPC are located at fixed values of φ, thus effectively equal for peak and bulk, and in the end, an integration over both $\Delta\eta$ and $\Delta\varphi$ is done, so only a single number will be necessary for correction, which contributes to a smaller systematical uncertainty of the final result.

5.2 Making the Right Choices

5.2.1 Data and Event Selection

The main results presented in this thesis are obtained for the Pb–Pb data recorded in 2011 with a delivered integrated luminosity of $\mathcal{L} \simeq 146\mu b^{-1}$, resulting in 72 million recorded collision events passing the two relevant online trigger filters for this analysis: MB and CENT&SEMI, discussed in Sec. 4.5. These triggers are chosen to enrich the data with high multiplicity events, since the analysis is done for 0-10% centrality.

Only runs where both the ITS and TPC have performed as expected are selected. Moreover, only events with a primary vertex position in the beam direction reconstructed at least within 10 cm of the nominal interaction point, $|vtx_z| < 10$ cm, are considered. Furthermore, to remove pile-up events with multiple interactions, an additional requirement is set where the primary vertex position reconstructed with the SPD (the two innermost layers of the ITS) is within 0.5 cm from the primary vertex position reconstructed with tracks, i.e. $|vtx_z - vtx_z^{SPD}| < 0.5$ cm. Table 5.1 shows a summary of all event cuts applied, resulting in a final number of central events of $\sim 10.5 \times 10^6$ that are being analyzed in this study.

Table 5.1: Summary of event selection cuts

Data recorded	2011
Online triggers	MB, CENT, SEMI
Centrality	0-10%
Longitudinal position of primary vertex	$\|vtx_z\| < 10$ cm
Pile up rejection	$\|vtx_z - vtx_z^{SPD}\| < 0.5$ cm

The number of events for each centrality bin, after the above mentioned event selections, is shown in Fig. 5.3. Due to the offset of the online centrality trigger CENT, and the onset of SEMI, the shape of the global centrality distribution distribution seen in the figure will start to drop at the 9% centrality bin. To avoid a bias in centrality, which could contribute to results influenced stronger by more central events (which turns out to

be on the level of $\sim$ 2%), a correction weight to flatten out the centrality distribution is calculated by fitting the distribution in the flat 0-9% centrality interval to a constant representing the mean number of events, and scale it to the number of integrated events in the last 9-10% centrality bin, giving a weight factor of 1.33. This weight is applied to all V0s in this centrality bin when constructing the invariant mass distribution of the V0 candidates.

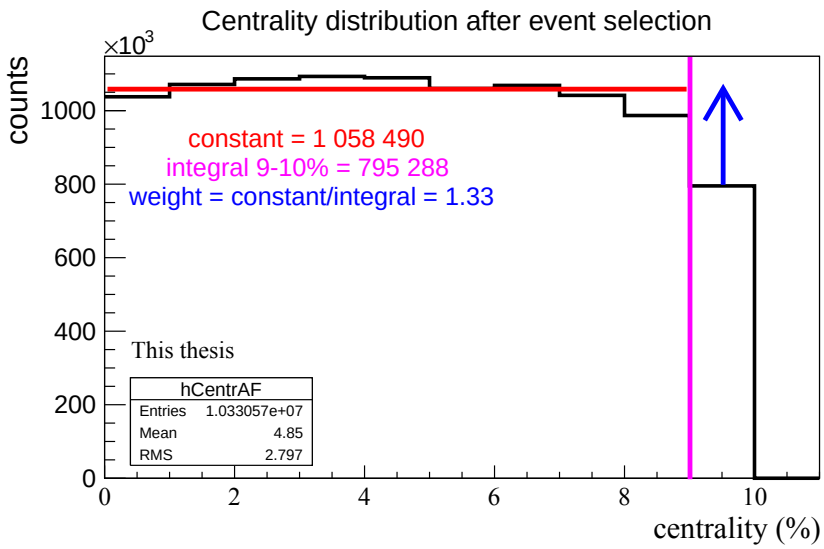


Figure 5.3: Centrality distribution for 2011 Pb–Pb data run showing a non-flat behavior in the centrality interval 9-10%, corrected for by a constant scaling weight.

Monte Carlo Data

The ALICE detector does not detect all V0 particles due to its limited detector acceptance (the non-sensitive regions between the TPC chambers also contribute to this), material deflection and absorption. In the next section it will become clear that we have to apply a number of selection criteria to be able to distinguish the V0 particles from all other particles produced in the collision. To calculate the reconstruction efficiency, we make Monte Carlo (MC) simulations.

The MC data sample used in this analysis are collision events simulated with the HIJING event generator [85] passing through a GEANT3 [86] simulated ALICE detector, to later be treated in the ALICE analysis framework, AliROOT [86], representing the state and condition of the detectors at the same time when the real data sample was recorded. After applying the same event selection criteria as for the real data discussed in the previous section, the number of MC events used for calculating the efficiency, and making additional comparisons to real data, is $\sim 1.5 \times 10^6$.

5.2.2 K^0_s and Λ Particle Selection

The analysis is tested by reproducing the previously published[3] inclusive K^0_s and Λ p_T spectra [66]. The K^0_s and Λ selection will therefore be described here, in connection to the inclusive analysis, while the trigger particle selection is defined in Sec. 5.5.

An advantage of using V0 in the analysis is that, in the longer run — outside the scope of this thesis — the analysis can easily be extended to much higher p_T, since the particle identification systematic uncertainties are largely independent of p_T. In such studies the aim would be to measure jet quenching modification of the ratios for sub-leading particles.

The K^0_s Particle

The K^0 and $\bar{K^0}$ are neutral mesons with quark content $d\bar{s}$ and $\bar{d}s$, with two weak eigenstates: one long-lived with a mean lifetime of $\tau = 5.18 \times 10^{-8}$s, called K^0_L, and one short-lived with a mean lifetime of $\tau = 8.95 \times 10^{-11}$s (thus giving a decay length of $c\tau = 2.6844$ cm), called K^0_s, with (approximately) the following quark content:

$$K^0_L: \quad \frac{d\bar{s} + s\bar{d}}{\sqrt{2}}$$

$$K^0_s: \quad \frac{d\bar{s} - s\bar{d}}{\sqrt{2}}$$

[3] When referring to "published" inclusive K^0_s and Λ spectra in the text or in figures, it is from now on assumed to be from [66].

Both have a mass of 497.648±0.022 MeV/c^2. With ALICE detection capabilities the short-lived K^0_s is detectable with good efficiency. K^0_s has two main decay channels [10]

$$K^0_s \rightarrow \pi^+ + \pi^- \quad \text{BR} : 69.20 \pm 0.05\%$$

$$K^0_s \rightarrow \pi^0 + \pi^0 \quad \text{BR} : 30.69 \pm 0.05\%$$

In this analysis, the K^0_s will be reconstructed using the charged decay mode with π^+ and π^- in the final state.

The Λ Particle

The Λ (anti-particle $\bar{\Lambda}$) is a neutral baryon with quark content uds ($\bar{u}\bar{d}\bar{s}$), a mass of 1115.638±0.006 MeV/c^2 and a mean lifetime of $\tau = 2.632 \times 10^{-10}$ s giving a decay length of $c\tau = 7.89$ cm. In this analysis, the $\bar{\Lambda}$ is not considered due to the discrepancy seen in the yields between Λ and $\bar{\Lambda}$, shown in the Appendix Fig. A.1, evaluated in the study of this thesis. This discrepancy is also seen in other ALICE analyses [65], and is currently being investigated.

The Λ particle has two main decay channels [10]

$$\Lambda \rightarrow p + \pi^- \quad \text{BR} : 63.9 \pm 0.5\%$$

$$\Lambda \rightarrow n + \pi^0 \quad \text{BR} : 35.8 \pm 0.05\%$$

In the analysis described here, the Λ will be reconstructed using the charged decay mode with p and π^- in the final state.

Finding Fancy V:s in the Detector

K^0_s, Λ, and $\bar{\Lambda}$ particles are with a common name called V0 particles since they are neutral, and their decay topology looks like a V in the detector due to their charged particle decay channel and long life time; to reconstruct a V0 particle is to detect and associate the V-shaped structure. In Fig. 5.4 a bubble chamber picture of V0 decays is shown to illustrate this.

In a collision, the V0 particles are created in the primary vertex and then travel a distance, determined by its life time and velocity, before they decay. The point of decay is the *secondary vertex*. The fact that both K^0_s and Λ decay in the same pattern simplifies the reconstruction since the

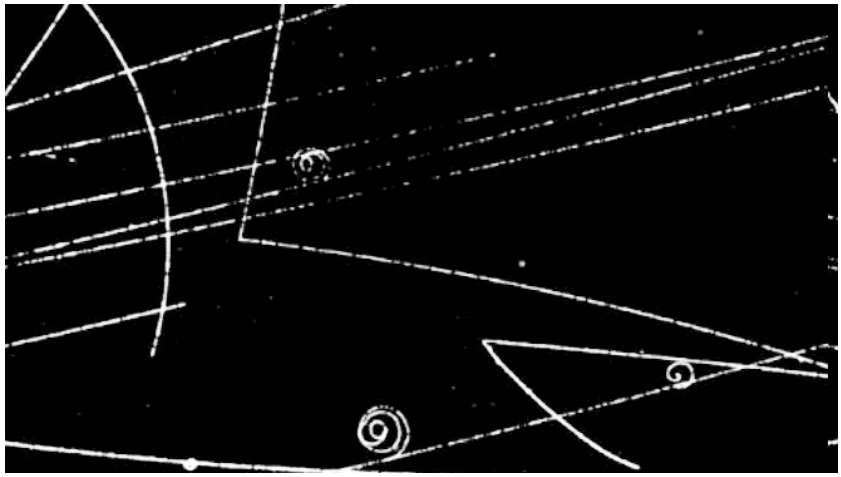


Figure 5.4: A bubble chamber picture of the K^0_S and Λ decay topology, nicely illustrating the V-shaped structure of their decay nature. Figure from [87].

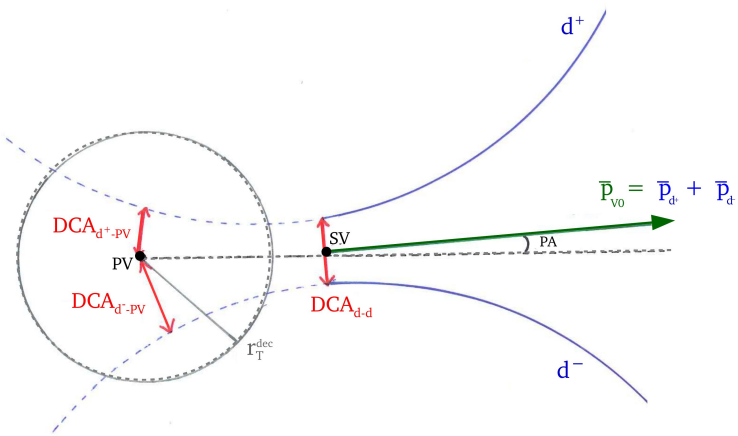


Figure 5.5: The V0 decay topology. PV is the primary vertex, SV is the secondary vertex, DCA_{d-d} is the distance between the reconstructed daughter tracks, DCA_{V0-PV} is the distance from the primary vertex to the extrapolation of the V0 momentum vector, PA is the angle between the V0 momentum and the V0 line of flight, DCA_{d-PV} is the minimal distance of the charged track to the primary vertex, and r_T^{dec} is the transverse decay radius.

same technique can be applied. ALICE has a V0 *finder* framework, which is an identification procedure based on determining secondary vertices from the decay topology of the V0s. This PID method was very shortly introduced in Sec. 4.7.2, but will be described in detail here. A graphical representation of the V0 topology is shown in Fig. 5.5.

Since all V0s decay into two particles of opposite charge in their main decay channel, and these two daughter particles naturally come from the same point in space, the algorithm searches for exactly these requirements; a combination of all reconstructed tracks that are:

(i) **Oppositely charged**

(ii) Close in space, and belonging to a secondary vertex — the distance of closest approach between the two daughter tracks, $\mathbf{DCA_{d-d}}$, must be shorter than a given value

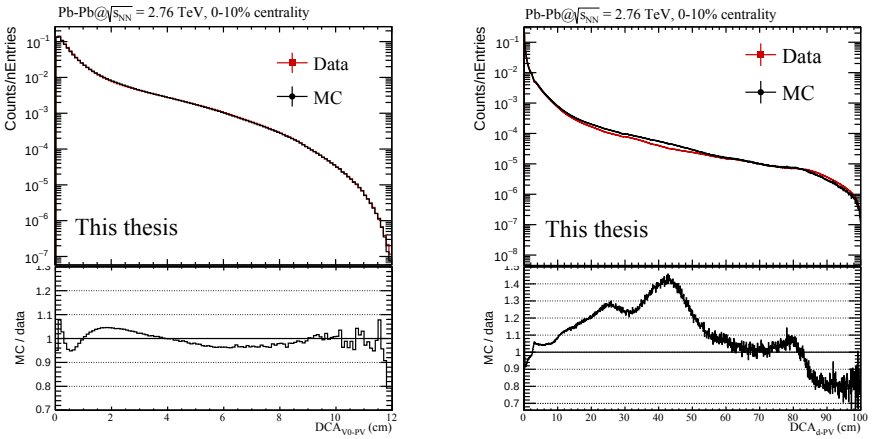
The minimization of $\mathrm{DCA_{d-d}}$ is performed numerically using a three dimensional helix track parameterization. The secondary vertex position is updated with the information of $\mathrm{DCA_{d-d}}$.

To reduce the combinations of track pairs which do not belong to a secondary vertex, i.e. the combinatorial background, additional requirements on the combined tracks and their assumed mother particle are enforced. Some of the cut threshold values vary depending on the V0 species – all *final*[4] cuts are summarized in Table 5.2.

$\mathbf{DCA_{V0-PV}}$: The momentum vector of the V0 candidate is calculated as the momentum sum of the two combined tracks, and the closest distance from the momentum vector to the primary vertex, $\mathrm{DCA_{V0-PV}}$, is required to be within a certain distance. The distribution for both data and MC for all V0 candidates without background subtraction can be seen in Fig. 5.6(a).

$\mathbf{DCA_{d-PV}}$: To minimize the risk of confusing the daughter tracks with a particle coming from the initial collision primary vertex, a minimal distance of the charged track to the primary vertex, $\mathrm{DCA_{d-PV}}$, is applied. The distribution for both data and MC for all V0 candidate daughters can be seen in Fig. 5.6(b).

[4]Where the analysis specific cuts are also considered; some ALICE-standard V0 finder cuts are too loosely set for the purpose of this analysis, and are therefore tightened "by hand".



(a) DCA_{V0-PV} (b) DCA_{d-PV}

Figure 5.6: The different cut parameters for V0 candidates with $p_T > 1.0$ GeV/c

cos(PA): Another default cut in the V0 finder algorithm is a selection of the V0 candidates which point back to the primary vertex with a small pointing angle, i.e. the angle between the V0 momentum (which is a sum of the daughter particle momenta) and the V0 line of flight. The actual experimental reconstructed variable is the *cosine* of this pointing angle, thus called cos(PA); a value of cos(PA)=1 would mean that the V0 momentum is exactly overlapping with the line of flight. The distribution for both data and MC for all V0 candidate daughters can be seen in Fig. 5.8(a).

Invariant Mass

Before moving on to analysis specific requirements, the concept of *invariant mass* is introduced: the invariant mass of a V0 candidate is determined from the V0 daughters four-momenta $(E, \bar{p})$ as:

$$m_{V0} = \sqrt{(E_1 + E_2)^2 - (\bar{p_1} + \bar{p_2})^2} \tag{5.1}$$

where $\bar{p_1}$ and $\bar{p_2}$ (with $\bar{p_{V0}} = \bar{p_1} + \bar{p_2}$) are the momenta of daughter particles 1 and 2, and $E_i = \sqrt{m_i^2 + p_i^2}$ the energy of daughter particle $i = 1, 2$. The masses of the expected V0 decay particles are assumed, e.g. m_π for

both K^0_s daughters and m_p and m_π for the Λ. The invariant mass distribution of the V0 will peak around the true mass of the V0. The peak will have a width determined by the resolution with which the momentum of the daughter particles can be measured.

Analysis Specific Requirements

Good V0 candidates are found by running the V0 finder over all reconstructed charged tracks. After this step, one can in principle construct the invariant mass of an assumed V0 by combining the masses of the daughter tracks associated with the V0 candidate to extract the yield. However, it is found that the background of the invariant mass can be reduced in a signal-to-background beneficial way (Fig. 5.7) — balancing with a satisfactory statistical significance — by tightening some of the default cuts in the V0 finder algorithm (stated in previous section), and by introducing some additional restrictions on both the V0s themselves, and their daughter particles, that allows identification of K^0_s and Λ up to high p_T.

In Fig. 5.7 the p_T-integrated ($1.0 < p_T < 10$ GeV/c) invariant mass spectra for K^0_s and Λ candidates are shown for the different cases where one of the cuts are loosened or completely removed, and the rest are kept at nominal values (the red distribution). This is to study the effect of the signal and background reduction to motivate the choice of the cut value. For example, the cos(PA) discussed in the previous section is shown as the green distribution for a loose value of >0.990, while the nominal value is >0.998. In the ratio plot (indicated by "no cut / nominal" in the figure) it is seen that, for K^0_s, the effect of this cut gives $\sim$20% background reduction, while the signal is not lost. For Λ, the background reduction is about the same as for K^0_s, and $\sim$5% of the signal is also lost.

The cuts already motivated in the previous section will not be discussed further, but quoted in the summary table with their final values, see Table 5.2. Here follows instead a detailed discussion of the additional cuts applied.

Decay radius, r_T^{dec}: Only the secondary vertices inside a given fiducial volume radius, r_T^{dec}, are kept. Too short decay radii will give a secondary vertex close to the primary vertex, which could be difficult to separate. There is a discrepancy between data and MC, studied in [65], concerning $r_T^{dec} < 5$ cm at low p_T. In this region, low-p_T tracks can be identified

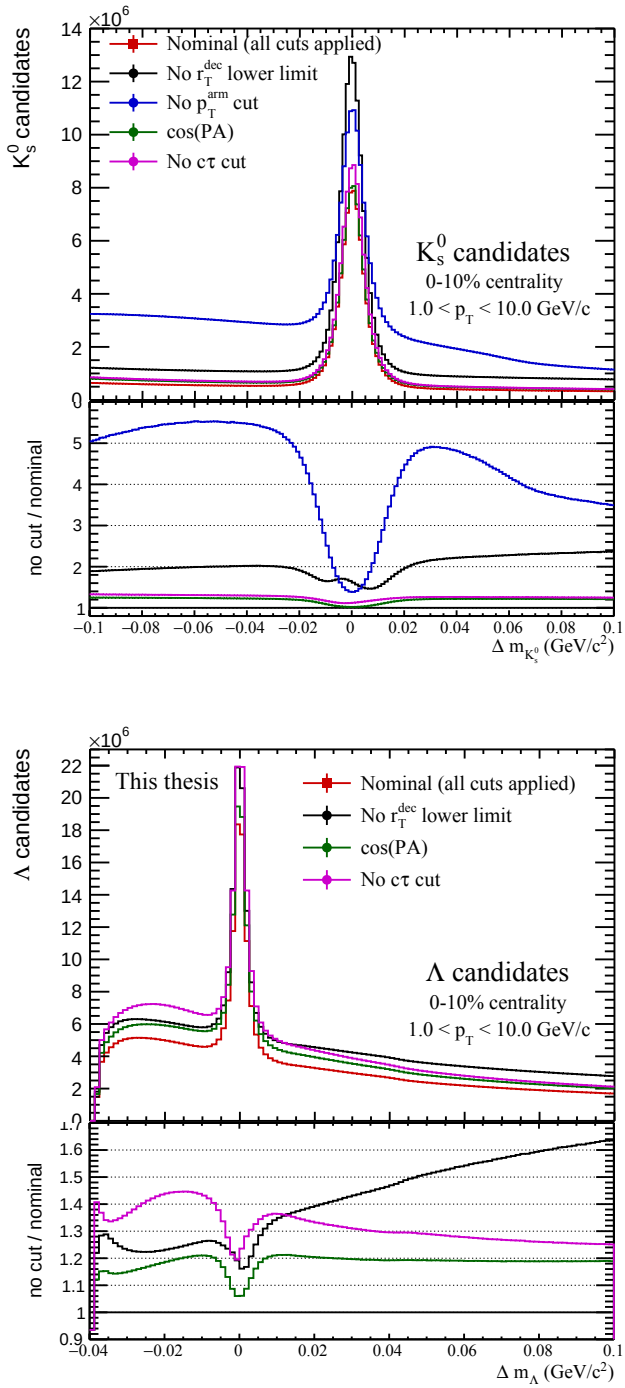


Figure 5.7: The effect of the cuts on the V0 candidate invariant mass distribution.

as primary tracks by picking up spurious ITS hits, and if the amount of spurious ITS clusters differ between data and MC, the efficiency will be wrongly calculated. This forces us to remove V0 candidates within a decay radius of 5 cm from the primary vertex, i.e. all secondary vertices inside the first SPD layer.

The distribution for both data and MC, for all V0 candidates without background subtraction, can be seen in Fig. 5.8(b). Following the black distribution in Fig. 5.7, it is noticed that this cut affects K^0_s more than Λ, due to the shorter mean decay length ($c\tau = 2.6844$cm) of the K^0_s— this effect, however, is mostly in the low p_T area ($p_T < 2$ GeV/c), where the correlation part of this analysis is not done due to the limited peak and bulk separation power. In any case, the removal of the low-p_T K^0_s's is corrected by the MC reconstruction efficiency.

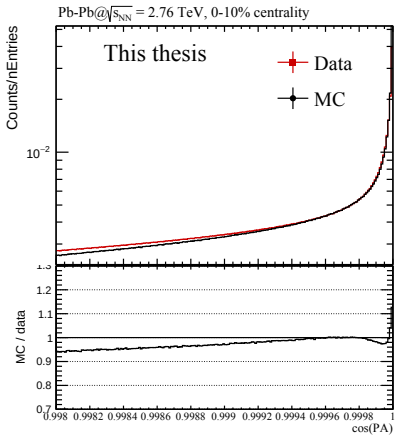
Decay length, $c\tau$: The distance between the reconstructed primary and secondary vertex is the measure of the V0 decay length, L^{dec}_{rec}. With this information, and with the momentum, p, of the V0 candidate, the reconstructed rest frame lifetime, $c\tau$, is calculated by assuming the true[5] mass of the V0 particle, m^{PDG}_{V0}, by

$$c\tau = m^{PDG}_{V0} \frac{L^{dec}_{rec}}{p} \tag{5.2}$$

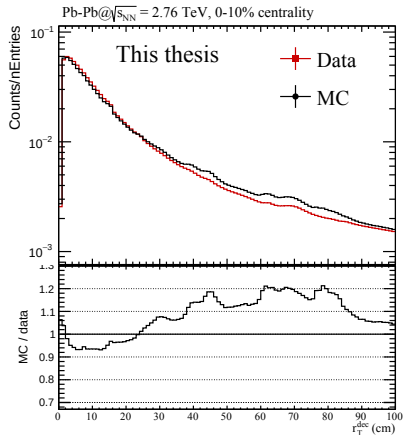
The measured $c\tau$ is required to be below 3 times the PDG value, $c\tau < 3.0 L^{dec}_{PDG}$, to reduce contributions from secondary particles. The distribution for both data and MC for K^0_s and Λ candidates without background subtraction can be seen in Fig. 5.8(c), also indicating the cut value. In Fig. 5.7 the magenta colored line represents the invariant mass distribution when this cut is removed. For both K^0_s and Λ this removes 30-40% of the background, and also has the advantage to make the background more smooth, contributing to a much better converging rate in the fitting procedure, especially for the Λ case.

Armenteros-Podolanski Diagram, p^{arm}_T: For K^0_s candidates, a selection is made on the so-called *Armenteros-Podolanski* diagram. It is a kinematic way to select V0s (in this analysis it is only used for K^0_S selection) from the daughter track information without identifying the daughter particles. The diagram is constructed by expressing the projection of

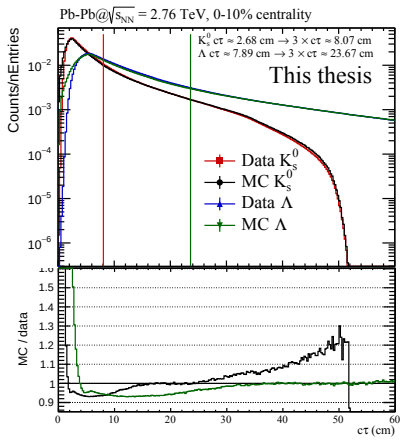
[5] From the Particle Data Group.



(a) cos(PA)



(b) r_T^{dec}



(c) $c\tau$

Figure 5.8: The different cut parameters for V0 candidates with $p_{\mathrm{T}} > 1.0$ GeV/c

the positive daughter momentum to the V0-momentum, i.e. the *relative transverse* momentum, p_T^{arm}, and like-wise for the negative daughter, illustrated in Fig. 5.9. The maximum p_T^{arm} of a V0, corresponds to the scenario when all the energy of the decay goes into the transverse momenta (relative to the V0 direction) of the decay particles. In this case, it means that $p_T^{daughter} = p_T^{arm}$, and that the daughters' transverse momenta are equal to their momenta in the rest frame of the mother particle.

This observable is then related to an observable describing the *relative longitudinal* momenta of the daughter particles with respect to the mother V0, called α_{arm}

$$\alpha_{arm} = \frac{p_L^+ - p_L^-}{p_L^+ + p_L^-} \tag{5.3}$$

where p_L is the longitudinal component of the total momentum vector for each daughter particle (+ and -) relative to the direction of the V0 momentum vector. It is thus expressing the asymmetry of longitudinal momenta of both decay particles.

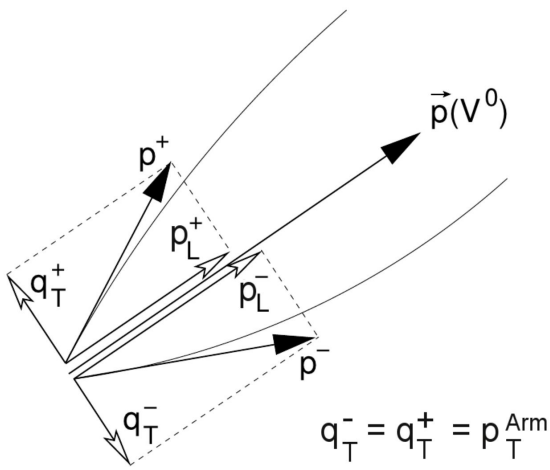


Figure 5.9: The parameters of the Armenteros-Podolanski Diagram derived from the transverse and longitudinal momentum components of the positively and negatively charged track, with respect to the direction of the reconstructed V0 momentum.

One large ("head") and two small ("ears") parts of ellipses can be seen in the diagram in Fig. 5.10, where the "head" clusters the K^0_S particles, and the "ears" group the Λ (right) and $\bar{\Lambda}$ (left) particles. The Λ-bands have their maximum at a smaller p_T^{arm}-value than the K^0_S, explained by the lower Q-value of this decay. The centers of the Λ-bands are shifted to larger (Λ) and smaller ($\bar{\Lambda}$) α_{arm}, considering the different mass of the decay products; the (anti-)proton carries a higher momentum than the pion due to the Lorentz boost. Generally, for a large value of α_{arm}, one of the decay particles needs to have a large longitudinal momentum, resulting in a small value of p_T^{arm}, which explains the shape of the bands.

It can be noted that the "ear"-ellipses overlap with the "head" ellipse, which means that some Λ and $\bar{\Lambda}$ particles contaminate the K^0_S sample, and vise versa. To reduce the contamination of Λ and $\bar{\Lambda}$ particles faking K^0_S candidates, a p_T^{arm} cut removing the "ears" is made by a linear function of α_{arm}, i.e. everything below the lines indicated in the figure. The blue distribution in Fig. 5.7 for K^0_S shows the benefit from this cut: the background is reduced 3.5-5.5 times, while the signal region does not loose more than 40%, and in addition the shape of the background improves the fitting performance due to its smooth shape. A similar cut is not optimal to remove K^0_S's from the Λ sample due to the fact that it introduces too irregular background shape in the invariant mass distribution. It should be understood here that events in the overlap areas will add to the background in invariant mass distributions, thus affecting the signal-to-background, but the integrated signal yields should be unaffected as long as the fitting procedure catches the signal correctly.

Pseudo-rapidity, η: A cut on pseudo-rapidity on both daughter particle tracks, and the mother V0 is done, so that only tracks within full TPC acceptance is kept, i.e. $|\eta_{\mathrm{V0}}| < 0.8$, and $|\eta_{\mathrm{daugh}}| < 0.8$.

A summary of all selection cuts is presented in Table 5.2.

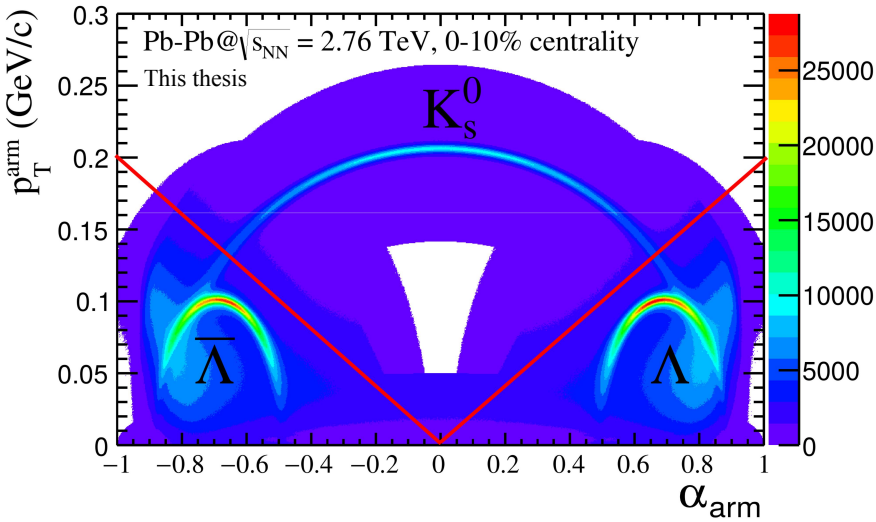


Figure 5.10: Armenteros-Podolanski Diagram indicating the different areas of V0 species clustering. The red lines demonstrate the cut for K^0_S to remove fake Λ.

Table 5.2: Summary of selection cuts used.

Observable	**Condition**
DCA_{d-d}	< 1 cm
Daughter tracks charge	opposite
DCA_{d-PV}	>0.1 cm
$\lvert \eta_{daug} \rvert$	<0.8
cos(PA)	>0.998
r_T^{dec}	5-100 cm
$c\tau$	$< 3.0 c\tau_{PDG}$
K^0_S only: p_T^{arm}	$< 0.2 \lvert \alpha_{arm} \rvert$
$\lvert \eta_{V0} \rvert$	<0.8

5.3 Inclusive Particle Yields

A good starting point of any study is to test that the particle selection, signal extraction procedure, MC corrections, and normalization are robust. Two ways of verifying that the framework built up to extract the results are correct will be presented, one of them being data driven and the other MC driven. Data closure is to run the analysis with the aim to reproduce already measured observables. In MC closure, the analysis is run over simulated data in the same way as for real data, with the difference that the results coming out can be compared with the true spectrum which was generated and reconstructed in the simulation, thus revealing flaws or systematic uncertainties in the analysis procedure if the results deviate.

In this analysis, the data-closure is to use the same approach for producing inclusive (i.e. a non-triggered selection of V0s) particle yields, concerning particle selection, signal extraction, and corrections, which will be used to obtain the peak and bulk yields in the correlation analysis. These results will then be compared to the results obtained with the published inclusive ALICE analysis [66]. A MC closure test will in addition be performed to the inclusive analysis, to make use of as many cross checks as possible along the way to the final correlation results. These inclusive data and MC closure tests are discussed in this section, thus explaining the procedure to obtain the K^0_s and Λ particle yields, which is also later used in the η-reflection correlation method.

5.3.1 The Transverse Momentum Spectra

The transverse momentum spectrum expresses the number, N, of an identified specific particle species per collision as a function of transverse momentum, $\mathrm{d}p_\mathrm{T}$, normalized to the rapidity region, $\mathrm{d}y$. The concept of particle spectra was discussed in Sec. 3.3.1. The spectra have to be corrected for detector acceptances, reconstruction efficiencies ($\mathrm{eff_{rec}}$), particle production branching ratios (BR), the fraction of secondary particle production, *feed-down* (fd), mainly from Ξ particles, and the number of analyzed events (N_{ev}):

$$\frac{1}{N_{ev}}\frac{d^2N}{dp_\mathrm{T}dy} = \frac{S_{raw}}{N_{ev}} \times \frac{1}{\Delta p_\mathrm{T}} \times \frac{1}{\Delta y} \times \frac{1}{\mathrm{eff}} \times fd \tag{5.4}$$

where S_{raw} is the raw number of detected particles, Δy is the rapidity window, and Δp_{T} is the p_{T} bin width. The efficiency correction, eff, in the above expression is defined as Eq. 5.7, discussed in Sec. 5.7, where also the feed-down is discussed.

5.3.2 Signal Extraction and Uncorrected Yields

The raw signal is extracted from the invariant mass spectra of the V0 candidates. The difference between the reconstructed invariant mass and the mass quoted by the Particle Data Group, $\Delta m_{V0} = m_{PDG} - m_{V0}$, is used in this analysis. In the top panel of Fig. 5.11 and 5.12, the Δm_{V0} vs. p_{T} of the V0 is shown in a two dimensional histogram. The projection of the invariant mass in two different p_{T} bins, 1.4-1.5 GeV/c, and 5.0-5.5 GeV/c, is shown in the lower panel together with the fit functions.

The invariant mass distributions are fitted with a sum of a third degree polynomial for the background and a double Gaussian for the signal region, where the mean of the two Gaussians is the same. The fitting function is the same as for the correlation analysis, and a more detailed discussion of the fitting function is therefore given in Sec. 5.6. The default fit range is $-0.1 < \Delta m_{\mathrm{K}^0_{\mathrm{s}}} < 0.1$ GeV/c^2 for $\mathrm{K}^0_{\mathrm{s}}$, and $-0.04 < \Delta m_{\Lambda} < 0.1$ GeV/c^2 for Λ. However, sometimes the fit fails and the range is then decreased within the default range until the fit converges.

The signal region is defined to be within 5σ of the double Gaussian width, from the mean value, μ_{signal}, of the fitted function. By counting the hits in each bin belonging to the signal region, a signal+background, $S + B$, yield is obtained. To access a clean signal, i.e. the raw yield, S_{raw}, the background, Bkg_{fit}, needs to be removed by subtracting the integral of the polynomial in the signal region:

$$S_{raw} = (S + B) - Bkg_{fit} \tag{5.5}$$

where the statistical error squared is the quadratic sum of each error contribution

$$\mathrm{Err}[(S + B)] = \sqrt{(S + B)}$$

$$\mathrm{Err}[Bkg_{fit}] = \sqrt{Bkg_{fit}}$$

$$\mathrm{Err}[S_{raw}] = \sqrt{\mathrm{Err}[(S + B)]^2 + \mathrm{Err}[Bkg_{fit}]^2} = \sqrt{(S + B) + Bkg_{fit}} \tag{5.6}$$

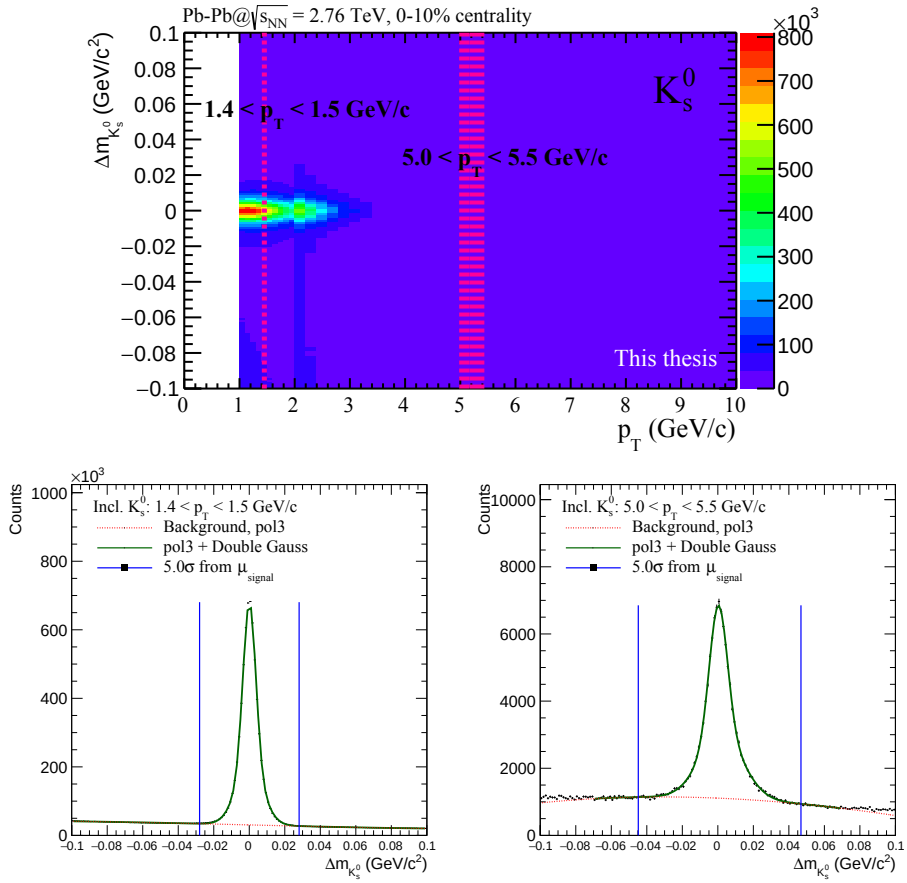


Figure 5.11: Invariant mass distribution of K^0_S candidates in Pb–Pb at $\sqrt{s_{NN}} = 2.76$ TeV, 0-10% centrality. The top figure shows the invariant mass vs. p_T, with two red bands indicating where the example projections are done for the lower two histograms. The projection-histograms thus show the invariant mass distribution for $1.4 < p_T < 1.5$ GeV/c and $5.0 < p_T < 5.5$ GeV/c, with the double Gaussian (signal) + polynomial (background) fitting function (green). The polynomial part of the fitting function is shown as the dashed red line to indicate the background. The two vertical blue lines represent the 5σ region in which the signal is extracted.

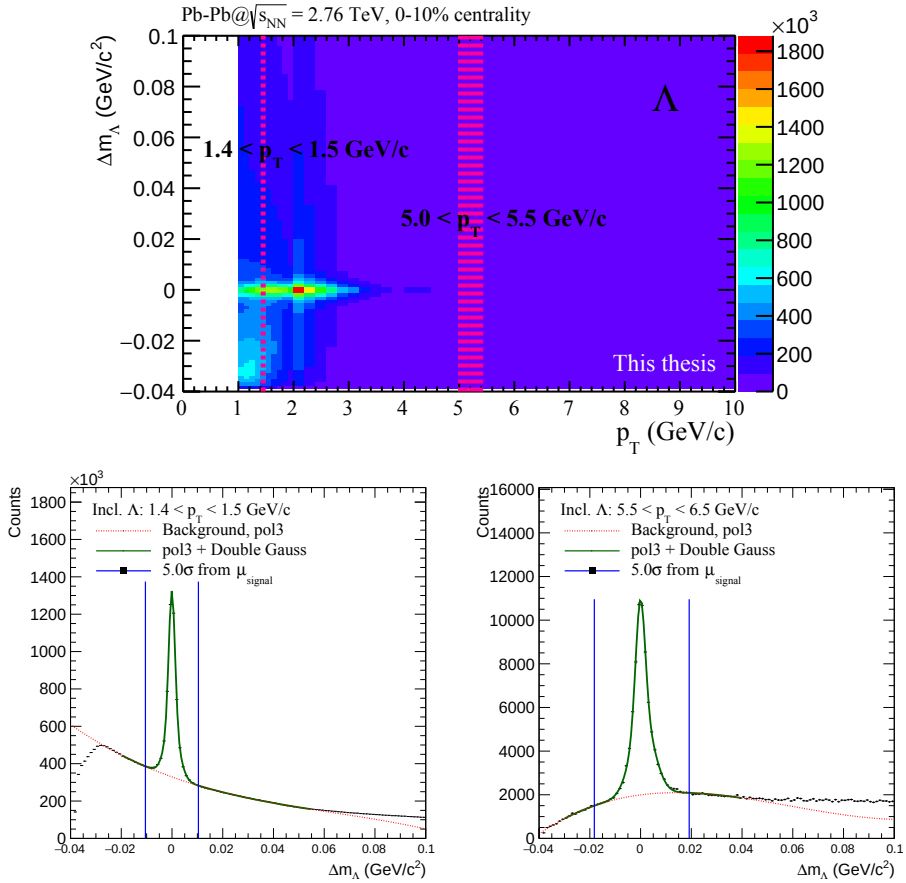


Figure 5.12: Invariant mass distribution of Λ candidates in Pb–Pb at $\sqrt{s_{\mathrm{NN}}} = 2.76$ TeV, 0-10% centrality. The top figure shows the invariant mass vs. p_{T}, with two red bands indicating where the example projections are done for the lower two histograms. The projection-histograms thus show the invariant mass distribution for $1.4 < p_{\mathrm{T}} < 1.5$ GeV/c and $5.0 < p_{\mathrm{T}} < 5.5$ GeV/c, with the double Gaussian (signal) + polynomial (background) fitting function (green). The polynomial part of the fitting function is shown as the dashed red line to indicate the background. The two vertical blue lines represent the 5σ region in which the signal is extracted.

The raw background subtracted signal for 0-10% centrality is shown in Fig. 5.13 for K^0_S and Λ.

5.3.3 Corrections

The first three factors in the yield expressed in Eq. 5.4 are straight forward: N_{ev} is the number of events analyzed, Δp_T is the p_T bin width, and Δy is the rapidity window; in this analysis the acceptance cut is done in pseudo-rapidity, but a conversion from pseudo-rapidity to rapidity is done before the final result, according to Appendix C.3. The last two terms of the yield are discussed next.

Efficiency

The efficiency corrects for detector coverage and acceptance (acc) limitations. Furthermore, it corrects for particle reconstruction imperfections and signal loss when applying selection cuts for identification (eff_{rec}). Thus, it recovers the V0s lost due to detector and reconstruction limitations. It also includes the branching ratio (BR) of the specific particle decay channel, to scale it to the total particle yield of K^0_S and Λ, which should have been observed in a perfect detector.

The efficiency can be expressed as

$$\text{eff} = \text{acc} \times \text{eff}_{rec} \times \text{BR} \tag{5.7}$$

and is calculated by MC simulations. In these simulations, Pb–Pb collision events are generated by, in this case, the HIJING generator [85], with a known distribution of different particle species, called MC_{gen}, having an identification label attached to the tracks. The HIJING generator tends to underestimate the number of strange particles compared to that created in real collisions. To solve this statistical issue, additional strange particles were added, or *injected*, at this level of the simulation.

The particles of each event are propagated through the GEANT3 simulation program, modelling the experimental aspects of the ALICE detector. The events are treated in the ALICE offline framework, AliROOT, tuned to match the real detector conditions at the time of the data taking. This generates detector response data, which is used to reconstruct tracks, called MC_{rec}, still associated with their truth particle ID label.

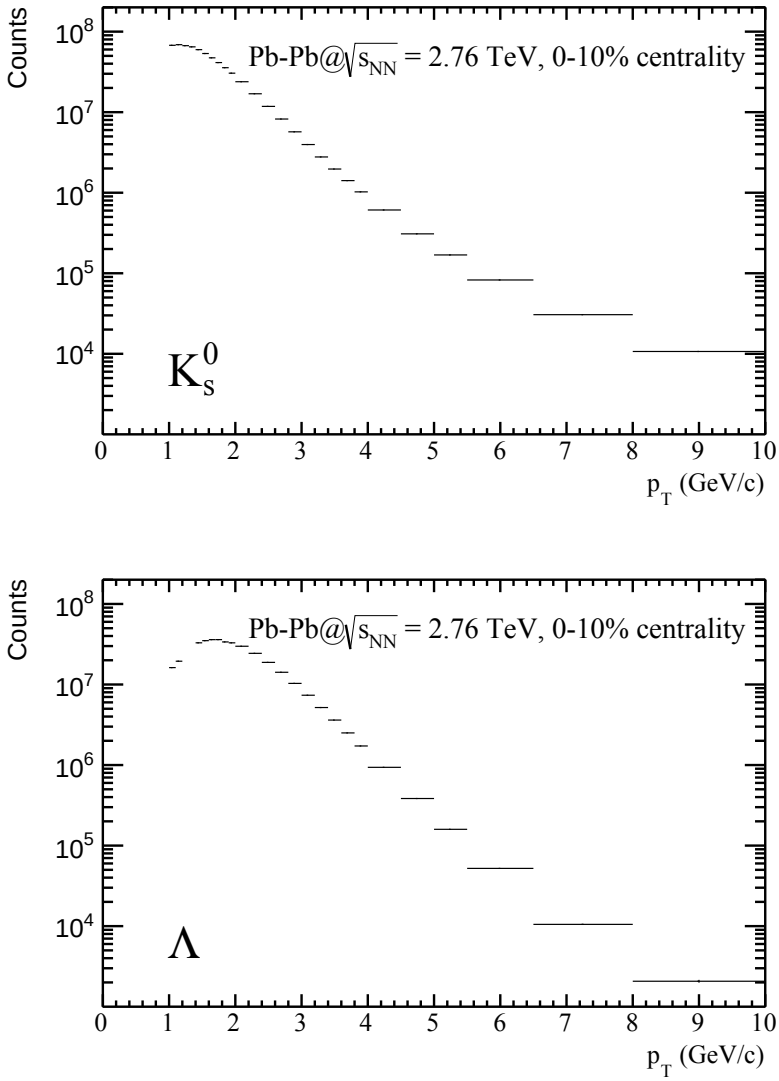


Figure 5.13: Uncorrected (with respect to efficiency and feed-down) p_{T} spectra for Pb–Pb at $\sqrt{s_{\mathrm{NN}}} = 2.76$ TeV, 0-10% centrality. The spectra are normalized to the p_{T} bin width.

The MC_{rec} particles undergo the particle identification procedure in the same way as for real data, i.e. all selection requirements are also applied to the simulated data (while the only cuts made at the generated level are the vertex and pseudo-rapidity selections). The only difference to real data is that the V0 candidates are required to be a K^0_s having decayed to $\pi^+ + \pi^-$ or a Λ having decayed to $p + \pi^-$. This requirement is fulfilled with the help of the ID labels attached to the particles generated in the event (being kept while propagating through the detector simulation). The p_T distribution of MC_{rec} is then compared to the p_T distribution of the MC_{gen}, representing the ideal case, where there are no detector or reconstruction effects causing the number of found V0 to decrease.

The MC_{rec} invariant mass distribution will not have a combinatorial background since the true V0 identification is known. However, the distribution will still be of some finite p_T-dependent width due to detector resolution, seen in Fig. 5.14 for K^0_s and Λ. It was found that, in addition to the MC label identification, the invariant mass of the MC_{rec} V0 should be required to be within 4σ of the mean. This might seem like a broad cut, but in fact around 5 % of the candidates are outside this region for $p_T \sim 6$ GeV/c. This is in agreement with the findings in the published analysis.

The efficiency is the ratio between the number of reconstructed *primary* V0 particles (MC_{rec}) with the same decay channel as considered for real data, and the number of generated V0 particles (MC_{gen}) – hence representing the fraction of successfully detected V0s. The efficiencies are calculated as a function of p_T to provide a correction to the raw yields.

In Fig. 5.15 the efficiency for K^0_s and Λ is shown for Pb–Pb at $\sqrt{s_{NN}} =$ 2.76 TeV, 0-10% centrality. The efficiency is lower but rises fast in the low-p_T region, to slowly flatten out at higher p_T.

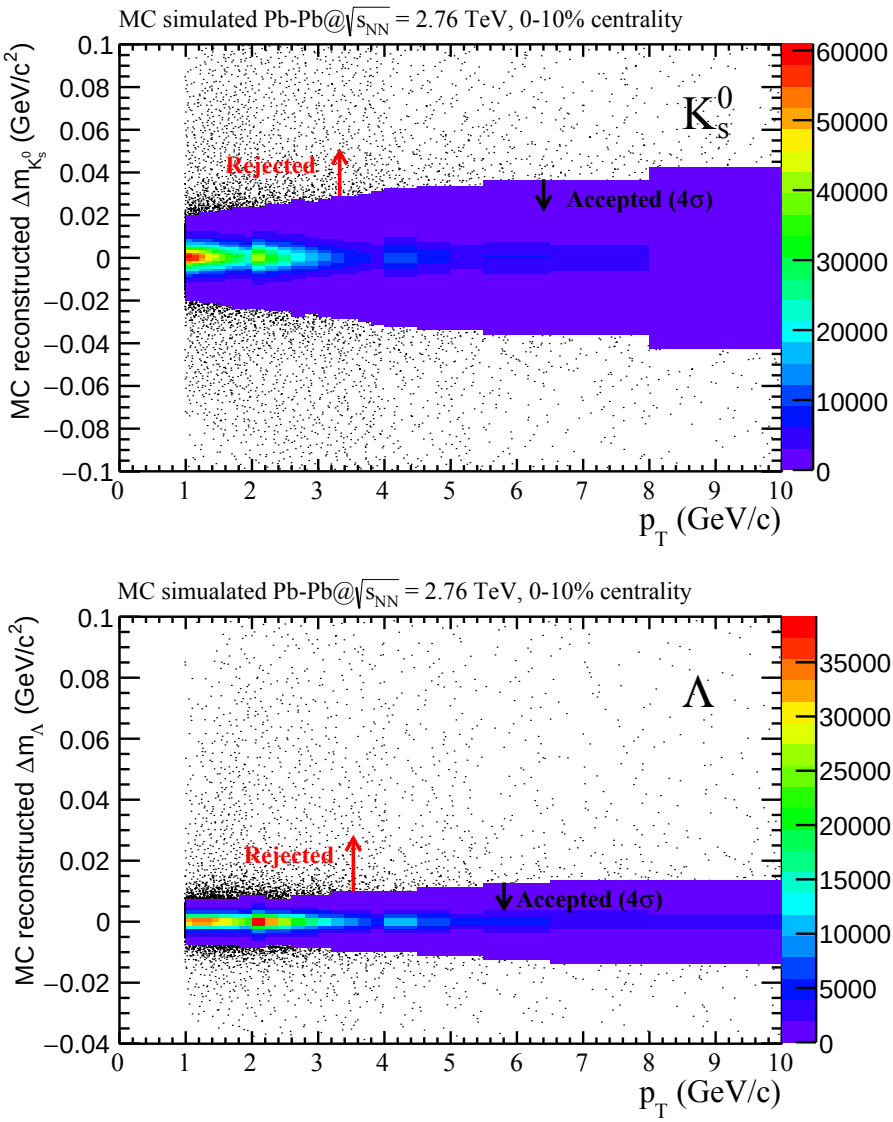


Figure 5.14: MC_{rec} invariant mass distribution as a function of p_T for K^0_s and Λ. The invariant mass of the MC_{rec} V0s is required to be within 4σ of the mean, indicated in the figures.

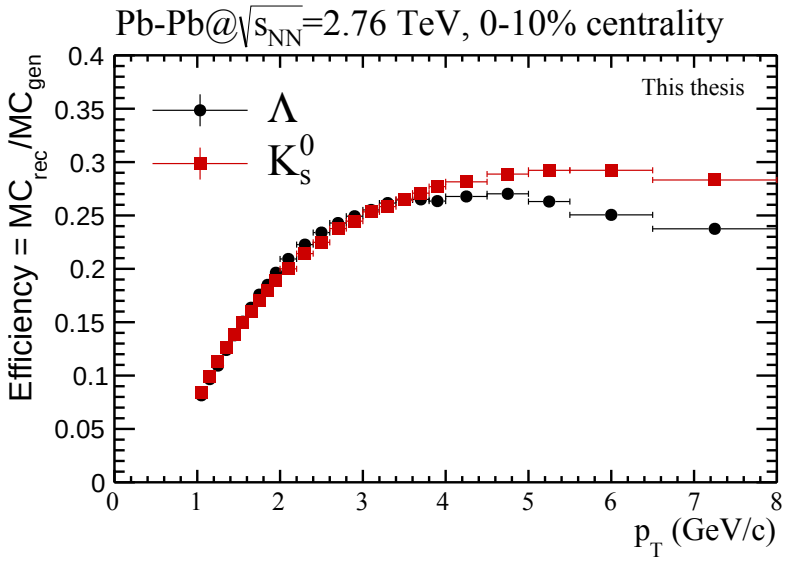


Figure 5.15: K^0_s and Λ efficiency for Pb–Pb at $\sqrt{s_{NN}} = 2.76$ TeV, 0-10% centrality.

Feed-down

The uncorrected p_T spectra are built up by primary particles originating from the collision, but the yield can be contaminated by particles from secondary decays that pass the identification cuts. This feed-down of particles is corrected for by estimating the number of secondary particles. In this case, it is relevant for the Λ only, since there is no significant contribution of particles decaying to K^0_s, while Λs could be produced in Ξ and Ω decays. The contribution from Ω is however negligible [66]; the main contribution is from Ξ^0 and Ξ^- decays.

The feed-down is calculated and discussed in detail in Ref. [66]. The general procedure is to create a MC matrix that correlates the production of Λ feed-down with Ξ, and then check whether the Λ is a daughter particle of the Ξ using the MC generated ID label. The matrix is filled with the transverse momentum of the Λ and its mother. The second step makes the approach data driven: the matrix is weighted with the ratio of the measured Ξ p_T spectrum from real data to the one in MC, since strangeness production in Pb–Pb collisions may not be correctly accounted for in MC. The results for Pb–Pb at $\sqrt{s_{NN}} = 2.76$ TeV in different centrality bins can

be seen in Fig. 5.16, with a function approximating the average contribution:

$$F_{sec} = 1 - (0.22 + 0.0323 p_T - 0.0174 p_T^2 + 0.00179 p_T^3 - 0.0000568 p_T^4) \quad (5.8)$$

where F_{sec} is the fraction of secondaries. This function is used to correct for the feed-down in this analysis. The Λ yield is contaminated with $\sim$ 25% secondaries at 1 GeV/c, with a decreasing trend towards higher p_{T} ($<$10% at 6 GeV/c).

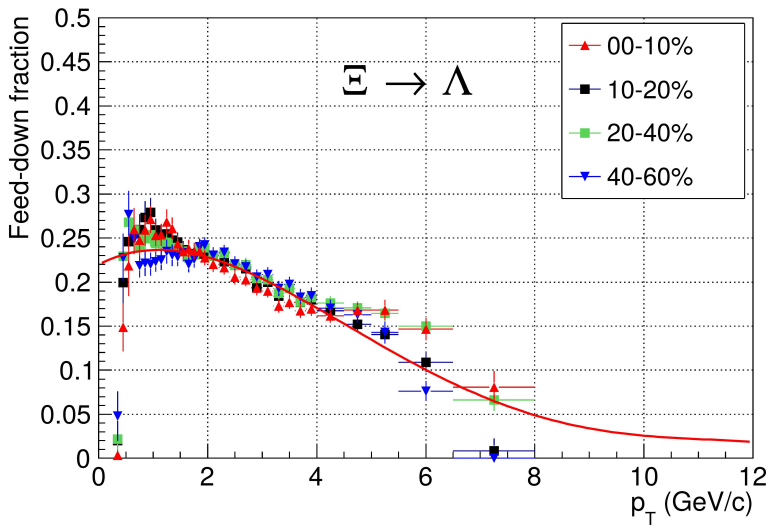
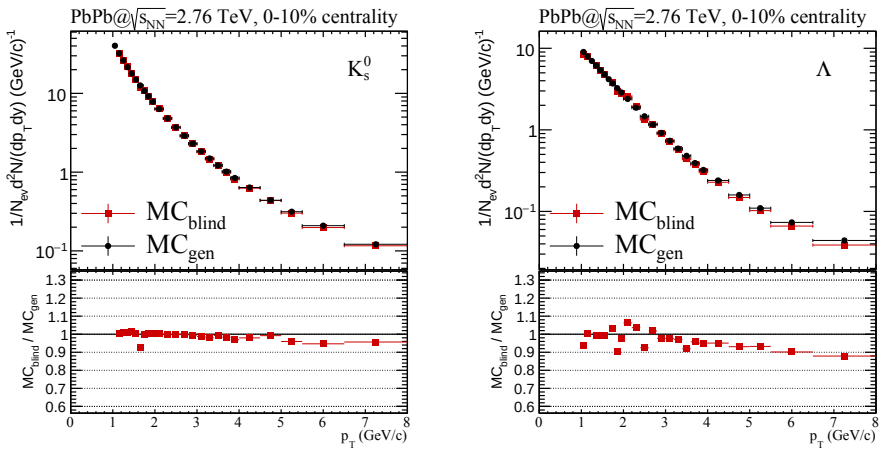


Figure 5.16: Feed-down corrections for different centrality selections calculated in the published inclusive analysis [66]. The red curve is the approximating polynomial used for the actual correction, see Eq. 5.8. Figure taken from [66].

5.3.4 MC Closure

The $\mathrm{MC_{rec}}$ data can be used without its particle ID label, and is then here referred to as $\mathrm{MC_{blind}}$ data. The invariant mass of the $\mathrm{MC_{blind}}$ will now have a background just like real data, and can be passed through the signal extraction and correction procedure to obtain a $\mathrm{MC_{blind}}$ p_{T} spectrum. To establish that the analysis procedure is self consistent, the $\mathrm{MC_{blind}}$ spectrum is used for a MC closure test by comparing it to the number

of generated particles, MC_{gen}, seen in Fig. 5.17. The K^0_S MC closure tests are better than 2% percent, and for Λ the test stays within 10%, which indicates that the method with all its steps is approached correctly. Also here, the secondary Λs have been corrected for using the published feed-down estimation, to make sure this can be used in the real data analysis. Using a feed-down correction obtained from a data driven method in the MC contributes to the larger deviations in the Λ MC_{blind} spectra in the MC closure.



(a) K^0_S (b) Λ

Figure 5.17: Inclusive MC closure test for 0-10% central events. The corrected reconstructed yields without applying the particle ID label, MC_{blind}, are compared to generated MC yields, MC_{gen}.

5.3.5 Corrected Inclusive Yields

With the corrections and normalization described above, the corrected inclusive p_T spectra can now be constructed for real Pb–Pb at $\sqrt{s_{NN}} = 2.76$ TeV, 0-10% centrality data, showed in Fig. 5.18 together with a comparison of the published spectra [66], using data from 2010.

Interpreting Data Closure

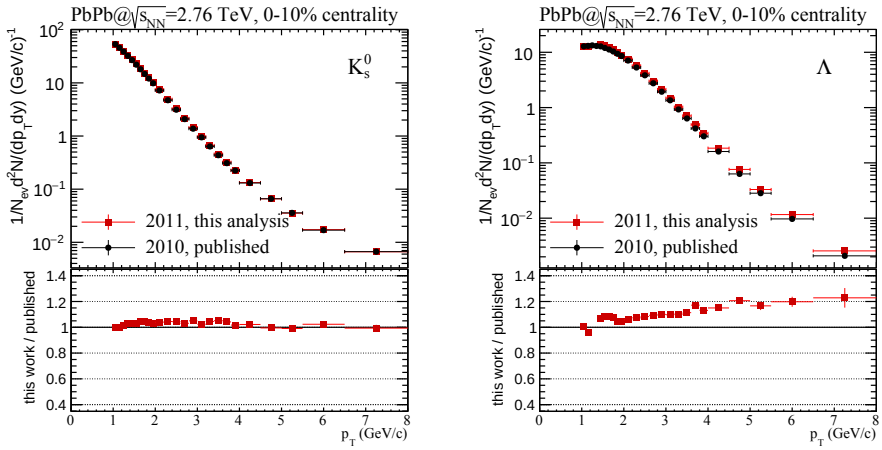
The important data closure cross check measurement is not as satisfying as anticipated. It is clear, from Fig. 5.18, that the results from the analysis performed with 2010 and 2011 Pb–Pb at $\sqrt{s_{\mathrm{NN}}} = 2.76$ TeV data set differ in the sense that the $\mathrm{K}^0_{\mathrm{s}}$ yields deviate by ∼5%, and Λ yields with ∼10% at low p_{T}, and ∼20% at higher p_{T}. Of course, if the analysis and corrections are done properly, the results between different data periods should agree if it is the same collision energy and centrality, even though the detector settings were different between the two runs. Interestingly, other analyses [84, 88] in ALICE, comparing results from the two periods 2010 and 2011, show the same deviations.

To be sure that there is not a bug in the analysis framework, the inclusive yields in the 2010 data set are produced with the same procedure and codes as used in the 2011 data analysis. Figure 5.19 show a comparison between the inclusive Pb–Pb spectra in 0-10% centrality from this analysis and the published results, now both produced with 2010 data. The agreement is within 4% for both $\mathrm{K}^0_{\mathrm{s}}$ and Λ. Let me stress the importance of this closure test: this is the comparison that really shows the solidity of the method since it is comparing the same data set, and it is seen that it is in even better agreement than the MC closure test. This leaves us with two possible explanations for the difference seen in 2011 data closure test:

- The deviation lies in the different experimental data periods, and the understanding of the detector has changed
- The deviation lies in the different anchored MC data set used for corrections

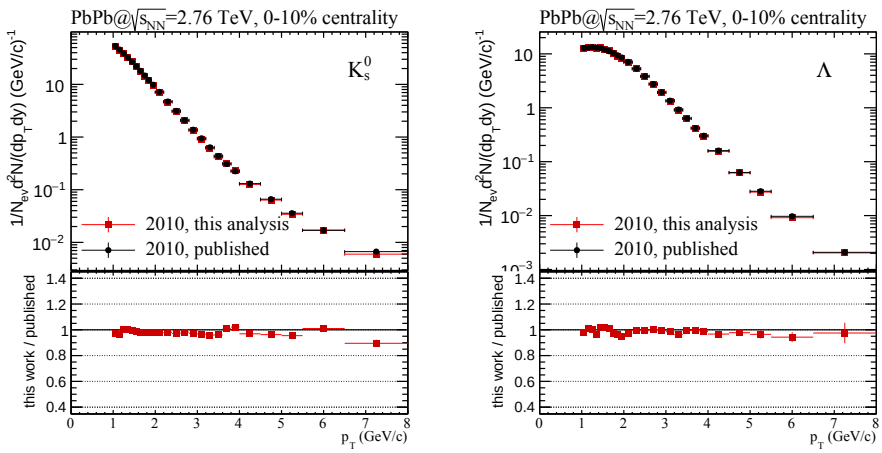
These two possibilities are investigated in the next section.

A final remark in this discussion is that, even though the rapidity range is different in the two analyses — this analysis has been extended to cover the full pseudo-rapidity $|\eta| < 0.8$, whereas the published analysis only covers a rapidity of $|y| < 0.5$ — the 2010 comparison confirms that the feed-down calculated for the published analysis, which is used in this analysis too, is valid since it gives good closure for the 2010 data analysis, indicating that this is also applicable in the larger η acceptance. The wide η-cut instead of a tighter y-cut will be important when performing



(a) K^0_S (b) Λ

Figure 5.18: 2011 corrected spectra (this analysis) compared to published (2010) results.



(a) K^0_S (b) Λ

Figure 5.19: 2010 corrected spectra (this analysis) compared to published (2010) results.

the η-reflection analysis, since it will cover the region in which the trigger particles are chosen, thus avoiding pairwise acceptance effects.

5.3.6 Investigating Experimental Period Dependences

The natural strategy to investigate the differences in the 2010 and 2011 data sets is to go back as far as possible in the analysis chain. The first comparison is between the uncorrected raw signal, before we move on to MC data comparisons.

Real Data

The raw data comparison is expected to be somewhat different due to the different detector settings, e.g. the gain of the TPC in 2011 was lower than in 2010. In Fig. 5.20 it is however noted that the raw yields are remarkably similar, to a level of ∼5%.

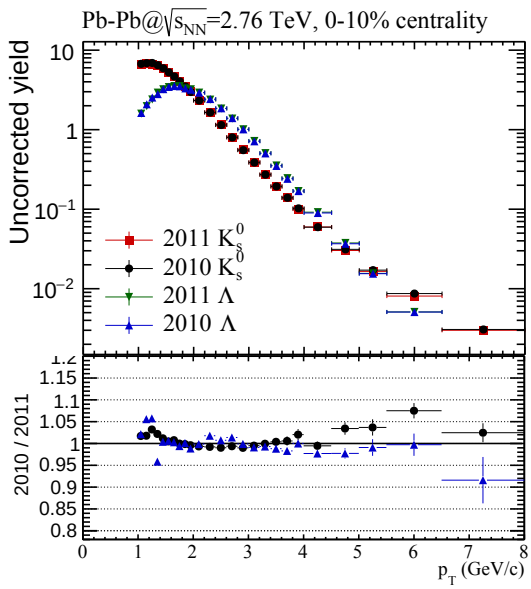


Figure 5.20: 2011 and 2010 uncorrected p_{T} spectra comparison for $\mathrm{K}^0_{\mathrm{s}}$ and Λ.

This result instead makes us draw the attention towards the efficiency correction, since the difference must be in the MC data.

MC Data

In Fig. 5.21 the efficiency for the 2010 and 2011 anchored MC data sets for Pb–Pb at $\sqrt{s_{NN}} = 2.76$ TeV are shown for K^0_s and Λ computed in 0-10% centrality, indicating a clear difference in the efficiency. The difference is largest for Λ at $p_T > 4$ GeV/c, reaching ∼20%, while it stays within 10% for K^0_s, i.e. the same magnitude as the 2010 vs. 2011 corrected yield difference. The origin of the deviation is hereby established, but the reason for the efficiency discrepancy is still unknown. In Fig. A.2 in the Appendix, the efficiency in positive and negative pseudo-rapidity is also plotted, excluding that the anomaly is due to an imbalance in pseudo-rapidity.

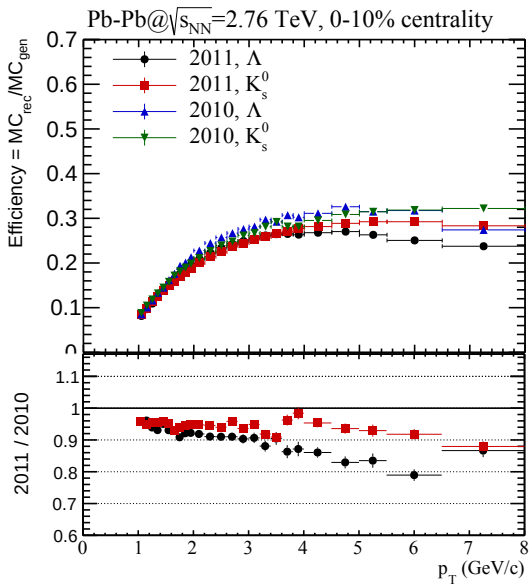


Figure 5.21: 2010 and 2011 periods 0-10% Pb–Pb efficiencies for K^0_s and Λ.

In an attempt to investigate this, the 2011 efficiency was first computed in groups of runs, or run-by-run, to see if the effect was attributed to a few runs only, but the deviation was found to be present in each single run.

The next idea is based on the fact that the TPC is segmented in sectors with a frame between them, so the question is if the effect could be caused

by the dead area between the sectors. This is examined by making a geometrical edge cut when selecting the V0 particles. The cut depends on charge, φ, p_{T}, and the polarity of the magnetic field, and works for tracks with $p_{\mathrm{T}} > 2$ GeV/c. First, we make sure that only V0s close to the beamline are considered, therefore the decay radius is set to $5 < r_T^{dec} < 10$cm, and then the V0 with daughter tracks close to the TPC sector edges are excluded. This test was performed for Λ, since the efficiency deviation is larger for Λ than $\mathrm{K}^0_{\mathrm{s}}$. An indication that this cut is working is that the number of clusters improves for high p_{T}. However, the efficiency difference remains, as seen in Fig. 5.22 where the efficiency for Λ close to the beam pipe is shown with and without the edge cut. It is concluded that the edge effect is negligible, thus ruling out TPC performance effects as a possible explanation for the difference.

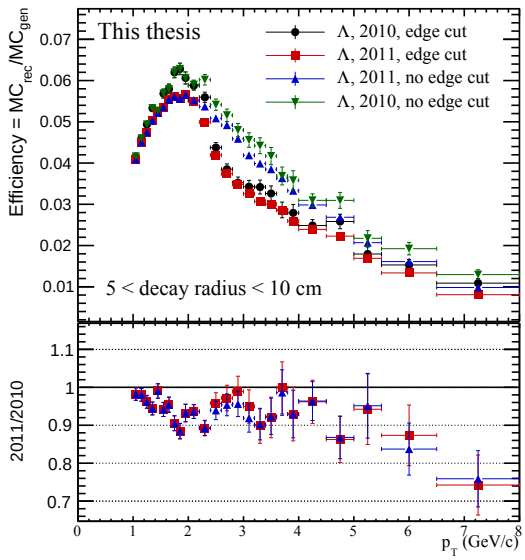


Figure 5.22: Λ efficiency for $5 < r_T^{dec} < 10$ cm, with and without the edge cut.

Since the issue is most prominent for high-p_{T} Λs, it suggests that it has to do with the high-p_{T} tracking, and since it is not a TPC edge effect, the last idea is to test if some of the high-p_{T} tracks are accidently duplicated during the MC reconstruction. Again, this test if performed

for Λ only, where events containing multiple (2 or more) Λ particles with $5 < p_T < 8$ GeV/c are filled in a matrix storing the p_T of these Λs, seen in Fig. 5.23(a). Excluding these events would exclude any duplicates, but in Fig. 5.23(b) it is seen that the effect does not account for the 20-30% deviation seen in the Λ efficiency at high p_T.

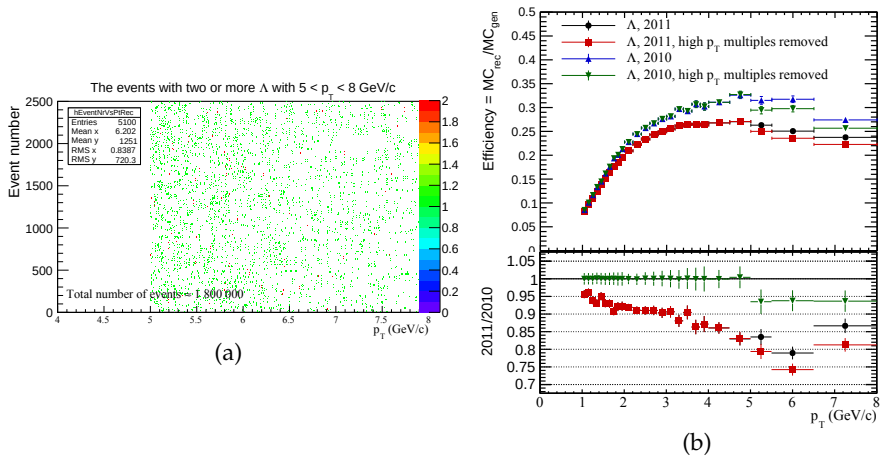


Figure 5.23: (a) Λ events with multiple high-p_T particles. (b) Λ efficiency with and without events containing multiple high-p_T particles.

Since the MC differences between 2010 and 2011 anchored periods is affecting many ALICE analyses, an experimental wide effort to solve this is now ongoing, and the hope is to resolve this discrepancy as soon as possible. For this analysis it is decided to put a systematic uncertainty of 6% to all spectra and ratios in the correlation analysis to cover for this difference. Important to note here is that, for the η-reflection method, the discrepancy is trivially propagated to the jet when subtracting the bulk from the peak region. I will perform the correlation analysis with both the 2010 and 2011 MC corrections to verify the systematic uncertainty.

5.4 A Word Before Starting the η-reflection Analysis

In Sec. 5.1, the method to subtract the V0 particles created in the underlying event from those created in the jet was introduced, and in Sec. 5.3 the inclusive V0 yields were constructed in order to compare the results to the published spectra. Even though a discrepancy is seen in the spectra, this is likely related to a difference in the MC, and not caused by the data analysis. When the same data period was analyzed here as for the period of the published inclusive analysis (that of 2010), the results agree very well, verifying that the analysis framework and procedure are accurate, allowing them to be applied to the main analysis. As will be seen later in this chapter, many other important cross checks will be carried out.

The analysis was started with the 2010 data period, but in central Pb–Pb the peak and bulk regions are similar to within a few percent — especially at low p_{T} — and to be able to subtract two similar, large, numbers, good accuracy is needed, which means a large number of events. In 2010 data it was seen that for $p_{\mathrm{T}} < 3$ GeV/c, the Λ peak and bulk could be considered as equal (to a level of 1σ) within the statistical errors, leading to difficulties in subtracting the bulk from the peak to obtain the jet. To gain better statistical precision, and to solve this problem, the analysis is now done with 2011 data.

The event and track selection criteria will be the same as for the inclusive analysis, but before selecting V0 candidates, the trigger particle to which the V0 is associated must be selected.

5.5 Trigger Particle and Region Selection

5.5.1 Track Quality

A trigger particle is selected from charged primary tracks with $p_{\mathrm{T}} > 5$ GeV/c, with the following additional requirements, summarized below. Note that the requirement that the trigger particle comes from the primary vertex excludes it from being a V0 daughter.

Since some parts of the SPD were switched off due to a cooling issue during many run periods, including the 2011 period, there are regions with inefficient reconstruction. To ensure uniform distributions in η and φ, the tracks used as trigger particles are a hybrid combination of two different track quality requirements. The *global* tracks (defined below) are

used when available, and otherwise the *global constrained* tracks (defined below) are used.

The global tracks should have at least one hit in the active part of the SPD. In addition, it must have a minimum of 70 crossed TPC pad-rows, i.e. the sum of the number of TPC pad-rows that the particle induced a signal on (number of *clusters*), and the number of identified missing clusters[6], to a given track. Related to this, a cut on the ratio of the number of crossed pad-rows to the number of geometrically possible clusters which can be assigned to a track ("findable clusters"), is set to 0.8 or higher. Furthermore, the χ^2 per ITS cluster is set to less than 36 units, and the χ^2 per TPC cluster must be less than 4 units in the first iteration. Moreover, pions and kaons identified via their weak decay topology ("kink topology") with daughter particles being a muon and a neutrino, are rejected. Lastly, the maximum distance of the track to the primary vertex position in the $x-y$ plane has a p_T dependence, thus requiring the tracks to be constrained to the primary SPD vertex. In addition to this, ITS and TPC refit (explained in Sec. 4.6) is required, which significantly improves the momentum resolution.

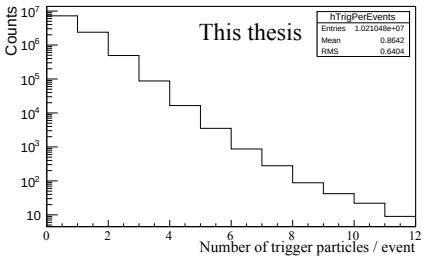
The global constrained tracks are defined with the same set of cuts as the global tracks, except that no ITS refit or SPD hits are required. Using these constrained tracks whenever the global definition of a track does not exist, fills the gaps in the azimuthal angle distribution caused by the missing SPD layers.

With these nominal conditions, and with the η selection region of $0.2 < |\eta_{trig}| < 0.8$, as explained in Sec. 5.1, the number of trigger particles per event is a steeply falling spectrum, as shown in Fig. 5.24(a). Here most events contain no trigger at all, but some events contain 1-2 trigger particles, and very rarely more than that[7]. Fig. 5.24(b) shows the p_T distribution of these trigger particles. To assure the quality of the selected triggers, the φ and η distributions are drawn in Fig. 5.24(c) and Fig. 5.24(d) respectively, indicating a flat, full 2π azimuthal coverage[8], and a close to symmetric η-window region.

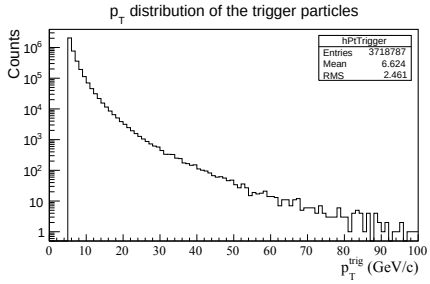
[6]Some TPC clusters can be missing due to an induced charge which is not high enough to exceed a given threshold.

[7]The total number of events is 10 210 480, whereof 7 228 064 without any trigger particles above 5 GeV/c, i.e. 29.21% of the events contain at least one trigger particle.

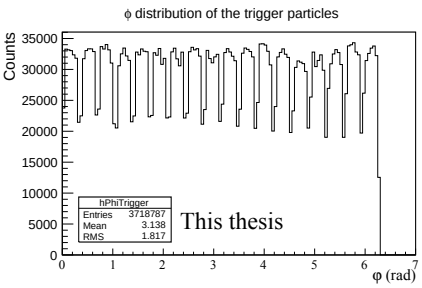
[8]The equidistant small gaps in the φ distribution correspond to the TPC sector edges.



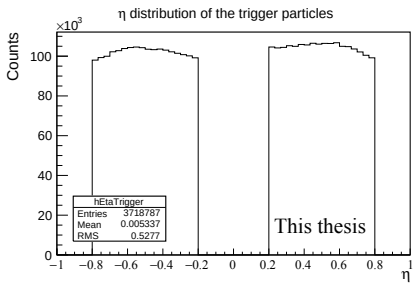
(a) Trigger particles per event



(b) p_{T} distribution of trigger particles

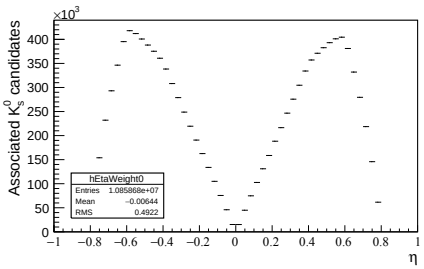


(c) φ distribution of trigger particles

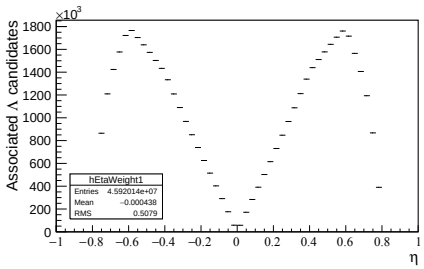


(d) η distribution of trigger particles

Figure 5.24: Quality assurance of the trigger particles.



(a) $\mathrm{K}^0_{\mathrm{S}}$



(b) Λ

Figure 5.25: The η distribution of V0 candidates with $p_{\mathrm{T}} > 1\,\mathrm{GeV}/c$, selected in both the bulk and peak regions.

5.5.2 Peak and Bulk Region

Once a trigger particle is found in an event, the analysis algorithm loops over all possible V0s, applying the same cuts as described in Sec. 5.2. A trigger associated V0 candidate is a V0 that passes all selection cuts, and in addition falls within the defined $\Delta\eta$ and $\Delta\varphi$ windows, introduced in Sec. 5.1, but stated again for convenience: both peak and bulk regions are sampled in $|\varphi_{\text{trig}} - \varphi_{V0}| < 0.92$, and then the peak V0s are within η ± 0.2 around the trigger particle ($|\eta_{\text{trig}} - \eta_{V0}| < 0.2$), and bulk V0s are within the symmetrically opposite η window ($|\eta_{\text{trig}} + \eta_{V0}| < 0.2$), giving rise to the V0 candidate η distribution seen in Fig. 5.25.

5.6 Signal Extraction

The signal extraction for the peak and bulk regions is based on the same principles as for the inclusive signal extraction. In Fig. 5.26, the invariant mass distributions for K^0_S and Λ particles with $2.0 < p_T < 3.0$ GeV/c are shown to illustrate how close the signals in the peak and bulk regions are — they only differ by a few percent at low p_T, therefore, care has to be taken to extract the signal as consistently as possible in the two regions.

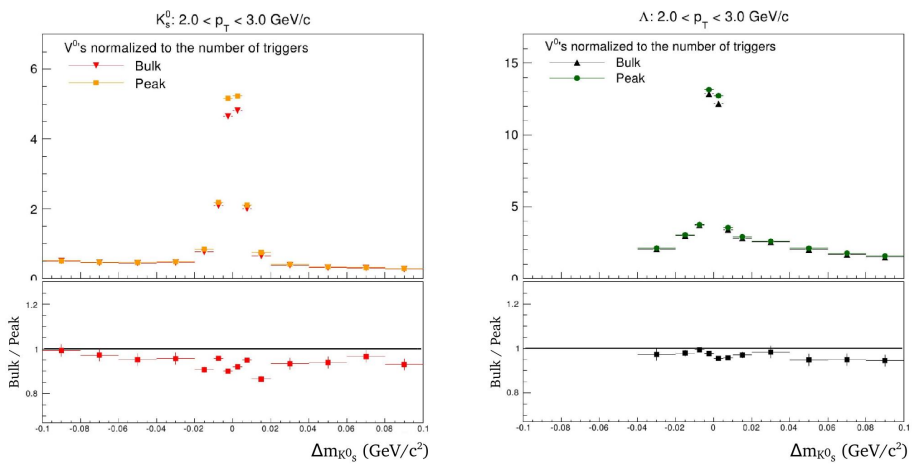


Figure 5.26: V0 peak and bulk invariant mass distribution for K^0_S (left) and Λ (right) in $2 < p_T < 3$ GeV/c. The ratio in the bottom panels shows bulk/peak.

To do this, the two p_{T}-differentiated invariant mass distributions for peak and bulk are, as a first step, added. This sum is fitted using a double Gaussian (signal) + a third degree polynomial (background) to describe the data (signal+background) as well as possible. Initially, a single Gaussian was used to fit the signal region, but it was discovered that a double Gaussian describes the shape better.

The fitting function is described by

$$f(x) = p_1 \cdot e^{-\left(\frac{x-p_2}{p_3}\right)^2} + p_4 \cdot e^{-\left(\frac{x-p_5}{p_6}\right)^2} + p_7 + p_8 \cdot x + p_9 \cdot x^2 + p_{10} \cdot x^3 \quad (5.9)$$

where p_i are the different fit parameters. The parameters representing the two mean values of the Gaussians, p_2 and p_5, are initially set to 0, while the two initial widths, p_3 and p_6, are set to 0.005 in the case of $\mathrm{K}^0_{\mathrm{s}}$, and 0.002 in the case of Λ due to its narrower distribution. The two Gaussian constants representing the integrated yields, p_1 and p_4, and the first constant in the polynomial, p_7, are initially set to half of the histogram's maximum value. Parameter p_8 and p_9 are not used in the first step, thus being reduced to a double Gaussian for the signal region, and a constant for the background region. The procedure is then to fit the sum of the peak and bulk histograms with this initial assumption, and then fit a second time with the parameters from the first fit as input for the parameters of the second fit, now including p_8 as a free parameter to describe the background better. The last step is to fit a third time with the parameters from the previous fit as input, finally including all parameters in the polynomial. It was found that this stepwise fitting significantly improved the fit convergence.

The mean and width of the signal part of the function, i.e. the double Gaussian, is extracted by filling a histogram with 100 000 random samplings from this function, and letting the RMS and mean of this histogram represent the width and the mean of the double Gaussian. To fit the separate peak and bulk regions, the extracted mean and width from the previous step is fixed for the double Gaussian which is about to be fitted to the separate regions. This is done to minimize fluctuations in these values, that would propagate to the uncertainty of the yield. The only free parameters when extracting the yields for the peak and bulk are thus the ones belonging to the yield and background, which, before the fit, are set as the output of the fit from the last step in the previous fitting. Examples

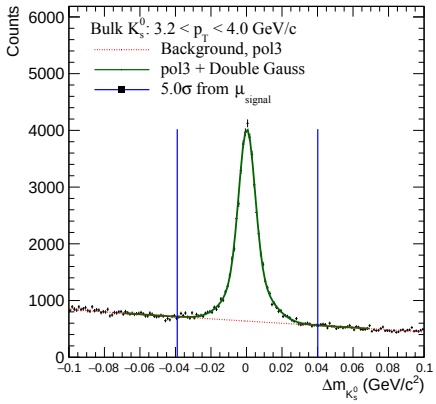
of the invariant mass fits are shown in Fig. 5.27. All fits can be seen in the Appendix, Fig. B.1–B.4.

The yield is extracted by summing the content in each bin in a region $\mu \pm 5\sigma$. The integral of the background polynomial in the same region, is then subtracted to obtain the signal yield. With the same argumentation as for the inclusive analysis, the statistical error is defined by Eq. 5.6.

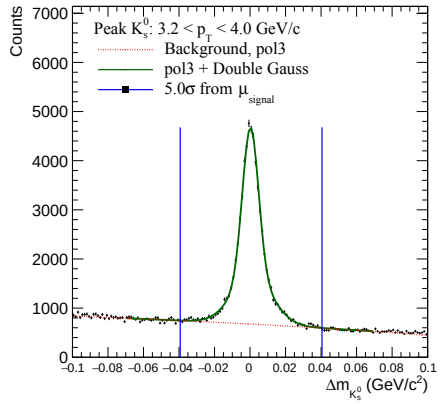
The mean and widths of all fits can be seen in Fig. 5.28. The systematic increase of the width with p_T reflects that the momentum resolution is worse at high transverse momentum. It is a minor effect of $\sim$5 MeV/c^2. The systematic variation with p_T shows that the fitting is robust. Likewise, the variation of the mean value is very smooth, but still at a very small level (about 1 electron mass). This also illustrates the robustness of the fitting, and that the absolute value of the momentum determination (the *vectors*, since the opening angle also enters into the invariant mass) is extremely good.

5.6.1 Raw p_T spectra

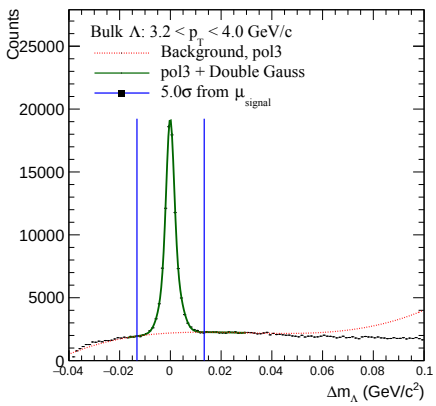
The p_T spectra for the peak and bulk are obtained from the yield extracted from the fits to the mass distributions for the two regions. The spectra are normalized to the number of trigger particles, and shown in Fig. 5.29 for Pb–Pb at $\sqrt{s_{NN}} = 2.76$ TeV, 0-10% centrality. From the zoomed in ratio of the peak and bulk (for the same V0) we can conclude that the region where it is statistically safe to subtract the bulk from the peak is for p_T >1.0 GeV/c for K^0_s, and from 2.0 GeV/c for Λ (and hence the jet Λ/K^0_s ratio should also be done from 2.0 GeV/c).



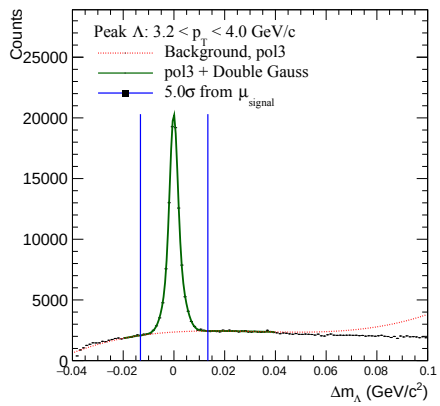
(a) Bulk K^0_s



(b) Peak K^0_s

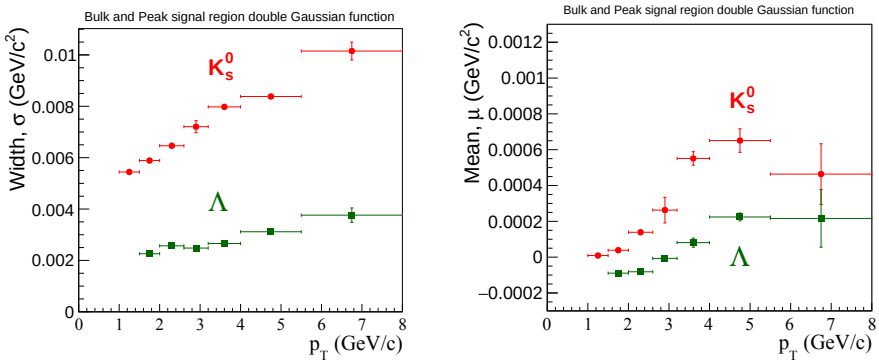


(c) Bulk Λ



(d) Peak Λ

Figure 5.27: K^0_s and Λ peak and bulk invariant mass distribution for $3.2 < p_T < 4$ GeV/c, fitted with a third degree polynomial (background) + double Gaussian (signal), where the polynomial is used for background subtraction. The signal region is extracted in a $\pm 5\sigma$ region around the mean.



(a) Width (b) Mean

Figure 5.28: The means and widths of the double Gaussian fitted to the peak and bulk signal region.

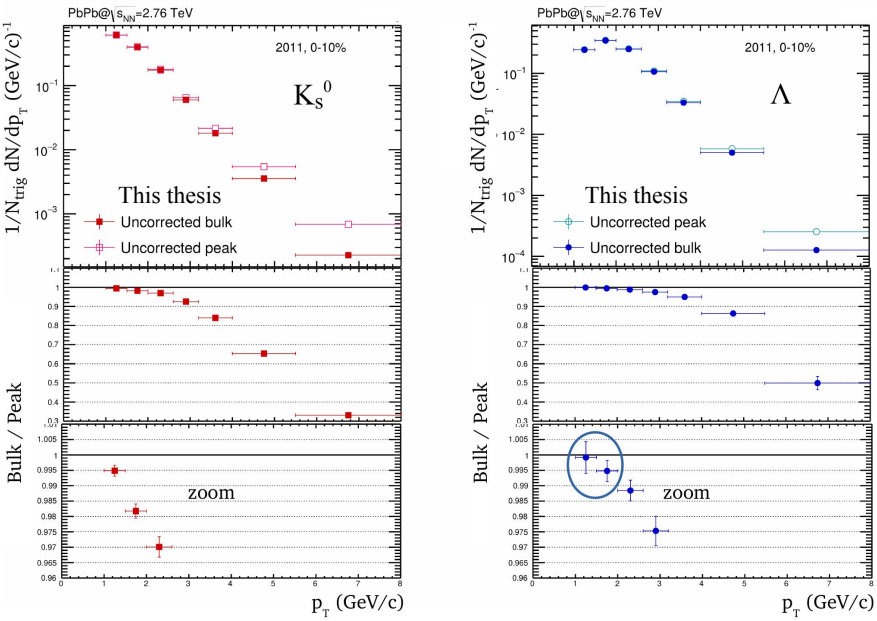


Figure 5.29: Uncorrected peak and bulk yields for K^0_S (left) and Λ (right), with the ratio showing bulk/peak The bottom panel shows a zoomed-in version of the ratio. The blue circle indicate that these two bins do not have enough statistical certainty to be able to subtract the bulk from the peak.

5.7 Corrections

To obtain the final yields for peak and bulk, the raw p_{T} spectra have to be normalized to the p_{T} bin width, the $\Delta\eta\Delta\varphi$ region ($\Delta\eta$ =0.4, and $\Delta\varphi$ =0.92), and corrected for efficiency and feed-down, which will be discussed later in this section. Since the trigger particle's η distribution has an exclusion gap at central η, propagating a non-uniform η distribution of the V0s, there will be some additional acceptance effects to consider, examined next.

5.7.1 Acceptance Effects

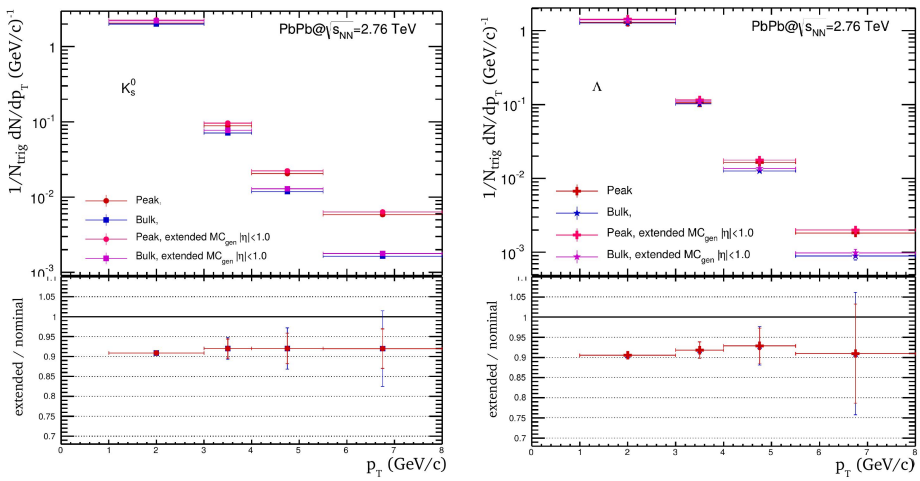
Recall that V0s are chosen in a region of $\pm$0.2 around η_{trig} and -η_{trig}. Therefore, in the case where the trigger particle has e.g. $\eta = 0.7$, part of the V0 peak and bulk region is placed outside the experimental acceptance of $|\eta| < 0.8$, and for a trigger particle at $\eta = 0.8$, approximately half the signal is lost due to the acceptance. Fig. 5.31(a) illustrates the problem. Analytically, the effect on the yields can be estimated (assuming boost invariance) to be $\sim$10%.

Cross-Checks

The analytical derivation of the impact of the acceptance effect can be verified and tested by MC simulations. With $\mathrm{MC_{gen}}$, the η detector acceptance region can be extended from $|\eta| < 0.8$ to $|\eta| < 1.0$, so that the peak and bulk windows associated with trigger particles having η_{trig} =0.8 are covered in the (simulated) detector acceptance region. The MC generated spectra with the η-extension are compared to the MC generated without the extension, and as can be seen in Fig. 5.30, the effect compares well with the analytical value of 10%.

Another similar cross check is done by using real data. Since the real case detector acceptance can not be extended as in MC simulations, the trigger particle acceptance region is instead decreased to $0.2 < |\eta_{trig}| < 0.6$ so that the full peak and bulk signal will be located inside the detector acceptance[9]. Also here, when comparing these spectra to the nominal η

[9]The reason why this is not used in the full analysis is because it reduces the statistics by $\sim$25%.



(a) K^0_S (b) Λ

Figure 5.30: Generated spectra with nominal V0 η-cut ($|\eta| < 0.8$) compared to an extended cut of $|\eta| < 1.0$ (old p_T binning with a subset of the full statistics).

region case, a 10 % effect was found, in support of the analytical argument.

Symmetrization – A Data Driven Solution

To correct for the acceptance effect it is decided to use a data driven correction with an "on-the-fly" *symmetrization*, based on the idea illustrated in Fig. 5.31(b): the associated V0 particles which, when *mirrored* with respect to the η_{trig}, falls outside the detector acceptance will be given a weight of 2. All other V0 keep a weight of 1. Fig. 5.32 shows how this method compares to the analysis done with no symmetrization. The effect is ∼10%, in agreement with the other methods discussed.

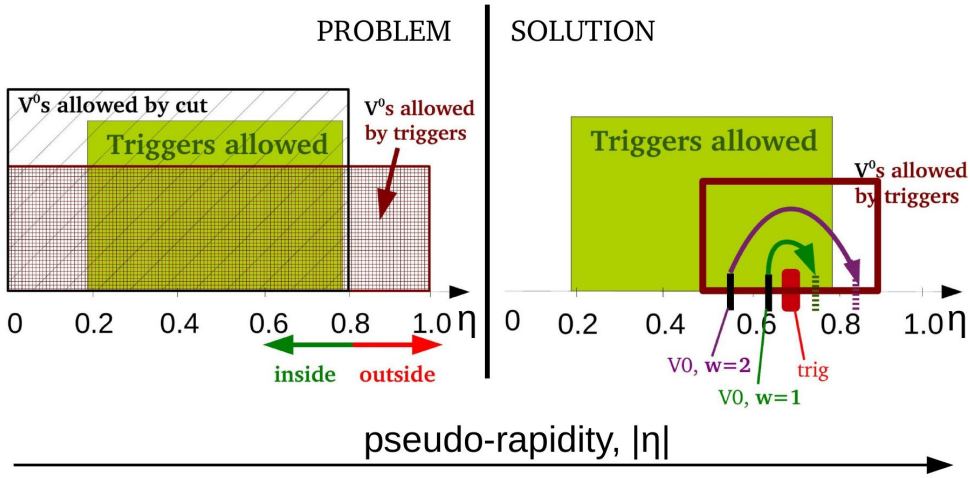
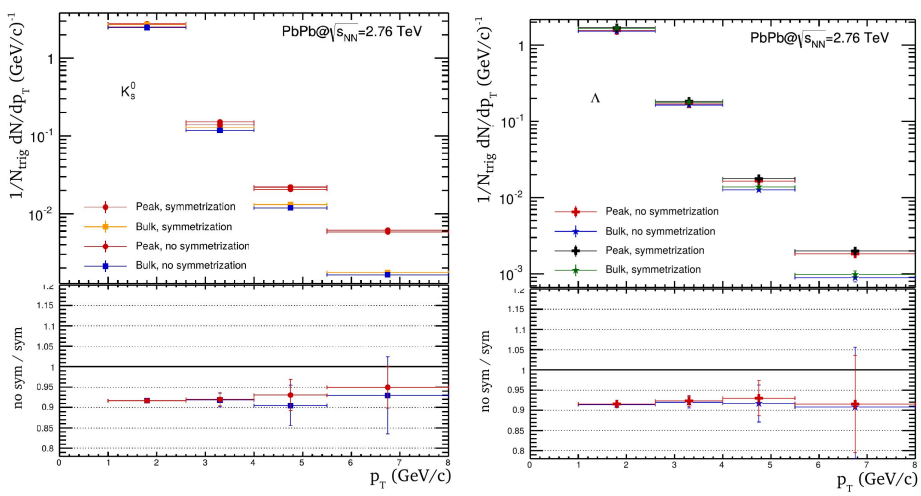


Figure 5.31: PROBLEM: Illustration of the acceptance effect: if $|\eta_{\text{trig}}| > 0.6$, part of the V0 peak and bulk region (± 0.2) will be located outside the experimental acceptance of $|\eta| > 0.8$. SOLUTION: Illustration of the symmetrization method used to correct for the acceptance effect, see text for details.



(a) K^0_s (b) Λ

Figure 5.32: Comparing the spectra with and without symmetrization (the study is done with an old p_T binning with a subset of the full data sample).

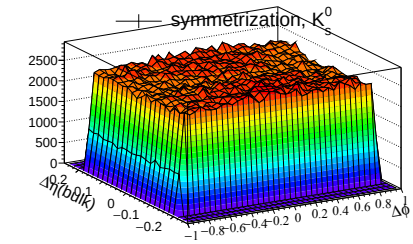
5.7.2 Underlying Event Structures

In the motivation of this analysis method, it was mentioned that the event mixing MC correction, normally used in correlation analysis, can be avoided since the peak and bulk regions are chosen symmetrically in η, and in the same φ-region, thus giving equal performance of the underlying event. Event mixing is used to solve acceptance effects, but introduces extra complications since particle identification is needed in each bin. In order to avoid event mixing in this analysis, the underlying event projected in $\Delta\eta$ needs to have a flat structure, confirmed in Fig. 5.33, where the $\Delta\eta \times\Delta\varphi$ and the projection to $\Delta\eta$ is shown.

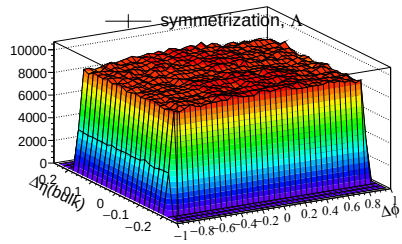
It is interesting to note that the symmetrization described in the previous section is really necessary to obtain the flat η structure in the underlying events; when the acceptance effect is not corrected for, the $\Delta\eta \times\Delta\varphi$ shows a clear triangular structure in $\Delta\eta$, visible in Fig. 5.34. However, this structure disappears when symmetrization is applied (as we saw in Fig. 5.33), or when a flat V0 particle acceptance can be used (when the trigger particles are limited to $0.2 < |\eta_{\text{trig}}| < 0.6$), so that the acceptance effect is not present, as in the case shown in Fig. 5.34(e)– 5.34(f).

5.7.3 Efficiency

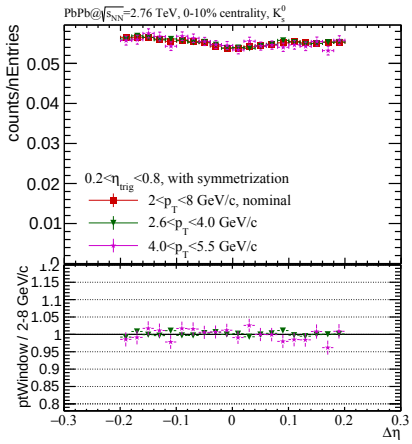
When computing the peak and bulk efficiencies with MC simulated data, the same strategy is used as for data, concerning the different cuts and η-region selections, and the symmetrization correction. Using the same nomenclature as when discussing the efficiency of the inclusive V0s, the MC_{rec} and MC_{gen} analysis differs only from the data analysis in the sense that the MC identification labels are used, rather than invariant mass fitting. For MC_{rec}, the exact same definition of primary V0s as for the data analysis is used, while for MC_{gen} only the geometrical acceptance cut is applied. The MC yields are normalized to the number of reconstructed trigger particles, and the number of generated trigger particles, respectively.



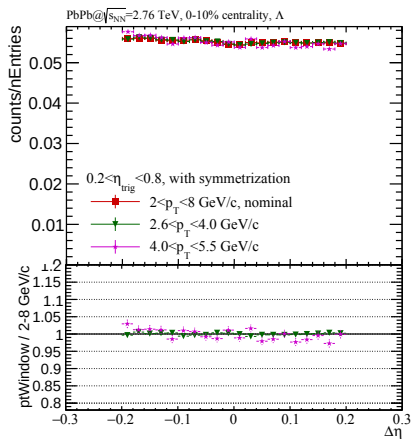
(a) K^0_s



(b) Λ

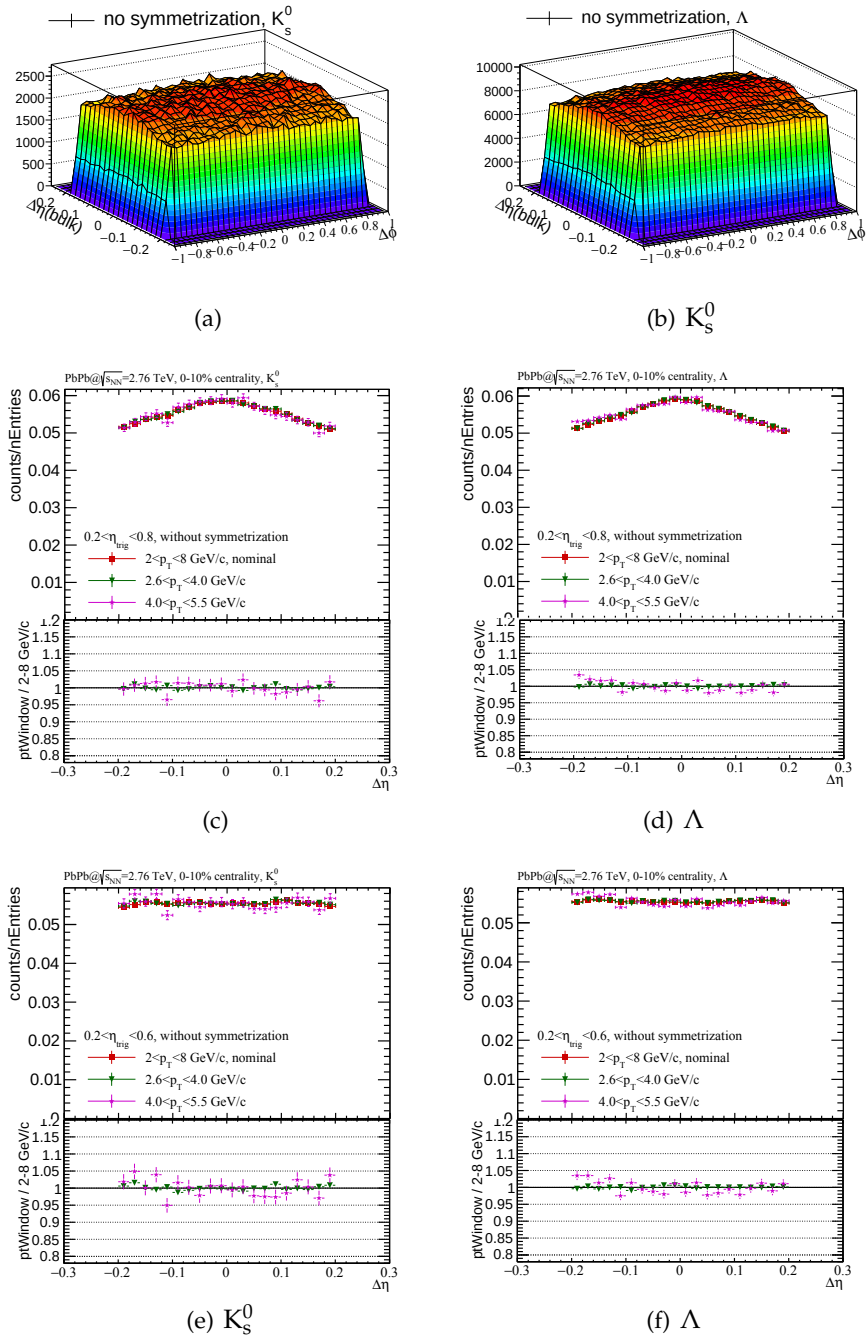


(c) K^0_s



(d) Λ

Figure 5.33: Top: $\Delta\eta\Delta\varphi$ for the bulk region with trigger particle acceptance region $0.2<|\eta_{\text{trig}}|<0.8$, and symmetrization applied. Bottom: Projection of $\Delta\eta$ for the bulk region for different p_{T}-intervals.



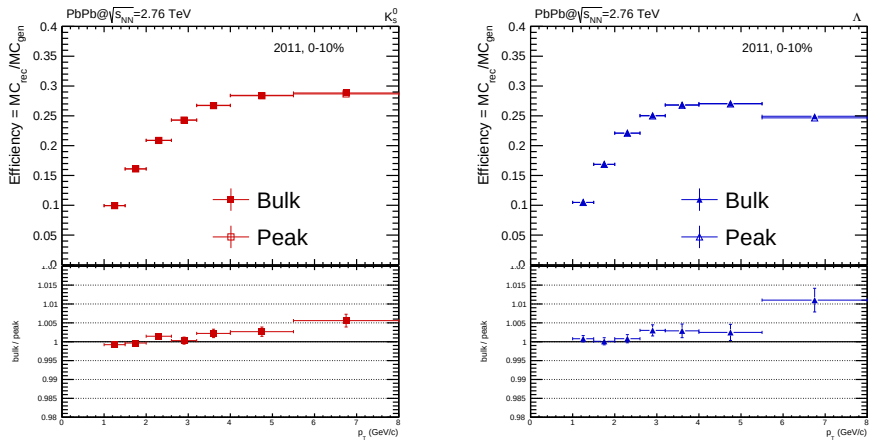
(a) (b) K^0_S

(c) (d) Λ

(e) K^0_S (f) Λ

Figure 5.34: Top: $\Delta\eta\Delta\varphi$ for the bulk region with trigger particle acceptance region $0.2<|\eta_{\text{trig}}|<0.8$, and *no* symmetrization applied. Middle: Projection of $\Delta\eta$ for the bulk region for different p_{T}-intervals. Bottom: Projection of $\Delta\eta$ for the bulk region *without* symmetrization, but in flat acceptance region $0.2<|\eta_{\text{trig}}|<0.6$.

The efficiency in the peak is then defined as: $\epsilon_{peak} = MC^{peak}_{rec}/MC^{peak}_{gen}$, and similarly for bulk: $\epsilon_{bulk} = MC^{bulk}_{rec}/MC^{bulk}_{gen}$. In Figure 5.35(a)– 5.35(b) one observes that $\epsilon_{peak} = \epsilon_{bulk}$ within 0.5%, as expected by the analysis definition.

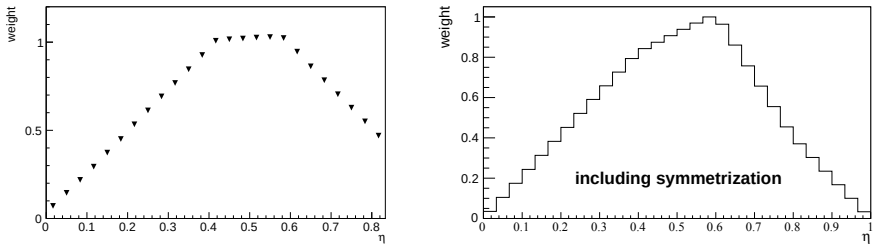


(a) K^0_S (b) Λ

Figure 5.35: Comparison between peak and bulk efficiency.

To keep the systematic uncertainties low, however, we want to use the inclusive K^0_S and Λ efficiencies, ϵ_{incl}, but due to a significant η-dependence of the inclusive efficiency — and since we in the η-reflection analysis by definition choose V0s with natural bias towards forward η (look back at Fig. 5.25) — a weighting function is computed from the trigger particle η_{trig} distribution (Fig. 5.24(d)) to compensate for this. Fig. 5.36(a) shows the unfolding of the trigger particle distribution, i.e. the weighting function obtained from the real data η-acceptance of all accepted triggers, integrated over all events, and normalized to be 1 at the maximum. Note that, as both generated and reconstructed V0s are weighted by this function, the overall normalization cancels. Fig. 5.36(b) shows the weighting function when the symmetrization method is applied, and this is the function implemented in the efficiency calculations.

In Figure 5.37(a)– 5.37(b), ϵ_{bulk} is compared to ϵ_{incl}. First to the "nominal" (un-weighted) ϵ_{incl} (the magenta points) to manifest the difference, and then to the weighted ("wgt") version of ϵ^{wgt}_{incl} (the green points) to il-

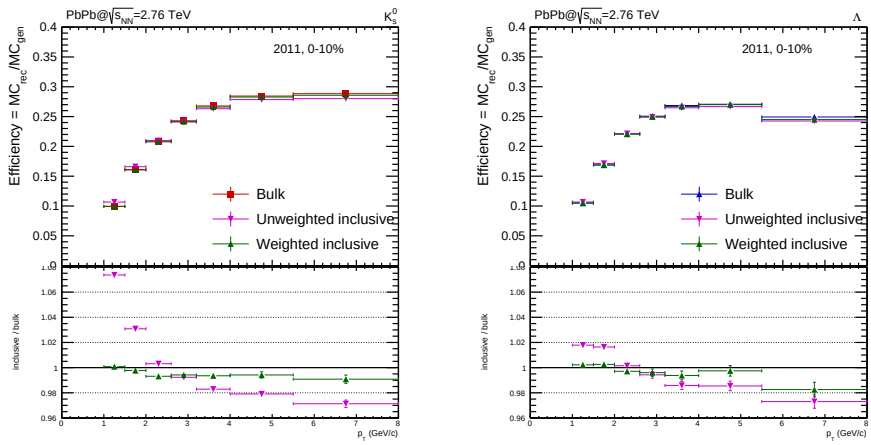


(a) Without symmetrization. (b) With symmetrization.

Figure 5.36: The relative acceptance for V0's with and without symmetrization used as the weight function.

lustrate the positive effect of the weighting: ϵ_{bulk} (and hence also ϵ_{peak}), agree with ϵ^{wgt}_{peak} to within 1%.

When discussing efficiencies, a final cross check is made to confirm that the injected particles in the MC are not affecting the efficiencies. In Appendix B, a comparison is made with and without injected particles, see Fig. B.5(a)–B.5(b). No difference is seen, hence, the injected MC sample can safely be used.



(a) K^0_S (b) Λ

Figure 5.37: The unweighed and weighted inclusive efficiency compared to the bulk.

5.7.4 Feed-down

Naively one can expect that the feed-down for the bulk is the same as for the inclusive feed-down. However, it is uncertain what the feed-down in the jet looks like. It is not necessarily the same as the inclusive and bulk feed-down, but is probably more similar to the feed-down in pp, where bulk effects are small. Still, due to nuclear modifications, the situation can be that the feed-down in the jet is very different.

A method of evaluating the feed-down, initially introduced in an ALICE study of $\Lambda/\mathrm{K}^0_\mathrm{s}$ in jet and bulk in pp collisions (not published), by looking at signal losses observed when changing the $DCA_{\mathrm{V0-PV}}$ cut, is tested here, with the goal to apply this method to the bulk and peak regions.

The signal losses, when changing the $DCA_{\mathrm{V0-PV}}$ cut, can be described by

$$\left(\frac{\Delta S}{S}\right)^{Data} = f_{prim}\left(\frac{\Delta S}{S}\right)^{MC}_{prim} + f_{sec}\left(\frac{\Delta S}{S}\right)^{MC}_{sec} \tag{5.10}$$

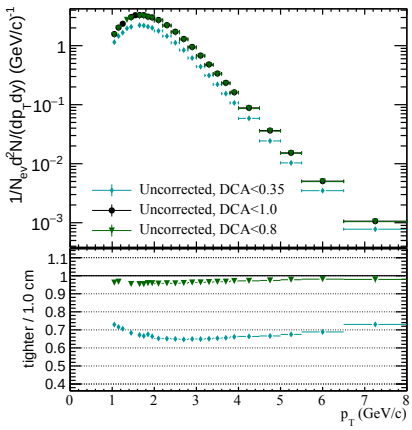
where ΔS is the signal loss when tightening $DCA_{\mathrm{V0-PV}}$, S is the signal at a loose $DCA_{\mathrm{V0-PV}}$ base value, f_{prim} and f_{sec} are the fraction of primaries and secondaries at the base $DCA_{\mathrm{V0-PV}}$, and f_{prim} and f_{sec} are assumed to add up to 1. Rewriting this, the fraction of secondaries can be expressed as

$$f_{sec} = \frac{R_{data} - R_{prim}}{R_{sec} - R_{prim}} \tag{5.11}$$

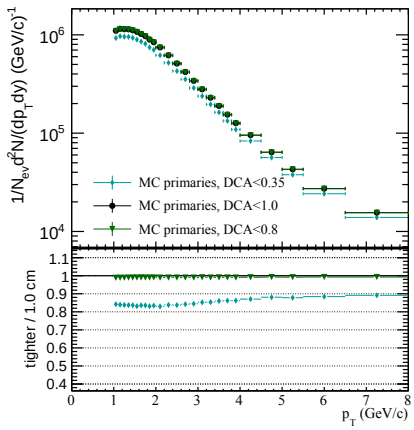
where $R = 1 - \frac{\Delta S}{S}$, i.e. the remaining signal fractions. To investigate if the method can be applied in this analysis, a study is done for the inclusive feed-down, and it is discovered that the test fails to reproduce the inclusive published feed-down in Pb–Pb [66], as will be demonstrated in the following.

In Fig. 5.38, R_{data}, R_{prim}, and R_{sec} are evaluated for several variations of the $DCA_{\mathrm{V0-PV}}$, with 1.0 cm as baseline. Calculating f_{sec}, i.e. the feed-down, from the R-values obtained from the ratios, it is seen from Fig. 5.39(a) that it is almost a factor 2 higher compared to the published inclusive feed-down (Fig. 5.16).

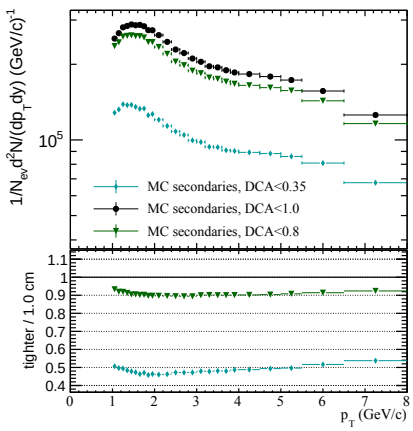
To investigate where this difference comes from, a comparison of the $DCA_{\mathrm{V0-PV}}$ distribution in data and $\mathrm{MC}_{\mathrm{blind}}$ was performed. This study



(a) Data



(b) Primaries, MC

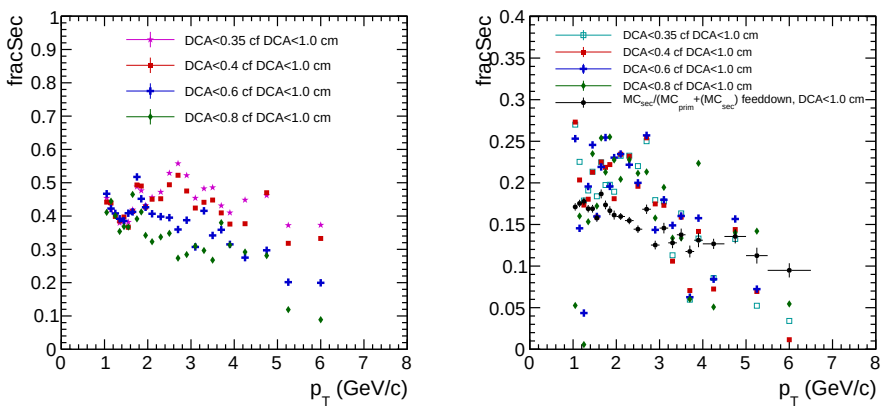


(c) Secondaries, MC

Figure 5.38: Λ p_{T} spectra with different $DCA_{\mathrm{V0-PV}}$ selection cuts in (a) uncorrected real data, (b) primary Λ in MC, and (c) secondary Λ in MC. The ratios show the variation compared to the loose $DCA_{\mathrm{V0-PV}}$ baseline, here set to 1.0 cm.

indicated that the distribution is similar for low p_{T}, low $DCA_{\mathrm{V0-PV}}$, but differs at larger p_{T}, suggesting that the difference in feed-down could be due to the relatively high baseline value. The fraction of secondaries with a $DCA_{\mathrm{V0-PV}}$ base of 0.5 cm was hence calculated, leading to an improvement in the sense that it is closer to the published feed-down. However, to truly understand if it is an improvement, the inclusive analysis has to be redone with the lower $DCA_{\mathrm{V0-PV}}$ cut, and with respect to the new p_{T} spectra, this feed-down fraction would probably be too high.

To conclude, it seems like this method needs further investigations and more detailed knowledge about the $DCA_{\mathrm{V0-PV}}$ resolution, unfortunately not carried out in this thesis due to time limitations. However, interestingly enough, it could be worth a deeper analysis since the method seems to be valid when computing the $\mathrm{MC_{blind}}$ test, seen in Fig. 5.39(b), where the result for the fraction of secondaries is compared to the inclusive published result.



(a) Data (b) $\mathrm{MC_{blind}}$

Figure 5.39: Fraction of secondaries with base $DCA_{\mathrm{V0-PV}} = 1.0$ cm.

In this analysis, a different approach is used. By going to high-p_{T} ($5 < p_{\mathrm{T}} < 6$ GeV/c), where we have demonstrated that the peak and bulk yields are significantly different (see Fig. 5.29), one can test if the $DCA_{\mathrm{V0-PV}}$ distributions are similar, thus revealing if the feed-down in the peak and bulk regions are similar. In Fig. 5.40 the $DCA_{\mathrm{V0-PV}}$ distribution for the

signal region, $|\Delta m_\Lambda| < 0.0025$ — although without background subtraction due to the "online" nature of the test[10], is shown for different bins of p_T. It is concluded that the distributions for peak and bulk are similar, even at the highest p_T bin (turquoise), and since the bulk feed-down should be comparable to the inclusive feed-down, this can be used for both regions. However, due to this rather vague approximation, a large absolute systematic uncertainty of 5 % (approximately 1/4 of the inclusive feed-down correction) is assigned.

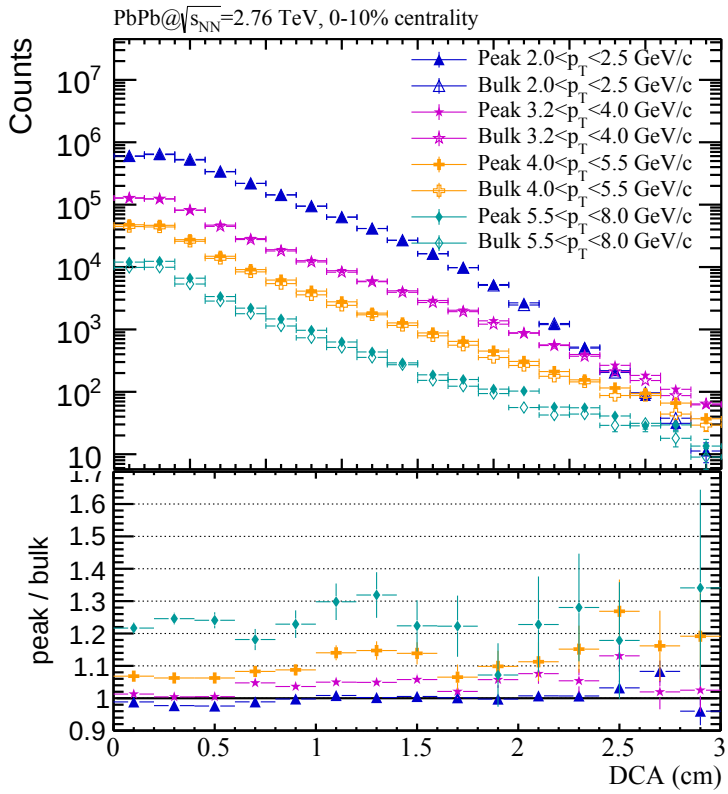
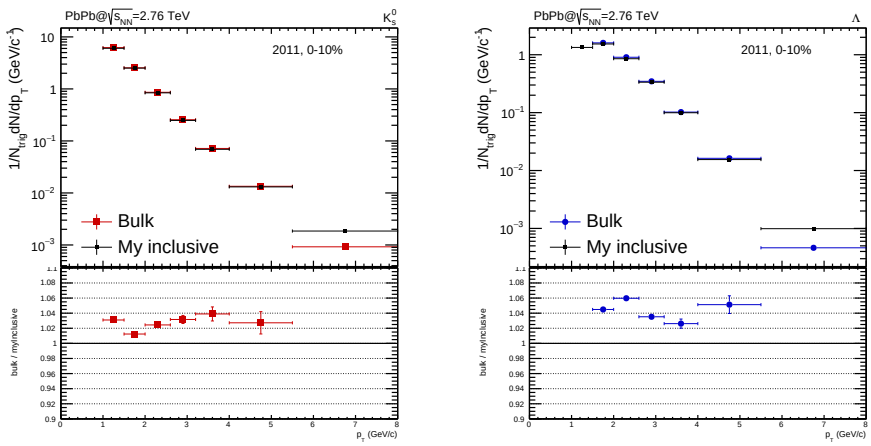


Figure 5.40: DCA_{V0-PV} distribution for $|\Delta m_\Lambda| < 0.0025$ GeV/c^2 in peak and bulk for different p_T bins.

[10] In this p_T-region, the background is low, so such a test is still legitimate.

5.7.5 Corrected Spectra And Ratios

The corrected bulk p_T spectra are shown in Fig. 5.41, where they are compared to the inclusive corrected yields. Here, the inclusive yields are scaled with $1/2\pi$ since they are integrated over φ, whereas the bulk is in $\Delta\varphi$. This comparison is a good cross check, since, at least at low p_T, where the bulk and peak are similar to within a few percent, the bulk yield should be comparable to the inclusive. The fact that the bulk yield is similar to the inclusive within 2-4% suggests that, also for the correlation analysis, all corrections have been done correctly. The last bin between 5.5-8 GeV/c is behaving differently, with the inclusive value much higher than the bulk, due to the requirement that the associated V0 must have a $p_T < p_T^{trig}$, thus selecting less V0s in the p_T region of the trigger particle (starting from 5 GeV/c).



(a) K_S^0 (b) Λ

Figure 5.41: The bulk corrected yields compared to the inclusive yields performed in this analysis.

The jet yield is obtained by subtracting the bulk histogram from the peak histogram, and the Λ/K_S^0 ratio is obtained by dividing the Λ p_T spectrum with the K_S^0 spectrum. This is done for both bulk and jet region. In Fig. 5.42, the Λ/K_S^0 in bulk and jet are shown with a comparison to the ratios obtained if the efficiency- and feed-down corrections are not

applied, i.e. the uncorrected ratios. It is noted that, in the case of the jet, the difference between corrected and uncorrected is small, high-lighting the robustness in extracting the jet. Before discussing the results, the evaluation of the systematic uncertainty will be done.

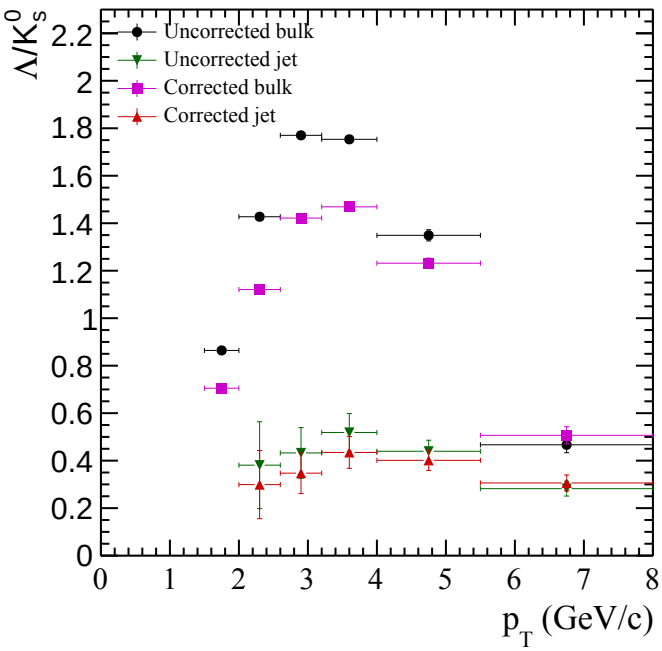
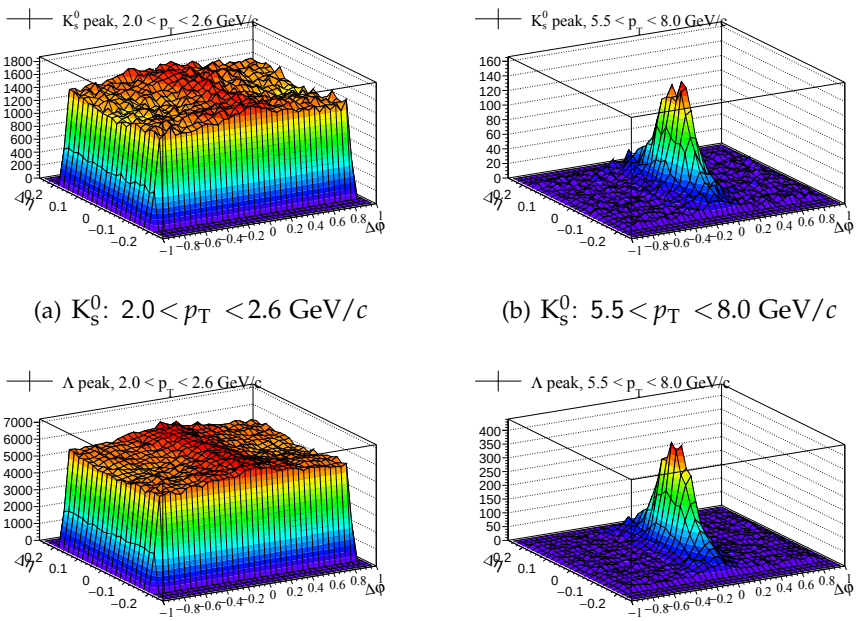


Figure 5.42: Corrected and uncorrected Λ/K^0_s ratios for the bulk and jet (peak-bulk) regions.

5.8 Varying $\Delta\eta$ And $\Delta\varphi$

In this section, an evaluation of the method parameters which are not affecting the systematic uncertainties of the study, but rather the physics performance, is discussed. These parameters are the choice of the $\Delta\eta$ and $\Delta\varphi$ regions. From Fig. 3.8 in Sec. 3.3.2 we know that there is a ridge structure extended in $\Delta\eta$, under the near-side peak, so we cannot be sure that the jet is contained in the nominal choice of $\Delta\eta < 0.2$.

The $\Delta\eta\Delta\varphi$ histograms in Fig. 5.43 show the uncorrected peak region distributions for V0 candidates (note that it is *not* after identification from signal extraction) at nominal values of $\Delta\eta$ and $\Delta\varphi$ for two different p_{T} bins. It shows that the jet at high p_{T} is well defined within the region, while it is difficult to extract any information about the coverage of the region from the low-p_{T} distributions (even though a peak-like behaviour is visible), due to the large bulk contribution. Therefore, a study is performed where the values of $\Delta\eta$ and $\Delta\varphi$ are varied, and the effects can be examined directly from the $\Lambda/\mathrm{K}^0_{\mathrm{s}}$ ratios.



(a) $\mathrm{K}^0_{\mathrm{s}}$: $2.0 < p_{\mathrm{T}} < 2.6$ GeV/c

(b) $\mathrm{K}^0_{\mathrm{s}}$: $5.5 < p_{\mathrm{T}} < 8.0$ GeV/c

(c) Λ: $2.0 < p_{\mathrm{T}} < 2.6$ GeV/c

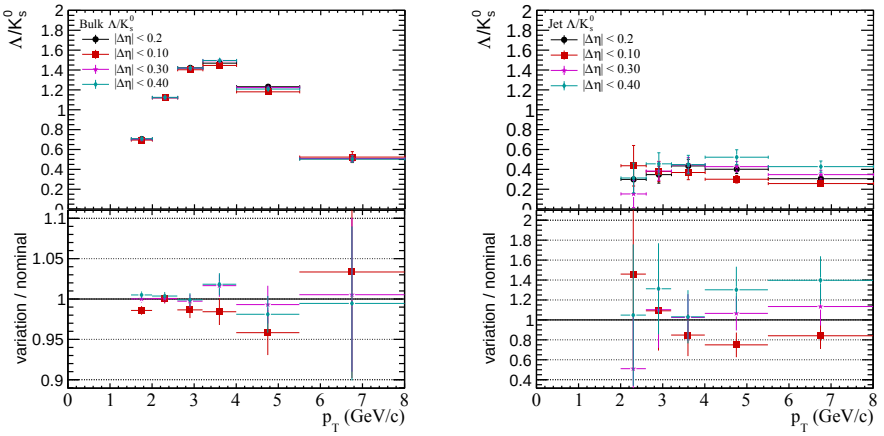
(d) Λ: $5.5 < p_{\mathrm{T}} < 8.0$ GeV/c

Figure 5.43: Peak $\Delta\eta\Delta\varphi$ at nominal values of $\Delta\eta$ and $\Delta\varphi$, for two different p_{T}-regions.

In the $\Delta\eta$ variation study, i.e. where we vary the η-window around η_{trig}, the central η_{trig} exclusion hole is extended to match the $\Delta\eta$ value in according to $|\eta_{\mathrm{trig}}| < \Delta\eta$. The efficiency and weighting function is then recalculated. The main point in this study is that the $\Lambda/\mathrm{K}^0_{\mathrm{s}}$ bulk does not

change with varying $|\Delta\eta|$, see Fig. 5.44(a), which means that there is very little contamination of jet-particles in the bulk.

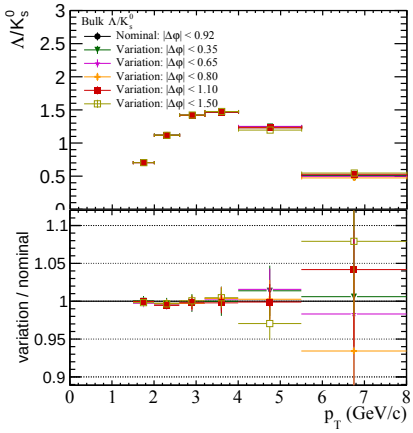
It is also observed that the results for the jet Λ/K^0_S, shown in Fig. 5.44(b), is not very different comparing the nominal value of $|\Delta\eta| < 0.2$ to the variation of $|\Delta\eta| < 0.3$, indicating that the jet size is covered by the nominal cut. When varying $\Delta\eta$ to a tighter value of $|\Delta\eta| < 0.1$, there is a clear overlap of the real jet size and the bulk region.



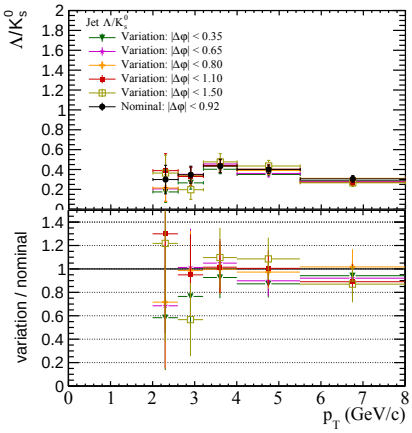
(a) Bulk Λ/K^0_S (b) Jet Λ/K^0_S

Figure 5.44: Varying $\Delta\eta$

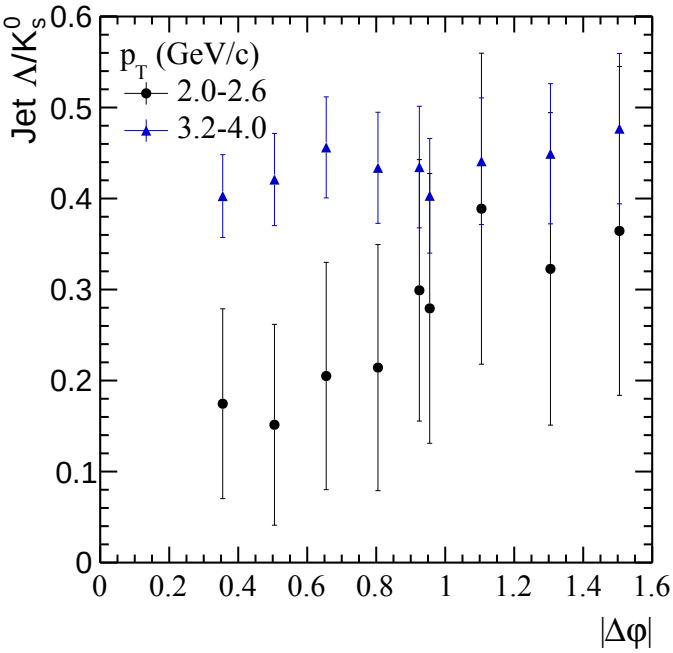
Varying $\Delta\varphi$ from the nominal value of $|\Delta\varphi| < 0.92$ to equally distant steps from $|\Delta\varphi| < 0.35$ up to $|\Delta\varphi| < 1.5$, it is concluded from Fig. 5.45(a) that the $\Delta\varphi$ region has no impact for the bulk, as expected. In the case of the jet, in Fig. 5.45(b), it becomes clear that, at low p_T, cutting on $\Delta\varphi$ reduces the data sample size, and makes the low-p_T bins fluctuate. The question is if this is a systematical increase. For this, a more detailed plot is prepared: jet Λ/K^0_S vs. $\Delta\varphi$ for two different p_T bins, Fig. 5.45(c), and here it is seen that it is *not* a clear monotonous growth. In addition, it is noted that the p_T-dependence of the jet yields differs less at high values of $\Delta\varphi$, compared to lower $\Delta\varphi$, confirming that the choice of $|\Delta\varphi| < 0.92$ is good.



(a) Bulk Λ/K^0_s



(b) Jet Λ/K^0_s



(c) Jet Λ/K^0_s vs. $\Delta\varphi$ for different p_T bins

Figure 5.45: Varying $\Delta\varphi$

5.9 Systematic Uncertainties

While statistical uncertainties express the spread of the results when repeating the *same* experiment — in this context it means to have many collisions of the same sort — the systematic uncertainty is an attempt to quantify the expected results from *different* experiments measuring the same quantity. In this study, it does not refer to changing the experimental settings, but instead to varying the method of particle identification and signal extraction, with the goal to reflect the *range* in which the true result can be located. To perform a study of the systematics, and to assign them to the measured values, is incredibly important when comparing the results to other measurements or models.

In this analysis, the systematic uncertainties are evaluated in three main groups, which are uncorrelated, covering different aspects of the analysis. The first group covers the event- and trigger particle selection criteria, the V0 track cuts belongs to the second group, and the signal extraction procedure is in the third group. In addition, there are systematic uncertainties that do not belong to any of these groups, such as those introduced by the MC corrections. These will be considered separately.

Since the contributions from each group are independent, the total systematic uncertainty is calculated as the quadratic sum of the the contributions from each group, including the MC correction uncertainties as individual contribution to this sum. Both the individual contributions and the total uncertainty will be discussed in the following, as well as summarized in figures and tables.

5.9.1 Uncertainties Associated to Corrections

Feed-down

Before entering the discussion about variation checks, a short summary of the already examined systematic uncertainty is given, all stated in Table 5.4- 5.7. In Sec. 5.7, the feed-down was introduced, and after a feed-down dependent DCA analysis, it was concluded that the inclusive published feed-down will be used, based on arguments that the DCA has the same shape for the peak and bulk regions, and the bulk region must mimic the inclusive behavior. A systematic uncertainty of 5% is applied to the Λ spectra and ratios in order to account for this approximation.

2010-2011 efficiency difference

To handle the 2010-2011 efficiency differences (Sec. 5.3.6), a 6% uncertainty is assigned at spectrum level, while 3% is assigned to the ratios due to partial cancellation of the effect. This is about half of the difference seen in the final Λ/K^0_s ratio when comparing the corrected 2011 analysis with the 2010 and 2011 efficiency, respectively, as seen in Fig. 5.46. It should be noted that this number is only temporary until the final publication.

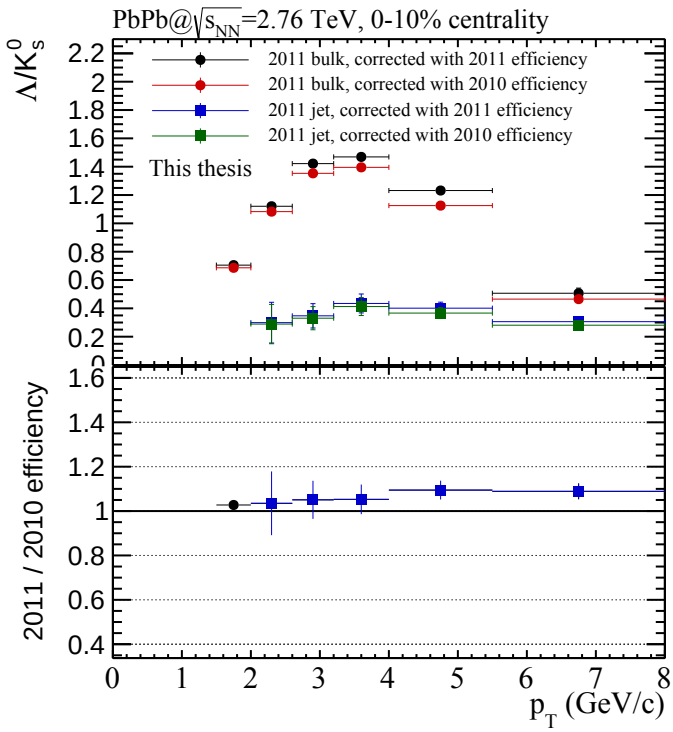


Figure 5.46: A comparison between the 2011 Λ/K^0_s ratio in jet and bulk, corrected with the 2010 and 2011 efficiency respectively.

Material Budget

The systematic uncertainties due to the experimental material budget is inherited from the published inclusive analysis [89, 66], where the maximum value is assumed: 1.5% for K^0_s, and 3.4% for Λ.

5.9.2 Selection Criteria Variations

In this section the systematic study is performed, where applicable, for every "arbitrary" (although motivated) choice made — e.g. event or track cuts, V0 candidate selections, and invariant mass signal extraction region.

It is important to note here, that each variation stands for an execution of the *full* analysis for the specific variation. One parameter at the time is varied, keeping the other parameters at their nominal values. For each separate variation, the efficiency will change. Therefore, the same variation is done in MC to re-calculate the corresponding efficiency.

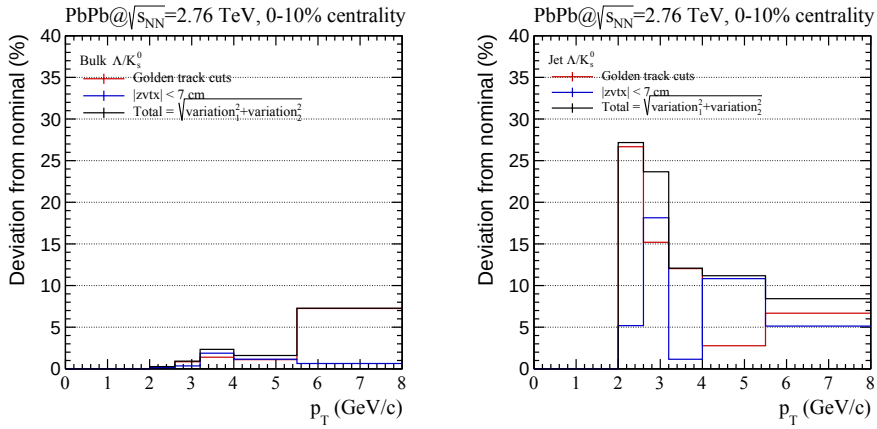
Vertex Region and Trigger Particle Tracks

To evaluate the systematic uncertainty related to the position of the primary vertex in the z-direction, the analysis is run with $|vtx_z| < 7$ cm. With this variation, the particle acceptance is more uniform. In Fig. B.6 (in the appendix), the results can be seen for bulk, peak, and jet spectra. For bulk and peak yields, the effect is only ∼1-3% for both K^0_s and Λ, while for the jet spectra it is 5-10% for K^0_s, and up to 15% for Λ in p_T =3 GeV/c, although decreasing fast towards higher p_T.

Fig. 5.47 shows the results for the Λ/K^0_s ratio. The bulk Λ/K^0_s ratio is very robust, only varying ∼1% with the vertex cut, while the jet Λ/K^0_s is in general more sensitive to variations, here suffering from effects fluctuating between a few percent up to 17% in the 2.6-3.2 GeV/c p_T bin.

A test is performed with a different set of cuts on the trigger particle than the nominal hybrid track cuts described in Sec. 5.5. These sets of cuts are called *Golden Track Cuts*. The main differences from the hybrid track sets are that the DCA_{V0-PV} is tighter, and that hits in the SDD is required instead of hits in the SPD, where the SPD ladders are not working. This results in a non-uniform φ-distribution.

In Appendix B it is seen that (in Fig. B.6), the bulk and peak spectra stay within 2% (except the highest p_T bin for Λ bulk spectra which are affected to 6%) with this variation of trigger particle cuts. The K^0_s jet yield variation is very low, only a few percent, while the Λ jet yield is affected more, around ∼5-15%. The Λ/K^0_s ratio results for this variation can be seen in Fig. 5.47, where, again, the bulk ratio is stable to a few percent, and the jet shows large fluctuations.



(a) Λ/K^0_s bulk (b) Λ/K^0_s jet

Figure 5.47: Systematic deviation for vertex region and trigger particle track.

Selection Cuts

For the selection cuts study, the amount of variation is motivated by a signal loss, and a signal-to-background change, of ∼10%. The variations are summarized in Table 5.3. The total systematic uncertainty in this group is obtained by the maximum deviation in each separate p_T bin. This approach is motivated by the fact that the group contain many individual variations correlated to each other.

Table 5.3: Systematic study of the selection cuts.

Selection	Variation, loose	Variation, tight	Nominal
Event: vtx_z (cm)	–	7.0	10.0
Decay length	$<4c\tau_{PDG}$	$<2c\tau_{PDG}$	$<3c\tau_{PDG}$
Cosine of pointing angle	–	>0.9995	>0.9980
Arm.-Pod. for K^0_s	$p_T^{arm} < 0.25\lvert\alpha\rvert$	$p_T^{arm} < 0.15\lvert\alpha\rvert$	$p_T^{arm} < 0.2\lvert\alpha\rvert$
Decay radius (cm)	$2.0 < r_T^{dec} < 150.0$	$8.0 < r_T^{dec} < 90.0$	$5.0 < r_T^{dec} < 100.0$
DCA_{d-PV} (cm)	–	>0.2	>0.1
DCA_{d-d} (cm)	<0.5	–	<1.0

The sensitivity of the results when varying the parameters one by one

are examined by observing the deviation of the results from the nominal value. The comparison with the nominal results are done at fully corrected K^0_s and Λ spectra separately, and then for the bulk and jet Λ/K^0_s ratio, i.e. the systematic uncertainties are not propagated from the spectra to the ratio, but determined individually. The efficiency to the corresponding variation is re-evaluated with every change of parameter. The results can be seen in Fig. B.7 in the Appendix, and Fig. 5.48 shown here.

Tightening the lower limit of the cosine of the pointing angle from 0.998 to 0.9995 results in a bulk and peak spectral change of 1-5% for K^0_s, and up to 14% effect on the low-p_T Λ peak and bulk spectra, although the jet spectra for both K^0_s and Λ are roughly similar, and not exceeding 10% – as for the bulk and jet Λ/K^0_s.

Concerning the life time cut, $c\tau$, it is both tightened ($<2c\tau_{PDG}$) and loosened ($<4c\tau_{PDG}$) with respect to the nominal value ($<3c\tau_{PDG}$). This gives an almost negligible effect on the K^0_s bulk and peak spectra (except the highest p_T bin in the bulk spectra, where the effect of both the tight and loose cut is $\sim$5%), while the effect of the tight cut on Λ bulk and peak spectra is 5-10%, largest at low p_T. On the jet spectra, the effect fluctuates around 5% for both K^0_s and Λ, except for Λ in $2.6 < p_T < 3.2$ GeV/c where the deviation from the nominal value is as large as 20%. In the bulk Λ/K^0_s, the $c\tau$ cut gives one of the dominating systematic uncertainties in the low-p_T region where the values differ 5-10% from the nominal, while it is not the dominating – although significantly contributing – effect in the jet Λ/K^0_s with its 5-15%.

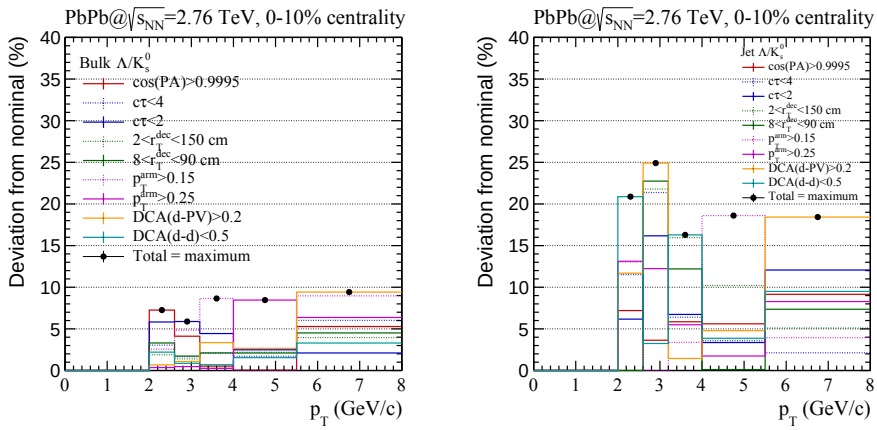
Varying the decay radius to a tight ($8 < r^{dec} < 90$ cm) and loose ($2 < r^{dec} < 100$ cm) value with respect to the nominal ($5 < r^{dec} < 100$ cm) contributes to a maximum 5% effect on the K^0_s and Λ bulk and peak spectra, and slightly higher (5-10%) in the jet spectra and Λ/K^0_s ratios (for both K^0_s and Λ particle specie).

The distance of closest approach from the daughter track to the primary vertex, DCA_{d-PV}, has a nominal minimal value of 0.1 cm. For a systematic study this limit is varied to a tighter value of 0.2 cm, producing peak and bulk spectra with a maximum deviation of 5% (the highest deviation at high p_T) with respect to the nominal spectra, showing a slightly higher effect in the Λ spectra compared to K^0_s. The jet spectra and Λ/K^0_s for the bulk experience effects of 5-10%, and the jet Λ/K^0_s show a fluctuating change with values ranging from a few percent up to a dominating

20-25% effect.

Tightening the DCA between the daughter tracks, DCA_{d-d}, from being within 1.0 cm to 0.5 cm will reject V0 candidates that are not close. However, the small changes of the spectra show that most of the daughter particles must be very close in space. The change in the peak and bulk spectra is only a few percent, while for the K^0_s jet spectra and bulk Λ/K^0_s it is about 5%, and a fluctuating 5-15% for Λ jet spectra and jet Λ/K^0_s.

The additional cut for K^0_s is the Armenteros-Podolanski cut of $p_T^{arm} < 0.2|\alpha_{arm}|$ which is varied to a tighter value of $p_T^{arm} < 0.15|\alpha_{arm}|$ and a looser value of $p_T^{arm} < 0.25|\alpha_{arm}|$. This is the dominating effect (mostly coming from the loose variation) on the K^0_s peak and bulk spectra with a $\sim$ 7% change, and 5-20% uncertainty on the jet spectra. At mid-p_T this is still the dominating effect for the Λ/K^0_s.



(a) Λ/K^0_s bulk (b) Λ/K^0_s jet

Figure 5.48: Systematic deviation for V0 cut variations.

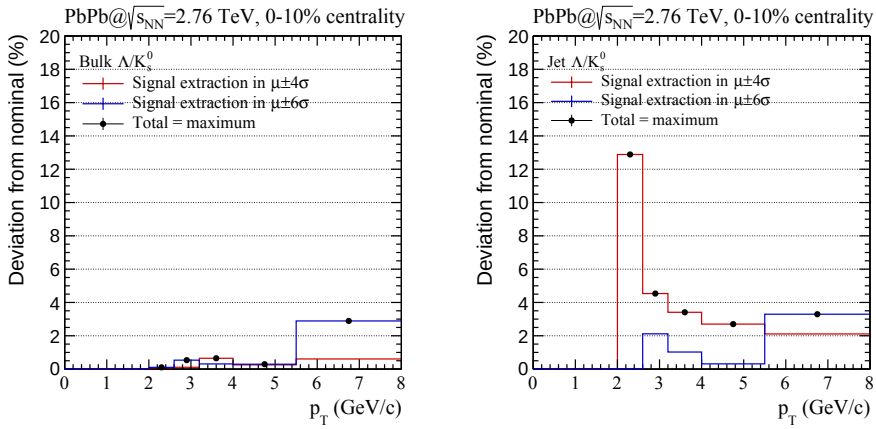
Signal Extraction

Errors related to the signal extraction are estimated by varying the bin counting region in which the signal is obtained. This is done from the nominal value of $\mu \pm 5\sigma$ to $\mu \pm 4\sigma$ and $\mu \pm 6\sigma$. The spectra obtained by the variation can be seen in Fig. B.8 where it is clear that the effect is $<1\%$ for peak and bulk spectra, and $\sim$ 5% for K^0_s jet spectra, and 5-10% in the

Λ jet spectra case.

The effect on the Λ/K^0_S ratio is seen in Fig. 5.49, where it is concluded that the bulk Λ/K^0_S is not suffering from deviations in the signal extraction region, except for the very last bin where it has an effect of 3% for the loose region case. The jet Λ/K^0_S, however, experiences a deviation (dominated by the tight extraction region) from the nominal region up to 10% for the lowest bin, but is kept within 5% for the other p_T bins.

The total systematic uncertainty in this group is set as the maximum deviation, indicated by a black point in the histograms.



(a) Λ/K^0_S bulk (b) Λ/K^0_S jet

Figure 5.49: Systematic deviation for varying signal extraction.

5.9.3 Total Systematic Uncertainties

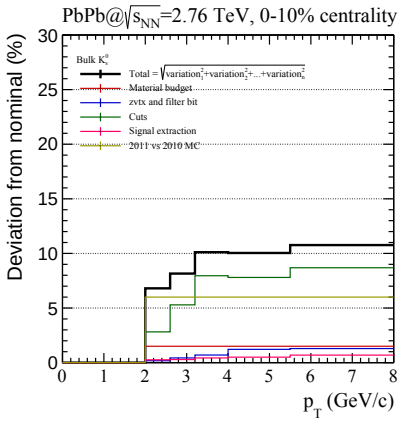
The overall systematic uncertainty assigned to the p_T spectra was constructed as a quadratic sum of the total value for each contributing group, assuming that these sources are not correlated. In Fig. 5.50 and 5.51, the total systematic uncertainties are calculated and summarized in Table 5.4-5.7.

For the K^0_S and Λ peak and bulk spectra, the smallest contribution to the systematic uncertainties is the signal extraction region. For K^0_S peak and bulk spectra the total uncertainty is ~10%, with a slight increase towards higher p_T, and where the largest contribution is from the cut varia-

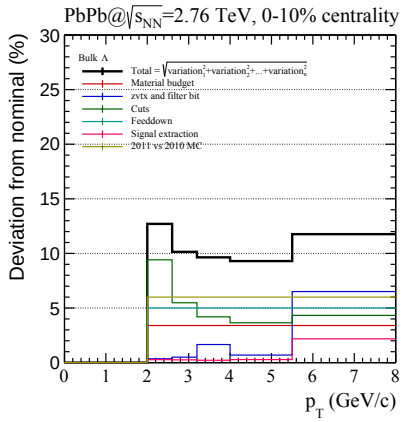
tion and 2010-2011 efficiency differences. In the Λ peak and bulk spectra, the dominating effects are the same as for K^0_s, but with the additional feed-down contribution of 6%. The p_T-dependence of the total uncertainty is reverse, i.e. higher at low p_T, where it reaches $\sim$16%, and then decreases to $\sim$10%.

In the jet K^0_s and Λ spectra, the total systematic uncertainty is fluctuating between 10 and 30%, with the dominating uncertainties arising from the vtx_z and trigger particle definition, and the cut variations.

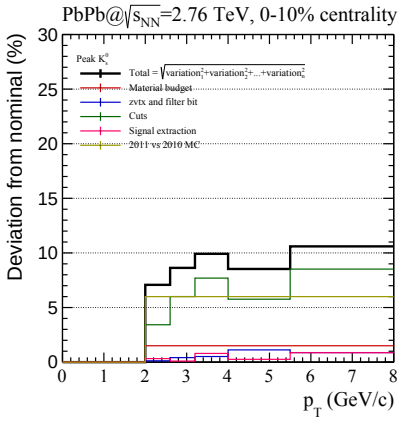
For the Λ/K^0_s evaluation, the bulk has a systematic variation between 10 and 15%, which is similar to the systematic uncertainties in the published inclusive results. The jet Λ/K^0_s varies from 20-40%.



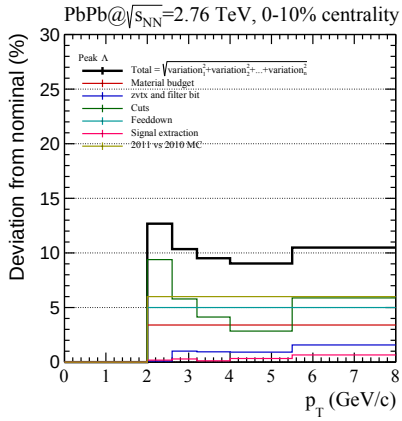
(a) K^0_s bulk



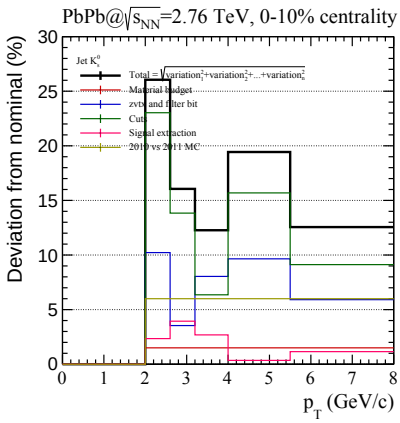
(b) Λ bulk



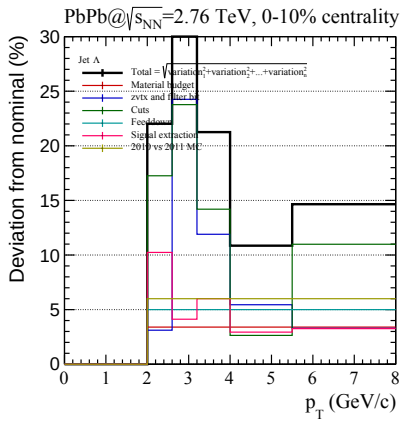
(c) K^0_s peak



(d) Λ peak

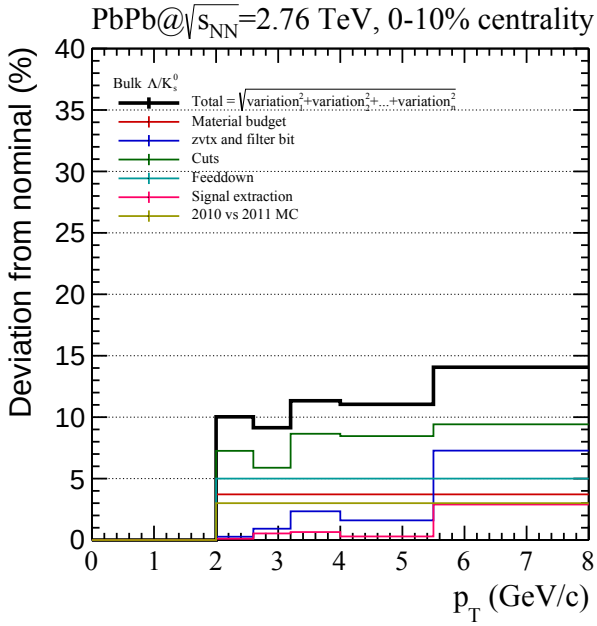


(e) K^0_s jet

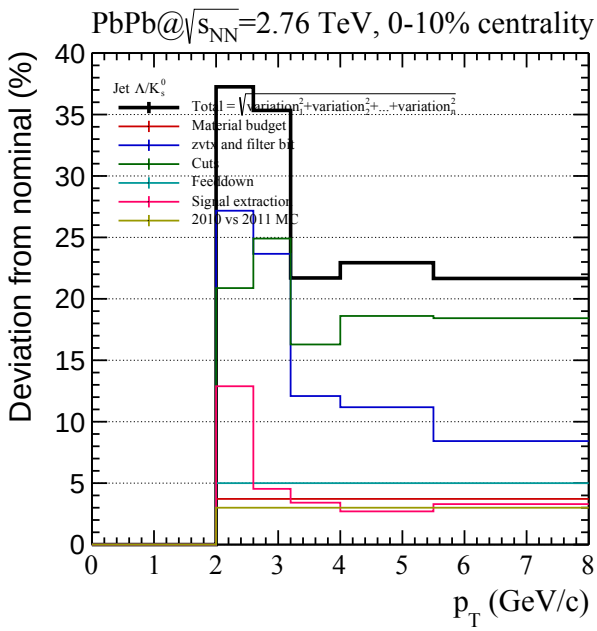


(f) Λ jet

Figure 5.50: Total systematic uncertainty.



(a) Λ/K^0_s bulk



(b) Λ/K^0_s jet

Figure 5.51: Total systematic uncertainty.

Table 5.4: Total systematic uncertainties for K^0_s bulk and peak yields.

Group	K^0_s bulk yield (%)						K^0_s peak yield (%)					
p_T (GeV/c) →	1.5-2.0	2.0-2.6	2.6-3.2	3.2-4.0	4.0-5.5	5.5-8.0	1.5-2.0	2.0-2.6	2.6-3.2	3.2-4.0	4.0-5.5	5.5-8.0
Material budget	1.5	1.5	1.5	1.5	1.5	1.5	1.5	1.5	1.5	1.5	1.5	1.5
zvtx and filter bits	0.4	0.2	0.4	0.7	1.2	1.3	0.2	0.1	0.4	0.5	1.1	0.9
Cuts variation	5.7	2.8	5.3	8.0	7.8	8.7	5.7	3.4	6.0	7.7	5.8	8.5
Signal extr.	0.2	0.3	0.3	0.4	0.5	0.7	0.2	0.3	0.1	0.8	0.3	0.9
2010-2011 diff.	6.0	6.0	6.0	6.0	6.0	6.0	6.0	6.0	6.0	6.0	6.0	6.0
$\sqrt{}$Quadratic sum	0.0	6.8	8.2	10.1	10.0	10.8	0.0	7.1	8.6	9.9	8.5	10.6

Table 5.5: Total systematic uncertainties for Λ bulk and peak yields.

Group	Λ bulk yield (%)						Λ peak yield (%)					
p_T (GeV/c) →	1.5-2.0	2.0-2.6	2.6-3.2	3.2-4.0	4.0-5.5	5.5-8.0	1.5-2.0	2.0-2.6	2.6-3.2	3.2-4.0	4.0-5.5	5.5-8.0
Material budget	3.4	3.4	3.4	3.4	3.4	3.4	3.4	3.4	3.4	3.4	3.4	3.4
zvtx and filter bits	0.4	0.3	0.5	1.7	0.7	6.5	0.3	0.1	1.0	0.9	0.9	1.6
Cuts variation	13.8	9.4	5.5	4.2	3.7	4.3	13.4	9.4	5.8	4.1	2.8	5.9
Signal extr.	0.3	0.3	0.3	0.2	0.3	2.2	0.2	0.2	0.3	0.1	0.3	0.7
Feed-down	5.0	5.0	5.0	5.0	5.0	5.0	5.0	5.0	5.0	5.0	5.0	5.0
2010-2011 diff.	6.0	6.0	6.0	6.0	6.0	6.0	6.0	6.0	6.0	6.0	6.0	6.0
$\sqrt{}$Quadratic sum	0.0	12.7	10.1	9.6	9.3	11.8	0.0	12.7	10.4	9.5	9.0	10.5

Table 5.6: Total systematic uncertainties for K^0_s and Λ jet yields.

Group	K^0_s jet yield (%)					Λ jet yield (%)				
p_T (GeV/c) →	2.0-2.6	2.6-3.2	3.2-4.0	4.0-5.5	5.5-8.0	2.0-2.6	2.6-3.2	3.2-4.0	4.0-5.5	5.5-8.0
Material budget	1.5	1.5	1.5	1.5	1.5	3.4	3.4	3.4	3.4	3.4
zvtx and filter bits	10.2	3.5	8.0	9.7	5.9	3.1	24.3	11.9	5.4	3.3
Cuts variation	23.0	13.8	6.4	15.7	9.1	17.3	23.8	14.2	2.6	11.0
Signal extr.	2.3	3.9	2.7	0.4	1.2	10.2	4.1	6.0	2.9	3.3
Feed-down	0.0	0.0	0.0	0.0	0.0	5.0	5.0	5.0	5.0	5.0
2010-2011 diff.	6.0	6.0	6.0	6.0	6.0	6.0	6.0	6.0	6.0	6.0
$\sqrt{}$Quadratic sum	26.0	16.1	12.3	19.4	12.6	22.0	35.3	21.3	10.9	14.7

Table 5.7: Total systematic uncertainties for bulk and jet Λ/K^0_s ratios.

Group	Bulk Λ/K^0_s (%)					Jet Λ/K^0_s (%)				
p_T (GeV/c) →	2.0-2.6	2.6-3.2	3.2-4.0	4.0-5.5	5.5-8.0	2.0-2.6	2.6-3.2	3.2-4.0	4.0-5.5	5.5-8.0
Material budget	3.7	3.7	3.7	3.7	3.7	3.7	3.7	3.7	3.7	3.7
zvtx and filter bits	0.3	0.9	2.3	1.6	7.3	27.2	23.7	12.1	11.2	8.4
Cuts variation	7.3	5.9	8.6	8.5	9.4	20.9	24.9	16.3	18.6	18.4
Signal extr.	0.1	0.5	0.6	0.3	2.9	12.9	4.5	3.4	2.7	3.3
Feed-down	5.0	5.0	5.0	5.0	5.0	5.0	5.0	5.0	5.0	5.0
2010-2011 diff.	3.0	3.0	3.0	3.0	3.0	3.0	3.0	3.0	3.0	3.0
$\sqrt{}$Quadratic sum	10.0	9.1	11.3	11.0	14.1	37.3	35.3	21.7	22.9	21.7

"I don't have a song stuck in my head, no, no — I have the keyboard sound of 'new TBrow -tab' stuck in my head; it goes: bompabombompom bom."
(20 Oct 2015)

Chapter 6

Results

The inclusive Λ/K^0_s ratio was shown in Sec. 3.4.4, followed by a discussion concerning the hadron production mechanism behind the baryon-to-meson enhancement seen at intermediate p_T, which, in Pb–Pb is understood in the coalescence and/or hydrodynamic flow picture.

This thesis presents the novel η-reflection method, in which it is possible to subtract the bulk from the peak region to obtain a jet-like contribution in order to disentangle different hadronization processes, to investigate if the origin of the baryon-to-meson anomaly is due to parton fragmentation (hard) or collective effects (soft). The bulk is chosen such that it should not contain any contribution from either the near-side jet, or the opposite away-side jet.

Let me repeat the language defined in Sec. 5.1. The peak region is in the direction of a high-p_T trigger particle, with a p_T threshold of 5 GeV/c — well above the soft processes. The assumption is that this trigger particle is the leading particle in a jet. The bulk region is chosen in a direction as far away as possible from the regions with momentum conservation effects relative to the trigger particle, i.e. we use instead the same azimuthal direction, but opposite pseudo-rapidity compared to the trigger particle. Assuming that the particle production is symmetric with respect to η =0, we have an estimate of the bulk contribution in the peak region. Subtraction of the bulk from the peak contribution should then reveal the contribution correlated with the trigger particle, i.e. the jet.

In this chapter, the results obtained with this analysis method, of the K^0_s and Λ yields, and Λ/K^0_s ratio, associated with a trigger particle, will

be presented. Furthermore, the K^0_S and Λ yields and ratios for the underlying bulk events, i.e. the V0s not associated with any hard scattering, are reported.

Before going into the discussion about the results, I want to make a small language disclaimer. The term *jet* is often used here and in other texts. Strictly speaking, the only thing one knows experimentally is that there has been a number of particles with momenta exceeding those of soft production, and obeying some geometrical restrictions (they have to be close in momentum space). In QCD, a jet is the result of a hard scattering between partons giving rise to a large momentum transfer. In heavy ion collisions the momentum balance can normally not be established. Hence, comparing results using different jet definitions is not straightforward. It is an experimental observable, and it depends on the cuts made. We have chosen to make very loose cuts on which particles to include in the jet. We even allow transverse momenta which are well inside the reach for the soft processes. In all cases, when talking about a jet, we mean the measured quantity.

6.1 The K^0_S and Λ Bulk, Peak and Jet Yield

In Fig. 6.1 the corrected K^0_S and Λ peak and bulk trigger-associated yields for 0-10% central Pb–Pb collisions at $\sqrt{s_{NN}}$ =2.76 TeV are shown, with both systematic and statistical uncertainties indicated. The minimum p_T value of the trigger particle is 5.0 GeV/c, and the trigger particle has to point to the primary vertex, i.e. it is not part of the V0 sample.

It is seen that the peak and bulk spectra are similar at low p_T, while at higher values of p_T, the peak spectra are flatter than the bulk spectra. The shapes are expected to differ due to the different dominating hadronization mechanism; the thermal nature of the soft bulk, and the presence of hard fragmentation hadronization related to a jet. Figure 6.1 also shows the spectra of the jet associated with a trigger particle with $p_T > 5$ GeV/c. The jet spectrum is obtained by subtracting the bulk spectrum from the peak.

It is observed that the jet spectra are much harder than the bulk. The jet spectrum is almost 2 orders of magnitude lower than the bulk at low p_T, but higher than the bulk at high p_T. The integral of the jet spectrum is

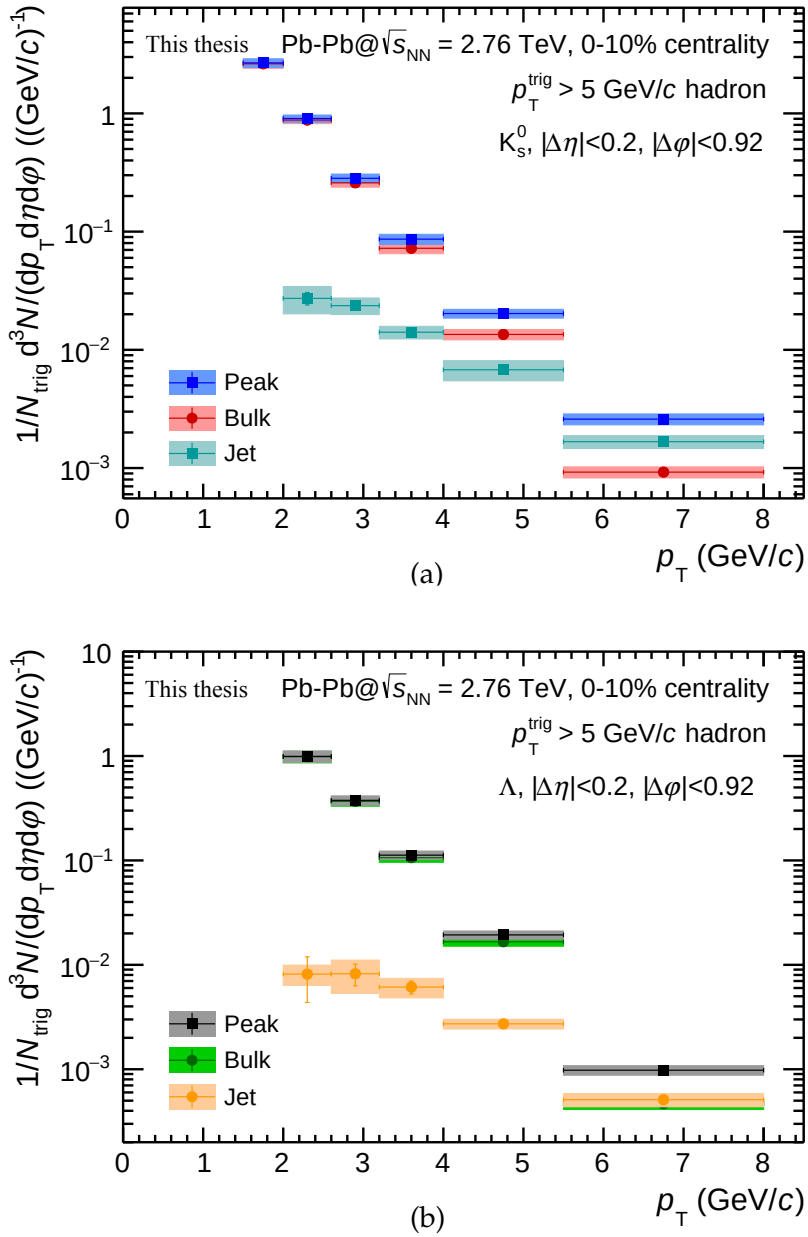


Figure 6.1: Corrected bulk, peak and jet yields as a function of p_{T}, for (a) $\mathrm{K}^0_{\mathrm{s}}$, and (b) Λ, with the 2011-recorded Pb–Pb collisions at the center-of-mass energy $\sqrt{s_{\mathrm{NN}}}$ =2.76 TeV, in the 0-10% centrality bin. Full statistical (bars) and systematic (boxes) uncertainties are applied.

about 1% of the integral of the bulk spectrum. Without being able to lead this in evidence, it appears to be a reasonable order of magnitude ratio between hard scattering and bulk particle production. With this result, we have shown that the η-reflection procedure is able to separate out a hard jet component all the way down to $\sim$2 GeV/c, even though the jet contribution is very small.

6.2 The Λ/K^0_s Ratio

Having established a clear kinematical difference between jet and bulk, similar for Λ and K^0_s, and finding that the jet spectra are much harder than the bulk, we now continue to study the particle production in the two categories.

Using the K^0_s and Λ bulk and jet spectra, the Λ/K^0_s ratio in central (0-10%) Pb–Pb collisions at $\sqrt{s_{NN}}$ =2.76 TeV is constructed for the two regions of interest, seen in Fig. 6.2, where the green markers represent the bulk, and the red markers represent the jet. The bars and boxes are statistical and systematic uncertainties, respectively. For comparison, included in the same figure, are the inclusive Λ/K^0_s ratios extracted with this analysis (blue crosses). In addition, the published inclusive Λ/K^0_s ratio measured in proton-proton collisions (magenta open squares) at $\sqrt{s}$ =7 TeV (note the higher energy) is shown in the figure.

The aim of illustrating the relative production of K^0_s with respect to Λ, i.e. the Λ/K^0_s ratio, in the different regions of the QGP, is to detach the two known hadron production mechanisms — the thermal production (soft production, related to the bulk) and fragmentation (hard production, related to a jet) — and the processes associated with them. By doing this, the origin of the baryon-to-meson anomaly seen in central Pb–Pb collisions can hopefully be derived.

Many comparisons and physics conclusions can be drawn from this ratio, and will be discussed in the following:

1. The bulk Λ/K^0_s ratio in central Pb–Pb collisions is strongly enhanced compared to the jet ratio
2. The bulk Λ/K^0_s ratio is similar to the inclusive ratio in Pb–Pb in the same centrality class
3. The jet Λ/K^0_s ratio in central Pb–Pb collisions shows no enhancement compared to the ratio in minimum bias pp collisions (at $\sqrt{s}$ =7 TeV) — in fact, the ratios are similar

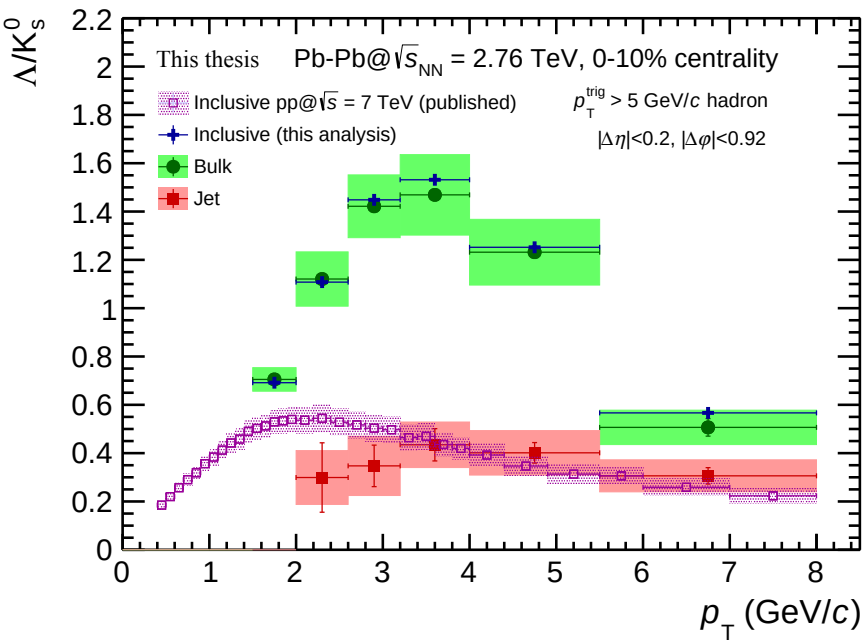


Figure 6.2: Λ/K^0_s ratio for bulk and jet as a function of p_T from 2011-recorded Pb–Pb collisions at the center-of-mass energy $\sqrt{s_{NN}}$ =2.76 TeV, in the 0-10% centrality bin. Full statistical (bars) and systematic (boxes) uncertainties are applied.

First of all, the fact that the bulk Λ/K^0_s ratio in central Pb–Pb collisions is enhanced with a factor of 3 at p_T =3.5 GeV/c compared to the jet ratio, indicates that there indeed *is a large difference* in the relative production of K^0_s and Λ, going from the bulk to the jet-like region. In the same centrality (in this case 0-10%), the bulk ratio mimics the inclusive ratio to a good approximation.

As discussed in Sec. 3.5, the enhancement could be an effect of the presence of an additional parton recombination hadronization mechanism, where low-p_T bulk quarks coalesce, leading to a larger production of baryons than mesons. There are two different recombination models that could cause this: the soft and the hard recombination, where the recombination in the soft model only occurs for thermal radially flowing partons [64], while the hard model accounts for recombination between jet fragments and partons from the medium *or* other jets. The results presented favor the soft recombination model.

The more intriguing result, however, is the Λ/K^0_s ratio associated with the high-p_T trigger particle representing the jet region, hence associated to the parton fragmentation hadronization mechanism. As seen in Fig. 6.2, the ratio is approaching the inclusive Λ/K^0_s seen in pp collisions. This result suggests that the particle production in a jet is not affected very much by the medium created in Pb–Pb collisions. The two lowest bins are deviating slightly from this observation, showing a value which is slightly lower than the pp results.

It should be noted that the pp Λ/K^0_s ratio is *inclusive*, and not differentiated in a specific jet- and underlying event region. It is clear that the ratio in pp undergoes a maximum at the intermediate p_T range, just as in Pb–Pb data. The maximum is however lower than in Pb–Pb. If this is due to a flow-like boost of heavier particles also in pp remains to be understood. In pp collisions, the underlying events could be corresponding to the multi-parton interactions, which, according to recent studies [62], could posses collective properties. One can then question if the inclusive pp Λ/K^0_s ratio is a valid reference for the comparison with the jet differentiated Λ/K^0_s results in Pb–Pb collisions. A deeper understanding of the pp results is required, and a more thorough analysis with a differentiation in hard processes (jet) and "bulk" in pp Λ/K^0_s ratio has to be done.

An analysis of the pp differentiated jet and bulk Λ/K^0_s ratio was initiated with the η-reflection method in this thesis, but not finalized due to

time constraints. However, the preliminary results are shown in Fig. 6.3(a) for both $\sqrt{s}$ =2.76 and 7 TeV, using corrected (with respect to efficiency and feeddown) K^0_S and Λ bulk and jet yields, but without a systematic uncertainty evaluation. The preliminary results show that there is a difference between the jet and the underlying event. It appears that the difference between the jet in Pb–Pb, and the ratio in minimum bias pp collisions, is due to the underlying event in the pp result.

With these results, one can conclude that, by separating the underlying events from the jet-like structures, the baryon-to-meson enhancement seems to be an effect arising in the underlying event in Pb–Pb, thus originating from the collective, soft, hadronization processes, while the jet-like contributions appear to be unmodified compared to the fragmentation of a vacuum jet.

A p–Pb study was also initiated with the η-reflection method, and preliminary results for Λ/K^0_S are shown in Fig. 6.3(b) for $\sqrt{s}$ =5.02 TeV, although using uncorrected (with respect to efficiency and feeddown) K^0_S and Λ bulk and jet yields, and without a systematic uncertainty evaluation. In order to evaluate the size of the effect of using uncorrected spectra on the ratios, a study in the Pb–Pb system comparing the uncorrected and corrected jet Λ/K^0_S ratio, see Fig. 5.42, shows that the final corrected *jet* result is similar to the uncorrected, which makes us believe that the first uncorrected jet results from p–Pb are reasonably close to what the final corrected ratios will be.

"...just added "Make new TODO-list" to my TODO-list. Every-day-life-sadness." (23 Sep 2015)

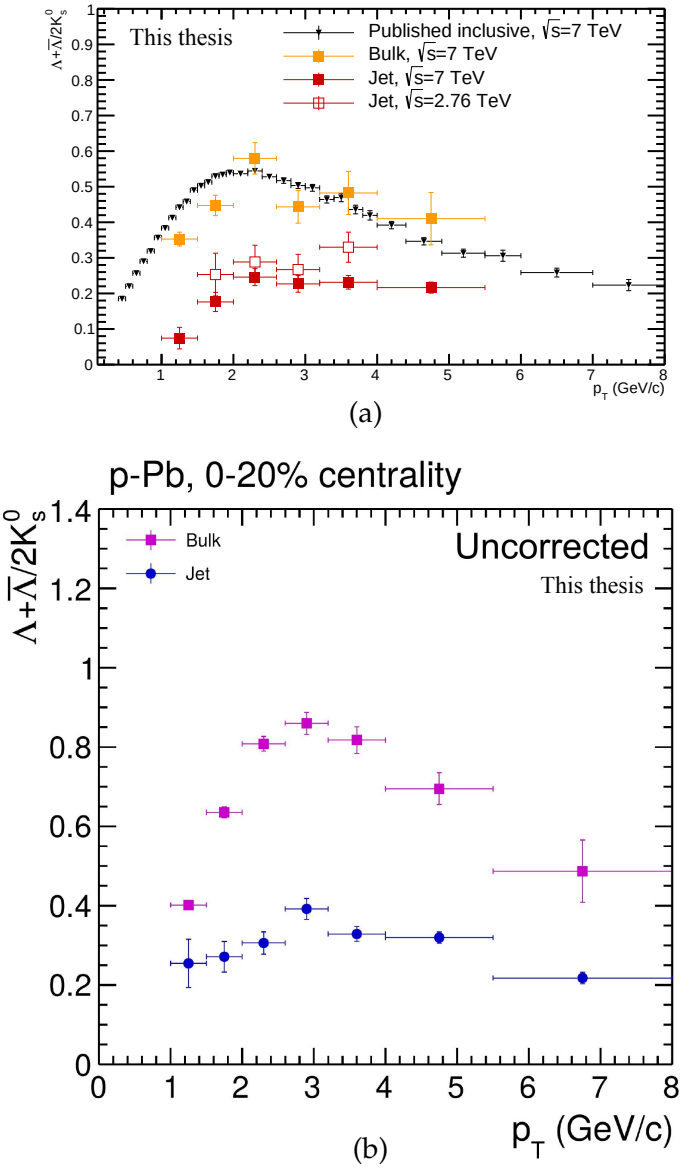


Figure 6.3: (a) Uncorrected preliminary $\Lambda/\mathrm{K}^0_\mathrm{s}$ ratio in jet and bulk for minimum bias pp collisions at $\sqrt{s}$ =2.76 and 7 TeV. (b) $\Lambda/\mathrm{K}^0_\mathrm{s}$ ratio in bulk and jet with the η-reflection method (carried out in this thesis) for 0-20% highest multiplicity p–Pb collisions at $\sqrt{s_{\mathrm{NN}}} = 5.02\,\mathrm{TeV}$.

Chapter 7

Discussion and Conclusion

7.1 Surface bias

The result that the hadronic composition of jets in heavy ion collisions composition is similar to vacuum jets, raises the question if the jets observed are from hard scatterings on the surface, and we in fact observe escaping jets which then should be unaffected by the medium.

For jet quenching it is still not understood what fraction of the $R_{\mathrm{AA}} << 1$ is caused by energy loss so that a final jet with reduced energy is observed, and what fraction is caused by absorption where jets are fully absorbed. These two cases are important for how we interpret the results. In the case of energy loss dominance, supposedly the jet sample selected by the trigger condition selects an ensemble of jets with varying degrees of energy loss, and since the average energy loss is large (R_{AA} is small), we can conclude that energy loss does not significantly affect the chemistry in the jet. If absorption is dominant, then we could have the situation where we mainly observe the jets from hard scatterings close to the surface, which then should be unaffected by the medium. With this hypothesis, the results of the bulk and jet $\Lambda/\mathrm{K}^0_{\mathrm{s}}$ analysis presented in Sec. 6.2 would have to limit the conclusions to the first two bullets, i.e. that the relative production of $\mathrm{K}^0_{\mathrm{s}}$ and Λ differ in the hard processes compared to the underlying event processes, and that the baryon-meson anomaly seems to come from the physics of the bulk.

In the following the question of a surface bias will be discussed based on the current understanding from theory and experiment.

7.1.1 Theoretical Considerations

Recent theoretical studies performed in [90] with the JEWEL MC event generator [91, 92] "strongly suggest" (quoting the article) that the path length dependence of the di-jet asymmetry, i.e. the momentum imbalance between a leading ("near-side") and a sub-leading ("away-side") jet pair, observed in central Pb–Pb collisions when studying jet quenching, is a *sub-leading* effect. This study claims that the surface bias is presumably significantly smaller than naively suggested. The di-jet asymmetry is instead dominated by fluctuations arising from e.g. recoil radiation and energy loss fluctuations, with only a small contribution from the relative path length difference.

Two scenarios are studied, one where the full geometry is considered, meaning that the location of di-jet production in the collision volume is distributed according to the Glauber model distribution of binary collisions, and one where the production of di-jets is limited to the center of the nuclear collision volume such that the path lengths are the same. It is seen that the difference between the asymmetry in the two cases is small, thus showing that the surface bias is small in this model.

The path-lengths for the leading and sub-leading jets are calculated from the di-jet production point. The distribution of the path-length difference ($\Delta L = L_{away} - L_{near}$) in this study is shown in Fig. 7.1, together with distributions obtained in single-inclusive jet ("leading jet") events fulfilling the cuts for a leading jet in a di-jet event, but with no reconstructed sub-leading jet. The small shift towards positive path length difference, meaning that L_{away} is slightly larger than L_{near}, demonstrates a mild preference of longer path lengths for the away-side (sub-leading) jet, but this effect is not large. The study shows that only "34% of the leading jets has longer path-length" [90].

7.1.2 Experimental Considerations

The charged particle yield associated with a high-p_{T} trigger particle ($8 < p_{\mathrm{T}} < 15$ GeV/c) has been measured in Pb–Pb at $\sqrt{s_{\mathrm{NN}}} = 2.76$ TeV in ALICE [93], where the per-trigger yields are extracted from azimuthal di-hadron correlations. From the azimuthal angle difference (between the trigger particle and the associated particles) dependence of the yield, it is observed that the away-side gives a non-negligible contribution, seen in

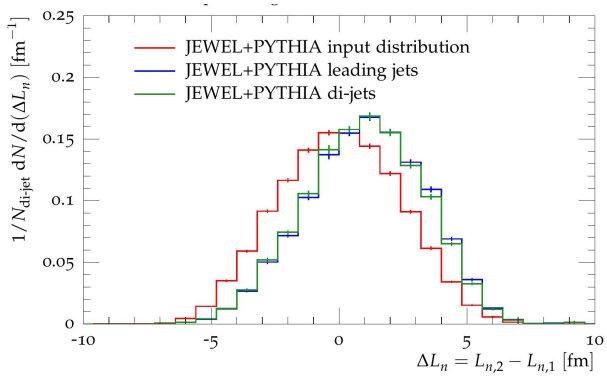


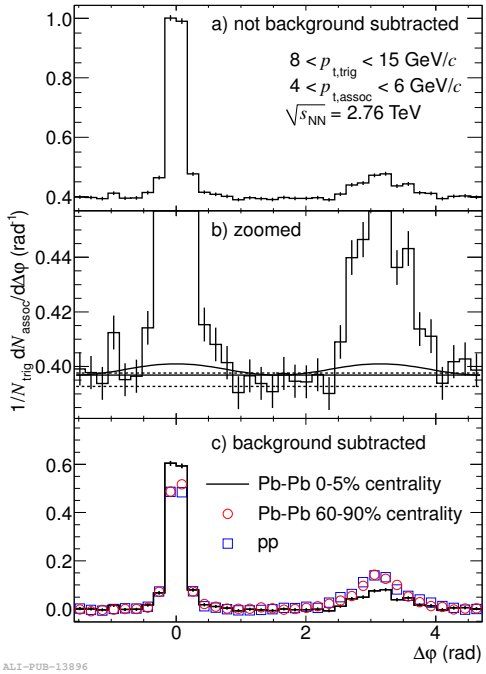
Figure 7.1: Comparison of differences in path-lengths between leading and subleading jet (red), leading jets (blue), and di-jets (green). Figure taken from [90].

Fig 7.2(a). This implies that the away-side jet is not *completely* quenched, and, relating to the surface bias discussion important for the analysis in this thesis, the leading particle in an away-side jet is also likely to pass the selection cuts for the trigger particle, thus giving a contribution of jets that are not created on the surface, but has actually traversed the medium.

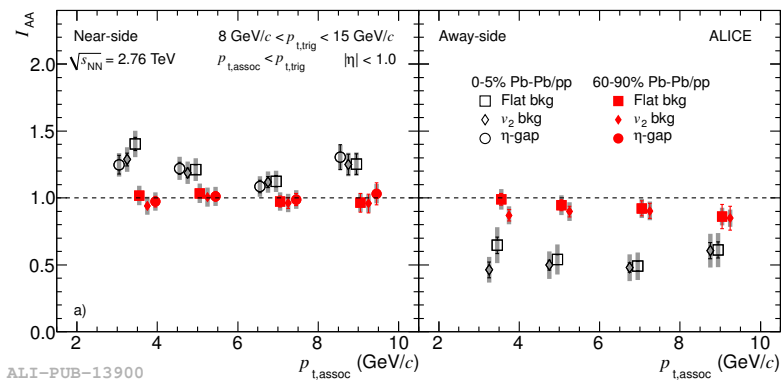
The I_{AA} shown in Fig. 7.2 [93] is constructed by comparing the yields obtained in Pb–Pb collisions to the yields in pp collisions at the same energy, thus revealing jet in-medium energy loss (similar to R_{AA} for single particles). In the 0-5% most central collisions, the away-side I_{AA} (open black symbols) shows a suppression of $\sim$40% compared to pp collisions, indicating that there is a sizable probability that the recoiling parton survives the passage through the medium, and could be part of the particles we trigger on. Furthermore, the near-side I_{AA}, telling us about the fragmenting jet leaving the medium, show an *enhancement* of 20-30%[1], meaning that this is also affected by the medium. The important information to keep in mind for the sake of the surface bias discussion, is that even though we trigger on the near-side jet, these also traverse the medium to some extent, and cannot be argued to fully come from the surface.

In addition to the I_{AA} studies supporting a non-negligible in-medium

[1]The enhancement is argued in [93] to arise from a softening of the fragmentation function by the medium, making hadrons carry a smaller fraction of the initial parton momentum. Therefore, hadrons will originate from a parton with a larger average momentum, leading to more associated particles.



(a) Corrected per-trigger pair yield for central and peripheral Pb–Pb collisions, and pp collisions, the lowest panel showing the background subtracted yields.



(b) I_{AA} for central (0-5% Pb–Pb/pp, open black symbols) and peripheral (60-90% Pb–Pb/pp, filled red symbols) collisions. Results using different background subtraction schemes are presented. The shaded bands denote systematic uncertainties.

Figure 7.2: Figures taken from [93].

modification of the near-side jet, CMS has studied isolated-photon+jet correlations in Pb–Pb collisions [94]. Since photons do not interact strongly with the medium, they don't lose energy while traversing it (their R_{AA} is found to be ∼1 [95]), thus the transverse momentum of the photon can be used to estimate the p_{T} of the associated parton jet, and a precise energy loss of the parton can be estimated. In the context of the surface bias discussion this measurement is important since we know that the triggered photons do not suffer any surface bias, hence neither do the measurements of the associated jets. In Fig. 7.3 the $\mathrm{R}_{J\gamma}$, i.e. the average fraction of isolated photons ($p_T^{\gamma} > 60$ GeV/c) with an associated jet above 30 GeV/c is shown as a function of $\mathrm{N}_{\mathrm{part}}$. It is seen that $\mathrm{R}_{J\gamma}$ for central Pb–Pb collisions (high $\mathrm{N}_{\mathrm{part}}$) show a suppression compared to the peripheral collision, the pp reference, and MC calculation, but is significantly *above zero*. This tells us that only a limited fraction (maximum ∼50%, since if a jet loses energy and goes below 30 GeV/c, it will also be considered as missing) of the jets are absorbed for central Pb–Pb collisions, and the rest comes out as a measurable jet, no matter where in the medium (surface or bulk) they are created.

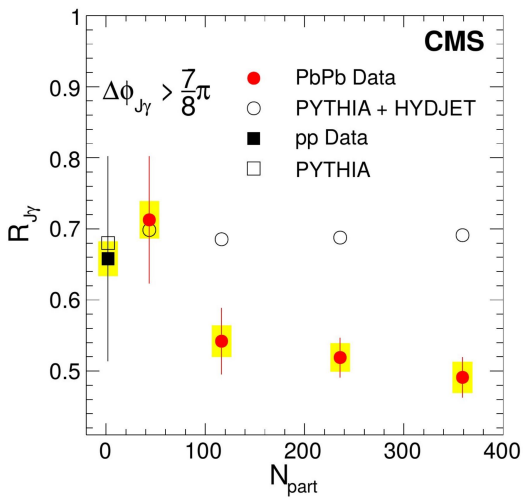


Figure 7.3: Average fraction of isolated photons with an associated jet above 30 GeV/c, $\mathrm{R}_{J\gamma}$, as a function of $\mathrm{N}_{\mathrm{part}}$. The yellow boxes indicate point-to-point systematic uncertainties and the error bars denote the statistical uncertainty. Figure and caption taken from [94].

7.2 The Λ/K^0_s Ratio Compared To Other Results

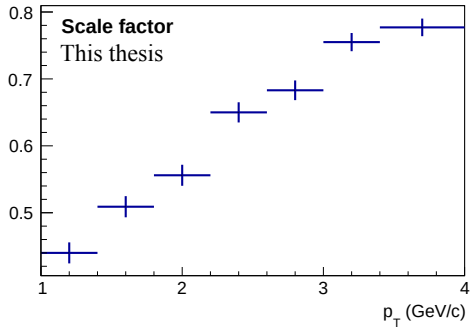
Other results addressing similar physics questions are important to compare to. The K^0_s jet yield is here compared to the charged kaon ($K^{\pm}$) jet spectra (only the low-p_T end of the presented K^0_s spectra) obtained by a similar two-hadron angular correlation study, performed within the ALICE Collaboration, using protons and pions as associated particles [83]. It is not a trivial comparison since the $K^{\pm}$ analysis uses a circular peak region with a σ dependent radius, $3\sigma(p_T)$, while the peak region in the η-reflection analysis is constant and larger in $\Delta\eta\Delta\varphi$. To be able to compare the jet spectra from the different analyses, the $K^{\pm}$ spectrum is scaled down to match the yield as if the η-reflection jet region was used. This is done for each p_T bin, generating $\Delta\eta\Delta\varphi$ from a two-dimensional Gaussian, with a width from the following polynomial (the analysis is described in [83])

$$\sigma(p_T) = 0.544 - 0.193p_T + 0.0244p_T^2$$

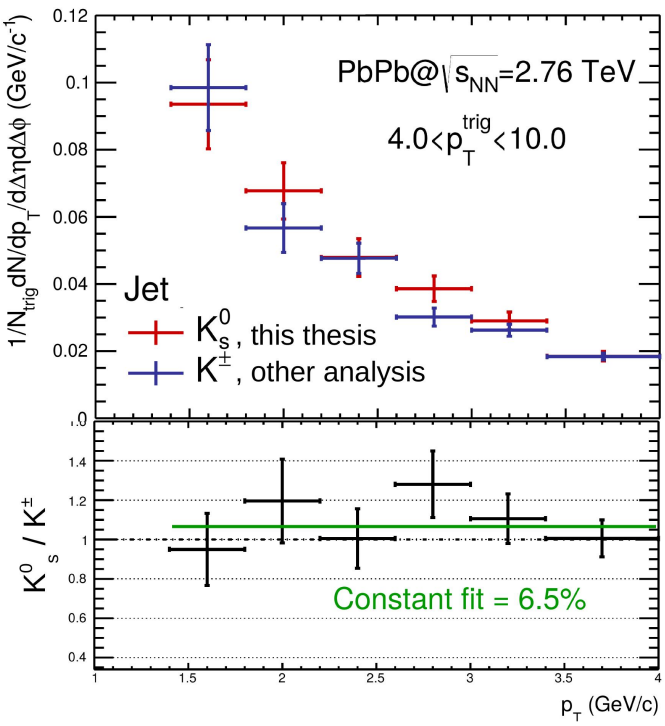
If the $\Delta\eta\Delta\varphi$ falls within the η-reflection definition of the region, it is accepted, and the scale factor, seen in Fig. 7.4(a), is then formed by dividing the accepted with the generated. The agreement between the different jet spectra is within the systematic uncertainties.

In the same two-particle angular correlation study of the p/π ratio in a jet-like region around a trigger particle, presented in [83], and shown in Fig. 7.5, a similar conclusion as for the Λ/K^0_s study presented in this thesis can be drawn, namely that the baryon-to-meson ratio in the jet is not enhanced, but in fact comparable to the ratio measured in pp collisions. This result strengthens the physics message concluded from the analysis carried out in this thesis, i.e. that the enhancement originates from the bulk region, suggesting that it is driven by collective behavior in the medium. It is however worth mentioning that the ratio is much larger for Λ/K^0_s than for p/π, although Λ and K^0_s are closer in mass than p and π. This difference might be attributed to the strange quark content of Λ and K^0_s.

In the p–Pb study carried out in [88], and shown in Fig. 7.6(a), charged particle jets are reconstructed on an event-by-event basis using an anti-k_T algorithm with resolution parameter R = 0.2, 0.3, or 0.4, and requiring one charged track with $p_T > 10$ GeV/c. The Λ and K^0_s yields are measured within the jet cone and corrected for the underlying event before the ratio is constructed. When the ratio is compared to the inclusive ratio, the



(a) Scale factor



(b) K^0_S and $K^{\pm}$ jet yield

Figure 7.4: Comparing K^0_S and $K^{\pm}$ jet yields for trigger particles in $4.0 < p_T^{\text{trig}} < 10$ GeV/c.

same conclusion can be drawn even for this collision system; the baryon-to-meson enhancement originates from the bulk, and is not present in the jet structure. A surprise, however, is that such a bulk system exists in proton induced reactions; the flow-like behaviour of small systems is an area of intense study. This conclusion is also supported by new results from studying similar phenomena in PYTHIA8 simulated pp collisions [96], which can be used in order to separate soft and hard processes by identifying events with large and low numbers of multi-parton interactions. This result is also shown in Fig. 7.5 as the blue line.

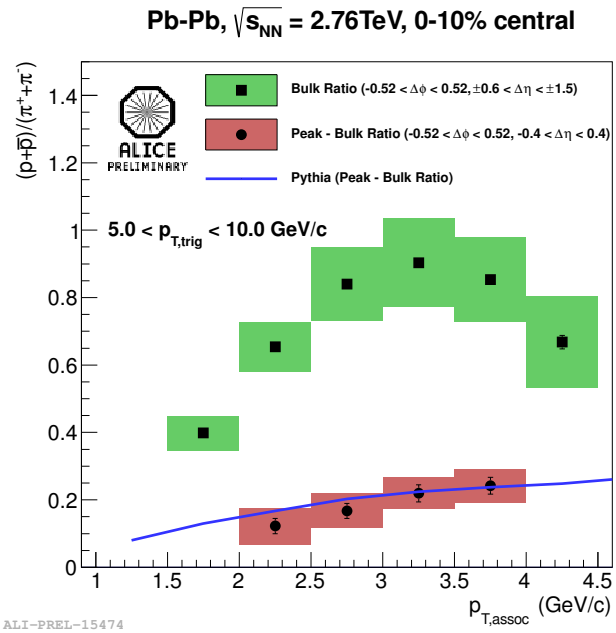
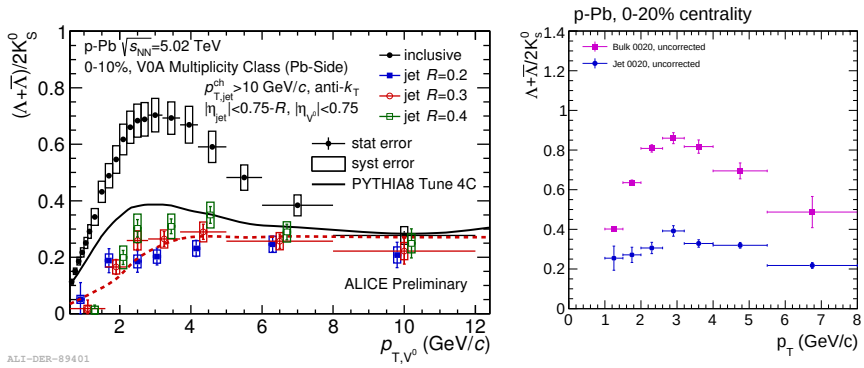


Figure 7.5: p/π ratio as a function of associated particle p_{T}, in bulk and peak-bulk for 0-10% central Pb–Pb collisions at $\sqrt{s_{\mathrm{NN}}} = 2.76\,\mathrm{TeV}$, with a leading (trigger) particle p_{T} between $5 - 10\ \mathrm{GeV}/c$ [96].

Although much work remains until the p–Pb results from the η-reflection method are final, one can say that, based on the comparison between the corrected and the uncorrected result in Fig. 5.42, the final results will not deviate much from the present, and they are likely to be consistent with the results in Fig. 6.3(b) (also shown in Fig. 7.6(b), to be able to compare



(a) Jet reconstruction analysis (b) This thesis

Figure 7.6: (a) Λ/K^0_s ratio in jet with different radii reconstructed with the anti-k_T method compared to PYTHIA8 and the Pb–Pb inclusive ratio (full black circles) for 0-10% highest multiplicity p–Pb collisions at $\sqrt{s_{NN}} = 5.02\,TeV$ [88]. (b) Λ/K^0_s ratio in bulk and jet with the η-reflection method for 0-20% highest multiplicity p–Pb collisions at $\sqrt{s_{NN}} = 5.02\,TeV$, originally showed in Fig. 6.3(b), but shown again for comparison.

with the results shown in Fig. 7.6(a)). It should be noted that since in the p–Pb case one does not have symmetry around η =0, possibly effects that are not observed in symmetric systems may come into play.

7.3 Summary of Observations and Conclusions

7.3.1 Physics Conclusions

The summary of the observations made from the final results of the Λ/K^0_s ratio in the bulk and jet region in central Pb–Pb collisions, and the physics conclusions one can draw from these results, are presented in the following bullet points.

- It has been possible to disentangle the spectra of K^0_s and Λ in a soft and a hard component, associating the soft component with the hadronization bulk medium, and the hard component with fragmentation following hard scattering

- The bulk Λ/K^0_s is enhanced compared to the jet ratio, indicating that the relative production of K^0_s and Λ differs in the hard processes compared to the underlying bulk event processes, which are those of the expanding strongly interacting system

- The bulk Λ/K^0_s is similar to the inclusive ratio in Pb–Pb, giving the message that the dominating particle production mechanism is that of the bulk, and one possibility could be parton recombination at intermediate p_T

- The jet Λ/K^0_s in central Pb–Pb collisions is similar to the ratio in minimum bias pp collisions, suggesting that there is no striking modification within the jet due to the medium, and a preliminary analysis of bulk and jet regions in pp shows great similarity between jets in pp and Pb–Pb

- The previous observations lead to the final conclusion, which is that the baryon-to-meson enhancement seen in inclusive central Pb–Pb collisions originates from bulk effects

7.3.2 Method Conclusions

In addition to these physics messages obtained from the results, part of the goal of this thesis was to develop and test a completely new correlation technique to extract the jet from a large underlying event contribution in heavy ion collisions, where traditional jet reconstruction suffers from this large bulk effect (especially at low p_T), and standard correlation methods suffer from complications in the mixed events corrections and flow subtractions.

Here, we make use of the fact that the bulk is well defined and smeared out by the thermalization. However, it is not enough to assume that it is possible to randomly subtract the bulk found in one part of the medium from the peak in another part of the medium due to the different flow contributions. In a standard correlation technique, the flow components have to be taken into account and corrected for.

We expect that geometry driven flow is approximately boost invariant event-by-event in the mid-rapidity region, but fluctuates in azimuth. In the η-reflection method, we make a careful choice of the bulk region with

respect to the peak region in each case we have a trigger particle, to make sure that the flow contribution is the same in both regions. This is done by sampling both the peak and bulk regions in the same azimuthal angle, but exactly opposite pseudo-rapidity window to catch the same flow.

A number of cross checks has been performed to validate the method, and in addition, the final p_{T}-distributions show that the method is robust, and we can extract jet (and bulk) spectra for $\mathrm{K}^0_{\mathrm{s}}$ and Λ down to 2 GeV/c to study the strange particle composition in bulk and jet. The method has been approved internally in ALICE by the Physics Board, and a publication of the results is ongoing.

7.4 Outlook

The analysis procedure has been presented in detail, and many closure tests and cross-checks have been done. In some cases it is clear that further studies are needed, e.g. for estimating the feed-down from Ξs in the jet region, and the 2010-2011 MC efficiency difference, but in these cases conservative systematic uncertainties have been assigned to make sure that the final results will be consistent. The analysis method and the results have already been approved by the ALICE collaboration, and the publication of the results presented in this thesis is expected within the year of 2016.

With better statistical precision in Run2 the associated V0 particles can be extended down to lower p_{T} ($<$2 GeV/c), which will be interesting to do especially for the jet $\Lambda/\mathrm{K}^0_{\mathrm{s}}$. In addition, a study where the $p_{\mathrm{T}}^{\mathrm{trig}}$ has a higher threshold value than 5 GeV/c would be a valuable study, and has in fact already started.

An increase in statistics would also open up for a study in different centrality bins to see if the bulk $\Lambda/\mathrm{K}^0_{\mathrm{s}}$ enhancement is less pronounced, as for the inclusive case, and if the jet $\Lambda/\mathrm{K}^0_{\mathrm{s}}$ stays at the same level. This would strengthen the indication that the jet is indeed not modified by the medium. However, to be able to fully conclude on the jet $\Lambda/\mathrm{K}^0_{\mathrm{s}}$ similarities with pp collisions, the jet and bulk differentiated analysis in pp must be finalized with its systematic uncertainty evaluated. Furthermore, the p–Pb results need to be properly corrected for efficiencies and feed-down. An ideal case would of course be to perform the analysis in the three dif-

ferent collision systems at the same collision energy to rule out effects caused by differences in center-of-mass energies, and instead by the system size itself. In the light of ALICE recent results of collectivity in smaller collision systems, even the underlying event behavior in these systems is of great interest, since the large jet bias is presumably reduced.

"Igår gick jag in på konsum med inställningen att köpa precis vad jag önskade för att klara ev helgen – och INTE kolla på priset. Jag bad till och med den i kassan att inte säga summan högt (oj vad hon fnissade, stackars typartonåring). Idag är mina drygt 2 kg (15 förpackningar!) färska importerade säkert genmodifierade hallon och blåbär slut. Nu kollar jag på kvittot. Jäklar vad den här avhandlingen var dyr." (23 Apr 2016)

Appendix A

The Inclusive Analysis

A.1 Anti-Lambda

In the analysis performed in this thesis, both the inclusive and the η-reflection correlation analysis, the $\bar{\Lambda}$ is not included due to the discrepancy seen in the yields between Λ and $\bar{\Lambda}$, shown in Fig. A.1. This discrepancy is also seen in other ALICE analyses [65], and is currently being investigated.

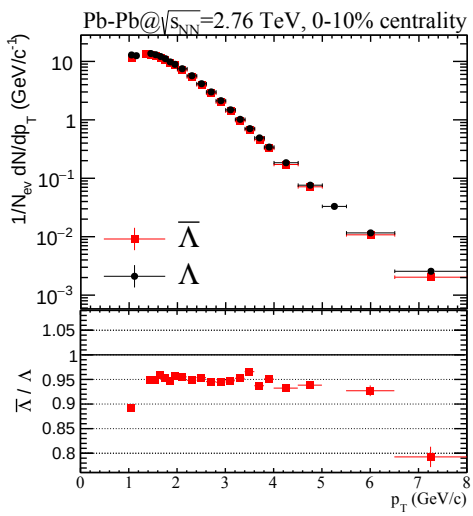


Figure A.1: $\bar{\Lambda}/\ \Lambda$ ratio measured in 2011 Pb–Pb at $\sqrt{s_{\mathrm{NN}}} = 2.76$ TeV, 0-10% centrality.

A.2 2010 vs. 2011 MC difference

In Fig. A.2, the efficiency in positive and negative pseudo-rapidity is computed, excluding that the 2010-2011 efficiency anomaly is due to an unbalance in pseudo-rapidity.

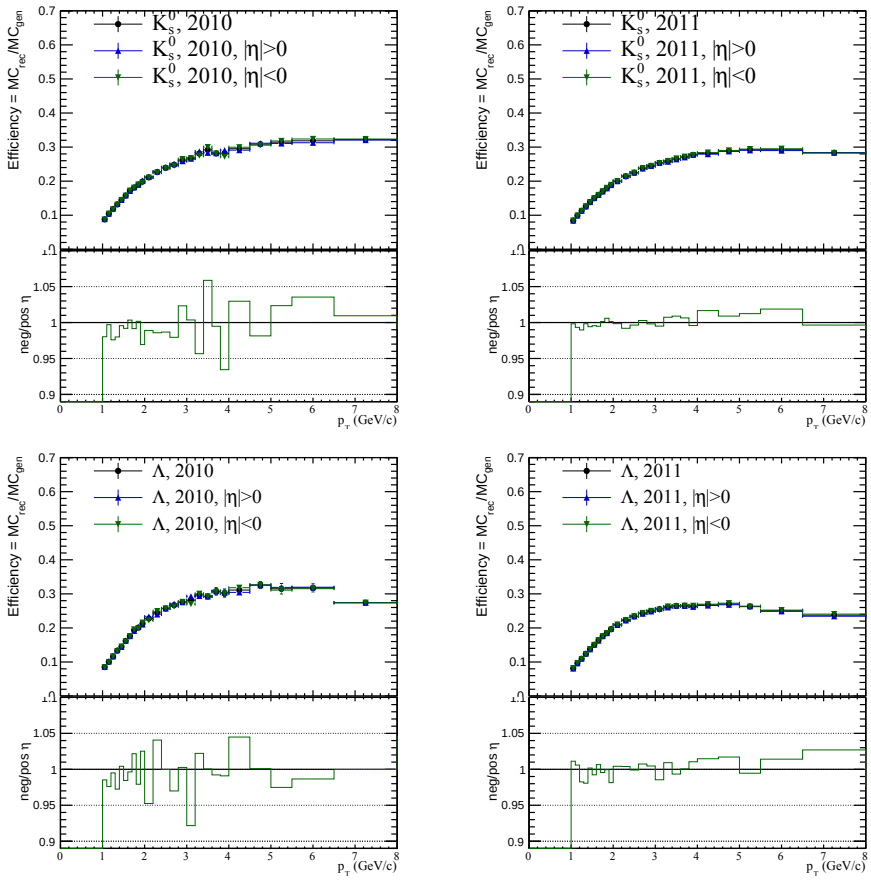


Figure A.2: 2010 and 2011 periods 0-10% Pb–Pb efficiencies for K^0_s and Λ comparing $\eta < 0$ and $\eta > 0$.

Appendix B

The η-reflection Correlation Analysis

B.1 Invariant Mass Distributions and Fits

The invariant mass distributions and fits for all p_{T} bins for the η-reflection analysis can be seen in Fig. B.1–B.4.

B.2 Injected MC Efficiency

Since the HIJING generator tends to underestimate the number of strange particles compared to that created in real collisions, additional strange particles were injected at $\mathrm{MC_{gen}}$ level. A cross check is made to confirm that the injected particles in the MC are not affecting the efficiencies. The comparison is made with and without injected particles, and can be seen in Fig. B.5(a)–B.5(b). No difference is observed.

B.3 Systematic Uncertainties for Spectra

In Sec. 5.9, the systematic variation is shown on the $\Lambda/\mathrm{K_s^0}$ ratio level. Here the variations for the peak, bulk and jet yield are shown in Fig. B.6–B.8. They are discussed in the main text (Sec. 5.9).

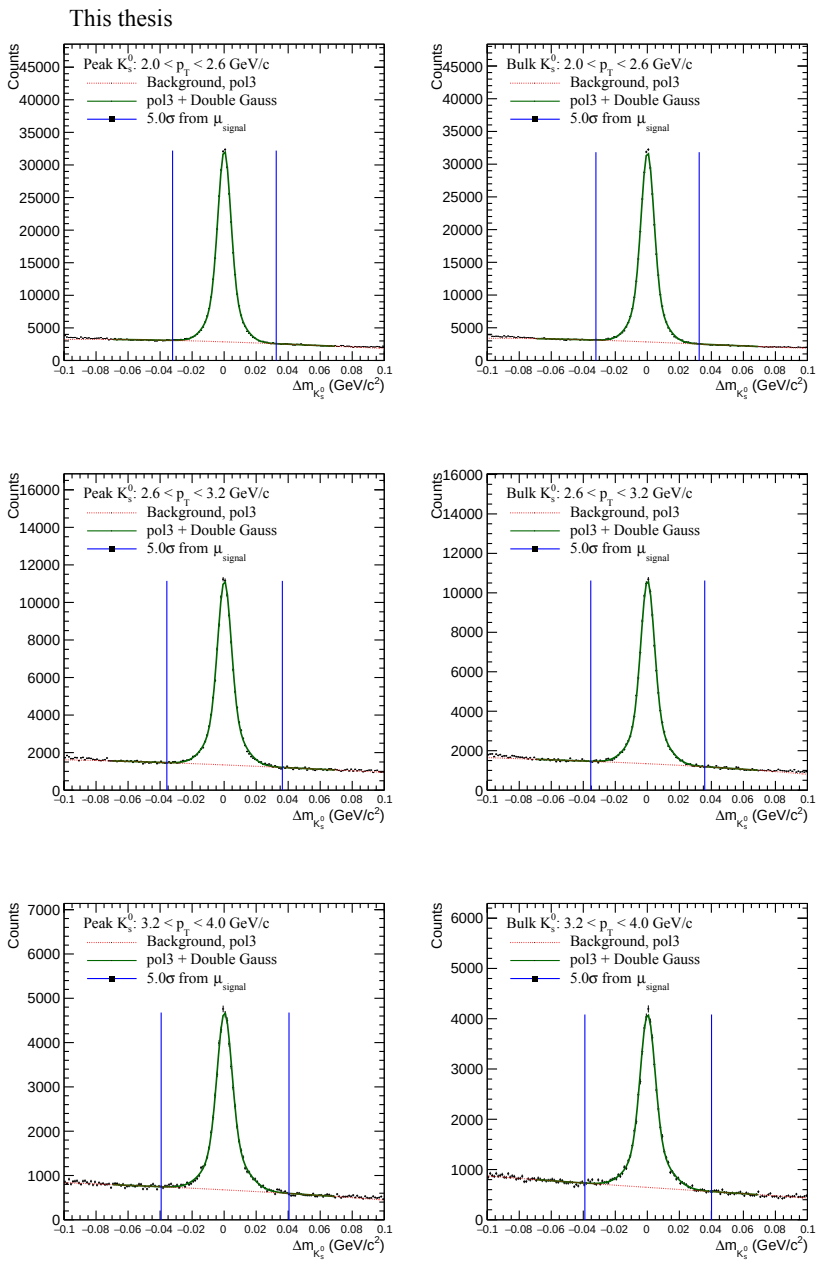


Figure B.1: K^0_s invariant mass distributions and fits for different p_T bins: 2.0-2.6, 2.6-3.2, 3.2-4.0 GeV/c.

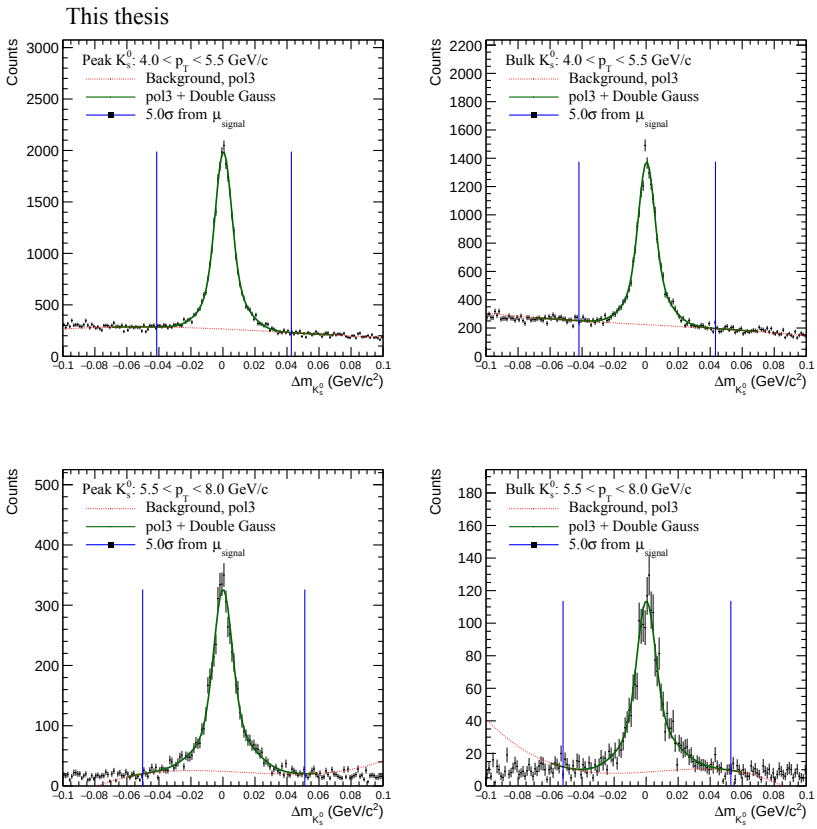


Figure B.2: K^0_s invariant mass distributions and fits for different p_T bins: 4.0-5.5, 5.5-8.0 GeV/c.

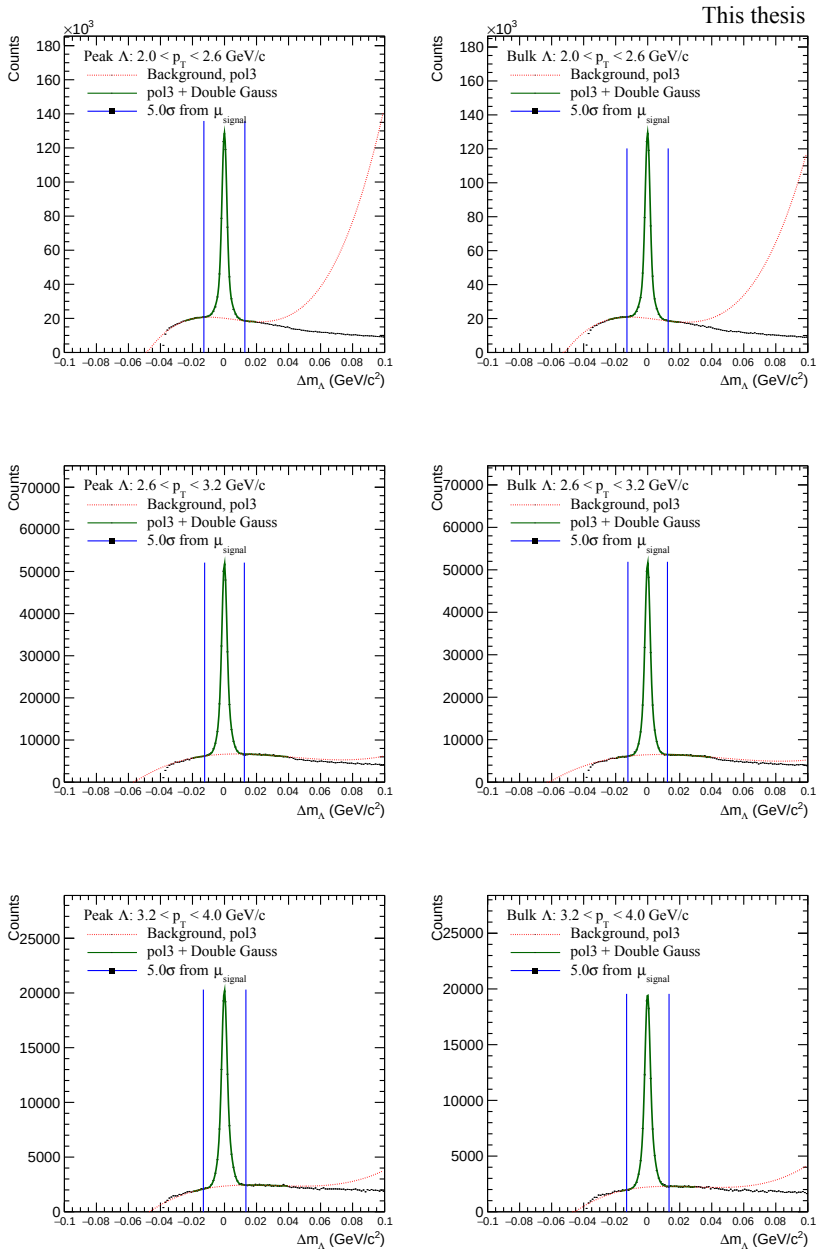


Figure B.3: Λ invariant mass distributions and fits for different p_{T} bins: 2.0-2.6, 2.6-3.2, 3.2-4.0 GeV/c.

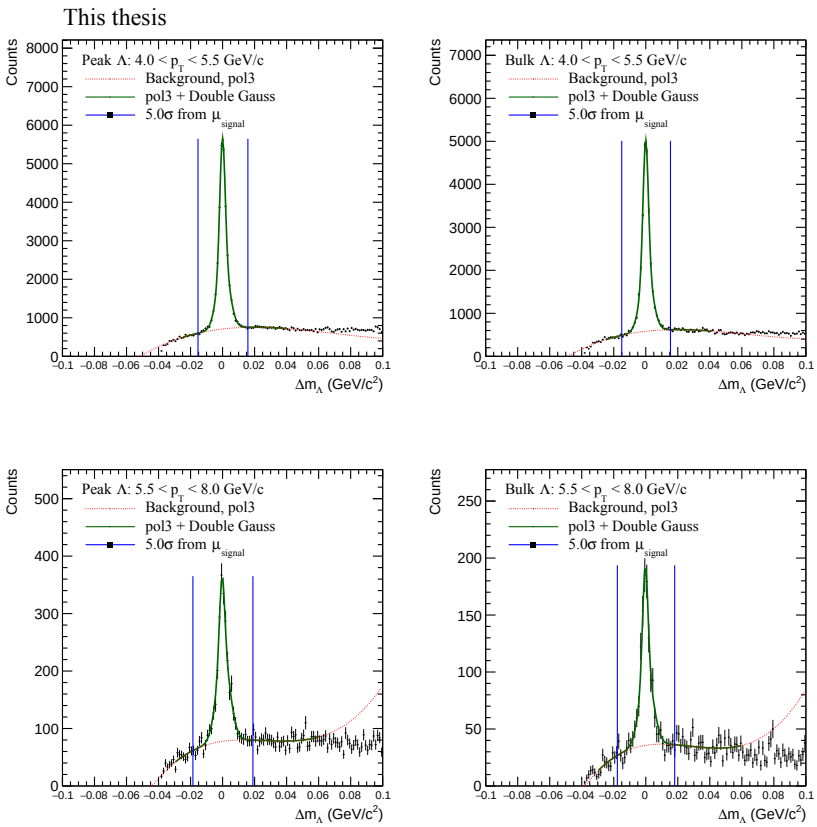
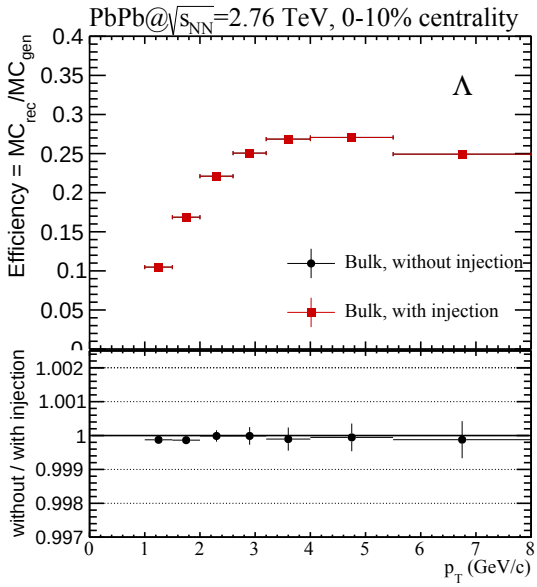
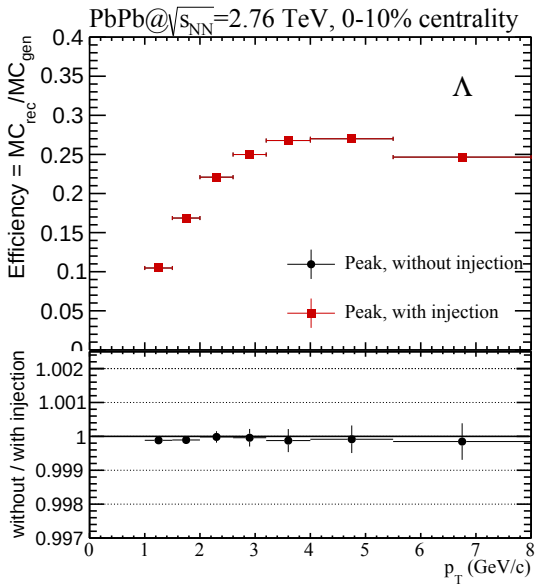


Figure B.4: Λ invariant mass distributions and fits for different p_{T} bins: 4.0-5.5, 5.5-8.0 GeV/c.

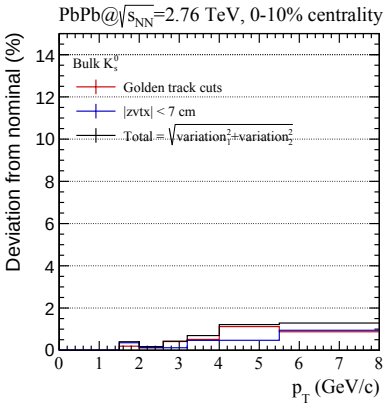


(a) Λ Bulk

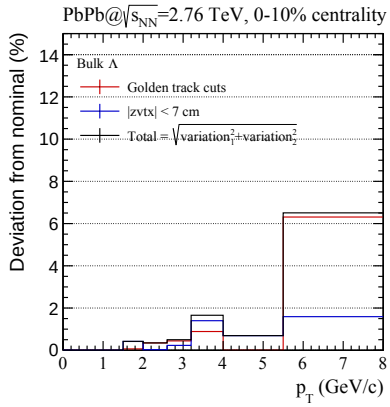


(b) Λ Peak

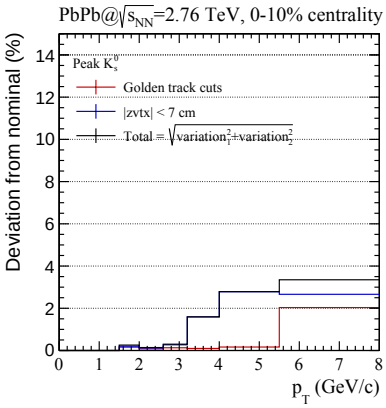
Figure B.5: The Λ peak and bulk efficiency with and without injected particles.



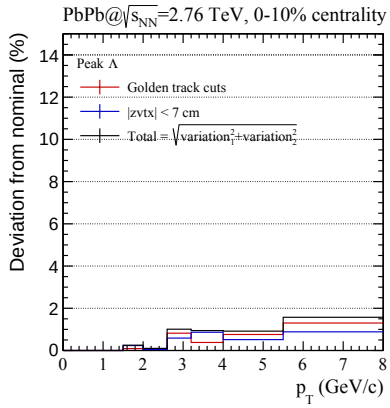
(a) K^0_s bulk



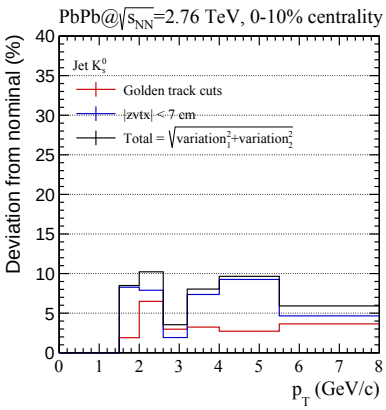
(b) Λ bulk



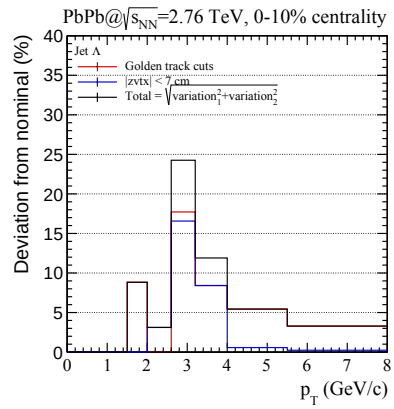
(c) K^0_s peak



(d) Λ peak

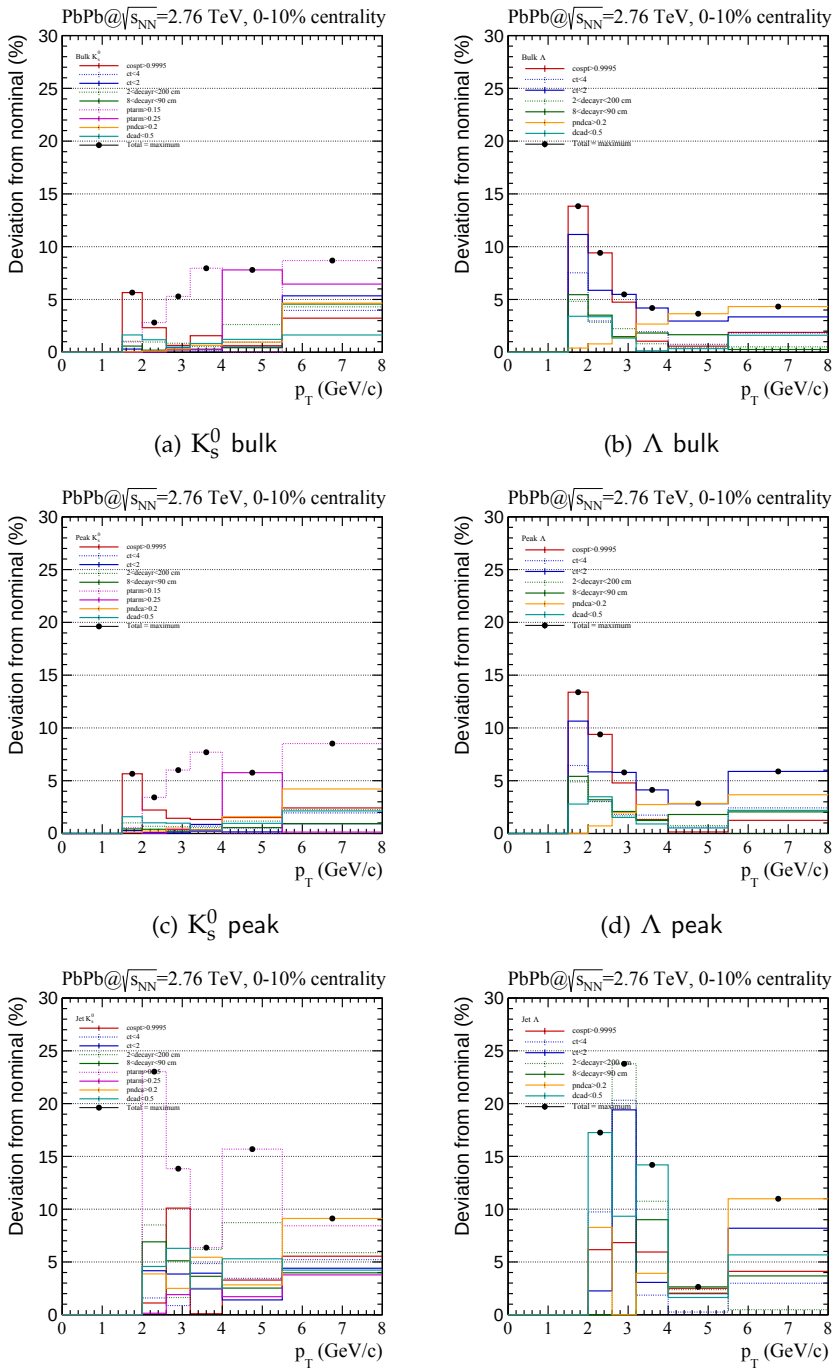


(e) K^0_s jet



(f) Λ jet

Figure B.6: Systematic deviation for vertex region and trigger particle track.

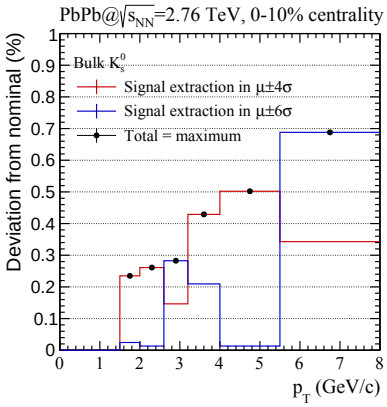


(a) K^0_S bulk (b) Λ bulk

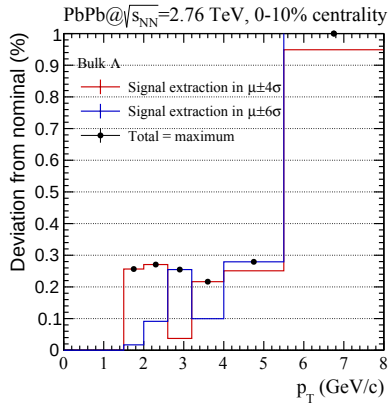
(c) K^0_S peak (d) Λ peak

(e) K^0_S jet (f) Λ jet

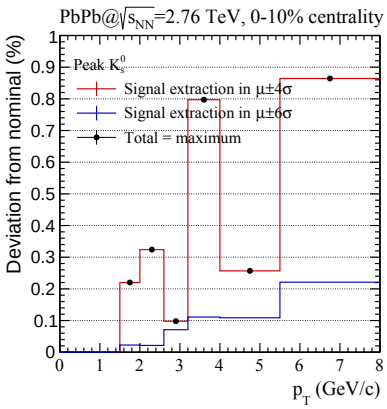
Figure B.7: Systematic deviation for cut variations.



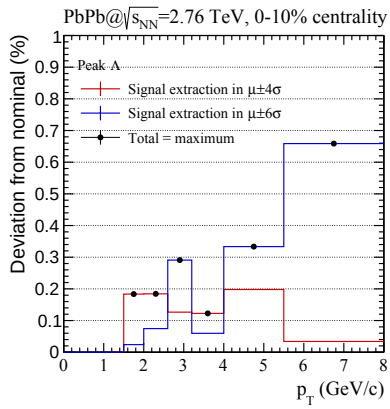
(a) K^0_s bulk



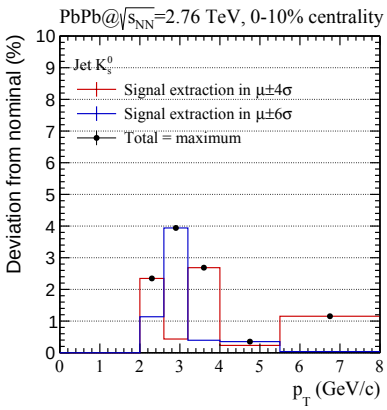
(b) Λ bulk



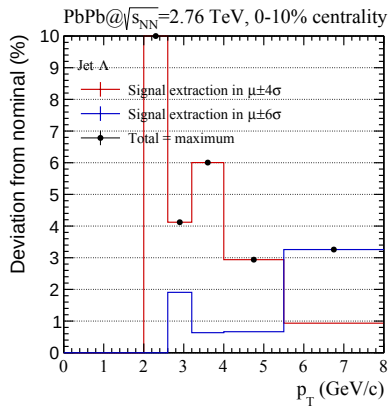
(c) K^0_s peak



(d) Λ peak



(e) K^0_s jet



(f) Λ jet

Figure B.8: Systematic deviation for varying signal extraction.

Appendix C

Units and variables

C.1 Rapidity and Pseudo-Rapidity

The dimensionless quantity *pseudo-rapidity* is related to the angle of the emitted particle with respect to the beam direction, defined as

$$\eta = -ln(tan\frac{\theta}{2}) \tag{C.1}$$

where θ is the polar angle to the beam axis, with $\theta = 0$ along the beam direction. Figure C.1 shows the pseudo-rapidity for different values of θ.

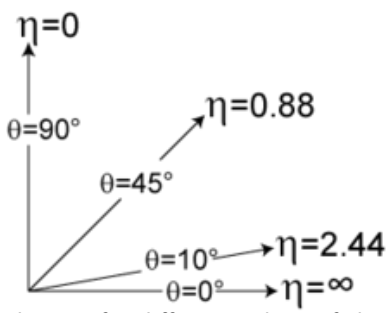


Figure C.1: Pseudo-rapidity, η, for different values of the angle between the beam axis and the emitted particle, θ, where $\theta = 0^\circ \rightarrow \eta = \text{inf}$ is in the beam direction, and $\theta = 90^\circ \rightarrow \eta = 0$ perpendicular to the beam.

The boost invariant *rapidity*, y, is defined as

$$y = \frac{1}{2} ln \left(\frac{E + p_L}{E - p_L} \right) \tag{C.2}$$

where E is the total energy and p_L is the longitudinal momentum of the particle. A particle with $y = 0$ is thus created in the center, while if $y > 0$ ($y < 0$) a particle is emitted in the forward (backward) region. When the transverse momentum of a particle is much larger than its mass (i.e. for high p_T particles), the rapidity can be approximated with the pseudo-rapidity.

The rapidity for a particle with mass m, transverse momentum p_{T}, and pseudo-rapidity η, is given by

$$y = \ln \left(\frac{\sqrt{m^2 + p_{\mathrm{T}}^2 \cosh^2 \eta} + p_{\mathrm{T}} \sinh \eta}{\sqrt{m^2 + p_{\mathrm{T}}^2}} \right) \tag{C.3}$$

ACKNOWLEDGMENTS

The Swedish participation in the ALICE collaboration is funded by the Swedish Research Council (VR), Knut & Alice Wallenberg Foundation (KAW) and FRN.

In addition, the following funding agencies have supported the building and running the ALICE detector: State Committee of Science, World Federation of Scientists (WFS) and Swiss Fonds Kidagan, Armenia; Conselho Nacional de Desenvolvimento Cient´ıfico e Tecnologico (CNPq), Financiadora de Estudos e Projetos (FINEP), Fundacao de Amparoa Pesquisa do Estado de Sao Paulo (FAPESP); National Natural Science Foundation of China (NSFC), the Chinese Ministry of Education (CMOE) and the Ministry of Science and Technology of China (MSTC); Ministry of Education and Youth of the Czech Republic; Danish Natural Science Research Council, the Carlsberg Foundation and the Danish National Research Foundation; The European Research Council under the European Community's Seventh Framework Programme; Helsinki Institute of Physics and the Academy of Finland; French CNRS-IN2P3, the 'Region Pays de Loire', 'Region Alsace', 'Region Auvergne' and CEA, France; German Bundesministerium fur Bildung, Wissenschaft, Forschung und Technologie (BMBF) and the Helmholtz Association; General Secretariat for Research and Technology, Ministry of Development, Greece; National Research, Development and Innovation Office (NKFIH), Hungary; Department of Atomic Energy and Department of Science and Technology of the Government of India; Istituto Nazionale di Fisica Nucleare (INFN) and Centro Fermi - Museo Storico della Fisica e Centro Studi e Ricerche "Enrico Fermi", Italy; Japan Society for the Promotion of Science (JSPS) KAKENHI and MEXT, Japan; Joint Institute for Nuclear Research, Dubna; National Research Foundation of Korea (NRF); Consejo Nacional de Cienca y Tecnologia (CONACYT), Direccion General de Asuntos del Personal Academico(DGAPA), Mexico, Amerique Latine Formation academique - European Commission (ALFA-EC) and the EPLANET Program (European Particle Physics Latin American Network); Stichting voor Fundamenteel Onderzoek der Materie (FOM) and the Nederlandse Organisatie voor Wetenschappelijk Onderzoek (NWO), Netherlands; Research Council of Norway (NFR); National Science Centre, Poland; Ministry of National Education/Institute for Atomic Physics and National Council of Scien-

tific Research in Higher Education (CNCSI-UEFISCDI), Romania; Ministry of Education and Science of Russian Federation, Russian Academy of Sciences, Russian Federal Agency of Atomic Energy, Russian Federal Agency for Science and Innovations and The Russian Foundation for Basic Research; Ministry of Education of Slovakia; Department of Science and Technology, South Africa; Centro de Investigaciones Energeticas, Medioambientales y Tecnologicas (CIEMAT), E-Infrastructure shared between Europe and Latin America (EELA), Ministerio de Econom´ıa y Competitividad (MINECO) of Spain, Xunta de Galicia (Conseller´ıa de Educacion), Centro de Aplicaciones Tecnolgicas y Desarrollo Nuclear (CEADEN), Cubaenergia, Cuba, and IAEA (International Atomic Energy Agency); Swedish Research Council (VR) and Knut & Alice Wallenberg Foundation (KAW); Ukraine Ministry of Education and Science; United Kingdom Science and Technology Facilities Council (STFC); The United States Department of Energy, the United States National Science Foundation, the State of Texas, and the State of Ohio; Ministry of Science, Education and Sports of Croatia and Unity through Knowledge Fund, Croatia; Council of Scientific and Industrial Research (CSIR), New Delhi, India; Pontificia Universidad Catolica del Peru.

Bibliography

[1] W. Florkowski. *Phenomenology of ultra-relativistic heavy-ion collisions*. World Scientific, 2010.

[2] Marek Gazdzicki. Quark gluon plasma in A + A collisions at CERN SPS. In *Nuclear matter in different phases and transitions. Proceedings, Workshop, Les Houches, France, March 31-April 10*, 1998.

[3] Brookhaven National Laboratory. *The Evidences for formation of Partonic matter by the four RHIC experiments are published the summary volume*. Nucl. Phys., A757, 2005.

[4] Elliott D. Bloom et al. High-Energy Inelastic e p Scattering at 6-Degrees and 10-Degrees. *Phys. Rev. Lett.*, 23:930–934, 1969.

[5] M. Gell-Mann. A schematic model of baryons and mesons. *Physics Letters*, 8:214–215, February 1964.

[6] G. Zweig. An SU(3) model for strong interaction symmetry and its breaking. Version 2. In D.B. Lichtenberg and Simon Peter Rosen, editors, *DEVELOPMENTS IN THE QUARK THEORY OF HADRONS. VOL. 1. 1964 - 1978*, pages 22–101. 1964.

[7] Fermilab. http://www.fnal.gov/pub/inquiring/matter/madeof/index.html.

[8] LIGO Scientific Collaboration and Virgo Collaboration. Observation of gravitational waves from a binary black hole merger. *Phys. Rev. Lett.*, 116:061102, Feb 2016.

[9] D.J. Gross and F. Wilczek. Ultraviolet behavior of non-abelian gauge theories. *Physical Review Letters*, 30:1343–1346, 1973.

[10] K. A. Olive et al. The Particle Data Group: Review of Particle Physics. *Chin. Phys.*, C38:090001, 2014.

[11] Quantum Diaries. http://www.quantumdiaries.org/2010/10/22/qcd-and-confinement/.

[12] B. Andersson, G. Gustafson, G. Ingelman, and T. Sjöstrand. Parton fragmentation and string dynamics. *Phys. Rept.*, 97(97):31 – 145, 1983.

[13] Torbjörn Sjöstrand. Jet fragmentation of multiparton configurations in a string framework. *Nuclear Physics B*, 248(2):469 – 502, 1984.

[14] J. Rafelski. *Melting hadrons, boiling quarks*. Eur.Phys.J. A51 (2015) no.9, 114, 2015.

[15] Thomas Schoerner-Sadenius, editor. *The Large Hadron Collider : Harvest of Run 1*. Springer International Publishing, Cham, 2015. English; http://inspirehep.net/record/1373790?ln=en.

[16] Peter Braun-Munzinger and Johanna Stachel. Hadron Production in Ultra-relativistic Nuclear Collisions and the QCD Phase Diagram: An Update. In Sabine Lee, editor, *From Nuclei to Stars: Festschrift in Honor of Gerald E Brown*, pages 103–115. 2011.

[17] The Ohio State University. https://u.osu.edu/vishnu/2014/08/06/sketch-of-relativistic-heavy-ion-collisions/.

[18] Michael L. Miller, Klaus Reygers, Stephen J. Sanders, and Peter Steinberg. Glauber modeling in high energy nuclear collisions. *Ann. Rev. Nucl. Part. Sci.*, 57:205–243, 2007.

[19] ALICE Collaboration. Centrality determination of Pb-Pb collisions at $\sqrt{s_{NN}}$ = 2.76 TeV with ALICE. *Phys. Rev.*, C88(4):044909, 2013.

[20] Toia Alberica. Participants and spectators at the heavy-ion fireball. *CERN COURIER*, 26 April 2013.

[21] Larry McLerran. The Color Glass Condensate and Glasma. *arXiv:0804.1736*, 2008.

[22] J. D. Bjorken and E. A. Paschos. Inelastic Electron-Proton and γ-Proton Scattering and the Structure of the Nucleon. *Physical Review*, 185:1975–1982, September 1969.

[23] C. Gwenlan. Combined HERA Deep Inelastic Scattering Data and NLO QCD Fits. *Nucl. Phys. Proc. Suppl.*, 191:5–15, 2009.

[24] ZEUS, H1. PDF Fits at HERA. *PoS*, EPS-HEP2011:320, 2011.

[25] Chiho Nonaka and Steffen A. Bass. Space-time evolution of bulk QCD matter. *Phys. Rev.*, C75:014902, 2007.

[26] Berndt Muller, Jurgen Schukraft, and Boleslaw Wyslouch. First Results from Pb+Pb collisions at the LHC. *Ann. Rev. Nucl. Part. Sci.*, 62:361–386, 2012.

[27] B. B. Back et al. The PHOBOS perspective on discoveries at RHIC. *Nucl. Phys.*, A757:28–101, 2005.

[28] Debasish Banerjee, Jajati K. Nayak, and Raju Venugopalan. Two introductory lectures on high energy QCD and heavy ion collisions. *Lect. Notes Phys.*, 785:105–137, 2010.

[29] BRAHMS Collaboration. Quark gluon plasma and color glass condensate at RHIC? The Perspective from the BRAHMS experiment. *Nucl. Phys.*, A757:1–27, 2005.

[30] P. Huovinen and P. V. Ruuskanen. Hydrodynamic Models for Heavy Ion Collisions. *Ann. Rev. Nucl. Part. Sci.*, 56:163–206, 2006.

[31] F. Becattini. An Introduction to the Statistical Hadronization Model. In *International School on Quark-Gluon Plasma and Heavy Ion Collisions: past, present, future Villa Gualino, Torino, Italy, arXiv:0901.3643*, 2009.

[32] ALICE Collaboration. Centrality dependence of π, K, p production in Pb-Pb collisions at $\sqrt{s_{NN}}$ = 2.76 TeV. *Phys. Rev.*, C88:044910, 2013.

[33] Ekkard Schnedermann, Josef Sollfrank, and Ulrich W. Heinz. Thermal phenomenology of hadrons from 200-A/GeV S+S collisions. *Phys. Rev.*, C48:2462–2475, 1993.

[34] ALICE Collaboration. Pion, Kaon, and Proton Production in Central Pb–Pb Collisions at $\sqrt{s_{NN}} = 2.76$ TeV. *Phys. Rev. Lett.*, 109:252301, 2012.

[35] Sergei A. Voloshin, Arthur M. Poskanzer, and Raimond Snellings. Collective phenomena in non-central nuclear collisions, arXiv:0809.2949. 2008.

[36] Huichao Song and Ulrich W. Heinz. Suppression of elliptic flow in a minimally viscous quark-gluon plasma. *Phys. Lett.*, B658:279–283, 2008.

[37] Chun Shen, Ulrich Heinz, Pasi Huovinen, and Huichao Song. Radial and elliptic flow in Pb+Pb collisions at the Large Hadron Collider from viscous hydrodynamic. *Phys. Rev.*, C84:044903, 2011.

[38] Iu. A. Karpenko, Yu. M. Sinyukov, and K. Werner. Uniform description of bulk observables in the hydrokinetic model of $A + A$ collisions at the BNL Relativistic Heavy Ion Collider and the CERN Large Hadron Collider. *Phys. Rev.*, C87(2):024914, 2013.

[39] Piotr Bozek. Collective flow in p-Pb and d-Pd collisions at TeV energies. *Phys. Rev.*, C85:014911, 2012.

[40] Piotr Bozek. Hydrodynamic flow from RHIC to LHC. *Acta Phys. Polon.*, B43:689, 2012.

[41] Domenico Elia. Strange and identified particle production with ALICE at the LHC. *EPJ Web Conf.*, 95:03008, 2015.

[42] J. Cleymans, I. Kraus, H. Oeschler, K. Redlich, and S. Wheaton. Statistical model predictions for particle ratios at s(NN)**(1/2) = 5.5-TeV. *Phys. Rev.*, C74:034903, 2006.

[43] A. Andronic, P. Braun-Munzinger, and J. Stachel. Hadron production in central nucleus-nucleus collisions at chemical freeze-out. *Nucl. Phys.*, A772:167–199, 2006.

[44] M. Petran, J. Letessier, J. Rafelski, and G. Torrieri. SHARE with CHARM. *Comput. Phys. Commun.*, 185:2056–2079, 2014.

[45] ALICE Collaboration. Production of charged pions, kaons and protons at large transverse momenta in pp and Pb–Pb collisions at $\sqrt{s_{\rm NN}}$ =2.76 TeV. *Phys. Lett.*, B736:196–207, 2014.

[46] Ulrich W. Heinz. The Strongly coupled quark-gluon plasma created at RHIC. *J. Phys.*, A42:214003, 2009.

[47] STAR Collaboration. Long range rapidity correlations and jet production in high energy nuclear collisions. *Phys. Rev.*, C80:064912, 2009.

[48] PHOBOS Collaboration. High transverse momentum triggered correlations over a large pseudorapidity acceptance in Au+Au collisions at s(NN)**1/2 = 200 GeV. *Phys. Rev. Lett.*, 104:062301, 2010.

[49] ALICE Collaboration. Harmonic decomposition of two-particle angular correlations in Pb-Pb collisions at $\sqrt{s_{NN}} = 2.76$ TeV. *Phys. Lett.*, B708:249–264, 2012.

[50] Arthur M. Poskanzer and S. A. Voloshin. Methods for analyzing anisotropic flow in relativistic nuclear collisions. *Phys. Rev.*, C58:1671–1678, 1998.

[51] Ante Bilandzic, Raimond Snellings, and Sergei Voloshin. Flow analysis with cumulants: Direct calculations. *Phys. Rev.*, C83:044913, 2011.

[52] Nicolas Borghini, Phuong Mai Dinh, and Jean-Yves Ollitrault. Flow analysis from multiparticle azimuthal correlations. *Phys. Rev.*, C64:054901, 2001.

[53] ALICE Collaboration. Elliptic flow of identified hadrons in Pb-Pb collisions at $\sqrt{s_{\rm NN}} = 2.76$ TeV. *JHEP*, 06:190, 2015.

[54] Huichao Song, Steffen A. Bass, Ulrich Heinz, Tetsufumi Hirano, and Chun Shen. Hadron spectra and elliptic flow for 200 A GeV Au+Au collisions from viscous hydrodynamics coupled to a Boltzmann cascade. *Phys. Rev.*, C83:054910, 2011. [Erratum: Phys. Rev.C86,059903(2012)].

[55] B. Müller B. Jacak. The exploration of hot nuclear matter. *Science*, 337, 2012.

[56] P. Kovtun, Dan T. Son, and Andrei O. Starinets. Viscosity in strongly interacting quantum field theories from black hole physics. *Phys. Rev. Lett.*, 94:111601, 2005.

[57] PHENIX Collaboration. Scaling properties of azimuthal anisotropy in Au+Au and Cu+Cu collisions at s(NN) = 200-GeV. *Phys. Rev. Lett.*, 98:162301, 2007.

[58] David d'Enterria. Jet quenching. *Landolt-Bornstein*, 23:471, 2010.

[59] Guang-You Qin and Xin-Nian Wang. Jet quenching in high-energy heavy-ion collisions. *Int. J. Mod. Phys.*, E24(11):1530014, 2015.

[60] I. Kozlov, Matthew Luzum, Gabriel S. Denicol, Sangyong Jeon, and Charles Gale. Signatures of collective behavior in small systems. *Nucl. Phys.*, A931:1045–1050, 2014.

[61] Sami S. Räsänen. ALICE overview. In *4th International Conference on New Frontiers in Physics (ICNFP 2015) Kolymbari, Greece, August 23-30, 2015, arXiv:1603.03320*, 2016.

[62] ALICE Collaboration. Transverse momentum distribution and nuclear modification factor of charged particles in p-Pb collisions at $\sqrt{s_{NN}} = 5.02$ TeV. *Phys. Rev. Lett.*, 110(8):082302, 2013.

[63] Tuva Richert. ALICE summary of light flavour results at intermediate and high p_T. *J. Phys. Conf. Ser.*, 636(1):012009, 2015.

[64] ALICE Collaboration. Centrality dependence of the nuclear modification factor of charged pions, kaons, and protons in Pb-Pb collisions at $\sqrt{s_{\rm NN}} = 2.76$ TeV. *Phys. Rev.*, C93(3):034913, 2016.

[65] Simone Schuchmann. *Modification of K^0_s and $\Lambda(\overline{\Lambda})$ transverse momentum spectra in Pb-Pb collisions at $\sqrt{s}NN$ = 2.76 TeV with ALICE*. PhD thesis, Frankfurt U., 2015-04-14.

[66] ALICE Collaboration. K^0_S and Λ production in Pb-Pb collisions at $\sqrt{s_{NN}}$ = 2.76 TeV. *Phys. Rev. Lett.*, 111:222301, 2013.

[67] K. Werner. Lambda-to-Kaon Ratio Enhancement in Heavy Ion Collisions at Several TeV. *Phys. Rev. Lett.*, 109:102301, 2012.

[68] K. Werner, Iu. Karpenko, M. Bleicher, T. Pierog, and S. Porteboeuf-Houssais. Jets, Bulk Matter, and their Interaction in Heavy Ion Collisions at Several TeV. *Phys. Rev.*, C85:064907, 2012.

[69] ALICE Collaboration. $K^*(892)^0$ and $\phi(1020)$ production in Pb-Pb collisions at $\sqrt{sNN}$ = 2.76 TeV. *Phys. Rev.*, C91:024609, 2015.

[70] R. J. Fries, Berndt Muller, C. Nonaka, and S. A. Bass. Hadronization in heavy ion collisions: Recombination and fragmentation of partons. *Phys. Rev. Lett.*, 90:202303, 2003.

[71] David G. d'Enterria. Quark-Gluon Matter. *J. Phys.*, G34:S53–S82, 2007.

[72] ALICE Collaboration. Performance of the ALICE Experiment at the CERN LHC. *Int. J. Mod. Phys.*, A29:1430044, 2014.

[73] ALICE Collaboration. Centrality dependence of the charged-particle multiplicity density at mid-rapidity in Pb-Pb collisions at $\sqrt{s_{NN}}$ = 2.76 TeV. *Phys. Rev. Lett.*, 106:032301, 2011.

[74] Saikat Biswas. ALICE TPC upgrade for High-Rate operations. In *7th International Conference on Physics and Astrophysics of Quark Gluon Plasma (ICPAQGP) Kolkata, West Bengal, India, arXiv:511.04988*, 2015.

[75] ALICE Public Pages. http://aliceinfo.cern.ch/public/en/chapter2/chap2_tpc.html.

[76] J. Alme et al. The ALICE TPC, a large 3-dimensional tracking device with fast readout for ultra-high multiplicity events. *Nucl. Instrum. Meth.*, A622:316–367, 2010.

[77] Arild Velure. Upgrades of the ALICE TPC Front-End Electronics for Long Shutdown 1 and 2. *IEEE Trans. Nucl. Sci.*, 62(3):1040–1044, 2015.

[78] Thorsten Kolleger. Using the High Level Trigger to compress TPC data. *ALICE Matters*, 2011.

[79] Antonin Maire. *Multi-strange baryon production at the LHC in proton-proton collisions with the ALICE experiment, CERN-THESIS-2011-263*. Theses, Université de Strasbourg, October 2011.

[80] ALICE Collaboration. Kalman Filtering Application for Track Recognition and Reconstruction in ALICE Tracking System. *ALICE-INT-1997-24, CERN-ALICE-INT-1997-24*, 1997.

[81] Veikko Karimäki. Effective Vertex Fitting. *CERN-CMS-NOTE-1997-051, CMS-NOTE-1997-051*, 1997.

[82] B.R. Martin and G. Shaw. *Particle Physics, Third Edition*. Wiley, 2008.

[83] Misha Veldhoen. p/π Ratio in Di-Hadron Correlations. *Nucl. Phys.*, A910-911:306–309, 2013.

[84] Xitzel Sanchez Castro. K^0_S *and* Λ *production associated to high-*p_T *particles in Pb-Pb collisions at* $\sqrt{s_{NN}}$ *= 2.76 TeV with ALICE*. PhD thesis, Strasbourg, IPHC, 2015-06-18.

[85] Xin-Nian Wang and Miklos Gyulassy. HIJING: A Monte Carlo model for multiple jet production in p p, p A and A A collisions. *Phys. Rev.*, D44:3501–3516, 1991.

[86] The ALICE Offline Pages. http://aliweb.cern.ch/offline/.

[87] Photo courtesy of Berkeley Lab. Source: Bc-340; xbb8511-9655 and 9656.

[88] Vít Kučera. Production of strange particles in charged jets in Pb–Pb and p–Pb collisions measured with ALICE. In *7th International Conference on Hard and Electromagnetic Probes of High-Energy Nuclear Collisions (Hard Probes) Montréal, Québec, Canada, arXiv:1511.02766*, 2015.

[89] ALICE Collaboration. Strange particle production in proton-proton collisions at sqrt(s) = 0.9 TeV with ALICE at the LHC. *Eur. Phys. J.*, C71:1594, 2011.

[90] José Guilherme Milhano and Korinna Christine Zapp. Origins of the di-jet asymmetry in heavy ion collisions. *arXiv:1512.08107*, 2015.

[91] Yacine Mehtar-Tani, Jose Guilherme Milhano, and Konrad Tywoniuk. Jet physics in heavy-ion collisions. *Int. J. Mod. Phys.*, A28:1340013, 2013.

[92] Korinna C. Zapp, Frank Krauss, and Urs A. Wiedemann. A perturbative framework for jet quenching. *JHEP*, 03:080, 2013.

[93] ALICE Collaboration. Particle-yield modification in jet-like azimuthal di-hadron correlations in Pb-Pb collisions at $\sqrt{s_{NN}} = 2.76$ TeV. *Phys. Rev. Lett.*, 108:092301, 2012.

[94] CMS Collaboration. Studies of jet quenching using isolated-photon+jet correlations in PbPb and pp collisions at $\sqrt{s_{NN}} = 2.76$ TeV. *Phys. Lett.*, B718:773–794, 2013.

[95] CMS Collaboration. Measurement of isolated photon production in pp and PbPb collisions at $\sqrt{s_{NN}} = 2.76$ TeV. *Phys. Lett.*, B710:256–277, 2012.

[96] Antonio Ortiz Velasquez, Peter Christiansen, Eleazar Cuautle Flores, Ivonne Maldonado Cervantes, and Guy Paić. Color Reconnection and Flowlike Patterns in pp Collisions. *Phys. Rev. Lett.*, 111(4):042001, 2013.

Printed by Media-Tryck, Lund University 2016
Nordic Ecolabel 341903



LUND UNIVERSITY
Faculty of science
Department of Physics
ISBN 978-91-7623-850-9 (Print)
978-91-7623-851-6 (PDF)

